Enhanced Simulation of the Milling Process for a Novel Roughing and Finishing Tool

Von der Fakultät für Maschinenbau
der Gottfried Wilhelm Leibniz Universität Hannover
zur Erlangung des akademischen Grades
Doktor-Ingenieur
genehmigte Dissertation

von
Dipl.-Ing. Roman Grabowski

2019

Tag der mündlichen Prüfung: 21.11.2019

1. Referent: Prof. Dr.-Ing. Berend Denkena
2. Referent: Prof. Dr.-Ing. Jörg Wallaschek

Vorsitzender: Prof. Dr.-Ing. Tobias Ortmaier

Preamble

Die vorliegende Arbeit entstand während meiner Tätigkeit als wissenschaftlicher Mitarbeiter am Institut für Fertigungstechnik und Werkzeugmaschinen (IFW) der Leibniz Universität Hannover.

Herrn Prof. Dr.-Ing. Berend Denkena, dem Leiter des Instituts für Fertigungstechnik und Werkzeugmaschinen, gilt mein besonderer Dank für die vertrauensvolle und wohlwollende Unterstützung, die ich während meiner Tätigkeit am Institut erfahren habe.
Herrn Prof. Dr.-Ing. Jörg Wallaschek danke ich für die Übernahme des Korreferates. Ebenso gilt mein Dank Herrn Prof. Dr.-Ing. Tobias Ortmaier für die Übernahme des Prüfungsvorsitzes.

Den Mitarbeiterinnen und Mitarbeitern des IFW danke ich für ihre stete Hilfsbereitschaft und die gute Zusammenarbeit. Mein besonderer Dank gilt Herrn Dr.-Ing. Volker Sellmeier, Herrn Dr.-Ing. Thilo Grove und Herrn Lars Ellersiek für die kritische Durchsicht dieser Arbeit und die wertvollen Anmerkungen. Ebenfalls bedanke ich mich bei meinen studentischen Hilfskräften, Bachelor- und Masterabeitern für ihre Unterstützung. Besonders hervorheben möchte ich stellvertretend Herrn Waldemar Ernst, Herrn Takayuki Hirano von der Keio University Tokyo und Herrn Oliver Pape. Ferner gilt mein Dank Herrn Dr.-Ing. Josef Kleckner von der Robert Bosch GmbH für die geduldige und ausführliche Vermittlung der fachlichen Grundlagen, auf denen diese Arbeit fundiert.

Mein größter Dank gilt schließlich meinen Eltern, die mir meine Ausbildung ermöglicht und mich immer unterstützt haben. Ebenso danke ich meinem Bruder für den Vorschlag Maschinenbau zu studieren. Meiner Frau Carolin danke ich für die Geduld und den bedinungslosen Rückhalt.

Roman Grabowski

Kurzfassung

Weiterentwickelte Simulation des Fräsprozesses für ein neuartiges Schrupp- und Schlichtwerkzeug

Schlagworte: Fräsen, Rattern, Prozessstabilität, Totzeiten, Oberflächengüte, Rundlauffehler

Bei der spanenden Fertigung von Werkstücken aus Aluminiumlegierungen wird häufig im ersten Schritt ein Schruppfräser eingesetzt, der einen möglichst hohen Materialabtrag ermöglicht. Um hohe Oberflächengüten zu erreichen, erfolgt im zweiten Schritt die Fertigung der Endkontur mit einem Schlichtfräser. Durch den Einsatz eines neuen und patentierten Werkzeugkonzeptes lassen sich sowohl Schrupp- als Schlichtvorgänge mit diesem einen Werkzeug durchführen. Die Besonderheit dieses Werkzeugkonzeptes basiert auf der unterschiedlichen geometrischen Auslegung der einzelnen Schneiden. Eine prozessoptimierte Auslegung der Werkzeuggeometrie des Prototypwerkzeuges kann anhand einer vorhergehenden Berechnung der Prozesskräfte und des dynamischen Verhaltens erfolgen. Hierfür wurden die entsprechenden mathematischen Modelle entwickelt. Anhand von experimentellen Untersuchungen erfolgte die Verifikation der Schrupp- und Schlichtfähigkeit des Werkzeugkonzeptes. Die Ergebnisse verdeutlichten, dass das Werkzeug in beiden Fällen vergleichbare Ergebnisse erzielt wie reine Schlicht- und Schruppfräser. Hieraus folgt, dass das neue Werkzeugkonzept durch die Verringerung der benötigten Werkzeuge zu einer Produktivitätssteigerung beitragen kann.

Abstract

Enhanced Simulation of the Milling Process for a Novel Roughing and Finishing Tool

Keywords: milling, chatter, process stability, time delays, surface quality, runout error

For milling of aluminum alloys a roughing cutter is often used in the first step to achieve a high material removal rate. In order to obtain a high surface quality, the final contour is produced using a finishing cutter. By using a new and patented tool concept, both roughing and finishing operations can be carried out with this one tool. The special feature of this tool concept is based on the different geometric design of the individual cutting edges. A process-optimized design of the tool geometry of the prototype tool can be performed based on a preliminary calculation of the process forces and the dynamic behavior. The corresponding mathematical models have been developed for this purpose. On the basis of experimental investigations, the verification of the roughing and finishing capability of the tool concept was carried out. The results showed that the tool achieved comparable results in both cases to pure finishing and roughing cutters. It follows that the new tool concept can increase productivity by reducing the number of necessary end mills.

Contents

Preamble iii

Kurzfassung/Abstract iv

Nomenclature viii

1 Introduction 1

2 State of the Art 2
- 2.1 Application-specific End Mill Geometries . . . 2
- 2.2 Process Dynamics Modeling of Milling Operations . . . 4
- 2.3 Influence of Tool Geometry and Process Forces on Process Dynamics . . . 8
  - 2.3.1 Macro Geometric Tool Attributes . . . 8
  - 2.3.2 Correlation of Cutting Edge Shape and Process Damping . . . 10
- 2.4 Disturbance Factors on Stability and Surface Finish . . . 13
  - 2.4.1 Tool Runout . . . 13
  - 2.4.2 Flank Face Deformation Error . . . 14
  - 2.4.3 Burr Formation . . . 16
  - 2.4.4 Thermal Load . . . 17
- 2.5 Conclusions on the State of the Art . . . 18

3 Objective and Approach 20

4 Mechanistic Modeling of Milling Forces 23
- 4.1 Generalized Process Force Calculation for Arbitrary Flute Geometries . . . 23
- 4.2 Undeformed Chip Thickness Based on Trochoidal Flute Movement . . . 29
- 4.3 Tool Runout . . . 34
- 4.4 Identification of Process Force Coefficients and Runout with Particle Swarm Optimization . . . 36

5 Modeling of the Dynamic Behavior of Milling Systems 40
- 5.1 Semi-Discrete Time-Domain Solution with Consideration of Multidimensional Distributed Time-Delays . . . 40
- 5.2 Time-Domain Simulation . . . 46

6 Model Based Estimation of the Machining Behavior 50
- 6.1 Process Forces . . . 50
  - 6.1.1 Comparison between Average and Instantaneous Cutting Force Method . 50
  - 6.1.2 Influence of Tool Runout on Process Force Coefficient Identification . . . 52
  - 6.1.3 Influence of Cutting Force Coefficients on Stability . . . 55
  - 6.1.4 Speed-Varying Process Force Coefficients . . . 58
  - 6.1.5 Estimation of Process Damping Forces . . . 59

6.2 Tool Geometry 62
6.2.1 Influence of Radial Offset on Time Delays and Stability 63
6.2.2 Influence of Tool Runout on Time Delays and Stability 68
6.2.3 Influence on Surface Deformation 73

7 Experimental Evaluation 77
7.1 Preliminary Experiments 77
7.1.1 Process Force Comparison with Sharp and Chamfered Tools 78
7.1.2 Identification of Cutting Force Coefficients 81
7.1.3 Cutting Speed Dependent Process Forces 86
7.1.4 Modal Analysis of Experimental Setup for Stability Tests 87
7.1.5 Identification of Runout Error 89
7.2 Process Stability Analysis 92
7.2.1 Comparison with Sharp and Chamfered Tools 92
7.2.2 Influence of the Radial Offset Value on Stability 100
7.3 Assessment of Surface Quality 102
7.3.1 Surface Topography 102
7.3.2 Burr Formation 105
7.3.3 Thermal Load 108

8 Design Recommendation 115

9 Summary and Outlook 118

Bibliography 122

Curriculum Vitae 136

Nomenclature

Acronyms

Symbol	Description
ACFM	average cutting force method
DOF	degree of freedom
EDX	energy dispersive X-ray spectroscopy
FEM	finite element method
ICFM	instantaneous cutting force method
PSO	particle swarm optimization
SD	Semi-Discretization
SEM	scanning electron microscope
STFT	short-time FOURIER transformation

Greek Symbols

Symbol	Unit	Description
α_{eff}	rad	effective clearance angle
α	rad	clearance angle
α_{f}	rad	chamfer angle
α_{v}	rad	effective direction angle of active force
δ_{j}	rad	helix angle of flute j
$\Delta\mathbf{q}$	m	relative dynamic displacement between the workpiece and tool
$\Delta\mathrm{R}$	µm	radial offset of a flute
$\Delta\mathrm{x}$, $\Delta\mathrm{y}$	m	relative dynamic displacement between the workpiece and tool in x- and y-direction
γ	rad	rake angle
$\varkappa_{\mathrm{j}}$	rad	cutting edge position angle of flute j
λ_{r}	rad	runout location angle
μ	–	friction coefficient in case of process damping
φ	rad	angular position of a tooth
$\mathbf{\Phi}_{\mathrm{exp}}$	–	expanded transition/monodromy matrix
ϱ_{r}	mm	runout offset
$\mathrm{r}_{\mathrm{im,j,u}}$	%	immersion rate for tooth pitch $\mathrm{p}_{\mathrm{j,u}}$
φ	rad	immersion angle

Latin Symbols

Symbol	**Unit**	**Description**
$\mathbf{A}$	–	state/system matrix
$A_{dyn,f}$	N/s	dynamic force signal area
a_e, a_p	mm	radial and axial immersion
A_j	mm^2	machining area of the j-tooth
A_{pd}^*	mm^3	precise numerical estimation of the indentation area
A_{pd}	mm^3	indentation area
$A_{stat,f}$	N/s	static force signal area
$\mathbf{B}$	–	input matrix
b_f	µm	chamfer width
$\mathbf{u}$	–	input vector
c_g	–	swarm confidence factor
c_l	–	self confidence factor
c_r	mm	center of rotation
c_t	mm	tool center point
$\mathbf{D}$	kg	modal damping matrix
D	mm	tool diameter
$\mathcal{F}$	Hz	sampling frequency
f_c	Hz	chatter frequency
f_d	Hz	discrete frequency step
F_f, F_{fN}, F_p	N	feed, feed normal and passive force
$f_{j,u}$	mm	effective feed per tooth between flute j and u
F_{min}	N	deviation between the simulated and experimental forces
f_s	Hz	spindle frequency
f_t	Hz	tooth passing frequency
F_t, F_r, F_a	N	tangential, radial and active force
f_z	mm	feed per tooth
$g_{j,u}$	–	HEAVISIDE step function between flute j and u
h	mm	undeformed/uncut chip thickness
h_0	mm	burr height
h_{dyn}	mm	pertubed/dynamic part of the undeformed/uncut chip thickness
h_{per}	mm	periodic part of the undeformed/uncut chip thickness
$\mathbf{I}$	–	identity matrix
$\mathbf{J}$	–	matrix of ones

j	–	index for the number of flutes
$\mathbf{K}$	kg	modal stiffness matrix
k, l, m, n	–	number of oscillators for workpiece in x- and y-direction (k and l) and tool in x- and y-direction (m and n)
K_{pd}	N/mm^3	process damping coefficient
K_{tc}, K_{rc}, K_{ac}	N/mm^2	specific tangential, radial and axial cutting coefficient
K_{te}, K_{re}, K_{ae}	N/mm	specific tangential, radial and axial edge coefficient
L	mm	cantilever length of the tool
l_2	mm	cutting length
l_4	mm	total length
$\mathbf{M}$	kg	modal mass matrix
m	–	period resolution
n	min^{-1}	spindle speed
N_k	–	number of discrete positions for one tool revolution
N_p	–	swarm members for the PSO algorithm
N_{rev}	–	number of discrete positions for the time for one tool revolution
N_s	–	number of movements for the PSO algorithm (swarm iterations)
N_t	–	number of teeth
N_z	–	number of discrete positions in z-direction
$\mathbf{p}$	rad	tooth pitch vector (assuming constant values in z-direction along flutes)
$\mathbf{p}_{g,k}$	–	position of the particle with best global fitness at current move k
$\mathbf{p}_{i,k}$	–	position of the i-th particle at current move k
$f_{j,u}$	mm	tooth pitch between flute j and u
$\mathbf{p}_{lb}$	–	lower boundary for $\mathbf{p}_{i,k}$
$\mathbf{p}_{l,i}$	–	best position of particle i in current and all previous moves
$\mathbf{p}_{ub}$	–	upper boundary for $\mathbf{p}_{i,k}$
$\mathbf{q}$	m	vector, which contains all oscillator in x- and y-direction
$\mathbf{r}$	mm	tooth radius vector (assuming constant values in z-direction along flutes)
R	mm	corner radius of the tool
r_{amp}	–	chatter amplitude ratio
r_j	mm	radius of flute j
$\mathbf{r}_{pg,i,k}$	–	weighting factor for the swarm influence
$\mathbf{r}_{pl,i,k}$	–	weighting factor for the particle memory
R_{th}	mm	kinematic/theoretical roughness
$\mathbf{r}_{v,i,k}$	–	random inertia factor
$\mathbf{r}_{v,i,k}$	–	weighting factor for the current motion of the particle swarm

S_j	mm	trajectory of flute j
T	s	sampling interval
t	s	continuous time step
T_{rev}	s	time for one tool revolution
t_d	s	discrete time step
t_{rev}	s	time vector for one tool revolution
u	–	second index for the number of flutes (hybrid tool specific extension to the main index j)
v_c	m/min	cutting velocity
v_f	m/min	feed forward velocity
$\mathbf{v}_{i,k}$	–	velocity of the i-th particle at current move k
w	–	total number of oscillators $w = k + l + m + n$
$\mathbf{x}$	–	state vector
z_d	mm	discrete value for z-direction
z_i	mm	incremental axial position

1 Introduction

Material removal rate, tool life, process stability, surface finish and the prevention of burr formation are important aspects of the machining performance of metallic materials [Arr13]. The relations between these key aspects, however, prevent a simultaneous optimization of all aspects at the same time. Therefore, tools are usually designed for roughing or finishing operations. Tools for roughing are designed to achieve high material removal rates at the lowest possible costs. Thus, high process stability is required. Finishing tools are optimized for surface quality and low burr formation.

For machining aluminum, different universal tools offer a compromise between roughing and finishing. Tools with uneven helix angles, unequal tooth pitch or a combination of these attributes are often used for combined roughing and finishing. The highest possible process stability can be reached by the use of chamfered cutting edges [Coo59]. However, chamfered cutting edges [Gro06, p. 100] or flank wear [Gil76] can decrease surface quality and lead to high burr formation. Furthermore, high temperatures result from the friction between workpiece and chamfered edge. Especially for the machining of aluminum, this increases material adherence to the cutting edge. Consequently, ordinary tools with chamfered cutting edges are not suitable for finishing or combined roughing and finishing operations.

A new and already patented hybrid tool [Den17] with chamfered and sharp cutting edges is proposed in this work. The chamfered cutting edges allow high process stability during roughing. To avoid contact with the final finish surface, the chamfered cutting edges have a smaller distance to the tool center point. The sharp cutting edges ensure the necessary surface quality during finishing. This work focuses on the simulation based analysis of the dynamics and mechanics of this tool concept. The interactions between the roughing and finishing flutes will be investigated with process stability as the main priority. This will allow for a more sophisticated and application optimized tool development.

2 State of the Art

One of the first mentions of chatter can be found in the first volume of the Transactions of the American Society of Mechanical Engineers, published in 1880, were Charles Talbot Porter described chatter as a state that mechanics try to avoid [Por80]. He stated that "perfection, both in form and finish", cannot be reached only by avoiding chatter and pointed out the importance of the "strength of the machine tool". At the beginning of the 20th century, when the production of cutting tools was carried out by smiths, Taylor found out for turning processes that the occurrence of chatter depends on the geometry of the tool [Tay07, p. 152 f.]. In this context, Airey and Oxford made extensive investigations on the influence of tool geometry on roughing operations [Air22]. One of their drawn conclusion was that excessive clearance fosters chatter, and thus, low clearance is favorable. This may be considered as one of the first cited findings that the contact between the flank face of the cutting wedge and the workpiece induce a stabilizing effect, often referred to as process-damping.

It can be stated that the tool geometry is of importance for stability (roughing) as well as surface quality (finishing). In Chapter 2.1 the essential requirements for roughing and finishing are compiled. Primarily it is shown which geometric tool shape properties contribute to a tool design that can be used for both applications. For a process-optimized design of the tool geometry, a corresponding mathematical modeling of the machining process is of importance. The basics of milling modeling are presented in Chapter 2.2. In this context, Chapter 2.3 discusses the influence of the cutting flute geometry (macro geometry of the tool) as well as the cutting edge geometry (micro geometry of the cutting edge) on the resulting process forces and the dynamic behavior of the milling process. This is especially important for roughing operations. Chapter 2.4 shows which disturbances significantly influence the finishing operation, and thus, surface quality. However, these disturbances can also have an effect on the stability and are therefore also of interest for roughing.

2.1 Application-specific End Mill Geometries

During roughing, the highest achievable removal rate which yields the lowest machining costs is considered the target value. Thus, high feed rates v_f as well as high axial and radial immersions a_p and a_e, respectively, are necessary for roughing. However, high removal rates, and thus, increased process forces, may lead to an unstable cutting condition. In order to ensure a stable machining operation with high removal rates, e.g. cutters with serrated flutes are used. The shape of such flutes cause a modulation of the uncut chip thickness due to vibrations, and thus, disrupt or interfere with the regenerative effect for certain process parameters [Dom10, Sté14]. This modification allows almost the same stability increase as tools with chamfered cutting edges. The goal of finishing is to achieve the required surface quality combined with the prevention of burr formation at the lowest possible costs. Thus, end mills with serrated or chamfered flutes should not be considered for this task. In general, this is no major problem in case of stability concerns, as radial immersion is rather low for finishing. However, if the workpiece is flexible, e.g. turbine blades, stability issues may still arise. Concerning avoidance of burr formation, Enomoto et al. concluded for machining of cast iron that high cutting speeds v_c and tools with sharp cutting edges should be used [Eno02]. Hence the rake and clearance angles γ and α, respectively, must be high to achieve a sharp wedge. In order to avoid deviations and vibrations of the tool or the workpiece, cutting forces need to be reduced. This can be achieved by lowering the feed per tooth f_z. Furthermore, the generated kinematic roughness is reduced. For the same reason, tools with increased numbers of teeth N_t are applied for finishing, since the necessary chip space is small compared to roughing operations. Additionally, flutes with large helix angle δ lead to a more constant cutting force [Ema89]. The resulting lower force fluctuation increases the quality of the finished surface. A further important aspect for finishing operations is tool runout, which results from the dynamical axial and radial deviation of the tool during machining [Wan09]. Tool runout causes a variation of the uncut chip thickness between the flutes, and thus, to a variation of the load on each flute [Kli83]. Flutes with higher loads lead to an increased wear. Looking at the workpiece, SCHMITZ et al. showed that tool runout not only has a negative effect on the surface finish, but might also affect process stability negatively [Sch07].

In addition to tools that are designed only for roughing or finishing, there exist tool concepts for both operations. Most of these concepts are based on unequal tooth pitches and helix angles, respectively. This geometric alteration causes a disruption of the regenerative effect, just as for end mills with serrated flutes. In general, however, the increase of process stability of these tool concepts is not comparable to tools with serrated or chamfered flutes. STÉPÁN et al. compared a conventional end mill with one with unequal helix angles and one with serrated flutes [Sté14]. They showed that the end mill with serrated flutes increased process stability for almost all investigated spindle speeds. Although there exist no direct comparison, the process stability which can be obtained by chamfered cutting edges [Sel12b] probably can be even higher as for serrated cutters [Den10]. The effect leading to an increase of stable cutting conditions is fundamentally different between these two types of tool concepts. Chamfered flutes do not affect the time delay, but, as stated in Chapter 1, may induce process damping forces.

There exist patents for similar concepts of end mills which have different kind of flutes for roughing and finishing [Kau87, Ser01, Pol06], as shown in Fig. 2.1. The roughing flutes of such end mills are serrated to ensure a stable process. However, to the best knowledge of the author, there exist currently no similar tool concept with chamfered flutes for roughing and sharp flutes for finishing. Since chamfered flutes allow a higher process stability increase compared to serrated flutes, it is assumed that this tool concept can achieve a higher productivity.

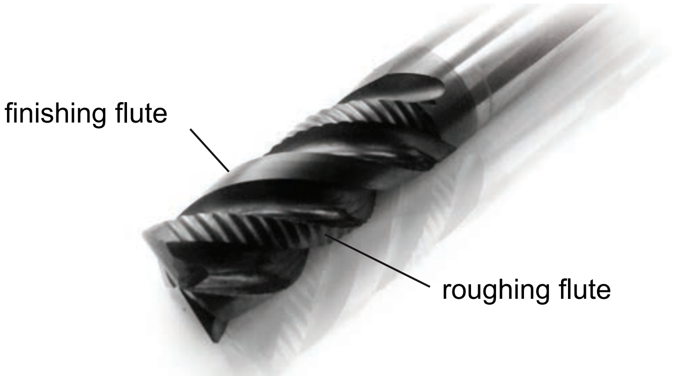

Gra/72777 ©IFW

Fig. 2.1: End mill with different flute shapes for roughing and finishing operations (Iscar Finishred, D = 16 mm).

2.2 Process Dynamics Modeling of Milling Operations

In many scientific fields, e.g. biological systems [Hem00, Kat02, Muk05], control theory [Cah05, Var07], computer science [Olg97, Tan07] or machining technology [Tob61], the behavior of dynamic systems is described by delayed differential equations (DDE) [Hen08]. Milling processes can be modeled mathematically by means of a time-delayed linear second order differential equation:

$$\mathbf{M}\ddot{\mathbf{q}}(t) + \mathbf{D}\dot{\mathbf{q}}(t) + \mathbf{K}\mathbf{q}(t) = \mathbf{F}_{\text{per}}(t) + \underbrace{\mathbf{Q}(t)\left(\mathbf{q}(t-\theta) - \mathbf{q}(t)\right)}_{=\ \mathbf{F}_{\text{dyn}}(t,\theta)} \tag{2.1}$$

The left part of Eq. 2.1 consists of the dynamic structure components of the system with the modal mass, damping and stiffness matrices **M**, **D** and **K**, respectively [1]:

$$\mathbf{M} = \mathbf{I}_{(w,w)} \circ \left(\mathbf{J}_{(w,1)} \begin{bmatrix} \mathbf{m}_{w,x} & \mathbf{m}_{w,y} & \mathbf{m}_{t,x} & \mathbf{m}_{t,y} \end{bmatrix}\right) \tag{2.2}$$

with the identity matrix **I** , the matrix of ones **J** and the modal masses of

$$\begin{array}{llll} \text{workpiece in x-direction} & : & \mathbf{m}_{w,x} & = \begin{bmatrix} m_{w,x_1} & m_{w,x_2} & \cdots & m_{w,x_k} \end{bmatrix} \\ \text{workpiece in y-direction} & : & \mathbf{m}_{w,y} & = \begin{bmatrix} m_{w,y_1} & m_{w,y_2} & \cdots & m_{w,y_l} \end{bmatrix} \\ \text{tool in x-direction} & : & \mathbf{m}_{t,x} & = \begin{bmatrix} m_{t,x_1} & m_{t,x_2} & \cdots & m_{t,x_m} \end{bmatrix} \\ \text{tool in y-direction} & : & \mathbf{m}_{t,y} & = \begin{bmatrix} m_{t,y_1} & m_{t,y_2} & \cdots & m_{t,y_n} \end{bmatrix}. \end{array} \tag{2.3}$$

w is the total number of oscillators w = k + l + m + n. The matrices **D** and **K** have the same structure as **M**. **q** (t) contains all oscillators of the modal system:

$$\mathbf{q}(t) = \begin{bmatrix} \begin{bmatrix} x_{w,1}(t) \\ x_{w,2}(t) \\ \vdots \\ x_{w,k}(t) \end{bmatrix}^T & \begin{bmatrix} y_{w,1}(t) \\ y_{w,2}(t) \\ \vdots \\ y_{w,l}(t) \end{bmatrix}^T & \begin{bmatrix} x_{t,1}(t) \\ x_{t,2}(t) \\ \vdots \\ x_{t,m}(t) \end{bmatrix}^T & \begin{bmatrix} y_{t,1}(t) \\ y_{t,2}(t) \\ \vdots \\ y_{t,n}(t) \end{bmatrix}^T \end{bmatrix}^T \tag{2.4}$$

The right part of Eq. 2.1 consists of the periodic and dynamic force components $\mathbf{F}_{\text{per}}(t)$ and $\mathbf{F}_{\text{dyn}}(t,\theta)$, respectively. **Q** (t) represents the time-variant cutting force contribution, which depends on the cutting force coefficients, process parameters and tool geometry. For an end mill with one tooth, **Q** (t) is periodic with one tool rotation and spindle speed, respectively.

---

[1] symbol ○: HADAMARD matrix multiplication [Eis70, p. 42]

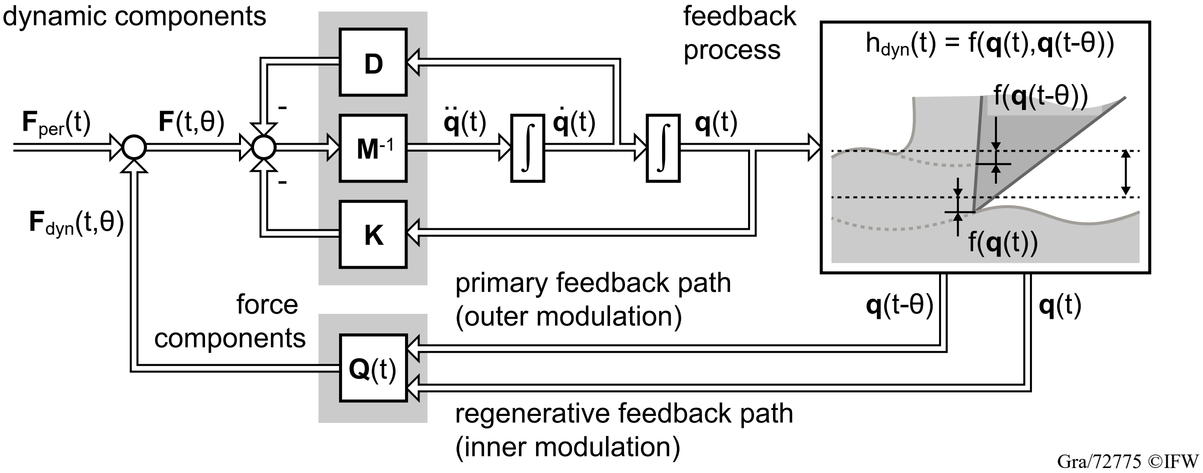
dynamic components
feedback process
$h_{dyn}(t) = f(\mathbf{q}(t),\mathbf{q}(t-\theta))$
D
$\mathbf{M}^{-1}$
K
$\mathbf{F}_{per}(t)$
$\mathbf{F}(t,\theta)$
-
-
$\ddot{\mathbf{q}}(t)$
$\dot{\mathbf{q}}(t)$
$\mathbf{q}(t)$
$\int$
$\int$
$f(\mathbf{q}(t-\theta))$
$f(\mathbf{q}(t))$
$\mathbf{F}_{dyn}(t,\theta)$
force components
$\mathbf{Q}(t)$
primary feedback path (outer modulation)
$\mathbf{q}(t-\theta)$
$\mathbf{q}(t)$
regenerative feedback path (inner modulation)

Gra/72775 ©IFW

Fig. 2.2: Block diagram of the milling process including the regenerative effect (feedback process based on [Mer65]).

An interpretation of Eq. 2.1 as a block diagram is shown in Fig. 2.2. The feedback process block illustrates how the uncut chip thickness h (t) changes due to the dynamic system behavior. As stated in [Lac09, p. 109], the chip thickness model, the cutting force model and the system dynamics are the three main components to model milling operations. The chip thickness can be described as follows:

$$h\,(t) \;=\; h_{per}\,(t) + h_{dyn}\,(t) \tag{2.5}$$

$h_{per}\,(t)$ is the periodic part and results from the predefined process parameters. If stability is investigated based on the Semi-Discretization (SD) method [Ins02], the periodic force part $h_{per}\,(t)$ can be omitted [Ins03a]. The pertubed or dynamic part $h_{dyn}\,(t)$ is a function of the current displacement between the tooth in cut and workpiece $f\,(\mathbf{q}\,(t))$ and the displacement of the previous tooth in cut $f\,(\mathbf{q}\,(t-\theta))$ with the time-delay θ. In the following, it will be explained how the stability of the system from Eq. 2.1 can be predicted.

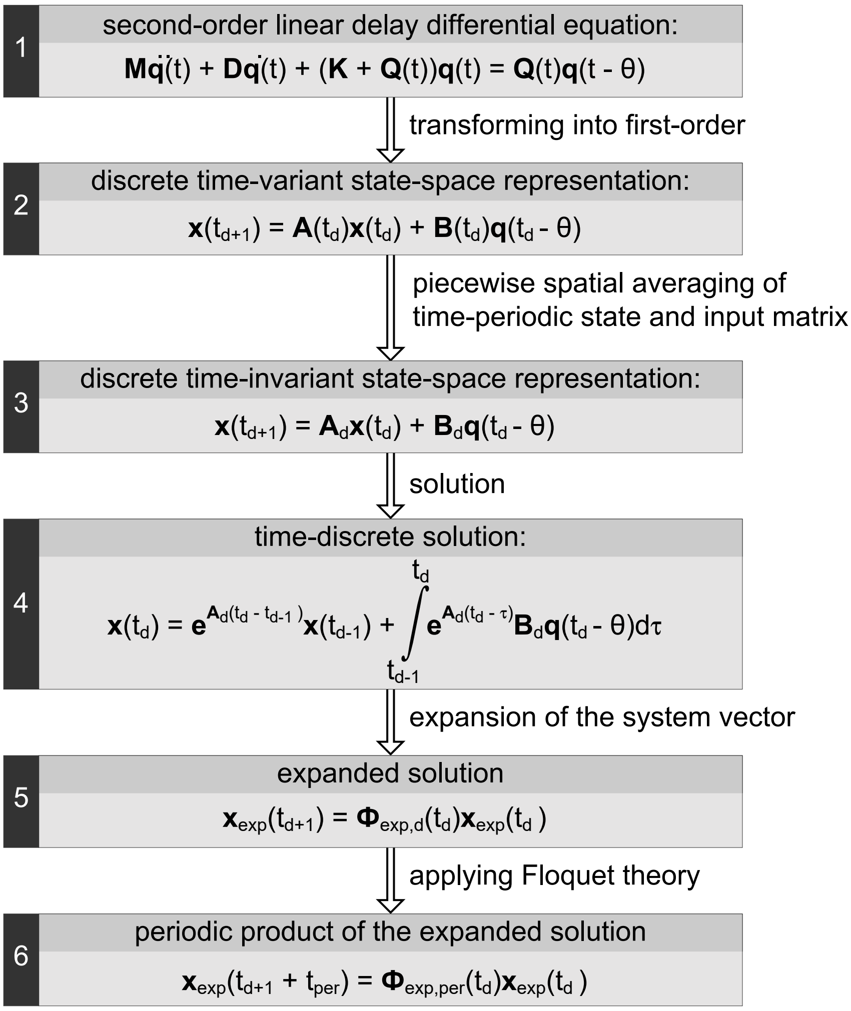
1
second-order linear delay differential equation:
$\mathbf{M}\ddot{\mathbf{q}}(t) + \mathbf{D}\dot{\mathbf{q}}(t) + (\mathbf{K} + \mathbf{Q}(t))\mathbf{q}(t) = \mathbf{Q}(t)\mathbf{q}(t - \theta)$
transforming into first-order
2
discrete time-variant state-space representation:
$\mathbf{x}(t_{d+1}) = \mathbf{A}(t_d)\mathbf{x}(t_d) + \mathbf{B}(t_d)\mathbf{q}(t_d - \theta)$
piecewise spatial averaging of time-periodic state and input matrix
3
discrete time-invariant state-space representation:
$\mathbf{x}(t_{d+1}) = \mathbf{A}_d\mathbf{x}(t_d) + \mathbf{B}_d\mathbf{q}(t_d - \theta)$
solution
4
time-discrete solution:
$\mathbf{x}(t_d) = \mathbf{e}^{\mathbf{A}_d(t_d - t_{d-1})}\mathbf{x}(t_{d-1}) + \int_{t_{d-1}}^{t_d} \mathbf{e}^{\mathbf{A}_d(t_d - \tau)}\mathbf{B}_d\mathbf{q}(t_d - \theta)d\tau$
expansion of the system vector
5
expanded solution
$\mathbf{x}_{exp}(t_{d+1}) = \mathbf{\Phi}_{exp,d}(t_d)\mathbf{x}_{exp}(t_d)$
applying Floquet theory
6
periodic product of the expanded solution
$\mathbf{x}_{exp}(t_{d+1} + t_{per}) = \mathbf{\Phi}_{exp,per}(t_d)\mathbf{x}_{exp}(t_d)$

Gra/72780 ©IFW

Fig. 2.3: Overview of the main transformation steps to predict the stability of the initial DDE.

Fig. 2.3 shows which transformations are necessary to predict the stability of milling processes with the SD method. A detailed description can be found in [Sel12a, p. 21 ff.]. **Step 1** is the definition of the system (Eq. 2.1). The initial differential equation is most ofteny transformed into a first order time discrete differential system (**step 2**). The state and input matrix $\mathbf{A}(t_d)$ and $\mathbf{B}(t_d)$, respectively, are time-variant. In case of constant process parameters, the milling process is periodic. Hence, a property of the FLOQUET Theory [Flo83] can be applied, which allows to substitute the time-variant matrices by t_d-piecewise constant values. Thus, the equation shown in **step 3** is only valid for the discrete time step t_d. The solution for this equation is shown in **step 4** [Ack83, p. 135]. In **step 5**, the solution $\mathbf{x}(t)$ is expanded, which allows to integrate the time-delay θ into the expanded solution $\mathbf{x}_{exp}(t)$ [Ack83, p. 136f.]. The transition matrix $\Phi_{exp}(t_d)$ contains the state and input matrices and is also time-periodic. As shown by FARKAS, the FLOQUET theorem can be applied onto DDE [Far94], which allows to expand the solution onto the length of one period t_{per}, as shown in **step 6**. The eigenvalues of the transition matrix $\Phi_{exp,per}(t_d)$ for one period contain the information if the system is stable for the given process parameters.

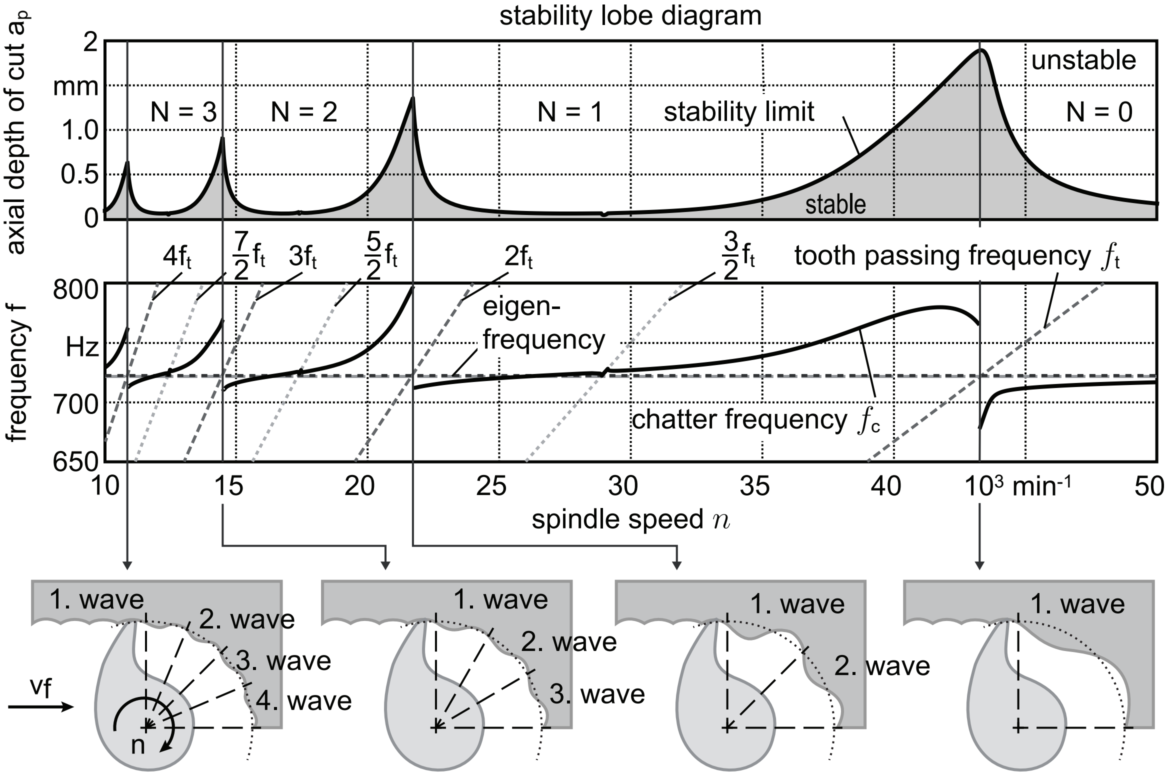

Gra/72779 ©IFW

Fig. 2.4: Representation of the stability behavior of milling processes based on a stability lobe diagram from [Gov05] and wavy surface generation as shown in [Tlu86, Alt04].

The information about the stability behavior can be represented as so called stability lobe diagrams [And61], as shown in Fig. 2.4. Based on such diagrams, process parameters can be identified for which a stable system behavior is present. In this respect, an increase in productivity can be accomplished. Smith and Tlusty showed that if the tooth passing frequency f_t equals an eigenfrequency of the system, stable cutting with the highest possible axial depth of cut a_p can be achieved [Smi90]. At these spindle speed positions, the inner and outer modulation (Fig. 2.2) have no phase shift [Alt04]. For very simple dynamic systems with only one eigenfrequency, the corresponding spindle speed position n can be calculated as follows:

$$n = \frac{f}{N} \tag{2.6}$$

f represents an eigenfrequency of the system and N is an integer number of waves, as shown in the bottom part of Fig. 2.4. With increasing spindle speeds, the wave number decreases. In case of a system with multiple eigenfrequencies, the prediction of the local maximum stability limit cannot be derived by superimposing the stability limits of the single modes [Ins04]. In such a case, Eq. 2.6 is not applicable.

2.3 Influence of Tool Geometry and Process Forces on Process Dynamics

In the first part of this chapter, it is shown how the spatial arrangement of the individual cutting flutes (macro geometry of the tool) influence the process forces and the dynamic process behavior. It is shown how several geometrical adjustments can be made to optimize the reciprocal dependencies of the cutting flutes. This information can be used for an enhanced tool design based on the machining process.
In 1897, FISCHER already mentioned that the geometry of the cutting edge (micro geometry of the tool) has an effect on the resulting cutting forces [Fis97]. In the second part of this chapter, the influence of the cutting edge shape on process forces as well as stability is shown.

2.3.1 Macro Geometric Tool Attributes

An unstable cutting behavior can be caused by mode coupling or the regenerative effect [Tlu81]. The former is based by the fact that the system vibration can be formed by multiple modes with different amplitudes and a phase shift [Gas98]. The latter is caused by the dynamic variation of the instantaneous chip thickness, as shown in Fig. 2.2. The regenerative effect can be attenuated by various tool geometry adaptions which cause a variation of time delays, as illustrated in Fig. 2.5.

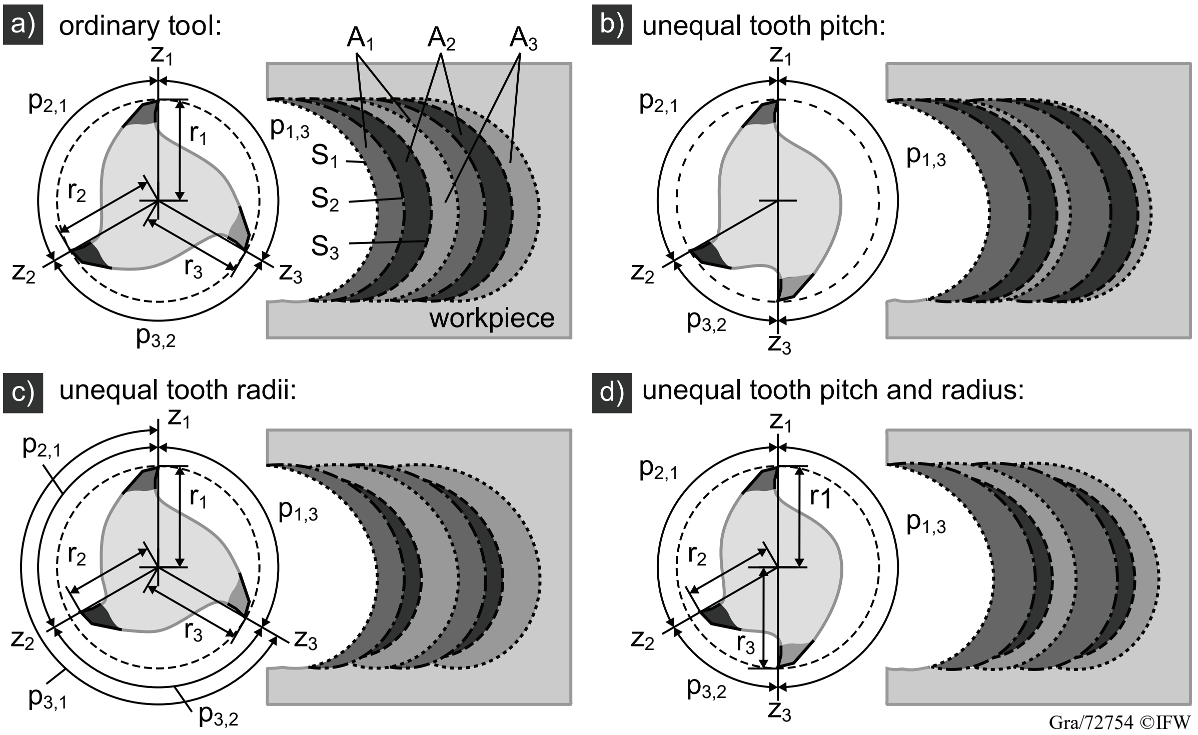
a) ordinary tool:
z_1
$p_{2,1}$
r_1
$p_{1,3}$
A_1
A_2
A_3
S_1
S_2
S_3
r_2
z_2
r_3
z_3
$p_{3,2}$
workpiece
b) unequal tooth pitch:
z_1
$p_{2,1}$
$p_{1,3}$
z_2
$p_{3,2}$
z_3
c) unequal tooth radii:
z_1
$p_{2,1}$
r_1
$p_{1,3}$
r_2
z_2
r_3
z_3
$p_{3,1}$
$p_{3,2}$
d) unequal tooth pitch and radius:
z_1
$p_{2,1}$
r1
$p_{1,3}$
r_2
z_2
r_3
$p_{3,2}$
z_3
Gra/72754 ©IFW

Fig. 2.5: Variation of the cross-section of the machining area A_j and tooth path S_j, respectively, due to the variation of tooth pitch and tooth radius.

In case of an ordinary tool, the teeth have the same tooth pitches ($p_{1,3} = p_{2,1} = p_{3,2}$) and the same radial distance from the tool center point ($r_1 = r_2 = r_3$), as shown in Fig. 2.5 a). Thus, each tooth is subjected to the same load during the machining operation. However, no geometric based disturbances of the regenerative effect can be achieved. One option to change time delays, and thus, disturb the regenerative effect, is the usage of unequal tooth pitches [Sla65, Van65, Opi66, Zat14], as shown in Fig. 2.5 b). This causes unequal loads, as it can be seen from the machining areas A_j for all j teeth. A larger (smaller) tooth pitch between a tooth j and its preceding tooth $j-1$ also means a larger (smaller) machining area A_j, and thus, a higher (lower) load. Another method to disturb the regenerative effect can be achieved by unequal tooth radii r_j, as illustrated in Fig. 2.5 c). In the shown example, the tooth z_2 is recessed. This leads to a later entry and an earlier exit of the tooth into and out of the workpiece, respectively. Furthermore, the actual feed per tooth f_z for this tooth is reduced by the radial offset $(r_1 - r_2)$. This also leads to the situation that the following tooth z_3 needs to remove more material. At the beginning and ending of its immersion, the tooth z_3 removes the material left behind by tooth z_1. It follows that at these immersion ranges, the time delays results from the tooth pitch $p_{3,1}$ which is formed between the teeth z_3 and z_1. In order to depict the length of the entry and exit immersion ranges as accurately as possible, modeling of the trochoidal tooth path is recommended. While unequal tooth pitches change time delays of a tooth for the entire immersion range, unequal tooth radii lead to a sudden change of time delays near the entry and exit positions. Both geometric adaptions can also be combined, as shown in Fig. 2.5 d). A suitable choice of the tooth pitches and the radial offsets can compensate the unequal load distribution between the teeth.

A further possibility to cause a disturbance of the regenerative effect is to vary the tooth pitch or radial offset along the z-axis, as shown in Fig. 2.6.

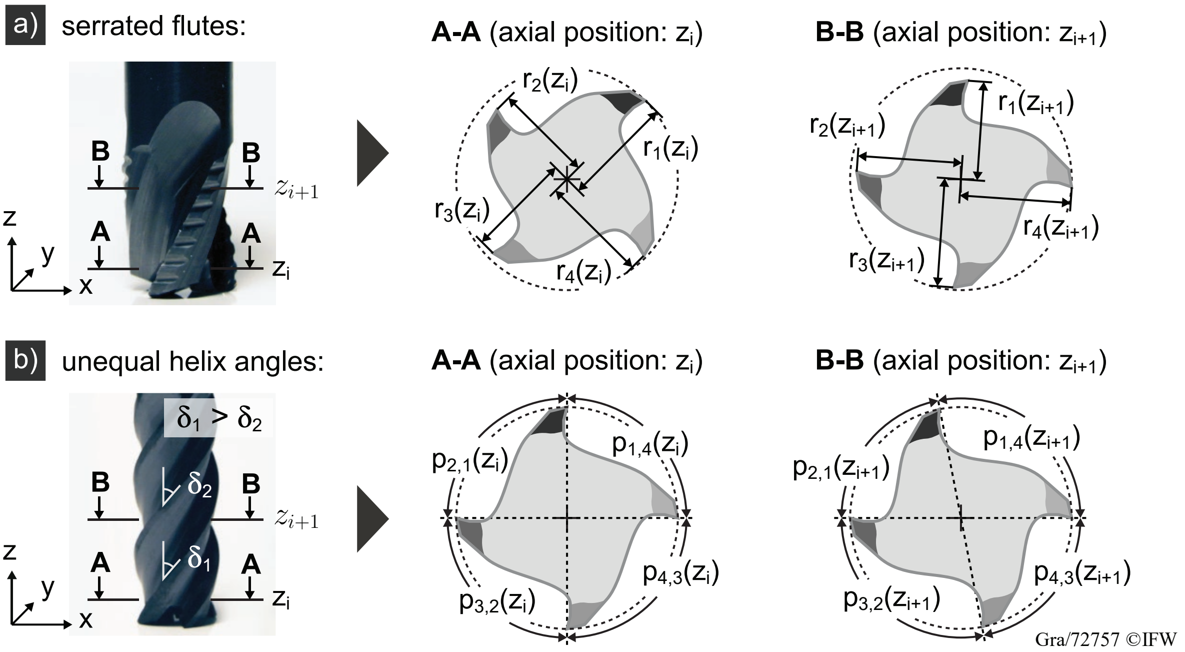
a) serrated flutes:
A-A (axial position: z_i)
B-B (axial position: z_{i+1})
B
B
A
A
z_{i+1}
z_i
z
y
x
$r_2(z_i)$
$r_1(z_i)$
$r_3(z_i)$
$r_4(z_i)$
$r_2(z_{i+1})$
$r_1(z_{i+1})$
$r_4(z_{i+1})$
$r_3(z_{i+1})$
b) unequal helix angles:
A-A (axial position: z_i)
B-B (axial position: z_{i+1})
$\delta_1 > \delta_2$
δ_2
δ_1
B
B
A
A
z_{i+1}
z_i
z
y
x
$p_{2,1}(z_i)$
$p_{1,4}(z_i)$
$p_{4,3}(z_i)$
$p_{3,2}(z_i)$
$p_{2,1}(z_{i+1})$
$p_{1,4}(z_{i+1})$
$p_{4,3}(z_{i+1})$
$p_{3,2}(z_{i+1})$
Gra/72757 ©IFW

Fig. 2.6: Varying geometric shape of the flutes along the z-axis.

The varying radii in case of a) serrated flutes have an influence on the duration of the time delay changes at the entry and exit immersion position [Cam02, Koc13]. Assuming a constant tooth pitch, the number of possible time delays equals the number of flutes for such end mills. Changing time delays arise in case of b) end mills with unequal helix angles δ [Sto70, Tur07, Tak13]. The unequal tooth pitches increase in axial direction, and thus, the time delays change as well.

For the prediction of the process stability of the hybrid tool, it is necessary to implement varying time delays during the immersion path (Fig. 2.5) as well as along the z-axis (Fig. 2.6). As stated in [Sch09, p. 220], the impact of the presented geometrical changes on stability depends on the machining system. As already mentioned, these geometrical changes have no effect if chatter is caused due to mode coupling [Tlu83]. A further possibility to increase stability, even in case of mode coupling chatter, is the change of the cutting edge shapes, as it will be described in the following.

2.3.2 Correlation of Cutting Edge Shape and Process Damping

It is well known that for very low cutting speeds the tendency of machining instability often decreases [Keg69]. Kegg summarized observations of low speed stability from various authors and for a wide range of turning and milling operations and work materials [Keg69]. This velocity dependent phenomenon, also known as process damping, arises when the clearance face and the work material interfere, causing a large amount of plastic flow and energy dissipation [Coo55, p. 39]. The contact between clearance face and work material, and thus, the resulting process damping force mainly depends on the shape of the cutting edge and the wavy workpiece surface, as illustrated in Fig. 2.7.

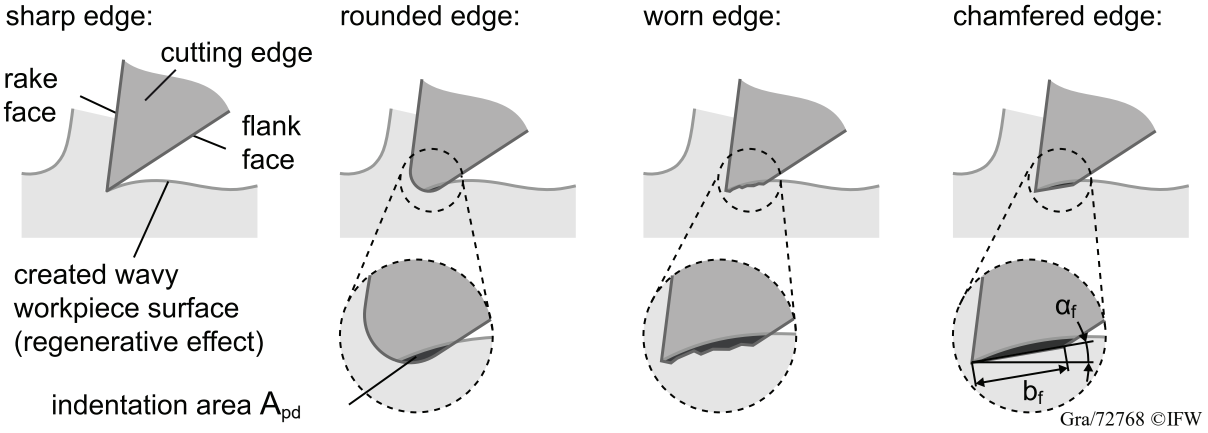

Fig. 2.7: Influence of the cutting edge shape on its contact with the just cut workpiece surface.

The waviness of the just cut work material is caused by the vibration of the tool and/or the workpiece, which leads to the regenerative effect (Fig. 2.2). If the cutting edge is sharp, a contact is solely caused by an elastic rebound of the work material [Coo59]. Large nose radii, large wear lands and small clearance angles are decisive for the indentation [Coo55, p. 56]. Tlusty confirmed that the use of tools with worn flank faces decrease vibrational amplitudes [Tlu78]. Similar to worn cutting edges [Ahm12, Alt08, Tyl13], rounded cutting edges lead to higher process stability at low cutting speeds as well [Tlu86, Bud10, Tun12]. Same applies for tools with low clearance angle, or alternatively, with a chamfer between the cutting edge an the flank face, defined by the length of chamfer b_f and the chamfer angle α_f [Lan05]. It must be noted that the interference load can strongly differ between the mentioned cases. It was shown in [Che88] that normal and shear stresses during cutting of AISI C1050 with a grind-on chamfered flank in comparison to a natural flank wear (with irregular wear land, grooving and crater wear) can be twice as high.

In order to estimate the process damping force, the contact between the cutting edge and the workpiece is modeled as an indentation area A_{pd} between the cutting edge and the workpiece

[Lee95, Ran99, Ahm11a, Gur16]. Depending on the shape of the cutting edge, the resulting indentation area changes. Wu proposed the following approach to model process damping forces [Wu89]:

$$\begin{bmatrix} F_{r,pd}(t) \\ F_{t,pd}(t) \end{bmatrix} = \begin{bmatrix} 1 \\ \mu_{pd} \end{bmatrix} K_{pd} A_{pd} a_p \tag{2.7}$$

The process damping force in radial direction $F_{r,pd}$ is equal to the process damping force in tangential direction $F_{t,pd}$ multiplied by a friction coefficient μ_{pd}. K_{pd} is the process damping coefficient. There exist various approaches for the determination of the value of K_{pd}. One of the known methods is based on the analysis of experimental stability charts. By comparing stability at low cutting speeds of tools with different levels of worn flank faces , the influence of process damping, and thus the value of K_{pd}, can be estimated based on the resulting stability limit [Bud10, Tyl13]. Wu estimated the value for K_{pd} based on material-specific properties [Wu88]. The mechanism of process damping can be illustrated by means of Fig. 2.8.

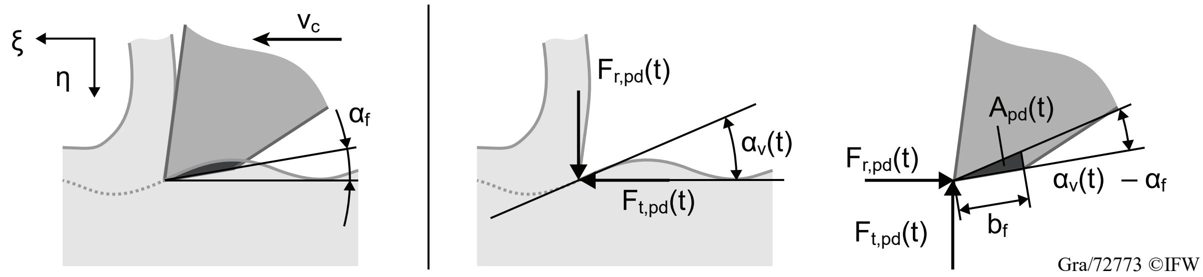

Fig. 2.8: Process damping forces based on [Wu89] and process damping area A_{pd} in accordance to [Chi98].

Depending on the cutting edge position, the indentation area A_{pd} varies and even disappears at some positions [Tlu78]. There are detailed approaches for modeling the indentation area for different cutting edge shapes as precisely as possible [Elb94, Ran99, Rah09, Ahm10, Ahm11b]. These methods are especially suitable for time-domain simulations, where the information of the workpiece surface representing the indentation area can be stored and retrieved with reasonable computational effort. It is important to note that the idea of an ideal indentation area is merely a simplification of a complex mechanism [Ahm10]. Therefore, Chiou and Liang proposed a simple method to approximate the indentation area A_{pd} for tools with flank wear [Chi98]. The worn tool edge was assumed to have a clearance angle α of 0°. This model can be extended in order to approximate the interference for tools with chamfered cutting edges. Thus, the indentation area A_{pd} is approximated as followed (based on [Chi98], compare with the graphic on the right in Fig. 2.8):

$$A_{pd} = \frac{1}{2} b_f^2 \tan\left(\alpha_f - \alpha_v(t)\right) \tag{2.8}$$

$\alpha_v(t)$ describes the gradient of the workpiece waviness (inner modulation) at the current postion of the cutting edge. According to Fig. 2.2, the inner modulation equals $\mathbf{q}(t)$. Thus, the gradient equals $\dot{\mathbf{q}}(t)$. This illustrates the velocity dependence of the process damping effect. Therefore, theoretically it adds to the structural damping term in Eq. 2.1. The distance of the peaks and valleys results from the effective dominant eigenfrequency and the cutting velocity v_c. In case of low system eigenfrequencies and high cutting speeds, this leads to a reduction in possible overlaps [Wu89], as it can be derived from Fig. 2.4. This is also the reason why the positive effects of the process damping on the stability is often associated with low cutting speeds, as shown in Fig. 2.9.

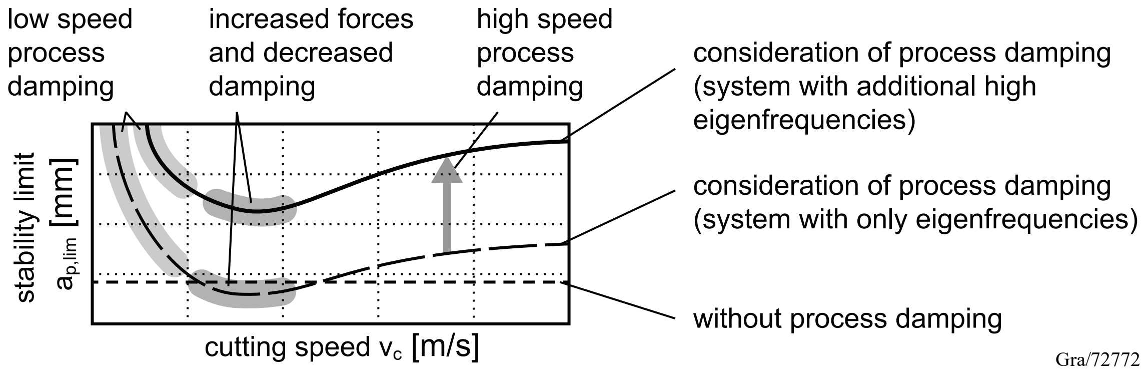

Gra/72772 ©IFW

Fig. 2.9: Increase of stability if process damping is included (after [Tlu78], interpretation of high speed process damping based on [Sel12b]).

However, Sellmeier and Denkena showed that for a system with at least one additional and equal dominant high eigenfrequency mode, the effect of damping also occurs at high cutting speeds [Sel12b]. If such a high frequency mode is excited, the distance of the peaks and valleys of the wavy surfaces are reduced which leads to an increased interference [Bud10]. Consequently, the stability limit $a_{p,lim}$ is considerably higher even for high cutting speeds. The local minimum occurring for the shown stability limits is also worth mentioning. This is due to a speed-dependent influence of the process forces. For Tlusty's analysis of turning Ck45N steel and small tool wear, this minimum occurred at approximately $v_c = 50$ m/min [Tlu78]. In [Sel12b], tools with chamfered cutting edges are used for milling of Al 7075 T651 and a minimum at rather high cutting speeds at approximately $n = 6,000\,\text{min}^{-1}$ or $v_c = 376\,\text{m/min}$ occurs. It is not clear if speed varying cutting forces or dynamical effects lead to this decrease. For reasons of productivity and increasingly powerful machine tools, the consideration of higher cutting speeds is of economic and scientific interest. However, with increasing cutting speeds, additional factors, especially heat development, have an influence on the process forces, as it will be shown in the next section.

As already mentioned, the idea of an indentation area is a simplification of a complex process. The already mentioned elastic rebound of the work material for sharp cutting edges and the resulting contact with the clearance face also applies for worn and chamfered cutting edges [Wal99]. Thus, it is assumed that there is a plastic as well as an elastic flow region of the workpiece near the cutting edge and further away from the cutting edge, respectively [Wal99, Smi00, Sel12b]. In [Sel09] process forces of sharp and chamfered cutting edges were exposed to adjustable vibrations. Even in case of no vibrations, and thus, no inner modulation, the process forces of the chamfered cutting edges were higher compared to sharp cutting edges. This might be caused by a solely elastic contact between the chamfered area and the workpiece and it is not clear if this additional non speed-dependent load actually contributes to damping. Furthermore, large portion of the interference energy leads to an increase of heat at the interface and consequently to a softening of the tool and workpiece [Abd73]. Depending on the process parameters, e.g. cutting speed v_c and feed velocity v_f, it can be assumed that this should also influence process damping and the cutting force.

2.4 Disturbance Factors on Stability and Surface Finish

A decreased surface quality as well as an unfavorable dynamic behavior can be caused by various disturbances. Especially runout error is of importance during machining with the hybrid tool, as this disturbance interferes with the the radial offset ΔR of the roughing flutes. This can adversely affect both roughing and finishing. A further disturbance is caused by tool deflection, which influences the topography of the machined workpiece. The desired workpiece geometry is also negatively affected by burr formation. In this context, the occurring thermal load during the cutting process is of interest, as it favors burr formation and may influence the process forces in general.

2.4.1 Tool Runout

Apart from the already mentioned intentional force variation techniques (Chapter 2.3.1), force variations can result from errors in the tool setting. These unintentional influences can in principle lead to the situation that the radial position of the recessed roughing flutes of the new hybrid tool may increase. This can cause an unwanted contribution of the roughing flutes on the surface finishing. Therefore, the occurrence of this situation must be prevented.

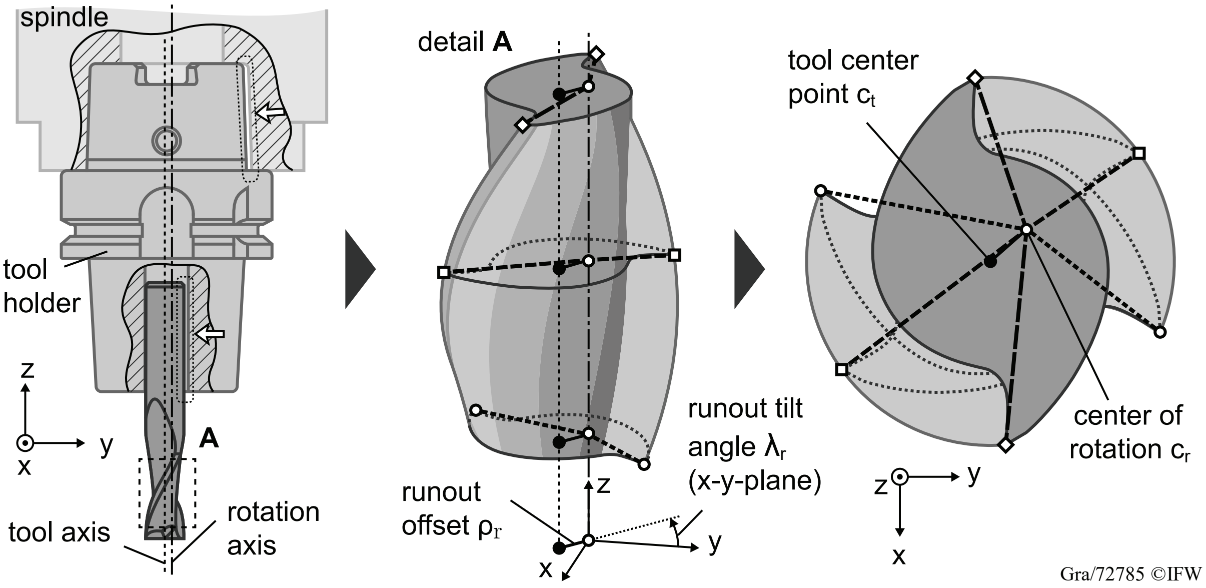

Fig. 2.10: Tooth radii and tooth pitch variation in axial direction due to radial runout (based on [Arm89]).

Radial runout is the result of a parallel offset between the tool and rotation axis, leading to an eccentricity as shown in Fig. 2.10. The most common tool setting errors are radial and axial runouts [Kli83]. Axial runout is defined as the tool axis tilt to the rotation axis. In this context, the tool clamping cause the dominant error shape in the tool motion [Krü13]. If side-lock-type chucks (Weldon chucks) are used, e.g., an eccentricity can be caused by its one-sided clamping principle. In [Ari09] a detailed description of the influence of runout on the surface topography can be found. Wan et al. investigated different axial and radial runout models [Wan09]. They concluded that the consideration of only radial runout is sufficient to reach good agreement between modeled and experimental process forces. Likewise, Wang and Liang stated that the magnitude of axial runout is small in relation to the axial depth of cut a_p [Wan96], and thus, can be neglected. Radial runout is characterized by two parameters (Fig. 2.10, detail A): runout offset ρ_r and runout location angle λr. The offset between the tool center point c_t and the center of rotation c_r, as illustrated on the right side in Fig. 2.10, leads to unequal tooth pitches and tooth radii, similar to the bottom right case from Fig. 2.5. For end mills with helical flutes, tooth pitches and tooth radii vary along the z-axis. Thus, besides negative effects like surface errors and increased wear, the dynamical behavior of the machining process is influenced [Kli83]. The periodicity of the system is changed and the resulting chatter frequencies shift from tooth passing frequency to spindle rotation frequency [Ins08]. Insperger et al. [Ins08] investigated the influence of tool runout on stability in case of low radial immersion conditions and a straight fluted tool ($\delta = 0°$). They modeled runout by adding a factor, which may differ for each tooth, to the dynamic force matrix **Q** for stability simulation based on the SD method. Schmitz et al. [Sch07] investigated the influence of runout on process stability based on time-domain simulations. Their results show that in case of low radial or axial immersion conditions, runout can have a negative effect on stability if the additional frequency content at spindle rotation frequency and its harmonics coincide with one of the system natural frequencies.

Lee determined a runout offset of $\rho_r = 47\,\mu$m for his experiments [Lee07]. The change of the tooth path trajectories can lead to an increase or decrease of the radial immersion a_e. This also leads to an influence on the theoretical surface roughness R_{th}, as described in [Hon95]. The resulting surface topography shows that the period of the typical cusped surfaces in milling increases and does not equal the feed per tooth f_z, as shown in [Sch07]. Furthermore, the change of a_e has an influence on the prediction of the specific process force coefficients. Grossi et al. implemented runout error in their model for the prediction of the coefficients [Gro15]. Furthermore, as shown in [Ma16], tool runout can lead to time delay changes.

2.4.2 Flank Face Deformation Error

Shirase et al. investigated how an irregular tooth pitch of an end mill affects the tool deflection, and thus, the flank face or surface deformation error of the workpiece [Shi96]. They showed in their investigations that the varying chip load of each flute due to the irregular tooth pitch can lead to a reduced deformation error. Based on these findings, it can be assumed that a radial offset of cutting flutes also has an effect on the surface deformation error. In addition, the influence of runout also needs to be considered. It can be assumed that the surface deformation error has a more significant influence on the surface quality than the kinematic roughness. In analogy to turning [Tön13, p. 354], the theoretical or kinematic roughness R_{th} for flank milling operations can be calculated as

$$R_{th} = \frac{D - \sqrt{D^2 - f_z^2}}{2}. \tag{2.9}$$

For a one fluted end mill with a diameter of D = 20 mm and a feed per tooth of $f_z = 0.28$ mm, this results in a theoretical roughness of $R_{th} = 0.98\ \mu$m. In comparison to this, the influence of the tool deflection during the machining operation on the resulting surface topography is significant higher. Thus, the consideration of tool deflection is of importance for finishing operations.

Hann investigated most of the common influential factors on tool deflection, e.g. feed per tooth f_z, axial immersion a_p and the number of teeth simultaneously in cut [Han83, p. 20 ff.]. An example of his results is shown in Fig. 2.11.

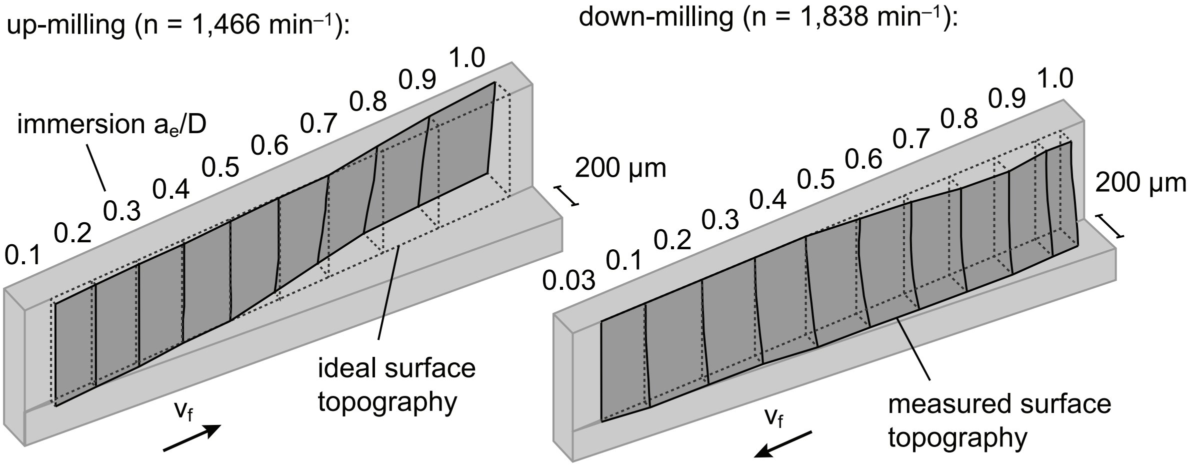

radial depth of cut: a_e = variable
axial depth of cut: a_p = 20 mm
spindle speed: n = variable
feed per tooth: f_z = 0.1 mm

process: variable
tool: D = 15 mm, $N_t = 3$, $\delta = 15°$
workpiece: AlCuMg2
machine: Heller FH 120-2

Gra/72811 ©IFW

Fig. 2.11: Influence of radial immersion a_e and tool rotation (up- and down-milling) on surface topography of the workpiece [Han83, p. 59 f.].

The left workpiece shows the measured surface topography after up-milling with decreasing radial immersion a_e in feed direction v_f. A tendency of increased material removal can be observed. The right workpiece shows a similar example for down-milling. The measured surface topography shows a reduced material removal. The decisive factor for tool deflection, and thus, surface deformation errors is the feed normal force [Han83, p. 20]. In up-milling, the force in normal direction supports the penetration of the cutter into the workpiece. As a consequence, during up-milling more material than desired is removed and therefore an increase of the process forces can be assumed. The opposite behavior can be observed in down-milling. Generally, the deflection is larger in case of down-milling. The reasons are higher feed normal forces and the fact that the tool deflects away from the workpiece without any resistance from the workpiece, as it is the case in up-milling [Bud94]. In general, it can be stated that with the usual cutting conditions for finishing, a better surface quality can be achieved with down-milling [Lan04, Mic14]. For the prediction of the tool deflection and surface deformation error, the tool is usually modeled as cantilever beam [Bud94, Des12, Bha14, Krü14]. This approach requires at least the knowledge of the material properties of the tool and its stiffness.

2.4.3 Burr Formation

Burr formation often occurs during machining. It can cause an impairment of the functionality of the machined surface and often a deburring process needs to be carried out, which is time-consuming and expensive [Aur09]. The most common burr types that occur during milling are shown in Fig. 2.12 a).

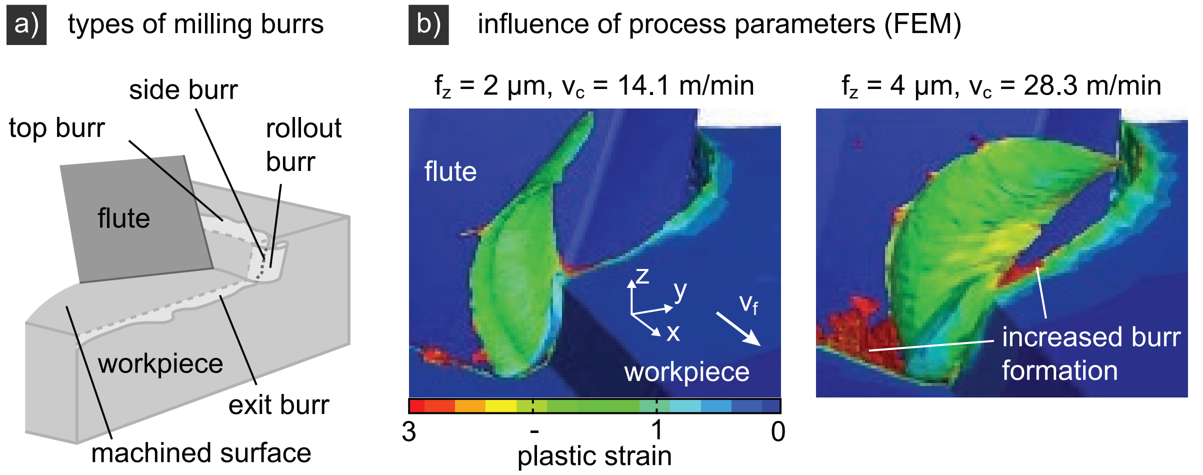

number of teeth:	N_t	= 2	tool diameter:	D = 492 µm
helix angle	δ	= 30°	tool material:	carbide (Dormer)
cutting edge radius	r_e	= 3 mm	process:	up-milling
rake angle:	γ	= 0°	workpiece material:	Al 6061 T6
clearance angle:	α	= 7°	radial depth of cut:	a_e = 125 µm
corner radius:	R	= 20 mm	axial depth of cut:	a_p = 50 µm

Gra/72769 ©IFW

Fig. 2.12: a) Possible types of burr in milling [Gil76, Has99] and b) influence of machining parameters on burr formation based on a FEM simulation of micro milling [Dav17].

Additional common burr formations, e.g. during the tool entry into the workpiece, are described in [Aur09]. Rollout burr can occur by a bending of the chip at the exit [Gil76]. Side and top burrs are formed mainly at the exit position due to the shearing of the workpiece material by the minor and major cutting edges [Has99]. Furthermore, shearing can cause top burr.

Apart from the ductility of the machined workpiece, formation of burrs mainly depends on the tool geometry and the process parameters. Rounded cutting edges induce a thermo-mechanical load, which increase shearing, and thus, burr size [Den12]. Same applies for chamfered cutting edges [Jin08]. GROPPE investigated end mills with chamfers on the flank face and showed that a larger chamfer length b_f and a small chamfer angle α_f (Fig. 2.8) increase burr formation [Gro06, p. 103]. A chamfer can increase the pressure between the cutting edge and the workpiece. This causes an elastic and thermal expansion of the machined surface [Gil76], which leads to burr formation. The influence of the process parameters on the burr formation is shown in Fig. 2.12 b). It shows finite element method (FEM) simulations carried out by DAVOUDINEJAD in order to analyze burr formation in micro milling of aluminum 6061. Top burr formation is visible in both shown examples. However, the reduction of the feed per tooth f_z as well as the cutting speed v_c noticeably reduces the plastic strain, and thus, the burr size [Dav17]. Similar results are reported in [Gro06, p. 103] for machining aluminum 7075 for end mills with chamfered cutting edges.

2.4.4 Thermal Load

Most of the cutting energy in machining is dissipated as heat [Tön13, p. 86]. In this respect, during the machining process, both the tool and the workpiece are exposed to a high thermal load. The thermal stress depends in particular on the process parameters. LAURO et al. measured the heat development of a Al 7050 workpiece during milling with a thermal imaging camera [Lau13]. They investigated the influence of the cutting direction (up- and down-milling), radial immersion a_e, cutting velocity v_c and feed per tooth f_z and concluded that the latter has the most significant influence on rising temperatures. Although higher feed rates lead to increased process forces, the heat flux into the workpiece at the machining position is reduced due to the faster tool movement. An example of the correlation between the feed rate f_z (analogous to chip thickness h in case of orthogonal cutting) is given in Fig. 2.13 for different tool edge geometries.

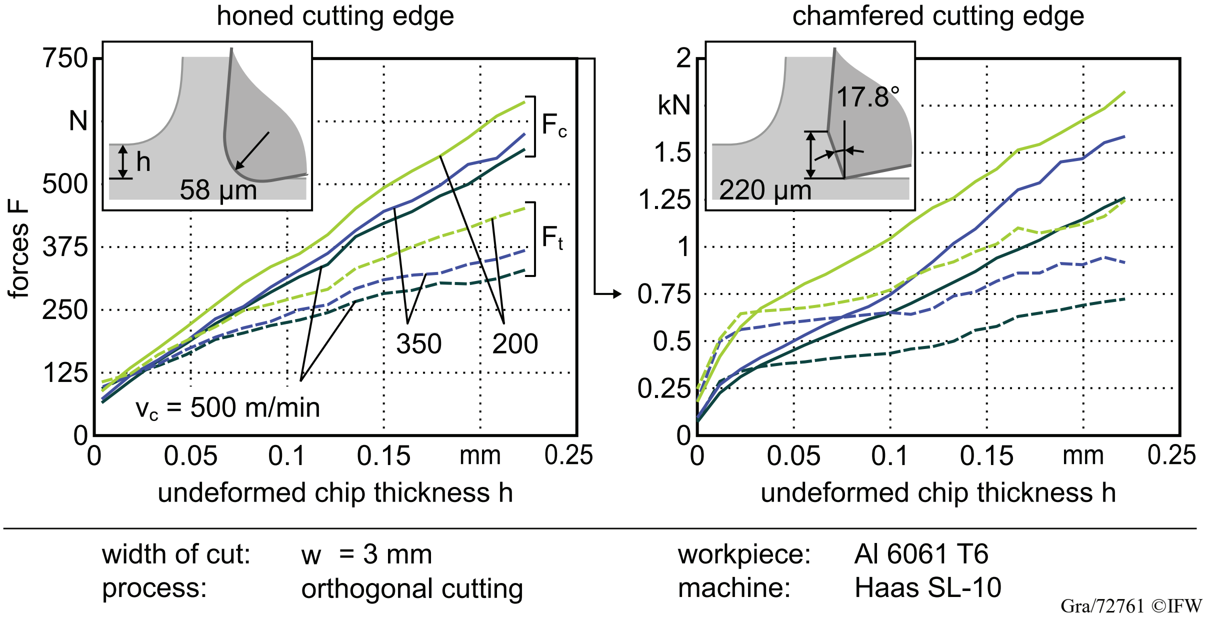

Fig. 2.13: Influence of tool edge geometry, undeformed chip thickness h and cutting speed v_c on process forces [Fan05].

As it can be seen, FANG and WU measured lower process forces with increasing cutting speeds v_c. The explanation for this correlation is a strain rate reduction in case of increasing cutting speeds, which changes the necessary plastic deformation [Sub13]. UHLMANN and RASPER showed that the process forces decrease if a Al 7075 workpiece is pre-heated up to 100 °C or if the cutting speed is increased [Uhl11]. They showed that the decreased forces also lead to higher process stability. However, different conclusions for the correlation between the cutting speed and heat generation during milling of aluminum can be found in literature. DAVIES showed that the correlation actually depends on the aluminum alloy [Dav90]. For example, in case of Al 6061 T651 and Al 2024 T351 cutting forces decreased with higher cutting speeds while an increase of the cutting forces was observed by the author for Al 2011 T3. The correlation may also change in case of heat treatment, as shown in [Dem09] for Al 6061. In case of 7075 T6, SUBRAMANIAN et al. showed that an increase of the cutting velocity cause an almost linear decrease of the process forces [Sub13]. As shown in Fig. 2.13, the cutting forces also depend on the cutting edge geometry [Fan05]. In this example, the cutting edge with a chamfered rake face produces forces that are more than twice as high as in case of the honed cutting edge. In this context, TANG et al. showed that increasing flank wear leads to rising temperatures in the workpiece 7050 T7451 [Tan09]. SELLMEIER investigated the influence of the flank face chamfer width b_f and chamfer angle α_f on the resulting process forces or process force coefficients [Sel12a, p. 84f.]. He observed a significant increase of the frictional force components with high values for b_f and increasing feed per tooth f_z in comparison to sharp cutting edges. However, the influence of v_c on the process temperatures during machining with cutting edges with chamfered flank faces is unknown.

Additionally, the contact between the chamfered area of the cutting edge and the workpiece increases frictional forces. Thus, compared to sharp cutting edges, it can be assumed that an increased amount of heat energy is induced into the workpiece. For aluminum alloys this may lead to thermally induced local structural changes, known as soft spots [Wei99, p. 95 f.]. Usually, these local areas have a significant reduced strength [Dav94, p. 336]. As stated by DAVIES, if soft spots occur during the machining of thin-walled airplane components, the machined workpieces are sorted out afterward. Hence, if for such machining tasks chamfered cutting edges are used to increase stability, thermal effects needs to be considered.

2.5 Conclusions on the State of the Art

Roughing and finishing tools are designed according to their field of application and with the consideration to achieve low machining costs. Furthermore, there exist end mills which are designed for roughing and finishing operations. Depending on the state of the final workpiece after machining, these end mills can reduce the machining costs by lifting the need to use different tools for both machining operations. In comparison to the existing tool concepts, the novel hybrid tool allows to increase process stability during roughing by using flutes with chamfered cutting edges. The flutes are recessed in order to keep them out of cut during finishing. Additional sharp cutting flutes without chamfers generate the final surface.

High removal rates in case of roughing carry the risk of chatter vibrations. With mathematical models based on differential equations, it is possible to predict the machining behavior of an end mill. This allows to identify process parameters which yield a stable machining process and high removal rates at the same time. Furthermore, the influence of the geometrical attributes of an end mill are also taken into account for the stability prediction. Thus, it is possible to design an end mill which is optimized for a specific machining task.

Depending on the process parameters, macro geometric tool attributes, e.g. unequal helix angles and unequal tooth pitches, can disrupt the regenerative effect, which yields higher process stability. Stability can be even more increased if the cutting edge shape of the tool induces process damping. This is possible with rounded as well as worn edges. The highest stability increase is gained by cutting edges with a chamfer on the flank face.

However, the mentioned macro geometric variations of the tool shape as well as chamfered cutting edges may deteriorate the final surface quality. Tool runout changes the actual position of the end mill teeth. This has an influence on the process dynamics. Additionally, in case of the novel tool concept, this can lead to a contact of the chamfered flutes with the final surface during finishing. Furthermore, the variation of the geometric attributes of the tool affects the cutting conditions, e.g. the number of flutes which are currently in cut. As a result, the deformation error of the machined flank face may increase. Another important factor with regard to surface quality is burr formation. Burr can cause an impairment of the functionality of the machined surface. A reduction of the feed velocity and cutting speed often helps to prevent burr. Rounded cutting edges lead to an increased contact with the workpiece. Thus, a thermo-mechanical load is induced into the workpiece which increases burr formation. Same applies for chamfered cutting edges. Furthermore, in case of aluminum machining, this may lead to local areas with a significant reduced strength. Such local soft spots often leads to a reject of the machined workpiece.

3 Objective and Approach

The scientific motivation for this work results from the known increase of process stability if chamfered cutting edges are used for the machining of aluminum alloys. End mills with such cutting edges are usually considered only for roughing operations due to the resulting surface roughness and burr formation. The tool concept consists of a combination of sharp cutting edges and chamfered cutting edges with a radial offset. Thus, this tool can be applied for roughing as well as finishing operations. The essential features of this tool concept for a 4-fluted end mill are shown in Fig. 3.1.

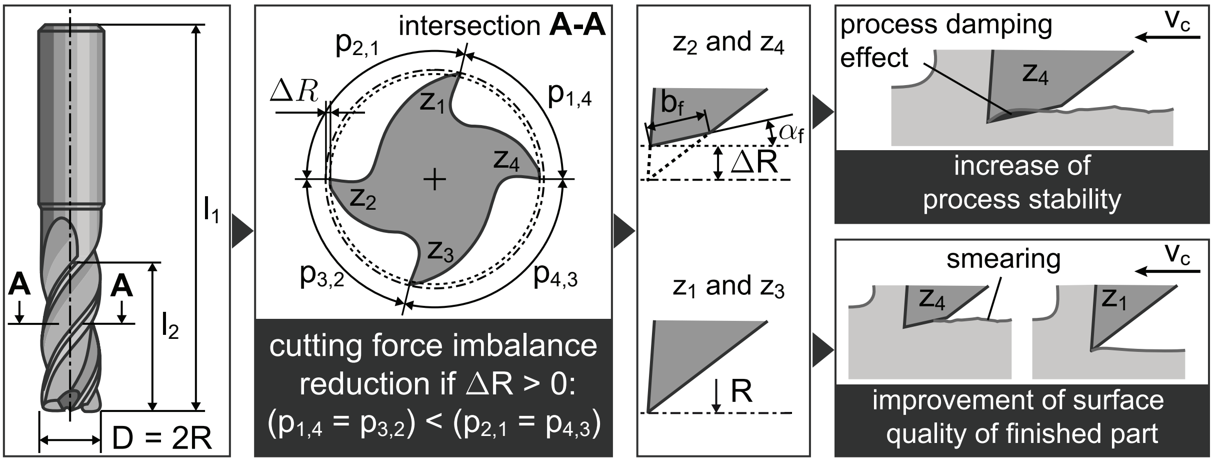
A
A
l_1
l_2
D = 2R
intersection **A-A**
$p_{2,1}$
ΔR
z_1
$p_{1,4}$
z_4
z_2
z_3
$p_{3,2}$
$p_{4,3}$
cutting force imbalance reduction if $\Delta R > 0$: $(p_{1,4} = p_{3,2}) < (p_{2,1} = p_{4,3})$
z_2 and z_4
b_f
α_f
ΔR
z_1 and z_3
R
process damping effect
v_c
z_4
increase of process stability
smearing
v_c
z_4
z_1
improvement of surface quality of finished part

Gra/72767 ©IFW

Fig. 3.1: Process optimized development of tool micro geometry

Both diametrically arranged flutes are identical. The finishing flutes z_1 and z_3 have sharp cutting edges and the roughing flutes z_2 and z_4 have chamfered cutting edges. The chamfered cutting edges contribute to process stability while the sharp cutting edges, due to the radial offset ΔR of the chamfered cutting edges, form the final surface with low roughness and burr formation.

The roughing and finishing ability, respectively, depends on the geometrical design of the tool. The adjustment of the geometric properties must be carried out according to the machining process requirements. A low radial offset of the roughing flutes may increase the achievable process stability. In case of unfavorable runout errors or tool deflection, a low radial offset may lead to the situation that the roughing flutes contribute to the finishing process. This affects the achievable surface quality. Based on the novel geometrical properties of the hybrid tool, the following hypothesis is stated:

By using an end mill with the proposed formation of roughing and finishing flutes (Fig. 3.1), roughing operations can be carried out with enhanced process stability without undermining the finishing ability.

From this hypothesis and the novelty of the proposed hybrid tool, the main aim of this thesis is derived:

- Simulation based investigation of a hybrid end mill with roughing and finishing flutes.

The achievement of the main objective is ensured by accomplishing the following subgoals:

- Mechanistic modeling of process forces with consideration of precise flute paths and including radial offset and runout.
- Dynamic modeling for process stability prediction.
- Model based estimation of the machining behavior by identifying significant parameters and influencing factors.
- Design recommendation based on experimental evaluation.

Accordingly, this thesis is structured on the basis of these subgoals, as shown in Fig. 3.2.

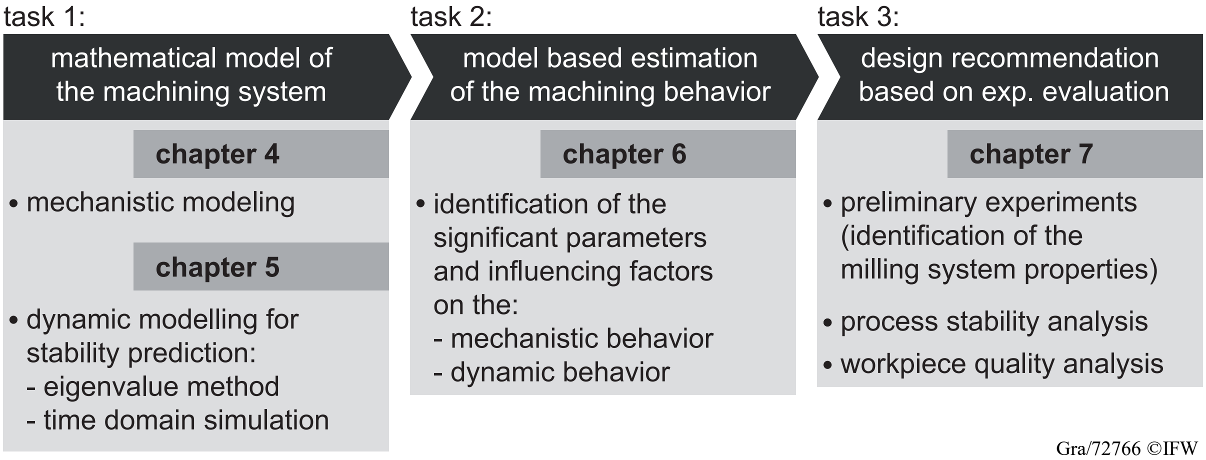
task 1:
mathematical model of the machining system
chapter 4
• mechanistic modeling
chapter 5
• dynamic modelling for stability prediction:
- eigenvalue method
- time domain simulation
task 2:
model based estimation of the machining behavior
chapter 6
• identification of the significant parameters and influencing factors on the:
- mechanistic behavior
- dynamic behavior
task 3:
design recommendation based on exp. evaluation
chapter 7
• preliminary experiments (identification of the milling system properties)
• process stability analysis
• workpiece quality analysis

Gra/72766 ©IFW

Fig. 3.2: Schematic representation of the approach to reach the main objective.

The first task is the derivation of a **mathematical model of the machining system** to predict the mechanistic and dynamic behavior of the machining process. Using mathematical models, a basic understanding of the relationships between the geometric shape of the hybrid tool and the resulting immersion conditions of the individual cutting flutes is acquired. From this, in turn, the process forces can be identified based on empirical force coefficients. Finally, this allows the prediction of the process stability. Known mathematical models for the stability prediction are extended to account for the time-delay changes which result from the immersion conditions of the hybrid tool. Process stability is determined using two methods. With the semi-discretization method, the stable areas can be determined unambiguously and with reasonable computing time based on an eigenvalue analysis (eigenvalue method). However, this approach does not consider nonlinear effects, which occur during the milling process. Therefore, a model for the simulation of the milling behavior in time domain is derived additionally.

The second task deals with the **model based estimation of the machining behavior**. It is investigated which influences, e.g. the radial offset of the chamfered cutting flutes or a runout error, may affect the mechanistic or dynamic behavior. Furthermore, it is also examined whether the shape of the machined surface deformation can be predicted solely based on the geometry of the tool and the resulting forces. Thus, during tool development the influence of the tool geometry on the surface deformation can be taken into account. This contributes to the evaluation of the finishing ability of the new hybrid tool. The assessment of the significance of the input parameters and influencing factors on the mechanistic and dynamic behavior is based on experimental findings from the literature. The results of these investigations serve as a guideline for carrying out the experimental investigations for the evaluation of the machining behavior of the new hybrid tool.

For the **experimental evaluation**, as the third task, the hybrid tool is compared to a tool that has only sharp flutes and a tool that only has chamfered flutes. First, the process forces of these tools are compared with each other in preliminary investigations. Furthermore, the required input variables (process force coefficients and modal parameters) are determined for the calculation of the stability charts. For the process stability investigations, hybrid tools with different radial offsets are considered. Finally, a comparison is made between the tools with regard to the achievable final workpiece quality. This includes the investigation of burr formation and surface deformation of the flank face. Additionally, a comparison between the heat generation during milling with sharp and chamfered cutting flutes is also considered, to investigate the influence of chamfered cutting edges on the heat input into the workpiece.

4 Mechanistic Modeling of Milling Forces

Each flute of the hybrid tool can have a unique shape, i.e. different radial offsets, sharp or chamfered cutting edges. Therefore, it is necessary to derive a process force model which takes into account arbitrary flute geometries. In this context, an important aspect of the force modeling is how the undeformed chip thickness is considered. The common method based on a circular flute trajectory would compromise the impact of the unique geometrical attributes of the hybrid tool concept on the modeled process forces as well as process stability prediction. Thus, the actual trochoidal flute movement will be considered for the calculation of the undeformed chip thickness. A new numerical method for the calculation of the undeformed chip thickness based on precise flute paths is presented. A further factor which influences the process forces, and consequently process stability, is tool runout. In order to take this into account, the same model as used in KRÜGER is applied [Krü14, p. 54 ff.]. In the last section of this chapter, a new method to identify the process force coefficients and runout based on a single cutting test is presented.

4.1 Generalized Process Force Calculation for Arbitrary Flute Geometries

Force modeling techniques can be classified into mechanistic, analytical, numerical and hybrid models [Arr13]. Analytical models are quite complex and in most cases they are only valid for a unique machining problem. An extensive summary and critical examination of literature dealing with the analytical modeling of cutting forces and it drawbacks is provided by ASTAKHOV [Ast05, Ast06]. Similar challenges apply for FEM based force prediction, which is limited by the predefined physics and assumptions of the used software [Ast06]. Mechanistic models offer the possibility to replicate the process forces of tools with complex geometric shapes based on empirical force data [Arr13]. This data can also be used to make predictions how the forces change if the end mill geometry, e.g. helix angle and tooth pitch, is modified. Therefore, the mechanistic approach is the most suitable for the proposed new hybrid tool. It should be noted, however, that for each new cutting wedge geometry, workpiece or tool material, additional experimental investigations are necessary.

FISCHER introduced a force model which considers shearing and ploughing effects separately [Fis97]. This model was later adopted by several authors [Mon91, Bud96, Lee96, Gra04]. As explained in [Gra04], this model has the advantage that it is suitable for analytical works, and thus, will be used in the following. Due to the fact that the hybrid tool has cutting edges with chamfered flank faces, the process damping model by [Wu89] will also be considered in the modeling of the forces. Additionally, two extensions are necessary to obtain the forces of the new proposed hybrid tool:

- Runout is of importance for the new tool concept (Chapter 2.4.1). As it can be seen in Fig. 2.10, runout leads to a variation of tooth radii and tooth pitches in z-direction. Thus, a discretization of the forces in z-direction is necessary. Same applies for tools with unequal helix angles or serrated flutes.
- For ordinary end mills, the amount of material being removed by a cutting flute only depends on the cutting path of the previous flute. In case of flutes with different radii, the removed

volume may depend on multiple preceding flutes, even the current flute itself, as shown in Fig. 2.5.

Taking into account these two points, the tangential $F_{t,j}(t, z_i)$, radial $F_{r,j}(t, z_i)$ and axial $F_{a,j}(t, z_i)$ force components acting at an incremental height z_d on the j-th flute, as shown in Fig. 4.1 a), can be resolved into:

$$\begin{bmatrix} F_{t,j}(t, z_i) \\ F_{r,j}(t, z_i) \\ F_{a,j}(t, z_i) \end{bmatrix} = \sum_{u=1}^{N_t} \left(\begin{bmatrix} K_{tc} \\ K_{rc} \\ K_{ac} \end{bmatrix} h_{j,u}(t, z_i) + \begin{bmatrix} K_{te} \\ K_{re} \\ K_{ae} \end{bmatrix} \frac{1}{\sin(\varkappa_j(z_i))\cos(\delta_j(z_i))} \right) g_{j,u}(t, z_i)\ z_d, \quad (4.1)$$

where K_{tc}, K_{rc} and K_{ac} are the cutting coefficients and K_{te}, K_{re} and K_{ae} are the edge coefficients in tangential, radial and axial direction, respectively. All input variables that change in the axial direction are a function of the incremental axial position z_i, which is defined as follows:

$$z_i = \frac{a_p}{N_z} i = z_d\, i \quad \text{with} \quad \{N_z \in \mathbb{N} \mid 0 < N_z\} \quad \text{and} \quad \{i \in \mathbb{N} \mid i \leq N_z\}. \quad (4.2)$$

This fulfills the first necessary extension (discretization of the forces in z-direction). If the helix angle does not change along the whole flute (δ_j = const.), the incremental tangential force $F_{t,j}(t, z_i)$ can be defined as orthogonal to the z-axis. This does not apply for the cutting edge position angle $\varkappa_j(z_i)$, which varies along the z-axis, as shown in the detailed view in 4.1 a). In this case, $F_{r,j}(t, z_i)$ and $F_{a,j}(t, z_i)$ change their orientation (compare $F_{r,j}(t, z_{i=3})$ and $F_{a,j}(t, z_{i=3})$ with $F_{r,j+1}(t, z_{i=1})$ and $F_{a,j+1}(t, z_{i=1})$, respectively). The edge force components depend on the actual flute length. Therefore, the flute length for each segment z_i needs to be calculated. The flute length depends on the discrete axial length z_d, the cutting edge position angle $\varkappa_j(z_i)$ and the helix angle $\delta_j(z_i)$, as visualized in Fig. 4.1 a). This is especially of importance if an end mill has unequal helix angles, which leads to different cutting edge lengths along the axial position z_i [Gra04].

The summation over the number of flutes N_t is part of the second necessary extension. It summarizes the contribution of all flutes to the resulting force of the j-th flute. The undeformed chip thickness $h_{j,u}(t, z_i)$ and the HEAVISIDE step function $g_{j,u}(t, z_i)$ from Eq. 4.1 are functions of the summation index u: If flutes have different radii, $h_{j,u}(t, z_i)$ and $g_{j,u}(t, z_i)$ may depend on the position of any of the previous teeth u, as shown in the bottom left example in Fig. 2.5. Thus, as a first step, all theoretical possible undeformed chip thickness values for the j-th tooth are calculated. For this purpose, the same derivation of $h_{j,u}(t, z_i)$ as for tools with serrated flutes can be used [Dom10]:

$$h_{j,u}(t, z_i) = \underbrace{f_{j,u}(z_i)\sin\left(\varphi_j(t, z_i)\right) + r_j(z_i) - r_u(z_i)}_{= h_{per,j,u}(t, z_i)} + \underbrace{\Delta\eta_j\left(t - \theta_{j,u}(z_i)\right) - \Delta\eta_j(t)}_{= h_{dyn,j,u}(t, z_i)}. \quad (4.3)$$

As already mentioned in Chapter 2.2, $h_{j,u}(t, z_i)$ consists of a periodic and a dynamic part $h_{per,j,u}(t, z_i)$ and $h_{dyn,j,u}(t, z_i)$, respectively [Ins03b]. The dynamic part is decisive for the stability analysis by means of the SD method. In this context, the periodic part $h_{per,j,u}(t, z_i)$ is of interest to identify a possible engagement between a segment of a flute along the z-axis and the workpiece material.

a) incremental process forces (acting in the direction of the workpiece)

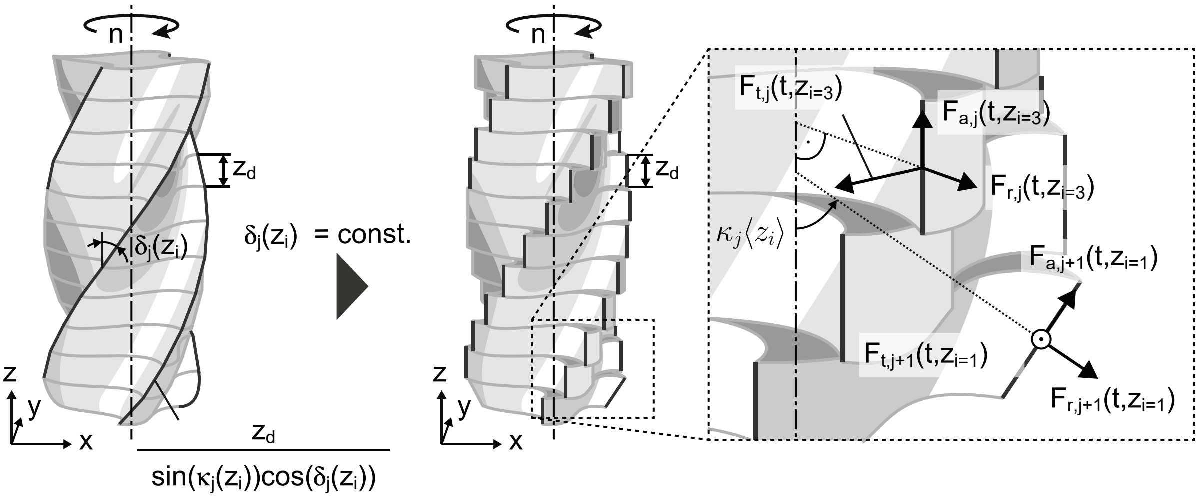
n
n
z_d
z_d
$\delta_j(z_i)$
$\delta_j(z_i)$ = const.
z
y
x
z
y
x
z_d
$\sin(\kappa_j(z_i))\cos(\delta_j(z_i))$
$F_{t,j}(t,z_{i=3})$
$F_{a,j}(t,z_{i=3})$
$F_{r,j}(t,z_{i=3})$
$\kappa_j\langle z_i\rangle$
$F_{a,j+1}(t,z_{i=1})$
$F_{t,j+1}(t,z_{i=1})$
$F_{r,j+1}(t,z_{i=1})$

b) undeformed chip thickness

c) angular position of a flute segment

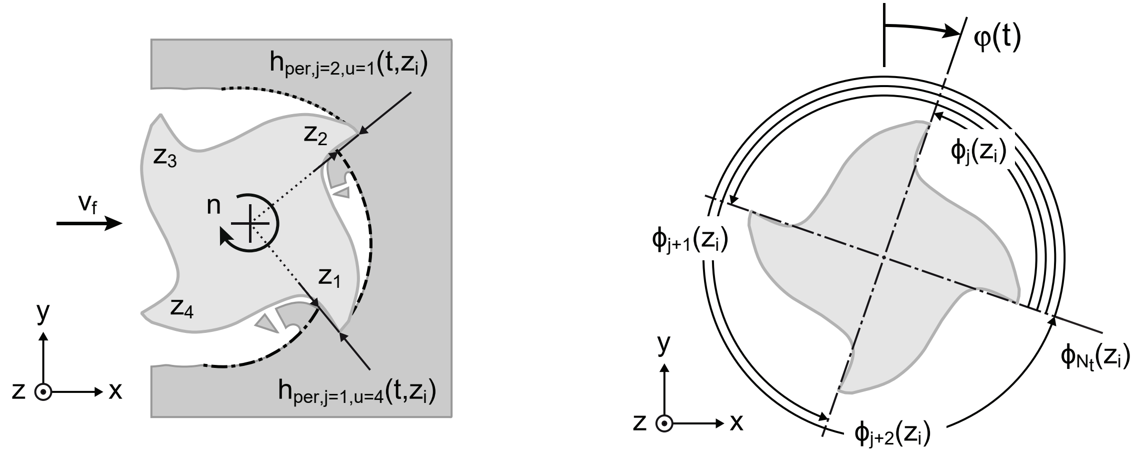
$h_{per,j=2,u=1}(t,z_i)$
z_2
z_3
v_f
n
z_1
z_4
y
z
x
$h_{per,j=1,u=4}(t,z_i)$
$\varphi(t)$
$\phi_j(z_i)$
$\phi_{j+1}(z_i)$
$\phi_{N_t}(z_i)$
y
z
x
$\phi_{j+2}(z_i)$

Gra/72765 ©IFW

Fig. 4.1: Dependence of the shape of the milling cutter on the resulting process forces.

An example of possible immersion conditions and the resulting uncut chip thickness of different flutes is shown in Fig. 4.1 b). The first term of $h_{per,j,u}(t, z_i)$ assumes a circular movement of the flute, first presented by FISCHER [Fis97]. The theoretically exact movement of a cutting flute corresponds to a trochoidal path. Compared to the circular flute movement, the immersion time of a flute is slightly longer in the case of the trochoidal path. In addition, the position of the maximum chip thickness is shifted and slightly larger than the feed per tooth. For reasons of clarity, the circular path model is used in the following. A model for the calculation of the trochoid trajectory is presented in the next section and a comparison of both path variants is made in Chapter 6.1.1. The second term of $h_{per,j,u}(t, z_i)$ considers the variation of flute radii. In order to make the presented derivations for the calculation of $h_{per,j,u}(t, z_i)$ more comprehensible, the example for a three flute end mill segment shown in Fig. 4.2 is used for clarification. The diagram in the top shows all possible values for $h_{per,1,u}(t, z_i)$. A full immersion operation is assumed. Due to the fact that the third flute u = 3 is recessed by $\Delta R = 200\,\mu m$, the values of $h_{per,1,3}(t, z_i)$ for $\varphi_1(t, z_i) = 0^\circ$ and 180° are > 0 mm. Whether a segment of the j-th flute is currently engaged is determined by the HEAVISIDE step function, as applied in Eq. 4.1.

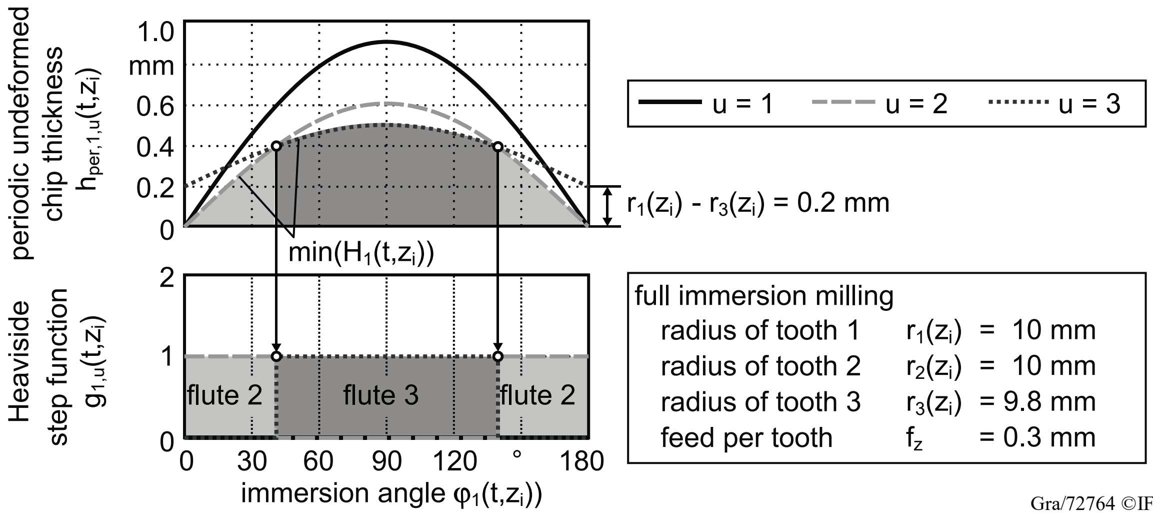

Gra/72764 ©IFW

Fig. 4.2: Example for the resulting periodic undeformed chip thickness $h_{per,j,u}(t, z_i)$ for a tool with three teeth, constant tooth pitch and different radii r (similar to the bottom left example in Fig. 2.5).

The value of $g_{j,u}(t, z_i)$ is set by the following case distinction:

$$g_{j,u}(t, z_i) = \begin{cases} 1 & , \varphi_e \leq \varphi_j(t, z_i) \leq \varphi_a \quad \wedge \quad \min\left(H_j(t, z_i)\right) > 0 \\ 0 & , \text{else.} \end{cases} \tag{4.4}$$

$\varphi_j(t, z_i)$ is the immersion angle for the discrete axial segment position z_i of flute j and is calculated as follows:

$$\varphi_j(t, z_i) = \varphi(t) - \varphi_j(z_i) \tag{4.5}$$

$\varphi_j(z_i)$ is the angular position of flute j, as shown in Fig. 4.1 c), and $\varphi(t)$ is the current rotational position of the tool. The value of $\varphi_j(t, z_i)$ must be in the range of the entry and exit angle φ_e and φ_a, respectively. Additionally, the lowest value of the undeformed chip thickness vector

$$H_j(t, z_i) = \left\{h_{per,j,1}(t, z_i), \ldots, h_{per,j,u}(t, z_i)\right\} \tag{4.6}$$

must have a value > 0 ($h_{per,j,u}(t, z_i) > 0$ mm). Otherwise, if the first condition is satisfied but not the second, it follows that the radius $r_j(z_i)$ of the j-th flute has such a high radial offset that the flute is currently out of cut. In case of the hybrid tool, this offset is part of the tool concept. However, this situation can also occur in the case of a runout error. The resulting values for $g_{1,u}(t, z_i)$ are shown in the bottom diagram in Fig. 4.2. For a regular tool, $g_{1,3}(t, z_i)$ has a value of 1 for the whole immersion range. In this case, the radial offset of flute $u = 3$ leads to the situation that for the immersion range from $\varphi_1 = 0^\circ$ to $\approx 40^\circ$, $g_{1,2}(t, z_i)$ has a value of 1 and $g_{1,3}(t, z_i) = 0$. Same applies from $\varphi_1 \approx 140^\circ$ to 180°. For these ranges, the smallest values of the undeformed chip vector $H_1(t, z_i)$ result from $h_{per,1,2}(t, z_i)$. This is also illustrated by the dashed line in the upper diagramm of Fig. 4.2. From $\varphi_1 \approx 40^\circ$ to $\approx 140^\circ$ the smallest undeformed chip thickness is associated with $h_{per,1,3}(t, z_i)$, and thus, the value of $g_{1,3}(t, z_i)$ is 1. The resulting immersion conditions for all flutes are also shown in the bottom left example in Fig. 2.5. As desired for the hybrid end mill, this mathematical model shows how the offset can affect the engagement conditions of a cutting edge which enters or exits the workpiece.

Furthermore, the radial offset of a flute also affects the feed per tooth. In analogy to variable pitch cutters, the effective feed per tooth $f_{j,u}(z_i)$ may vary for every tooth [Eng99]. The effective feed per tooth is calculated as follows:

$$f_{j,u}(z_i) = f_z N_t \frac{p_{j,u}(z_i)}{2\pi} \tag{4.7}$$

with the tooth pitch

$$p_{j,u}(z_i) = \varphi_u(z_i) - \varphi_j(z_i) + \underbrace{2\pi\left(1 - \left\lceil \frac{\varphi_u(z_i) - \varphi_j(z_i)}{2\pi} \right\rceil\right)}_{\text{ensures that } 0 \, < \, p_{j,u}(z_i) \, \leq \, 2\pi} . \tag{4.8}$$

Based on these derivations, $h_{per,j,u}(t, z_i)$ can now be calculated. Furthermore, the derivation of $p_{j,u}(z_i)$ is used for the calculation of the time delays, which are necessary for $h_{dyn,j,u}(t, z_i)$ (Eq. 4.3):

$$\theta_{j,u}(z_i) = \frac{1}{n} \frac{p_{j,u}(z_i)}{2\pi} \tag{4.9}$$

For stability prediction, the process forces must be transformed in order to correspond to the right side of Eq. 2.1. The following steps are well known from the literature. Below is a brief summary of the procedure from [Sel12a, p. 25 ff.], which is expanded by the hybrid tool specific mathematical extensions.

According to Chapter 2.2, the dynamic behavior of the system is determined in a fixed Cartesian coordinate system. Thus, a conversion of the forces from Eq. 4.1 is required:

$$\begin{bmatrix} F_f(t) \\ F_{fN}(t) \\ F_p(t) \end{bmatrix} = \sum_{j=1}^{N_t} \sum_{i=1}^{N_z} \mathbf{T}_j(t, z_i) \begin{bmatrix} F_{t,j}(t, z_i) \\ F_{r,j}(t, z_i) \\ F_{a,j}(t, z_i) \end{bmatrix} \tag{4.10}$$

$F_f(t)$ is the feed, $F_{fN}(t)$ the feed normal and $F_p(t)$ the passive force. In the following, the feed direction always corresponds to the x-coordinate and the feed normal direction corresponds to the y-coordinate. The direction of the passive force corresponds to the z-coordinate. The coordinate transformation is carried out by the rotational matrix

$$\mathbf{T}_j(t, z_i) = \begin{bmatrix} \cos(-\varphi_j(t, z_i)) & -\sin(-\varphi_j(t, z_i))\sin(\varkappa_j(z_i)) & -\sin(-\varphi_j(t, z_i))\cos(\varkappa_j(z_i)) \\ \sin(-\varphi_j(t, z_i)) & \cos(-\varphi_j(t, z_i))\sin(\varkappa_j(z_i)) & \cos(-\varphi_j(t, z_i))\cos(\varkappa_j(z_i)) \\ 0 & -\cos(\varkappa_j(z_i)) & \sin(\varkappa_j(z_i)) \end{bmatrix} \tag{4.11}$$

This rotational matrix takes into account the possible geometrical changes of the flutes ($\varkappa_j(z_i)$) and the different incremental flute positions ($\varphi_j(t, z_i)$) in the axial direction. According to Eq. 4.3 for the undeformed chip thickness, the forces from Eq. 4.1 are divided into a dynamic and periodic component. The periodic component is calculated by substituting $h_{,j,u}(t, z_i)$ within Eq. 4.1 with $h_{per,j,u}(t, z_i)$ from Eq. 4.3. The periodic component will be applied in the time-domain simulation (Chapter 5.2). The dynamic component is necessary for the stability prediction based on the SD method, as given in Eq. 2.1 and following. It can be calculated as follows:

$$\begin{bmatrix} F_{f,dyn}(t) \\ F_{fN,dyn}(t) \end{bmatrix} = \sum_{j,u=1}^{N_t} \sum_{i=1}^{N_z} \mathbf{Q}_{j,u}(t, z_i) \left(\begin{bmatrix} \Delta x\left(t - \theta_{j,u}(z_i)\right) \\ \Delta y\left(t - \theta_{j,u}(z_i)\right) \end{bmatrix} - \begin{bmatrix} \Delta x(t) \\ \Delta y(t) \end{bmatrix} \right) \tag{4.12}$$

with

$$\mathbf{Q}_{j,u}(t, z_i) = \mathbf{T}_{j,dyn}(t, z_i) \begin{bmatrix} 0 & K_{tc} \\ 0 & K_{rc} \end{bmatrix} \mathbf{T}_{j,dyn}^{-1}(t, z_i)\, z_d\, g_{j,u}(t, z_i)\,. \tag{4.13}$$

According to Eq. 4.3, the dynamic component of the chip thickness only has force components in the x-y plane, and thus, the z-coordinate is not considered here. Therefore, the dynamic transformation matrix is also reduced:

$$\mathbf{T}_{j,dyn}(t, z_i) = \begin{bmatrix} \cos(-\varphi_j(t, z_i)) & -\sin(-\varphi_j(t, z_i))\sin(\varkappa_j(z_i)) \\ \sin(-\varphi_j(t, z_i)) & \cos(-\varphi_j(t, z_i))\sin(\varkappa_j(z_i)) \end{bmatrix} \tag{4.14}$$

The rotation matrix $\mathbf{T}_{j,dyn}(t, z_i)$ is used twice in Eq. 4.12. First, to convert the forces into the feed and feed normal direction. Second, the inverse matrix of $\mathbf{T}_{j,dyn}(t, z_i)$ is used to transform the dynamic variation of the chip thickness according to Eq. 4.3 into the x-y-coordinate system. Furthermore, the dynamic system has a multiple of modes in x- and y-direction, which can be taken into account as follows:

$$\begin{bmatrix} F_{f,dyn}(t) \\ F_{fN,dyn}(t) \end{bmatrix} = \sum_{j,u=1}^{N_t} \sum_{i=1}^{N_z} \mathbf{Q}_{j,u}(t, z_i) \left(\Delta\mathbf{q}\left(t - \theta_{j,u}(z_i)\right) - \Delta\mathbf{q}(t) \right) \tag{4.15}$$

In analogy to Eq. 2.4, the vector $\Delta\mathbf{q}$ is defined, which contains the relative dynamic displacement of all modes:

$$\begin{bmatrix} \Delta x(t) \\ \Delta y(t) \end{bmatrix} = \begin{bmatrix} \sum\limits_{i=1}^{k} x_{w,i} - \sum\limits_{i=1}^{m} x_{t,i} \\ \sum\limits_{i=1}^{l} y_{w,i} - \sum\limits_{i=1}^{n} y_{t,i} \end{bmatrix} = \underbrace{\begin{bmatrix} \mathbf{1}_{1\times k} & \mathbf{0}_{1\times l} & -\mathbf{1}_{1\times m} & \mathbf{0}_{1\times n} \\ \mathbf{0}_{1\times k} & \mathbf{1}_{1\times l} & \mathbf{0}_{1\times m} & -\mathbf{1}_{1\times n} \end{bmatrix}}_{=\,\mathbf{T}_q} \mathbf{q}(t) = \Delta\mathbf{q}(t)\,. \tag{4.16}$$

$\mathbf{Q}_{j,u}(t, z_i)$ from Eq. 4.15 as well as the method of the summarized modes from Eq. 4.16 will be applied in the derivatives to predict the process stability based on the SD method (Chapter 5.1).

Analogous to the described procedure for the common process forces, the additional process damping forces, described in Chapter 2.3.2, can be transformed accordingly. The basic model of the process damping forces is given in Eq. 2.7 and 2.8. A detailed description can be found in [Sel12a, p. 40 ff.]. In analogy to the dynamic process forces, these velocity dependent force components are extended to take into account z-discretization and varying time delays:

$$\begin{bmatrix} F_{pd,f,dyn}(t) \\ F_{pd,fN,dyn}(t) \end{bmatrix} = \sum_{j,u=1}^{N_t} \sum_{i=1}^{N_z} \left(-\mathbf{Q}_{pd,j,u}(t, z_i) \right) \Delta\dot{\mathbf{q}}(t) \tag{4.17}$$

with

$$\mathbf{Q}_{\mathrm{pd},j,u}(t, z_i) = \frac{b_f^2}{2v_c}\mathbf{T}_{j,\mathrm{dyn}}(t, z_i)\begin{bmatrix}0 & 1\\0 & \mu_{\mathrm{pd}}\end{bmatrix}K_{\mathrm{pd}}\mathbf{T}_{j,\mathrm{dyn}}^{-1}(t, z_i)\, z_d\, g_{j,u}(t, z_i)\,. \tag{4.18}$$

$\mathbf{Q}_{\mathrm{pd},j,u}(t, z_i)$ will be used in the stability prediction based on the SD method.

4.2 Undeformed Chip Thickness Based on Trochoidal Flute Movement

MARTELLOTTI was one of the first to calculate the undeformed chip thickness under consideration of the trochoid trajectory of the teeth [Mar41]. The author assumed for his model that the teeth are evenly distributed around the circumference. FAASSEN stated that the method in [Mar41] involves complex equations and therefore proposed a new method [Faa07]. KUMANCHIK and SCHMITZ developed an analytical model which is also capable to consider tool runout [Kum07]. They compare their estimation of $h_{j,u}(t, z_i)$ with other models from literature and show that their model leads to lower error levels.

All mentioned models have in common that the undeformed chip thickness $h_{j,u}(t, z_i)$ of the j-th tooth is derived from the tooth path of the j-th and $(j-1)$-th tooth. For roughing tools with serrated flutes or the proposed tool concept, all generated tooth paths of a previous revolution need to be considered to determine the undeformed chip thickness. Thus, a more versatile model is required for such tools. Flutes with a radial offset, unequal tooth pitches and tool runout need to be considered. The numerical model proposed by SONG et al. fulfills these conditions [Son13]. Their developed algorithm is based on iterative steps to approximate $h_{j,u}(t, z_i)$. The new developed model in this thesis, which will be described in the following, requires no iteration to calculate $h_{j,u}(t, z_i)$. This yields an advantage in terms of computing time. Furthermore, the accuracy of the calculated undeformed chip thickness solely depends on the resolution of the discretization. Thus, for very small discretization steps, the error is insignificant low. The numerical method is based on matrix operations, which reduces calculation time notably, especially if MATLAB is used. For the following derivations, Fig. 4.3 is used for explanation. The following steps are carried out to determine the chip thickness $h_{j,u}(t, z_i)$:

- First, a vector is formed from the current cutting position $\mathbf{S}_j(t, z_i)$ and the tool center point $\mathbf{C}_t$ (upper illustration in Fig. 4.3).
- Next, the intersections $\mathbf{P}_j(t, z_i)$ between this vector and the cutting paths of the preceding cutting flutes $\mathbf{S}_{j,u}(t, z_i)$ are determined numerically (bottom illustrations in Fig. 4.3).
- Finally, from all resulting intersections, it is necessary to identify the intersection which is part of the calculation of the undeformed chip thickness $h_{j,u}(t, z_i)$ (case 1 from the bottom left illustration in Fig. 4.3).

The challenge in this procedure is the last step. In order to comply with the required conditions that any kind of cutting edge geometry needs to be considered, all possible intersections must be calculated to determine $h_{j,u}(t, z_i)$. This is a computationally intensive process. As already mentioned, the calculation time can be reduced with matrix operations.

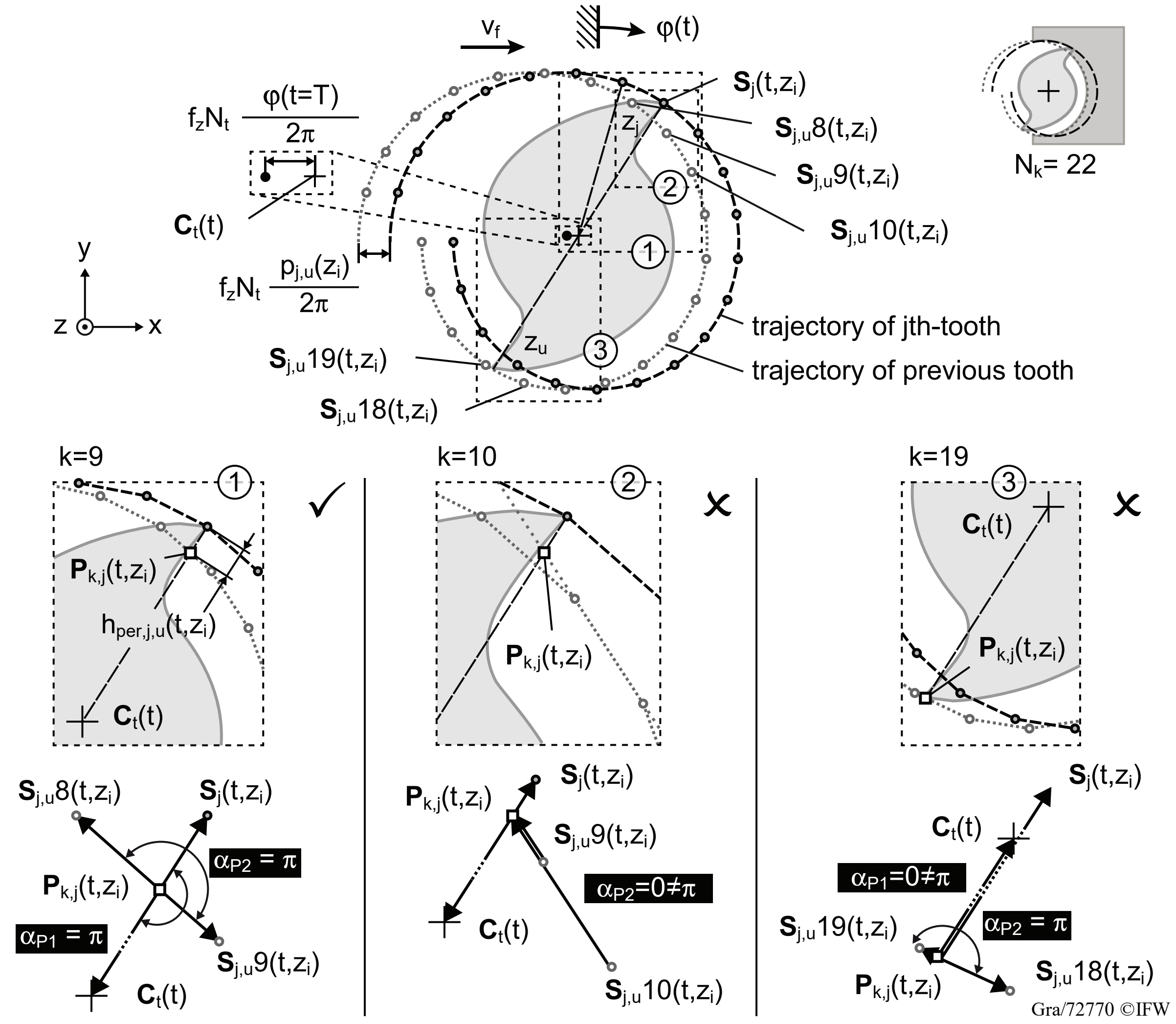
v_f
φ(t)
$f_zN_t \frac{\varphi(t=T)}{2\pi}$
C_t(t)
$f_zN_t \frac{p_{j,u}(z_i)}{2\pi}$
y
z
x
S_j(t,z_i)
S_j,u8(t,z_i)
S_j,u9(t,z_i)
S_j,u10(t,z_i)
z_j
z_u
1
2
3
N_k= 22
trajectory of jth-tooth
trajectory of previous tooth
S_j,u19(t,z_i)
S_j,u18(t,z_i)
k=9
k=10
k=19
P_k,j(t,z_i)
h_per,j,u(t,z_i)
C_t(t)
α_P2 = π
α_P1 = π
α_P2=0≠π
α_P1=0≠π
Gra/72770 ©IFW

Fig. 4.3: Procedure to determine the undeformed chip thickness for the trochoidal flute trajectory.

For the first step, the trochoidal trajectory of an incremental tooth segment $\mathbf{S}_j\,(t, z_i)$ in the x-y-plane can be derived as follows:

$$\mathbf{S}_j\,(t, z_i) = \begin{bmatrix} S_{x,j}\,(t, z_i) \\ S_{y,j}\,(t, z_i) \end{bmatrix} = r_j\,(z_i) \begin{bmatrix} \cos(-\varphi_j\,(t, z_i)) \\ \sin(-\varphi_j\,(t, z_i)) \end{bmatrix} + \underbrace{\begin{bmatrix} 1 \\ 0 \end{bmatrix} f_z N_t \frac{\varphi\,(t)}{2\pi}}_{= \mathbf{C}\,(t)} . \tag{4.19}$$

The first summand describes the rotation of the tooth. The second summand equals the tool center point $\mathbf{C}\,(t)$, which indicates the current tool position in feed direction. In analogy to the procedure in Chapter 4.1, the paths for all previous cutting flutes are calculated, including the current cutting flute j itself:

$$\mathbf{S}_{j,u}\,(t, z_i) = \begin{bmatrix} S_{x,j,u}\,(t, z_i) \\ S_{y,j,u}\,(t, z_i) \end{bmatrix} = \mathbf{S}_j\,(t, z_i) - \begin{bmatrix} 1 \\ 0 \end{bmatrix} f_z N_t \frac{p_{j,u}\,(z_i)}{2\pi} \tag{4.20}$$

The calculation of $p_{j,u}\,(z_i)$ is given in Eq. 4.8. In order to calculate all possible intersections between the current flute position $\mathbf{S}_j\,(t, z_i)$ and a preceding flute u at once, the entire trochoidal path of the flute u must be calculated for one tool revolution. In the upper illustration in Fig. 4.3, this is exemplified for a tool with two flutes. For reasons of clarity, the trajectory of the flute j for the preceding revolution ($\mathbf{S}_{j,u=j}\,(t, z_i)$) is not illustrated. First, the path is discretized into equidistant time intervals

$$T_{rev} = \frac{1}{n} = N_{rev}T \quad \text{with} \quad \{N_{rev} \in \mathbb{N} \mid 0 < N_{rev}\}\,. \tag{4.21}$$

T_{rev} is the time for one tool revolution, which is discretized into N_{rev} elements with the sampling interval T. With the time vector

$$\mathbf{t}_{rev} \;=\; [T, 2T, \ldots, kT, (N_{rev} - 1)T]\,, \tag{4.22}$$

all flute positions $\mathbf{S}_{j,u}\,(t, z_i)$ from Eq. 4.20 for one tool revolution are stored as follows:

$$\mathbf{S}_{j,u}\,(\mathbf{t}_{rev}, z_i) = \mathbf{S}_{rev,j,u}\,(z_i) = \begin{bmatrix} \mathbf{S}_{x,rev,j,u}\,(z_i) \\ \mathbf{S}_{y,rev,j,u}\,(z_i) \end{bmatrix} \tag{4.23}$$

$\mathbf{S}_{j,u}\,(\mathbf{t}_k, z_i)$ is a $2 \times N_{rev}$ matrix. The next step is to determine all $N_{rev} - 1$ possible intersection points

$$\mathbf{P}_{j,u}\,(t, z_i) = \begin{bmatrix} \mathbf{P}_{x,j,u}\,(t, z_i) \\ \mathbf{P}_{y,j,u}\,(t, z_i) \end{bmatrix} = \begin{bmatrix} \mathbf{P}_{1,j,u}\,(t, z_i)\,, & \ldots, & \mathbf{P}_{k,j,u}\,(t, z_i)\,, & \mathbf{P}_{N_{rev}-1,j,u}\,(t, z_i) \end{bmatrix} \tag{4.24}$$

between the trochoidal path of the preceding flute u, which corresponds to the matrix $\mathbf{S}_{j,u}\,(\mathbf{t}_k, z_i)$, and the vector consisting of the current flute position $\mathbf{S}_j\,(t, z_i)$ and the tool center point

$$\mathbf{C}_t\,(t) = \begin{bmatrix} C_{x,t}\,(t) \\ C_{y,t}\,(t) \end{bmatrix} \tag{4.25}$$

As illustrated in Fig. 4.3 for the three bottom cases, two consecutive positions of a preceding trochoidal path of the u-th flute form a line (e.g. case 1: $\mathbf{S}_{j,u}\,(8T, z_i)$ and $\mathbf{S}_{j,u}\,(9T, z_i)$), which is necessary for the calculation of one intersection. Therefore, the matrix

$$\mathbf{S}_{rev+T,j,u}\,(z_i) = \begin{bmatrix} \mathbf{S}_{x,rev+T,j,u}\,(z_i) \\ \mathbf{S}_{y,rev+T,j,u}\,(z_i) \end{bmatrix} = \mathbf{S}_{j,u}\,(\mathbf{t}_{rev} + T, z_i) \tag{4.26}$$

is used, additionally. This matrix contains the same values as $\mathbf{S}_{j,u}\,(\mathbf{t}_k, z_i)$, shifted by one sampling interval T ahead. As it will be shown in the following, it allows to calculate all intersection points at once. For the calculation of $\mathbf{P}_{j,u}\,(t, z_i)$, the two lines are represented in coordinate form:

$$\underbrace{\big(C_{y,t}\,(t) - S_{y,j}\,(t, z_i)\big)}_{=\,a_j\,(t, z_i)}\,x + \underbrace{\big(S_{x,j}\,(t, z_i) - C_{x,t}\,(t)\big)}_{=\,b_j\,(t, z_i)}\,y = \underbrace{C_{y,t}\,(t)\,S_{x,j}\,(t, z_i) - C_{x,t}\,(t)\,S_{y,j}\,(t, z_i)}_{=\,c_j\,(t, z_i)} \tag{4.27}$$

and

$$\begin{aligned}\underbrace{\left(\mathbf{S}_{y,rev+T,j,u}(z_i)-\mathbf{S}_{y,rev,j,u}(z_i)\right)}_{=\mathbf{a}_{j,u}(z_i)}x+\underbrace{\left(\mathbf{S}_{x,rev,j,u}(z_i)-\mathbf{S}_{x,rev+T,j,u}(z_i)\right)}_{=\mathbf{b}_{j,u}(z_i)}y\\=\underbrace{\mathbf{S}_{y,rev+T,j,u}(z_i)\circ\mathbf{S}_{x,rev,j,u}(z_i)-\mathbf{S}_{x,rev+T,j,u}(z_i)\circ\mathbf{S}_{y,rev,j,u}(z_i)}_{\mathbf{c}_{j,u}(z_i)}\end{aligned}\tag{4.28}$$

The symbol $\circ$ in Eq. 4.28 denotes the element by element HADAMARD matrix multiplication [Eis70, p. 42]. The HADAMARD matrix multiplication can also be carried out for all further steps, which are required to calculate the undeformed chip thickness. However, for the sake of clarity, the calculation of a single intersection will be derived in the following. Thus, Eq. 4.28 is changed to:

$$\begin{aligned}\underbrace{\left(S_{y,j,u}(t+T,z_i)-S_{y,j,u}(t,z_i)\right)}_{=a_{j,u}(t,z_i)}x+\underbrace{\left(S_{x,j,u}(t,z_i)-S_{x,j,u}(t+T,z_i)\right)}_{=b_{j,u}(t,z_i)}y\\=\underbrace{S_{y,j,u}(t+T,z_i)\,S_{x,j,u}(t,z_i)-S_{x,j,u}(t+T,z_i)\,S_{y,j,u}(t,z_i)}_{c_{j,u}(t,z_i)}\end{aligned}\tag{4.29}$$

These two straight line equations can be combined into a linear system of equations:

$$\left(\begin{array}{cc|c} a_j(t,z_i) & b_j(t,z_i) & c_j(t,z_i)\\ a_{j,u}(t,z_i) & b_{j,u}(t,z_i) & c_{j,u}(t,z_i)\end{array}\right)\tag{4.30}$$

The solutions of this system can be determined by applying CRAMER's rule (see [Zur97, p. 41] for further explanations) for the x-coordinate

$$P_{x,k,j,u}(t,z_i)=\frac{c_j(t,z_i)\,b_{j,u}(t,z_i)-c_{j,u}(t,z_i)\,b_j(t,z_i)}{a_j(t,z_i)\,b_{j,u}(t,z_i)-a_{j,u}(t,z_i)\,b_j(t,z_i)}\tag{4.31}$$

and the y-coordinate

$$P_{y,k,j,u}(t,z_i)=\frac{a_j(t,z_i)\,c_{j,u}(t,z_i)-a_{j,u}(t,z_i)\,c_j(t,z_i)}{a_j(t,z_i)\,b_{j,u}(t,z_i)-a_{j,u}(t,z_i)\,b_j(t,z_i)}\tag{4.32}$$

with

$$\mathbf{P}_{k,j,u}(t,z_i)=\begin{bmatrix}P_{k,x,j,u}(t,z_i)\\P_{k,y,j,u}(t,z_i)\end{bmatrix}\tag{4.33}$$

Next, it must be determined which intersection $\mathbf{P}_{k,j,u}(t,z_i)$ is needed for the calculation of $h_{per,j,u}(t,z_i)$. From the bottom illustrations in Fig. 4.3, it follows that the angle α_{P1} and α_{P2} must equal π. These angles can be calculated with the dot product. The first angle

$$\alpha_{P1}=\arccos\left(\frac{\left(\mathbf{C}_t(t)-\mathbf{P}_{k,j,u}(t,z_i)\right)\bullet\left(\mathbf{S}_j(t,z_i)-\mathbf{P}_{k,j,u}(t,z_i)\right)}{\left\|\mathbf{C}_t(t)-\mathbf{P}_{k,j,u}(t,z_i)\right\|\,\left\|\mathbf{S}_j(t,z_i)-\mathbf{P}_{k,j,u}(t,z_i)\right\|}\right)\overset{!}{=}\pi\tag{4.34}$$

determines if the intersection lies inside the line segment formed by the vectors $\mathbf{C}_t(t)$ and $\mathbf{S}_j(t,z_i)$.

In analogy, the angle

$$\alpha_{P2} = \arccos\left(\frac{\left(\mathbf{S}_{j,u}(t,z_i) - \mathbf{P}_{k,j,u}(t,z_i)\right) \bullet \left(\mathbf{S}_{j,u}(t+T,z_i) - \mathbf{P}_{k,j,u}(t,z_i)\right)}{\left\|\mathbf{S}_{j,u}(t,z_i) - \mathbf{P}_{k,j,u}(t,z_i)\right\| \left\|\mathbf{S}_{j,u}(t+T,z_i) - \mathbf{P}_{k,j,u}(t,z_i)\right\|}\right) \overset{!}{=} \pi \tag{4.35}$$

determines if the intersection lies inside the line segment formed by the vectors $\mathbf{S}_{j,u}(t,z_i)$ and $\mathbf{S}_{j,u}(t+T,z_i)$. This condition is fulfilled for case 1 and case 3, as shown in Fig. 4.3. For case 2, the intersection is outside the line segment. Both conditions are only met for case 1. Thus, the undeformed chip thickness can be calculated as follows:

$$h_{per,j,u}(t,z_i) = \left\|\mathbf{S}_j(t,z_i) - \mathbf{P}_{k,j}(t,z_i)\right\| \tag{4.36}$$

With this method, $h_{per,j,u}(t,z_i)$ in case of full immersion milling is calculated. By adding an additional line just like a previous flute at the radial depth of cut, up- or down-milling can be implemented, too. In analogy to the undeformed chip thickness in case of a circular flute movement, the value of the HEAVISIDE function from Eq. 4.4 can be determined. However, only the second condition needs to be considered ($\min\left(H_j(t,z_i)\right) > 0$). In case of the presented trochoidal flute path model, if the flute position is outside the entry and exit angle, the second condition is not satisfied. Thus, the first condition is obsolete.

The presented force model in Chapter 4.1 and the consideration of the trochoidal flute path allows a detailed analysis of the load on flutes with complex geometries, as it can be explained based on the end mills in Fig. 4.4. This illustration provides an overview of how the cutting geometry affects the removed material volume and the resulting forces. An end mill with different helix angles is shown in Fig. 4.4 a). Due to the increasing tooth pitch between flute 1 and flute 2 in axial direction, the undeformed chip thickness of flute 1 decreases, as illustrated on the left. Consequently, the removed material from flute 2 increases in z-direction. The diagram on the right shows the associated incremental radial forces $F_r(z_i)$. The increasing (decreasing) tooth pitch leads to higher (lower) peak force values. Furthermore, a shift in z-direction and along the immersion angle for the peak values results from the different helix angles. As a second example, an end mill with serrated flutes is shown in Fig. 4.4 b). As it can be seen in the left illustration, the immersion entry and exit varies along the z-direction. This is caused by the varying radial recessed flute segments. At axial positions were the contrary flute's radius is recessed, the undeformed chip thickness is increased. This leads to the interrupted and cusp shaped incremental process forces, as it can be seen in the right diagram in Fig. 4.4 b).
The spatial variation of the forces in case of both end mills applies similarly for time delays, which will be investigated in Chapter 6.2.1. As mentioned in Chapter 2.4.1, a further influence on time delays occurs in case of runout errors. In the following section, a model for the consideration of radial runout error in the process force calculation and consequently in the stability prediction will be presented.

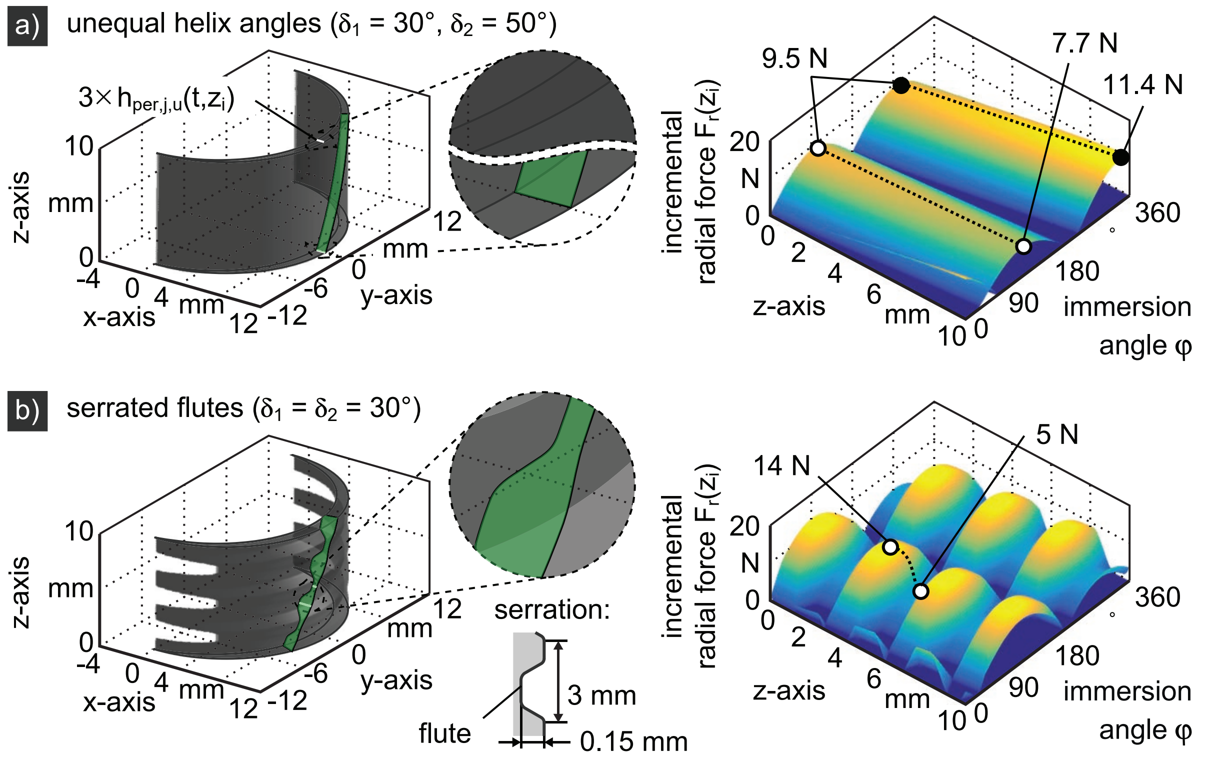

tool diameter:	$D = 20$ mm	tan. cutting coeff.:	$K_{tc} = 600$ N/mm^2
number of teeth:	$N_t = 2$	rad. cutting coeff.:	$K_{rc} = 200$ N/mm^2
radial depth of cut:	$a_e = D$	ax. cutting coeff.:	$K_{ac} = 50$ N/mm^2
axial depth of cut:	$a_p = 10$ mm	tan. edge coeff.:	$K_{te} = 8$ N/mm
feed per tooth	$f_z = 0.3$ mm	rad. edge coeff.:	$K_{ee} = 8$ N/mm
discretization	$N_k = 1440$, $N_z = 200$	ax. edge coeff.:	$K_{ae} = 4$ N/mm
process:	full immersion		

Gra/72852 ©IFW

Fig. 4.4: Incremental force distribution in case of an end mill with a) unequal helix angles and b) serrated flutes.

4.3 Tool Runout

Tool runout changes the kinematic of the flute movement. As described in Chapter 2.4.1, this can lead to the situation that the roughing flutes with recessed radii and chamfered cutting edges actually contribute to surface finish. Consequently, this condition must be avoided. To assess whether runout contradicts the tool concept, the radii r_j and radial positions φ_j of the flutes must be enhanced by the deviation caused by the geometric location of the runout offset ρ_r and runout location angle λ_r. These geometric relations are illustrated in Fig. 4.5. The tool on the left shows the actual tool geometry. By considering the tool runout position as the new tool center point, the actual spatial locations of the flutes correspond to the shown tool geometry on the right. Utilizing trigonometric relations, the position of the flutes extended by tool runout can be formulated as follows:

$$r_{r,j}(z_i) = \sqrt{\rho_r^2 + r_j(z_i)^2 - 2\rho_r r_j(z_i)\cos(\lambda_r - \varphi_j(z_i))}. \tag{4.37}$$

A detailed derivation is given in [Krü14, p. 56]. In case of flutes with helix angles $\delta > 0$, the location of the flutes in axial direction z varies due to runout (Fig. 2.10). Thus, the incremental axial position z_i is considered as a variable.

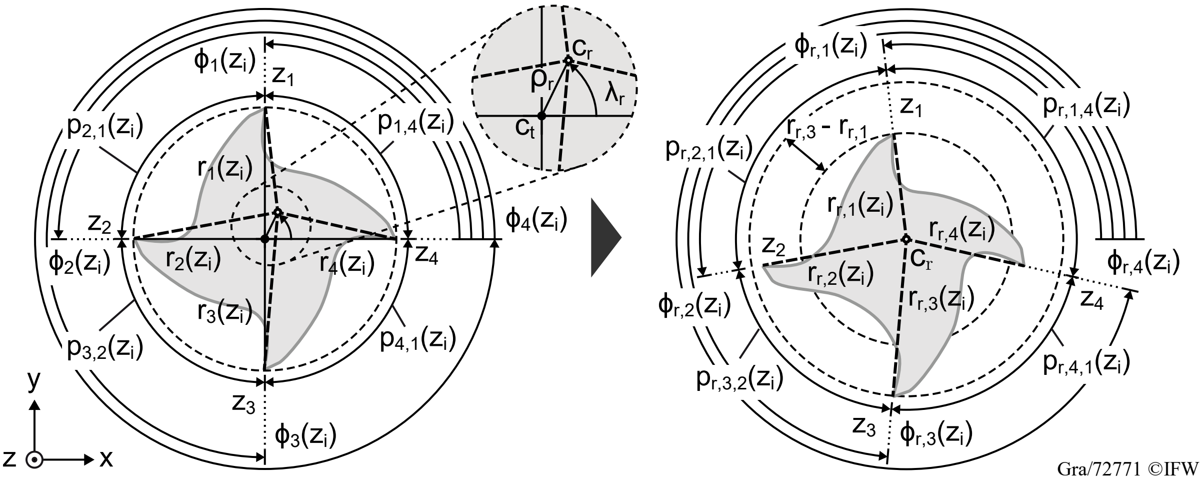
$\phi_1(z_i)$
z_1
$p_{2,1}(z_i)$
$p_{1,4}(z_i)$
$r_1(z_i)$
z_2
$\phi_2(z_i)$
$r_2(z_i)$
$r_4(z_i)$
z_4
$\phi_4(z_i)$
$r_3(z_i)$
$p_{3,2}(z_i)$
$p_{4,1}(z_i)$
z_3
$\phi_3(z_i)$
y
z
x
c_r
ρ_r
λ_r
c_t
$\phi_{r,1}(z_i)$
z_1
$p_{r,1,4}(z_i)$
$p_{r,2,1}(z_i)$
$r_{r,3} - r_{r,1}$
$r_{r,1}(z_i)$
$r_{r,4}(z_i)$
z_2
c_r
$r_{r,2}(z_i)$
$r_{r,3}(z_i)$
$\phi_{r,4}(z_i)$
$\phi_{r,2}(z_i)$
z_4
$p_{r,3,2}(z_i)$
$p_{r,4,1}(z_i)$
z_3
$\phi_{r,3}(z_i)$
Gra/72771 ©IFW

Fig. 4.5: Influence of tool runout on the geometrical properties of the tool based on [Krü14, p. 54].

As shown in Fig. 4.5, the radial position of the flutes also changes. The radial position extended by runout can be calculated as follows:

$$\varphi_{r,j}(z_i) = \arctan\left(\frac{r_{r,y}(z_i)}{r_{r,x}(z_i)}\right) + \pi \left\| \left\lfloor \frac{1}{10} \frac{r_{r,x}(z_i)}{\left|r_{r,x}(z_i)\right|} \right\rfloor \right\| \tag{4.38}$$

with

$$\begin{aligned} r_{r,x}(z_i) &= r_j(z_i)\cos(\varphi_j(z_i)) - \rho_r\cos(\lambda_r) \\ r_{r,y}(z_i) &= r_j(z_i)\sin(\varphi_j(z_i)) - \rho_r\sin(\lambda_r) \end{aligned} \tag{4.39}$$

The second summand in Eq. 4.38 takes into account in which quadrant $r_{r,j}(z_i)$ is located, with $\mathbf{c}_r$ as the center point of the coordinate system. With Eq. 4.37 and Eq. 4.38, the undeformed chip thickness values of the flutes can be calculated with tool runout consideration, as described in Chapter 4.2. Thus, the influence of tool runout on the kinematic of the flutes can be considered for the prediction of the dynamical tool behavior, which will be described in Chapter 5.

In order to be able to estimate whether ρ_r causes the recessed flutes to actually have a larger radius than the regular flutes, the extreme values for $r_{r,j}(z_i)$ from Eq. 4.37 must be determined. The maximum and minimum values result from the greatest possible and smallest possible spatial distance, respectively, between $r_{r,j}(z_i)$ and ρ_r:

$$\begin{aligned} \max\left(r_{r,j}(z_i)\right) &= \sqrt{\rho_r^2 + r_j(z_i)^2 + 2\rho_r r_j(z_i)} \quad \text{for} \quad \lambda_r = \pi + \varphi_j(z_i)\,. \\ \min\left(r_{r,j}(z_i)\right) &= \sqrt{\rho_r^2 + r_j(z_i)^2 - 2\rho_r r_j(z_i)} \quad \text{for} \quad \lambda_r = \varphi_j(z_i)\,. \end{aligned} \tag{4.40}$$

The most unfavorable case for the hybrid tool is when the maximum value occurs for a recessed flute. Assuming a tool with one recessed flute, denoted by the index u and $\lambda_r = \pi + \varphi_u(z_i)$, the radius of the remaining regular flutes is calculated as follows:

$$r_{r,j}(z_i) = \sqrt{\rho_r^2 + r_j(z_i)^2 - 2\rho_r r_j(z_i)\cos(p_{j,u}(z_i))}. \tag{4.41}$$

The formula for $p_{j,u}(z_i)$ is given in Eq. 4.8. In the next step, it is necessary to make sure if the radii of the regular flutes $r_{r,j\neq u}(z_i)$ are smaller than for the recessed flute $r_{r,j=u}(z_i)$. Otherwise, the recessed flute contribute to the machining of the final surface. To prevent this, the required minimum value for ΔR in case of $\rho_r > 0$ must be known. If we assume a tool with a helix angle of $\delta = 0^\circ$ and that all tooth radii are equal ($r_j = r$) besides one with a radial offset ΔR, the following inequation resulting from Eq. 4.40 and (4.41) must be solved for ΔR:

$$(r - \Delta R)^2 - 2\rho_r(r - \Delta R) < r^2 - 2\rho_r r \min\left(\cos(p_{j,u})\right). \tag{4.42}$$

The highest value for the right-hand side of this inequation arise in case of $\cos(p_{j,u} = \pi)$. This leads to the following sufficient condition for the prevention of the contact of a recessed flute with the final machined surface:

$$\Delta R > 2\rho_r \tag{4.43}$$

With the knowledge of Eq. 4.43 it is possible to design the hybrid tool with the consideration of tool runout. However, if this sufficient condition is not met, the calculation of all flute radii $r_{r,j}(z_i)$ from Eq. 4.37 is recommended to verify that a recessed flute has not a higher radius value than any of the regular flutes. The influence of tool runout on the tool concept regarding process forces and stability will be analyzed in detail in Chapter 6.

4.4 Identification of Process Force Coefficients and Runout with Particle Swarm Optimization

The average cutting force method (ACFM) is the most common approach for the identification of the specific process force coefficients [Kli82]. It is assumed that the mean values of the force components in feed, feed normal and axial direction are proportional to the feed per tooth. Thus, to determine the specific process force coefficients, experiments with different feed per tooth values f_z are carried out. In case of the mechanistic cutting force modeling, the influence of the cutting velocity v_c is estimated to be low in comparison to the feed rate, and thus, is usually neglected. A disadvantage of this mechanistic identification is the necessity of the analytical derivation to calculate the mean cutting forces [Gra04]. For each specific cutter geometry, the derivation of new equations are often necessary. This can be challenging in case of tools with complex geometric shapes and requires simplifications. For example, instead of the trochoidal flute movement, the simplified circular flute movement is used in the equations. The runout error is often likewise not taken into account.

An alternative approach is the instantaneous cutting force method (ICFM). For this method the process forces are calculated as described in Chapter 4, i.e., and can be fitted by a heuristic optimization method to match the experimental process force data. A variation of the feed per tooth is not necessary, which reduces the experimental efforts. SELLMEIER applied a genetic algorithm for the identification of the process force coefficients with the ICFM based on a time-domain simulation [Sel12a, p. 51ff.]. To reduce the influence of runout error on the coefficient identification, a one fluted tool was used. In the following, a more versatile identification method will be presented. This methods allows the identification of the process force coefficients, runout error and further geometric tool attributes, e.g. radial offset of flutes. Thus, no analog tool with a single flute needs to be used for the experiments. WANG presented a method to identify the runout error without the a priori knowledge of the process force coefficients [Wan03]. This method requires two cutting tests. The runout error is identified based on the calculation of an offset between both experimental cutting tests. The presented method in this work requires only one cutting test. Furthermore, all needed parameters can be identified simultaneously.

As it will be explained, the inclusion of the runout error and further parameters increase the computation time. Therefore, the Particle Swarm Optimization (PSO) method is applied for the identification. The PSO algorithm simulates the movement of swarm, e.g. flock of birds, to find the global optimum solution [Ken95]. As mentioned by KENNEDY and EBERHART, PSO has the advantage that each swarm member takes into account not only its own local optimum, but also the optimum of the entire swarm in its movement, and thereby increases the probability that a global optimum is identified. Furthermore, compared to other heuristic algorithms, the PSO algorithm has significantly shorter computation times [Per07].

The implementation of the PSO algorithm for the identification of the mentioned input quantities is shown in Fig. 4.6. First, the system, i.e. the tool geometry and the process parameters, must be defined. Then, for the first movement step k = 1, the position vector $\mathbf{p}_{i,k}$ and the direction vector $\mathbf{v}_{i,k}$ are set for all N_p swarm members. $\mathbf{p}_{i,k}$ contains the elements to be identified, for example:

$$\mathbf{p}_{i,k} \mathrel{\widehat{=}} \left[\underbrace{K_{tc} \quad K_{rc} \quad K_{ac}}_{\text{cutting coefficients}} \quad \underbrace{K_{te} \quad K_{re} \quad K_{ae}}_{\text{edge coefficients}} \quad \underbrace{\lambda_r \quad c_r}_{\text{runout}} \quad \underbrace{\mathbf{r} \quad \mathbf{p}}_{\text{tool geometry}} \right] \tag{4.44}$$

The runout error parameters, the flute radii **r** as well as the tooth pitches **p** can be included, theoretically. This allows an estimate of manufacturing errors of these attributes. Especially in the case of the hybrid tool with recessed flutes, this identification procedure can replace an additional measurement step. For the initial time step k = 1, the values of the position vector are defined by random numbers:

$$\mathbf{p}_{i,k} = \mathbf{p}_{lb} + (\mathbf{p}_{ub} - \mathbf{p}_{lb}) \circ \mathbf{r}_{p,i} \tag{4.45}$$

$\mathbf{r}_{p,i}$ contains the random numbers, which range between 0 and 1. The size of $\mathbf{r}_{p,i}$ equals the size of $\mathbf{p}_{i,k}$. Each swarm member i has an individual vector $\mathbf{r}_{p,i}$. Furthermore, for each element of the position vector $\mathbf{p}_{i,k}$, a reasonable minimum and maximum value as boundary must be defined for the elements (lower boundary $\mathbf{p}_{lb}$ and upper boundary $\mathbf{p}_{ub}$). To make the identification as efficient as possible, the boundaries should be within a reasonable range based on the values of the experimental forces, as it will be shown in Chapter 6.1.1. For the initial time step k = 1, all elements of the velocity vector $\mathbf{v}_{i,k}$ are set to zero for every particle i.

The algorithm includes two loops. The inner loop for counter i includes the number of swarm particles. The number of movement steps of the swarm is set by the outer loop by means of the counter k. For the application described here, a swarm size of $N_p = 30$ was chosen and a number of movements of $N_s = 200$.

Within these loops and based on the set initial values $\mathbf{p}_{i,k}$, the process forces for one tool revolution, as given in Eq. 4.1, are calculated. The models for the trochoidal flute path and the runout consideration from Chapter 4.2 and 4.3, respectively, are also included. The associated experimental forces are averaged over a period of one revolution, to filter noise. Next, the deviation F_{min} between the simulated and experimental forces is determined.

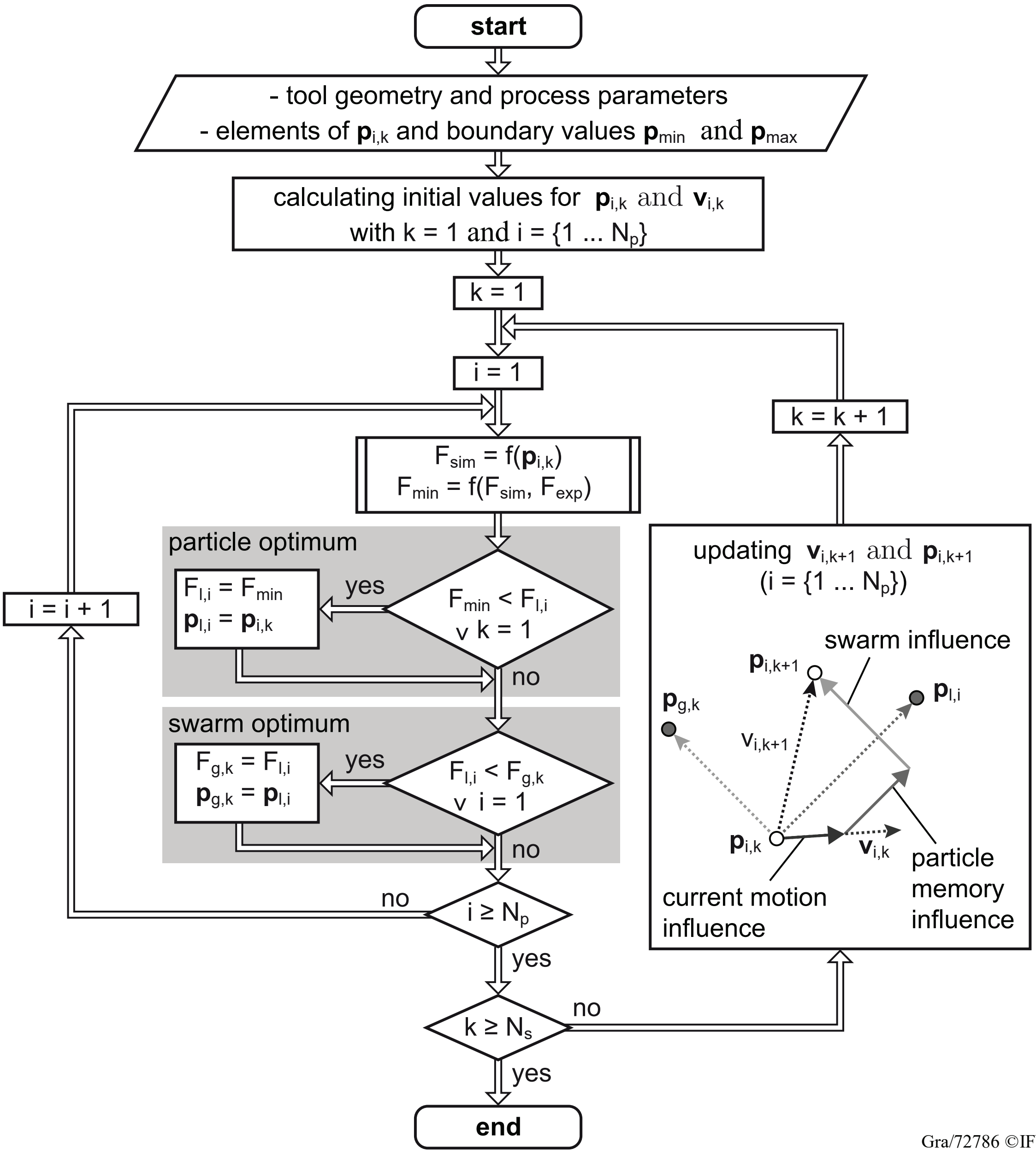
start
- tool geometry and process parameters
- elements of $\mathbf{p}_{i,k}$ and boundary values $\mathbf{p}_{min}$ and $\mathbf{p}_{max}$
calculating initial values for $\mathbf{p}_{i,k}$ and $\mathbf{v}_{i,k}$ with k = 1 and i = {1 ... N_p}
k = 1
i = 1
$F_{sim} = f(\mathbf{p}_{i,k})$
$F_{min} = f(F_{sim}, F_{exp})$
particle optimum
$F_{l,i} = F_{min}$
$\mathbf{p}_{l,i} = \mathbf{p}_{i,k}$
yes
$F_{min} < F_{l,i} \vee k = 1$
no
swarm optimum
$F_{g,k} = F_{l,i}$
$\mathbf{p}_{g,k} = \mathbf{p}_{l,i}$
yes
$F_{l,i} < F_{g,k} \vee i = 1$
no
i = i + 1
no
$i \geq N_p$
yes
$k \geq N_s$
no
yes
end
k = k + 1
updating $\mathbf{v}_{i,k+1}$ and $\mathbf{p}_{i,k+1}$ (i = {1 ... N_p})
swarm influence
$\mathbf{p}_{i,k+1}$
$\mathbf{p}_{g,k}$
$\mathbf{p}_{l,i}$
$v_{i,k+1}$
$\mathbf{p}_{i,k}$
$\mathbf{v}_{i,k}$
particle memory influence
current motion influence

Gra/72786 ©IFW

Fig. 4.6: PSO algorithm (depiction of updating the velocity and position $\mathbf{v}_{i,k+1}$ and $\mathbf{p}_{i,k+1}$, respectively, as shown in [Has05])

As an example, this can be realized as follows:

$$F_{min} = \frac{1}{N_{rev}} \sum_{k=1}^{N_{rev}} \left| F_{sim,k} - F_{exp,k} \right| \tag{4.46}$$

The procedure is extended accordingly to include the feed, feed normal and passive force simultaneously. As described in [Sel12a, p. 52 ff.], if only the cutting force coefficients have to be determined, the forces are calculated with $K_{t,c} = K_{r,c} = K_{a,c} = 1\ \frac{N}{mm^2}$ and $K_{t,e} = K_{r,e} = K_{a,ec} = 1\ \frac{N}{mm}$ and afterwards corrected with the actual values for the coefficients. Thus, the forces must be calculated only once for both loops from Fig. 4.6. This considerably reduced the computational time. As a requirement for this procedure, neither runout error nor geometric attributes of the tool are allowed to be included in the identification. Otherwise, the flute paths and thus the engagement conditions changed so that for each particle of the swarm N_p as well as each time step k, the forces must be recalculated.

Next, the particle optimum is identified for each i-th swarm particle, as shown in the upper gray box (particle optimum) in Fig. 4.6:

$$\text{if} \quad F_{min} < F_{l,i} \vee k = 1, \quad \Rightarrow \quad F_{l,i} = F_{min} \quad \wedge \quad \mathbf{p}_{l,i} = \mathbf{p}_{i,k} \tag{4.47}$$

For the first time step k = 1, the value of F_{min} for all particles automatically equals the local fit $F_{l,i}$. The particle inherits the value of its own local optimum position $\mathbf{p}_{l,i}$ for the following time steps k and is updated if the fitness increases. The swarm optimum is determined as shown in the lower gray box (swarm optimum) in Fig. 4.6:

$$\text{if} \quad F_{l,i} < F_{g,k}, \quad \Rightarrow \quad F_{g,k} = F_{l,i} \quad \wedge \quad \mathbf{p}_{g,k} = \mathbf{p}_{l,i} \tag{4.48}$$

with $F_{g,k}$ as the best global fit value and $\mathbf{p}_{g,k}$ as the best position for the entire swarm. After the position $\mathbf{p}_{i,k}$ for all swarm particles ($i = N_p$) for one time step k is determined, the next position $\mathbf{p}_{i,k+1}$ is calculated as follows [Ken95]:

$$\mathbf{p}_{i,k+1} = \mathbf{p}_{i,k} + \mathbf{v}_{i,k+1} \tag{4.49}$$

with the velocity term

$$\mathbf{v}_{i,k+1} = \underbrace{\mathbf{r}_{v,i,k} \circ \mathbf{v}_{i,k}}_{\text{current motion}} + \underbrace{\mathbf{r}_{pl,i,k} \circ \left(\mathbf{p}_{l,i} - \mathbf{p}_{i,k}\right)}_{\text{particle memory influence}} + \underbrace{\mathbf{r}_{pg,i,k} \circ \left(\mathbf{p}_{g,k} - \mathbf{p}_{i,k}\right)}_{\text{swarm influence}} \tag{4.50}$$

The procedure is illustrated in the framed box in Fig. 4.6, based on [Has05]. Note that in Eq. 4.49 and Eq. 4.50 it appears as if velocities and positions, and thus different physical units, are added. However, as stated by EBERHART and SHI, the velocity is regarded over a single time increment (iteration k), and thus, this approach is valid [Ebe07, p. 88]. The individual terms in Eq. 4.50 are each multiplied by a weighting factor ($\mathbf{r}_{pl,i,k}$, $\mathbf{r}_{v,i,k}$ and $\mathbf{r}_{pg,i,k}$). The convergence of the PSO algorithm depends on the chosen values for these factors [Tre03, Has05]. However, since the choice of the optimal values for these factors would increase the setup complexity, random values are chosen for the factors for each element of the velocity vector $\mathbf{v}_{i,k}$ and all position vectors $\mathbf{p}$, analogous to Eq. 4.45. After the last time step, the position vector $p_{g,k}$ with $k = N_s$ contains the best identified values of the coefficients and all other elements, as defined in Eq. 4.44.

In order to assess the quality of this identification method, it is evaluated in Chapter 6.1.1 and 6.1.2 on the basis of predefined values for the coefficients and runout error, respectively. Furthermore, a comparison between the ICFM and ACFM is carried out.

5 Modeling of the Dynamic Behavior of Milling Systems

The process stability prediction will be analyzed using two different calculation methods. With the Semi-Discrete method stability charts can be determined by an eigenvalue analysis in the time-domain. The difference between a stable and unstable process can be clearly determined by the eigenvalue. Analogous to the derivations of the process forces from Chapter 4.1, an extension of the SD method is performed in order to take into account runout errors as well as varying time delays caused by the radially recessed flutes of the hybrid tool. The time delays are determined based on the trochoidal flute path model from Chapter 4.2.

Additionally, time-domain simulations are carried out for stability prediction. This methods allows the consideration of nonlinear effects. In order to be able to generate stability maps in analogy to the SD method, a method is presented which serves as a criterion for establishing a stability limit. It should be noted, however, that the required computation time is significantly higher compared to the SD method.

5.1 Semi-Discrete Time-Domain Solution with Consideration of Multidimensional Distributed Time-Delays

To predict the stability of the hybrid tool, the basic concept of the semi-discretization time-domain solution, as described in Chapter 2.2, needs to be modified to include multidimensional time-delays in the calculation. Accordingly, the right side of Eq. 2.1 is exchanged by Eq. 4.15 and the velocity depending force component, which may act as a process damping force component, is added:

$$\mathbf{M}\ddot{\mathbf{q}}(t) + \mathbf{D}\dot{\mathbf{q}}(t) + \mathbf{K}\mathbf{q}(t) = \mathbf{T}_q^T \sum_{j,u=1}^{N_t} \sum_{i=1}^{N_z} \left(\mathbf{Q}_{j,u}(t, z_i) \left(\Delta\mathbf{q}\left(t - \theta_{j,u}(z_i)\right) - \Delta\mathbf{q}(t) \right) - \mathbf{Q}_{pd,j,u} \Delta\dot{\mathbf{q}}(t) \right) \tag{5.1}$$

The transpose of the matrix $\mathbf{T}_q$ from Eq. 4.16 is added to the force components to expand it to the number of modes. An example of the structure of this matrix, which depends on the number of modes, is shown in Fig. 5.1.

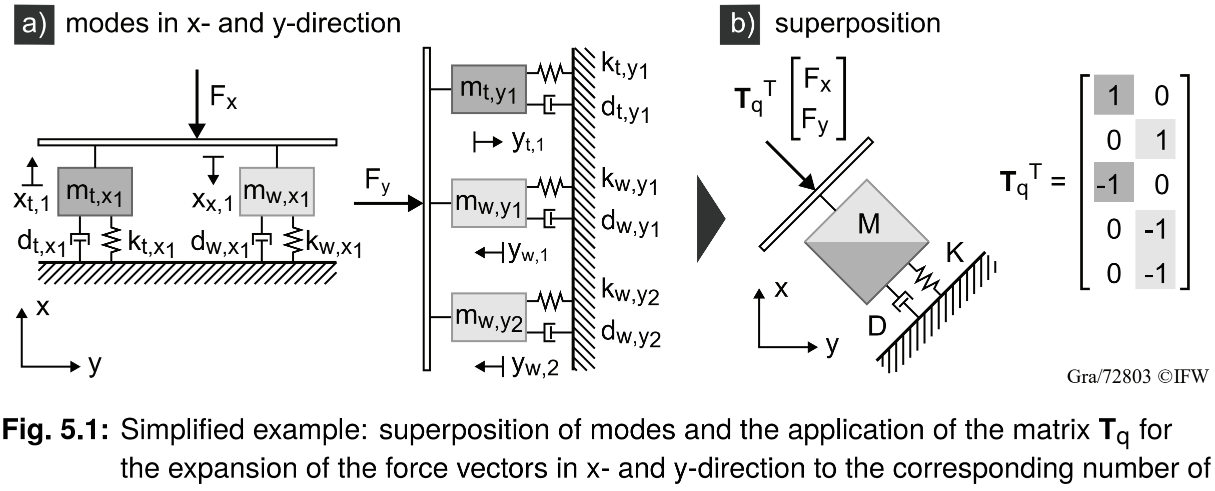
a) modes in x- and y-direction
F_x
$x_{t,1}$
m_{t,x_1}
$x_{x,1}$
m_{w,x_1}
d_{t,x_1}
k_{t,x_1}
d_{w,x_1}
k_{w,x_1}
x
y
F_y
m_{t,y_1}
k_{t,y_1}
d_{t,y_1}
$y_{t,1}$
m_{w,y_1}
k_{w,y_1}
d_{w,y_1}
$y_{w,1}$
m_{w,y_2}
k_{w,y_2}
d_{w,y_2}
$y_{w,2}$
b) superposition
$\mathbf{T}_q^T \begin{bmatrix} F_x \\ F_y \end{bmatrix}$
M
K
D
x
y
$\mathbf{T}_q^T = \begin{bmatrix} 1 & 0 \\ 0 & 1 \\ -1 & 0 \\ 0 & -1 \\ 0 & -1 \end{bmatrix}$
Gra/72803 ©IFW

Fig. 5.1: Simplified example: superposition of modes and the application of the matrix $\mathbf{T}_q$ for the expansion of the force vectors in x- and y-direction to the corresponding number of modes.

Next, the necessary steps for the eigenvalue analysis, as shown in Fig. 2.3, need to be carried out. First, $\Delta\mathbf{q}\,(t)$ and $\Delta\dot{\mathbf{q}}\,(t)$, which result from the outer modulation and process damping forces, respectively, are shifted into the left side of the eq (5.1):

$$\begin{aligned}
\mathbf{M}\ddot{\mathbf{q}}\,(t) + \mathbf{Q}_d\,(t)\,\dot{\mathbf{q}}\,(t) + \mathbf{Q}_k\,(t)\,\mathbf{q}\,(t) \;&=\; \mathbf{T}_q^T \sum_{j,u=1}^{N_t}\sum_{i=1}^{N_z} \mathbf{Q}_{j,u}\,(t,z_i)\left(\Delta\mathbf{q}\left(t-\theta_{j,u}\,(z_i)\right)\right)\\
\text{with}\quad \mathbf{Q}_k\,(t) \;&=\; \left(\mathbf{K} + \mathbf{T}_q^T \sum_{j,u=1}^{N_t}\sum_{i=1}^{N_z} \mathbf{Q}_{j,u}\,(t,z_i)\,\mathbf{T}_q\right) \qquad (5.2)\\
\text{and}\quad \mathbf{Q}_d\,(t) \;&=\; \left(\mathbf{D} + \mathbf{T}_q^T \sum_{j,u=1}^{N_t}\sum_{i=1}^{N_z} \mathbf{Q}_{pd,j,u}\,(t,z_i)\,\mathbf{T}_q\right)
\end{aligned}$$

This shift requires to transform the summarized displacement and velocity vectors $\Delta\mathbf{q}\,(t)$ and $\Delta\dot{\mathbf{q}}\,(t)$ back into $T_q\mathbf{q}\,(t)$ and $T_q\dot{\mathbf{q}}\,(t)$, as given in Eq. 4.16. Next, this second-order differential equation is transformed into a first-order differential equation by the state-space representation

$$\begin{aligned}
\underbrace{\begin{bmatrix}\dot{\mathbf{q}}\,(t)\\ \ddot{\mathbf{q}}\,(t)\end{bmatrix}}_{=\;\dot{\mathbf{x}}\,(t)} \;&=\; \underbrace{\begin{bmatrix}\mathbf{0}_{(w,w)} & \mathbf{I}_{(w,w)}\\ \mathbf{M}^{-1}\mathbf{Q}_k\,(t) & \mathbf{M}^{-1}\mathbf{Q}_d\,(t)\end{bmatrix}}_{=\;\mathbf{A}\,(t)} \underbrace{\begin{bmatrix}\mathbf{q}\,(t)\\ \dot{\mathbf{q}}\,(t)\end{bmatrix}}_{=\,\mathbf{x}(t)}\\
&+ \sum_{j,u=1}^{N_t}\sum_{i=1}^{N_z} \underbrace{\begin{bmatrix}\mathbf{0}_{(w,2)}\\ \mathbf{M}^{-1}\mathbf{T}_q^T\mathbf{Q}_{j,u}\,(t,z_i)\end{bmatrix}}_{=\;\mathbf{B}_{j,u}\,(t,z_i)} \Delta\mathbf{q}\left(t-\theta_{j,u}\,(z_i)\right), \qquad (5.3)
\end{aligned}$$

where $\mathbf{A}\,(t)$ is the state or system matrix, $\mathbf{B}_{j,u}\,(t,z_i)$ is the input matrix, $\mathbf{x}\,(t)$ is the state or system vector and $\Delta\mathbf{q}\left(t-\theta_{j,u}\,(z_i)\right)$ is the input vector. $\mathbf{I}$ stands for the identity matrix. For a discrete time-invariant state-space representation (step 3 from Fig. 2.3), the time-periodic state and input matrices are replaced by averaged constant values within one discrete time step t_d:

$$\mathbf{A}_d = \frac{1}{T}\int_{t_d}^{t_{d+1}} \mathbf{A}\,(t)\,dt \qquad (5.4)$$

and

$$\mathbf{B}_{d,j,u}\,(z_i) = \frac{1}{T}\int_{t_d}^{t_{d+1}} \mathbf{B}_{j,u}\,(t,z_i)\,dt \qquad (5.5)$$

with the discrete time step defined as

$$t_d \;= d\,T + T \quad \text{and} \quad \{d \in \mathbb{N} \mid 0 < d\}\,. \qquad (5.6)$$

T is the sampling interval. Based on [Ack83, p. 135] and as shown in step 4 in Fig. 2.3, the time-discrete solution can be written as follows:

$$\mathbf{x}(t_d) = e^{\mathbf{A}_d(t_d - t_{d-1})}\,\mathbf{x}(t_{d-1}) + \sum_{j,u=1}^{N_t}\sum_{i=1}^{N_z}\int_{t_{d-1}}^{t_d} e^{\mathbf{A}_d(t_d - \tau)}\,\mathbf{B}_{d,j,u}(z_i)\,\Delta\mathbf{q}\left(\tau - \theta_{j,u}(z_i)\right)d\tau \tag{5.7}$$

or by replacing the discrete time step t_d by the sampling interval T:

$$\mathbf{x}(dT + T) = e^{\mathbf{A}_d T}\,\mathbf{x}(dT) + \sum_{j,u=1}^{N_t}\sum_{i=1}^{N_z}\int_{dT}^{dT+T} e^{\mathbf{A}_d(dT + T - \tau)}\,\mathbf{B}_{d,j,u}(z_i)\,\Delta\mathbf{q}\left(\tau - \theta_{j,u}(z_i)\right)d\tau \tag{5.8}$$

To derive the expanded solution (step 5 from Fig. 2.3) the delayed terms need to be substituted by discretized values:

$$\left(m_{j,u}(z_i) - \gamma_{j,u}(z_i)\right)T \overset{!}{=} \theta_{j,u}(z_i) \tag{5.9}$$

with

$$\left\{m_{j,u}(z_i) \in \mathbb{N} \mid 1 \leq m_{j,u}(z_i)\right\} \quad \text{and} \quad \left\{\gamma_{j,u}(z_i) \in \mathbb{R} \mid 0 \leq \gamma_{j,u}(z_i) < 1\right\} \tag{5.10}$$

However, the actual time-domain terms are not discretized, which is why this method is referred to as a semi-discretization. Ackermann described how to approximate τ if the time delay is smaller than the sampling interval T [Ack83, p. 135]. However, for cutting processes it can be generally assumed that $\theta_{j,u}(z_i) >> T$. Otherwise, the sufficient condition of the Nyquist–Shannon sampling theorem is not satisfied [Sel12a, p. 38]. The following case analysis is valid for any value of $\theta_{j,u}(z_i)$:

$$\tau - \theta_{j,u}(z_i) = \begin{cases} dT - m_{j,u}(z_i)\,T & \text{if} \quad dT \leq \tau < dT + (1 - \gamma_{j,u}(z_i))T \\ dT - (m_{j,u}(z_i) - 1)T & \text{if} \quad dT + (1 - \gamma_{j,u}(z_i))T \leq \tau \leq dT + T \end{cases} \tag{5.11}$$

Thus, by implementing Eq. 5.11 into Eq. 5.8, it follows:

$$\begin{aligned} \mathbf{x}(dT + T) = {} & e^{\mathbf{A}_d T}\,\mathbf{x}(dT) \\ & + \sum_{j,u=1}^{N_t}\sum_{i=1}^{N_z}\Bigg[\int_{dT}^{dT+(1-\gamma_{j,u}(z_i))T} e^{\mathbf{A}_d(dT+T-\tau)}\,\mathbf{B}_{d,j,u}(z_i)\,d\tau\,\Delta\mathbf{q}\left(dT - m_{j,u}(z_i)\,T\right) \\ & + \int_{dT+(1-\gamma_{j,u}(z_i))T}^{dT+T} e^{\mathbf{A}_d(dT+T-\tau)}\,\mathbf{B}_{d,j,u}(z_i)\,d\tau\,\Delta\mathbf{q}\left(dT - (m_{j,u}(z_i) - 1)T\right)\Bigg] \end{aligned} \tag{5.12}$$

To reduce the integration efforts, the integration limits are exchanged based on

$$v \mathrel{\widehat{=}} v(\tau) = dT + T - \tau \Rightarrow \frac{dv(\tau)}{d\tau} = -1 \Leftrightarrow d\tau = -dv, \tag{5.13}$$

which yields the following integration limits:

$$\begin{aligned} v\left(\tau = dT + (1-\gamma_{j,u}(z_i))T\right) &= dT + T - [dT + (1-\gamma_{j,u}(z_i))T] = \gamma_{j,u}(z_i)\,T \\ v\,(\tau = dT) &= dT + T - [dT] = T \\ v\,(\tau = dT + T) &= dT + T - [dT + T] = 0 \end{aligned} \tag{5.14}$$

Thus, Eq. 5.12 is transformed into

$$\begin{aligned} \mathbf{x}\,(dT+T) &= e^{\mathbf{A}_d T}\,\mathbf{x}\,(dT) + \sum_{j,u=1}^{N_t}\sum_{i=1}^{N_z}\Bigg[-\int_{T}^{\gamma_{j,u}(z_i)T} e^{\mathbf{A}_d v}\,\mathbf{B}_{d,j,u}(z_i)\,dv\Delta\mathbf{q}\left(dT - m_{j,u}(z_i)\,T\right) \\ &\quad - \int_{\gamma_{j,u}(z_i)T}^{0} e^{\mathbf{A}_d v}\,\mathbf{B}_{d,j,u}(z_i)\,dv\Delta\mathbf{q}\left(dT - (m_{j,u}(z_i)-1)T\right)\Bigg] \\ &= e^{\mathbf{A}_d T}\,\mathbf{x}\,(dT) + \sum_{j,u=1}^{N_t}\sum_{i=1}^{N_z}\Bigg[\int_{\gamma_{j,u}(z_i)T}^{T} e^{\mathbf{A}_d v}\,\mathbf{B}_{d,j,u}(z_i)\,dv\Delta\mathbf{q}\left(dT - m_{j,u}(z_i)\,T\right) \\ &\quad + \int_{0}^{\gamma_{j,u}(z_i)T} e^{\mathbf{A}_d v}\,\mathbf{B}_{d,j,u}(z_i)\,dv\Delta\mathbf{q}\left(dT - (m_{j,u}(z_i)-1)T\right)\Bigg] \end{aligned} \tag{5.15}$$

and can be further summarized as

$$\begin{aligned} \mathbf{x}\,(dT+T) &= \boldsymbol{\Phi}_d\,(T)\,\mathbf{x}\,(dT) \\ &\quad + \sum_{j,u=1}^{N_t}\sum_{i=1}^{N_z}\Bigg[\underbrace{\left(\boldsymbol{\Gamma}_{d,j,u}(T,z_i) - \boldsymbol{\Gamma}_{d,j,u}\left(\gamma_{j,u}(z_i)\,T,z_i\right)\right)}_{=\ \boldsymbol{\Gamma}_{d,j,u,1}(T,z_i)}\Delta\mathbf{q}\left(dT - m_{j,u}(z_i)\,T\right) \\ &\quad + \underbrace{\boldsymbol{\Gamma}_{d,j,u}\left(\gamma_{j,u}(z_i)\,T,z_i\right)}_{=\ \boldsymbol{\Gamma}_{d,j,u,2}(T,z_i)}\Delta\mathbf{q}\left(dT - (m_{j,u}(z_i)-1)T\right)\Bigg] \end{aligned} \tag{5.16}$$

with

$$\boldsymbol{\Phi}_d\,(t) = e^{\mathbf{A}_d t} \quad \text{and} \quad \boldsymbol{\Gamma}_{d,j,u}(t,z_i) = \int_0^t e^{\mathbf{A}_d v}\,\mathbf{B}_{d,j,u}(z_i)\,dv \tag{5.17}$$

Since $\mathbf{A}_d$ is nonsingular, the antiderivative is

$$\boldsymbol{\Gamma}_{d,j,u}(t,z_i) = \mathbf{A}_d^{-1}\left(e^{\mathbf{A}_d t} - \mathbf{I}_{(2w,2w)}\right)\mathbf{B}_{d,j,u}(z_i)\,. \tag{5.18}$$

The discrete representation of the time delay terms allows to expand the state vector as follows (step 5 in Fig. 2.3):

$$\mathbf{x}_{\mathrm{exp}}(\mathrm{dT}) = \begin{bmatrix} \mathbf{x}(\mathrm{dT}) \\ \Delta\mathbf{q}(\mathrm{dT}-\mathrm{T}) \\ \Delta\mathbf{q}(\mathrm{dT}-2\mathrm{T}) \\ \vdots \\ \Delta\mathbf{q}(\mathrm{dT}-\mathrm{mT}) \end{bmatrix} \quad \text{with} \quad \mathrm{m} = \max\left(\mathrm{m}_{\mathrm{j,u}}(\mathrm{z_i})\right) \tag{5.19}$$

With the expanded state vector $\mathbf{x}_{\mathrm{exp}}(\mathrm{dT})$ Eq. 5.16 can be transformed into:

$$\mathbf{x}_{\mathrm{exp}}(\mathrm{dT}+\mathrm{T}) = \boldsymbol{\Phi}_{\mathrm{exp,d}}(\mathrm{T})\,\mathbf{x}_{\mathrm{exp}}(\mathrm{dT}) \tag{5.20}$$

$\boldsymbol{\Phi}_{\mathrm{exp,d}}(\mathrm{T})$ is the monodromy matrix. To acquire a better understanding of the composition of the monodromy matrix from Eq. 5.20, a graphical representation of the components is given in Fig. 5.2.

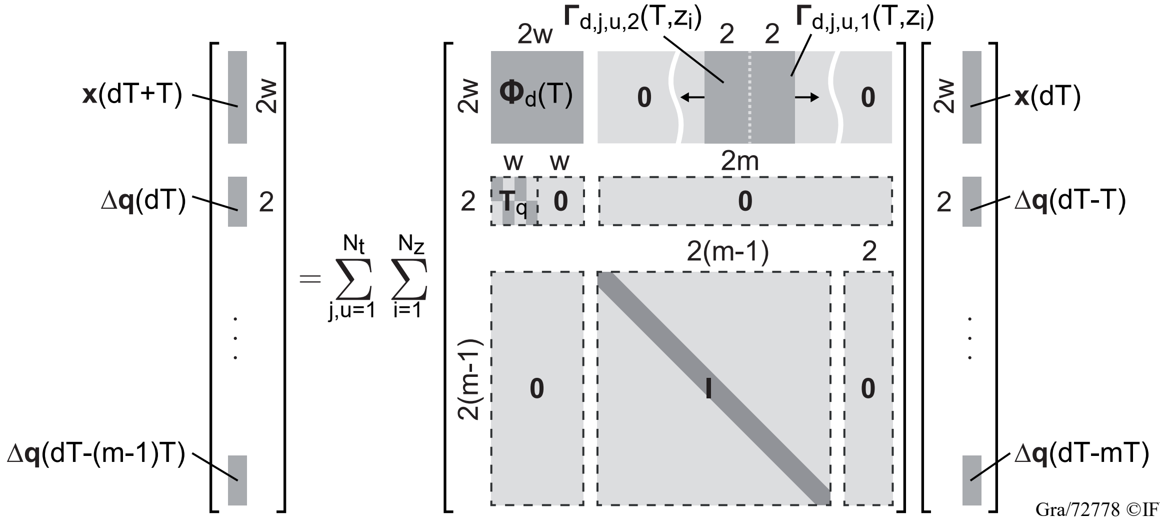

Fig. 5.2: Monodromy matrix from Eq. 5.20 with multiple delays. Elements with dashed frame contain constant values.

The upper columns with a height of 2w contain the elements from Eq. 5.16 and deliver the system vector values for the next sampling interval $\mathbf{x}(\mathrm{dT}+\mathrm{T})$. All information about the structural dynamics, represented by the state matrix $\mathbf{A}(\mathrm{t})$ as given in Eq. 5.3, are stored in the matrix $\boldsymbol{\Phi}_{\mathrm{d}}(\mathrm{t})$. Additionally, the matrices $\boldsymbol{\Gamma}_{\mathrm{d,j,u,1}}(\mathrm{T},\mathrm{z_i})$ and $\boldsymbol{\Gamma}_{\mathrm{d,j,u,2}}(\mathrm{T},\mathrm{z_i})$ represent the influence of the time delay. Depending on the discrete axial position or varying immersion conditions the value of the time delay may change at every sampling interval T and during the teeth and axial summation $\mathrm{N_t}$ and $\mathrm{N_z}$, respectively, as described in Chapter 4.1. This means that the position of $\boldsymbol{\Gamma}_{\mathrm{d,j,u,1}}(\mathrm{T},\mathrm{z_i})$ and $\boldsymbol{\Gamma}_{\mathrm{d,j,u,2}}(\mathrm{T},\mathrm{z_i})$ can shift to left or right. All other values at the upper columns with a height of 2w and a length of 2m are set to 0 to eliminate not included time delays, which are stored in the expanded system vector $\mathbf{x}_{\mathrm{exp}}(\mathrm{dT})$. The elements of the monodromy matrix below the height of 2w are of importance to store the time delay values for the next sampling interval. The $2 \times 2\mathrm{w}$ is used to extract the displacement data from the system vector $\mathbf{x}(\mathrm{dT})$. The matrix $\mathrm{T_q}$ summarizes the displacement value of all modes in x- and y-direction. The matrix filled with zeros eliminates

the velocity elements of **x** (dT), which are not stored. Accordingly, all other columns at that height are 0. Due to the fact that the summarized displacement values are stored and not the displacement of each mode, the size of the monodromy matrix is significantly reduced. Same applies for the eliminated velocity components of the system vector. The lower blocks are used to transmit the summarized displacement values and shift them by one sampling interval.
For the prediction of the stability based on the eigenvalues of the monodromy matrix, the monodromy matrix needs to be calculated for the entire system period

$$\mathrm{T_{per}} = \mathrm{mT}, \tag{5.21}$$

as shown in step 6 in Fig. 2.3. The system period $\mathrm{T_{per}}$ depends on the tooth pitch [Sel11]. If runout is considered, the period corresponds to one tool revolution. Based on the FLOQUET theory [Flo83] the monodromy matrix for the entire system period can be calculated as follows:

$$\begin{aligned} \mathbf{x}_{\mathrm{exp}}(\mathrm{T}+\mathrm{T}) &= \mathbf{\Phi}_{\mathrm{exp},1}(\mathrm{T})\,\mathbf{x}_{\mathrm{exp}}(\mathrm{T}) \\ \mathbf{x}_{\mathrm{exp}}(\mathrm{T}+2\mathrm{T}) &= \mathbf{\Phi}_{\mathrm{exp},2}(\mathrm{T})\,\mathbf{x}_{\mathrm{exp}}(\mathrm{T}+\mathrm{T}) \\ &\vdots \\ \mathbf{x}_{\mathrm{exp}}(\mathrm{T}+(\mathrm{p}-1)\mathrm{T}) &= \mathbf{\Phi}_{\mathrm{exp},(\mathrm{r}-1)}(\mathrm{T})\,\mathbf{x}_{\mathrm{exp}}(\mathrm{T}+(\mathrm{p}-2)\mathrm{T}) \\ \mathbf{x}_{\mathrm{exp}}(\mathrm{T}+\mathrm{pT}) &= \mathbf{\Phi}_{\mathrm{exp},\mathrm{p}}(\mathrm{T})\,\mathbf{x}_{\mathrm{exp}}(\mathrm{T}+(\mathrm{p}-1)\mathrm{T}) \end{aligned} \tag{5.22}$$

Due to the periodicity of the system, the following applies for one period $[\mathrm{T}, \mathrm{T}+\mathrm{T_{per}}]$:

$$\mathbf{x}_{\mathrm{exp}}\left(\mathrm{T}+\mathrm{T_{per}}\right) = \mathbf{x}_{\mathrm{exp}}(\mathrm{T}+\mathrm{pT}) = \mathbf{\Phi}_{\mathrm{exp,per}}(\mathrm{T})\,\mathbf{x}_{\mathrm{exp}}(\mathrm{T}) \tag{5.23}$$

with

$$\mathbf{\Phi}_{\mathrm{exp,per}} = \prod_{\mathrm{d}=1}^{\mathrm{p}} \mathbf{\Phi}_{\mathrm{exp,d}}(\mathrm{T}) \tag{5.24}$$

Finally, the stability of the system can be predicted by the eigenvalues of the monodromy matrix:

$$\mathrm{eig}\left(\mathbf{\Phi}_{\mathrm{exp,per}}(\mathrm{T})\right) \begin{cases} < 1 & \text{, stable} \\ = 1 & \text{, stability limit} \\ > 1 & \text{, unstable.} \end{cases} \tag{5.25}$$

The calculation of the monodromy matrix $\mathbf{\Phi}_{\mathrm{exp,per}}$ and the corresponding eigenvalues requires a significant amount of computational operations, and thus, is very time consuming [Ins11, p.62 f.]. HENNINGER and Eberhard proposed a decomposition of the monodromy matrix in order to reduce computational time [Hen08]. However, it strongly depends on the used programming language. For example, the computational software MATLAB is optimized for matrix operations and such an approach might even lead to higher computational time. Furthermore, new techniques like parallel computing (MATLAB spmd command) or graphics processing unit (GPU) computing (i.e. NVIDIA CUDA) can be applied to shorten the calculation time. A time benefit of these techniques highly depends on the structure of the program code. For large matrices, i.e. large number of oscillators w or high discretization value m, GPU computing can shorten the calculation time remarkably and can be implemented without much effort. Parallel computing can be applied for loops. Another possibility to save calculation time is to use single instead of double precision for the multiplication for Eq. 5.20 in MATLAB. With an increasing number of modes, the savings in calculation time increases accordingly.

5.2 Time-Domain Simulation

Using time-domain simulations, additional effects which are not considered by the SD method can be investigated. This includes the influence of the frictional force components or nonlinear influences, such as out of cut incidents during the immersion of a flute [Tlu81, Cam03]. In addition, the shape of the workpiece can be varied so that dynamic effects caused by a change in the engagement conditions can be examined. This also includes the entry and exit of the tool into the workpiece. However, the calculation of the instantaneous undeformed chip thickness as well as the instantaneous process forces at every time step during the simulation requires considerable more calculation time in comparison to the SD method. Detailed descriptions and different approaches of the calculation of process dynamics in the time-domain can be found in literature, e.g. [Cam03] and [Lös15, p. 23 ff.]. In the following, new extensions and a brief summary of the general steps are presented, which can be summarized as shown in Fig. 5.3 a).

a) main steps of the time-domain simulation

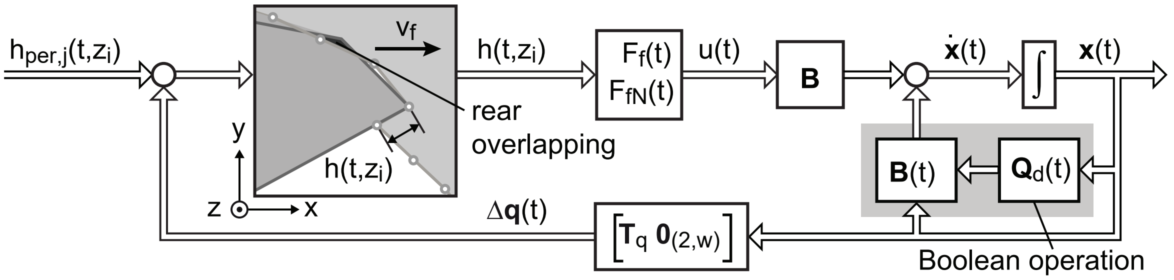
$h_{per,j}(t,z_i)$
v_f
y
z
x
$h(t,z_i)$
$h(t,z_i)$
rear overlapping
$F_f(t)$
$F_{fN}(t)$
$u(t)$
B
$\dot{\mathbf{x}}(t)$
$\int$
$\mathbf{x}(t)$
$\mathbf{B}(t)$
$\mathbf{Q}_d(t)$
$\Delta\mathbf{q}(t)$
$[\mathbf{T}_q\ \mathbf{0}_{(2,w)}]$
Boolean operation

b) threshold value to determine stability limit

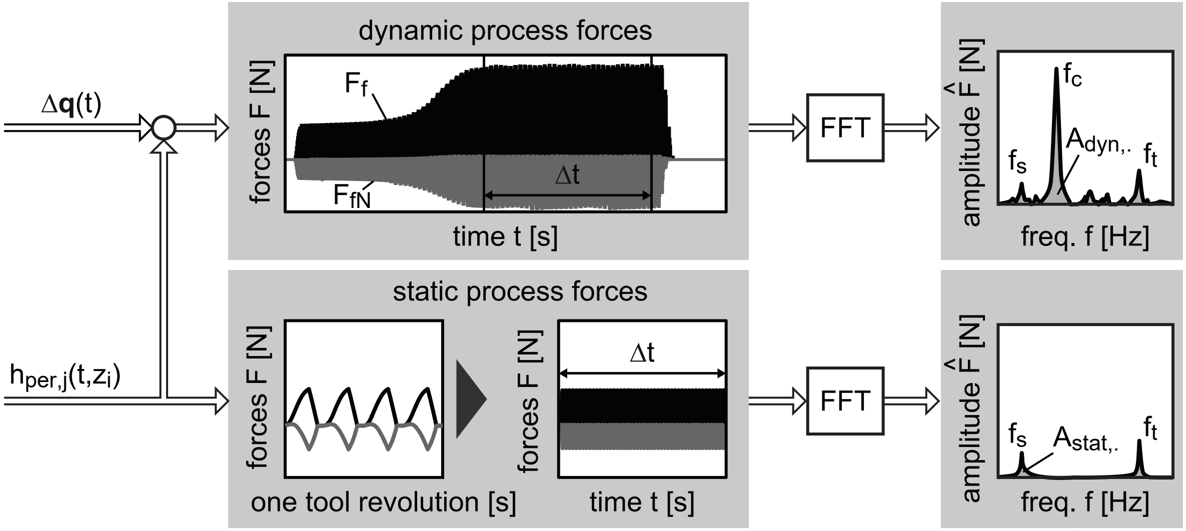
$\Delta\mathbf{q}(t)$
$h_{per,j}(t,z_i)$
dynamic process forces
forces F [N]
F_f
F_{fN}
Δt
time t [s]
FFT
amplitude $\hat{F}$ [N]
f_c
f_s
$A_{dyn,\cdot}$
f_t
freq. f [Hz]
static process forces
forces F [N]
one tool revolution [s]
forces F [N]
Δt
time t [s]
FFT
amplitude $\hat{F}$ [N]
f_s
$A_{stat,\cdot}$
f_t
freq. f [Hz]

Gra/72853 ©IFW

Fig. 5.3: Main steps to simulate the milling process in time-domain as a) a block diagram and b) method to set a threshold value for the stability limit.

For the calculation of the instantaneous chip thickness, the model from Chapter 4.2 is applied. The path of the current cutting flute is compared with the workpiece geometry, on which the path of the previous cutting edges and the relative movement between the tool and the workpiece is inherited. After determining the intersection between the cutting edge and the workpiece, the shape of the workpiece geometry is updated accordingly.

From the intersection and the cutting edge position, a value for the chip thickness from Eq. 4.3 is determined, which already includes the dynamic displacement. This means that the calculated chip thickness includes the periodic and dynamic part. The resulting process forces can be calculated based on the periodic part from Eq. 4.1. These calculated forces serve as input quantities in the calculation of the solution of the equation of motion according to Chapter 5.1. The elimination of the time delay component simplifies the state space representation from Eq. 5.3 as follows:

$$\underbrace{\begin{bmatrix} \dot{\mathbf{q}}(t) \\ \ddot{\mathbf{q}}(t) \end{bmatrix}}_{=\ \dot{\mathbf{x}}(t)} = \underbrace{\begin{bmatrix} \mathbf{0}_{(w,w)} & \mathbf{I}_{(w,w)} \\ \mathbf{M}^{-1}\mathbf{K} & \mathbf{M}^{-1}\mathbf{Q}_{d}(t) \end{bmatrix}}_{=\ \mathbf{A}(t)} \underbrace{\begin{bmatrix} \mathbf{q}(t) \\ \dot{\mathbf{q}}(t) \end{bmatrix}}_{=\ \mathbf{x}(t)} + \underbrace{\begin{bmatrix} \mathbf{0}_{(w,2)} \\ \mathbf{M}^{-1}\mathbf{T}_{q}^{T} \end{bmatrix}}_{=\ \mathbf{B}} \underbrace{\begin{bmatrix} F_{f}(t) \\ F_{fN}(t) \end{bmatrix}}_{=\ \mathbf{u}(t)} \tag{5.26}$$

In accordance to [Rub17], process damping is included in the modal damping matrix. The process damping model presented in Chapter 5.1 is applied. However, with the time-domain simulation it is possible to identify an overlap between the workpiece and the tool even if the overlap occurs only at the rear of the chamfer. This is done by identifying the overlap area based on a BOOLEAN operation. The influence of the overlapping between the workpiece with the rear part of the chamfer on process damping forces in general will be analyzed in Chapter 6.1.5.

Due to the process damping implementation the system matrix is transient. In analogy to Eq. 5.4 it is substituted by a piecewise stationary representation. The input matrix **B** is stationary. Thus, the solution from Eq. 5.8 can be calculated as follows [Lun08, p. 237 f.]:

$$\mathbf{x}(dT + T) = e^{\mathbf{A}_{d}T}\,\mathbf{x}(dT) + \int_{0}^{T} e^{\mathbf{A}_{d}\tau}\,d\tau\,\mathbf{B}\mathbf{u}(dT) \tag{5.27}$$

or after the solution of the integral:

$$\mathbf{x}(dT + T) = e^{\mathbf{A}_{d}T}\,\mathbf{x}(dT) + \mathbf{A}_{d}^{-1}\left(e^{\mathbf{A}_{d}T} - \mathbf{I}_{(2w,2w)}\right)\mathbf{B}\mathbf{u}(dT)\,. \tag{5.28}$$

The state vector **x** includes the displacement and velocity of the workpiece and tool in x- and y-direction, respectively, and is taken into account for current calculation of the chip thickness.

The time-domain simulation provides the displacement of the tool and the workpiece as well as the dynamic process forces at each time step.

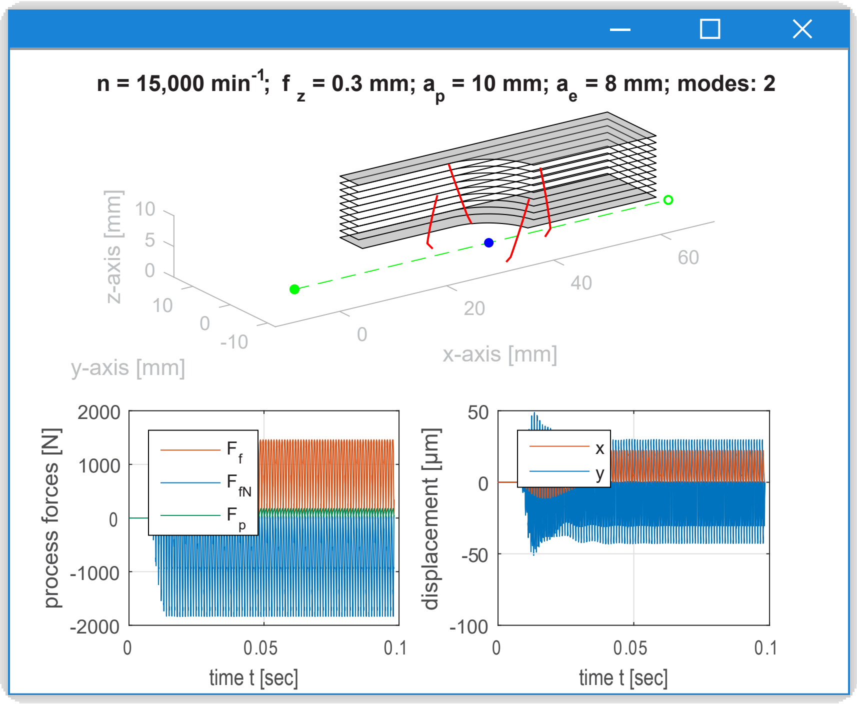

Gra/72851 ©IFW

Fig. 5.4: Graphical user interface of the time-domain simulation (graphical user interface based on [Sel12b, p. 50]).

A graphical user interface was created to represent the results, which can be seen in Fig. 5.4. In the upper part of the window, the discretized tool and workpiece are shown. The lower part shows the relevant outputs. After the simulation is finished, the simulated surface can be visualized to analyze the surface quality. Furthermore, the forces acting on the workpiece while the machined surface is generated can be extracted. This allows to predict the shape of the resulting surface deformation of the flank face, as it will be shown in Chapter 6.2.3.

The simulation data can also be used to create stability maps. Simulations are carried out within a range of values for the spindle speed n and the axial immersion a_p. Depending on the chosen incremental steps for n and a_p, the necessary high computational time needs to be considered. By using the determination of the actual chip width according to the method from Chapter 4.2, the computational effort can be reduced. Furthermore, a criterion for the stability limit has to be established on the basis of the simulated data. Rubeo and Schmitz defined a threshold value, which results from the quotient of the displacement amplitude of the chatter frequency and the highest displacement amplitude of a periodic frequency, e.g. tooth passing frequency or spindle frequency, during stable cutting conditions [Rub17]. Using multiple examples from the literature, they showed that with their presented method a clear stability limit comparable with results from the SD method can be achieved. Based on this method, a more generalized approach is used in the following. Instead of comparing the displacement amplitudes of single frequencies, the whole FFT signal of the process forces within a defined frequency range is considered to derive a threshold value. With this approach all significant periodic frequency components can be taken into account. The basic concept is shown in Fig. 5.3 b). First, the time-domain simulation is carried out and the FFT of the process force signals in feed and feed normal direction F_f and F_{fN}, respectively, is calculated. In the following, F_f is used to explain the method. Before the FFT is carried out, the constant part of the force component is removed by subtracting the mean value $\bar{F}_f$:

$$F_f(t_d) - \bar{F}_f \xrightarrow{\text{FFT}} F_f(f_d)\,. \tag{5.29}$$

This eliminates high peaks at f = 0 Hz. Otherwise, the decisive amplitude components would be leveled by this constant component. The discrete frequency step f_d is defined in analogy to Eq. 5.6 as follows:

$$f_d = d\mathcal{F} + \mathcal{F}, \tag{5.30}$$

with $\mathcal{F}$ as the sampling frequency. Within a defined frequency range, from 0 Hz up to the defined highest considered frequency f_{max}, the FFT signal is integrated numerically by applying the trapezoidal rule:

$$A_{dyn,f} = \frac{1}{2}\mathcal{F}\sum_{d=1}^{N_d}\left(F_f(f_{d-1}) + F_f(f_d)\right) \tag{5.31}$$

with

$$N_d = \frac{f_{max}}{\mathcal{F}} \quad \text{and} \quad \{N_d \in \mathbb{N} \mid 0 < N_d\}\,. \tag{5.32}$$

In case of chatter, additional amplitudes occur near the chatter frequency, which increase the value of the dynamic force signal area $A_{dyn,f}$. As a counter part to $A_{dyn,f}$, the static force signal area $A_{stat,f}$ is determined. Based on Chapter 4, the process forces are calculated solely on the periodic part of the uncut chip thickness, as shown in Fig. 5.3 b). To avoid errors resulting from the FFT operation, the calculated force signal for one revolution is duplicated multiple times to reach the same signal length as the time domain simulation. As a final step, the amplitude ratio of these two values is calculated:

$$r_{amp} = \max(r_{amp,f}, r_{amp,fN}), \quad \text{with} \quad r_{amp,f} = \frac{A_{dyn,f}}{A_{stat,f}}. \tag{5.33}$$

If chatter occurs, then $A_{dyn,f} >> A_{stat,f}$. The final chatter amplitude ratio r_{amp} is chosen in accordance to the severeness of chatter in feed and feed normal direction. Theoretically, it follows that $r_{amp} > 1$ in case of chatter. However, perturbations in the time-domain simulation, e.g. entry and exit conditions, may cause additional peaks in the frequency domain. To ensure a sufficiently large safety factor, the threshold value is set to the double of the the theoretical sufficient value:

$$r_{amp}\begin{cases} < 2 & \text{, stable} \\ = 2 & \text{, stability limit} \\ > 2 & \text{, unstable.} \end{cases} \tag{5.34}$$

The presented method is examined in Chapter 6.2 and will be applied in the experimental investigations in Chapter 7.2.1.

6 Model Based Estimation of the Machining Behavior

Based on theoretical investigations, it will be estimated in the following which impact the essential input and disturbance parameters have on the new tool concept. The findings of these studies are used as a preparation for the experimental investigations of the new tool concept.

6.1 Process Forces

A major factor influencing the achievable stability is the occurring process forces. Therefore, for the prediction of stability, the cutting force coefficients are of importance. A wrong identification can substantially influence the predicted stability [Kle08]. To ensure a correct identification of the coefficients, the impact of the main factors affecting a correct identification is of interest. First, errors which arise based on the goodness of the process force model are considered. In this context, the ACFM is compared with the ICFM. Discrepancies resulting from the applied flute path model as well as tool runout are investigated for both methods. The theoretical data from [Gra04] is used for the evaluation. These results are considered for the experimental identification of the specific process force coefficients. Based on these results, it is considered to what extent the stability can change depending on the cutting force coefficients. Furthermore, the dependence of the coefficients on the cutting speed is considered. Since process damping is important for the recessed flutes of the hybrid tool, the difficulties in modeling process damping forces are also addressed.

6.1.1 Comparison between Average and Instantaneous Cutting Force Method

GRADIŠEK et al. investigated the identification of the specific process coefficients with the ACFM for different types of end mills [Gra04]. As a first step, they simulated process forces to evaluate their identification method. The used input data is shown in Fig. 6.1. The theoretical and identified coefficients for all investigated radial immersions a_e (full, up- and down-milling: 50%, 25%, and 10%) agrees well. As usual for the ACFM, the authors used the circular path model for the simulation of the process forces and identification of the coefficients. If the process forces are simulated with the developed trochoidal path model (Chapter 4.2), only small differences to the circular path model are apparent, as shown in Fig. 6.1 a) for the feed normal force F_{fN}. The average cutting forces $\bar{F}_{fN,circular}$ and $\bar{F}_{fN,trochoidal}$ differ by 7 N only. In this case, the percentage difference

$$\Delta\bar{F}_{fN}(f_z) = \left(\frac{\bar{F}_{fN,circular}(f_z)}{\bar{F}_{fN,trochoidal}(f_z)} - 1\right) \cdot 100\% \qquad (6.1)$$

equals 4.3%. This is the highest difference for the investigated process parameters in down-milling, as shown in Fig. 6.1 b). With increasing immersion and decreasing feed per tooth the deviations get smaller. The dotted line with the circular markers in Fig. 6.1 b) represents the deviation for 10%-immersion for different feed per tooth values. This low error levels might be considered as not relevant, initially. However, this error levels matter for the coefficient identification. The identified specific process force coefficients are listed in Table 6.1. If the trochoidal path model is used to simulate the process force data and the circular path model for the identification, the presumed low error levels have an impact. For full immersion milling, the deviations are small. However, in case of low immersion the deviation between the values of the theoretical

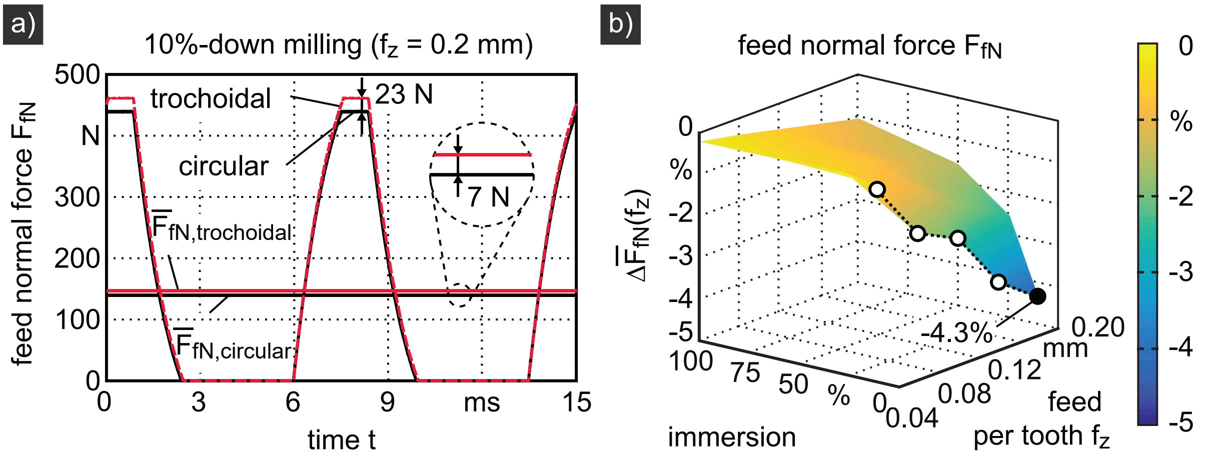

tan cutting coeff.:	K_{tc} = 1,844.1 N/mm^2		radial depth of cut:	a_e = variable
rad. cutting coeff.:	K_{rc} = 513.0 N/mm^2		axial depth of cut:	a_p = 4 mm
ax. cutting coeff.:	K_{ac} = 1,118.7 N/mm^2		process:	down-milling
tan. edge coeff.:	K_{te} = 33.9 N/mm		tool diameter:	D = 8 mm
rad. edge coeff.:	K_{re} = 60.8 N/mm		helix angle:	δ = 45°
ax. edge coeff.:	K_{ae} = -4.2 N/mm		number of teeth:	N_t = 2

Gra/72794 ©IFW

Fig. 6.1: Comparison between circular and trochoidal flute movement (data from [Gra04]).

Table 6.1: Identified specific process force coefficients by the ACFM. Trochoidal path model was used for the simulated process forces.

immersion	K_{tc} [N/mm^2]	K_{rc} [N/mm^2]	K_{ac} [N/mm^2]	K_{te} [N/mm]	K_{re} [N/mm]	K_{ae} [N/mm]
full	1,872.2	503.0	1,145.0	33.2	61.1	–4.8
50%-down	1,917.8	498.2	1,154.2	32.6	60.7	–5.0
50%-up	1,849.4	548.8	1,131.3	33.4	60.4	–4.5
25%-down	1,974.5	522.6	1,181.7	32.2	60.4	–5.3
25%-up	1,878.7	569.9	1,146.8	33.0	60.5	–4.7
10%-down	2,089.8	577.1	1,235.5	32.1	60.5	–5.5
10%-up	1,964.3	621.1	1,190.9	32.7	60.6	–5.0

and identified coefficients is significant. The identified radial cutting force coefficient K_{rc} for 10%-up-milling deviates from the actual theoretical value by 21%.

To reduce this systematical error, the developed PSO algorithm (Chapter 4.4) is used to identify the coefficients from the instantaneous cutting forces. Based on the mean value of the simulated forces for f_z = 0.16 mm, the following lower and upper boundary values were chosen:

$$\begin{array}{lcl}
\mathbf{p}_{i,k} & \widehat{=} & \left[\begin{array}{cccccc} K_{tc} & K_{rc} & K_{ac} & K_{te} & K_{re} & K_{ae} \end{array}\right] \\
\mathbf{p}_{lb} & = & \left[\begin{array}{cccccc} 1,000\,\frac{N}{mm^2} & 300\,\frac{N}{mm^2} & 800\,\frac{N}{mm^2} & -50\,\frac{N}{mm} & -50\,\frac{N}{mm} & -50\,\frac{N}{mm} \end{array}\right] \\
\mathbf{p}_{lb} & = & \left[\begin{array}{cccccc} 2,200\,\frac{N}{mm^2} & 700\,\frac{N}{mm^2} & 1,400\,\frac{N}{mm^2} & 100\,\frac{N}{mm} & 100\,\frac{N}{mm} & 100\,\frac{N}{mm} \end{array}\right]
\end{array} \qquad (6.2)$$

Numerical heuristic optimization methods tend to fall into a local optimum. Thus, the algorithm was executed 500 times to find the best solution. The results are listed in Table 6.2. As the results

Table 6.2: Identified specific process force coefficients by PSO algorithm based on the ICFM. Trochoidal path model was used for the simulated process forces (f_z = 0.16 mm).

immersion	K_{tc} [N/mm^2]	K_{rc} [N/mm^2]	K_{ac} [N/mm^2]	K_{te} [N/mm]	K_{re} [N/mm]	K_{ae} [N/mm]
full	1,843.8	513.1	1,118.7	33.9	60.8	–4.2
50%-down	1,844.1	513.0	1,118.8	33.9	60.8	–4.2
50%-up	1,844.3	513.0	1,118.7	33.9	60.8	–4.2
25%-down	1,844.0	513.0	1,118.7	33.9	60.8	–4.2
25%-up	1,844.1	513.0	1,118.7	33.9	60.8	–4.2
10%-down	1,843.8	511.9	1,118.7	33.9	60.8	–4.2
10%-up	1,843.7	512.4	1,118.7	33.9	60.8	–4.2

show, there is almost no deviation (highest error:–0.2% for K_{tc} at 10%-down-milling). Fig. 6.2 shows an example of the progress of the PSO algorithm for 500 executions.

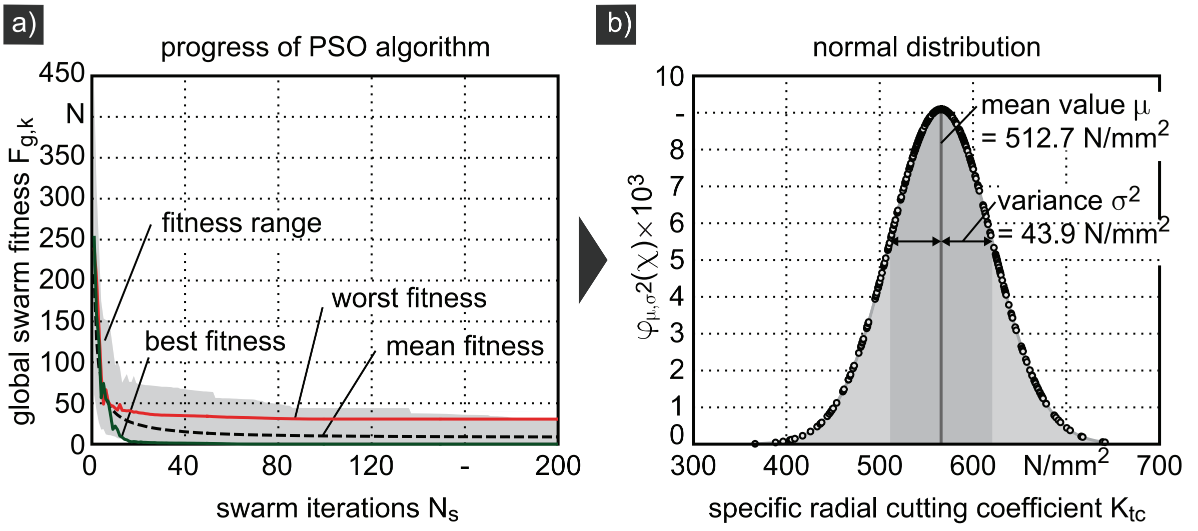

radial depth of cut: a_e = 8 mm
axial depth of cut: a_p = 4 mm
process: full immersion milling
feed per tooth: f_z = 0.16 mm

Gra/72795 ©IFW

Fig. 6.2: Evaluation and analysis of the PSO results.

After 20 swarm iterations, the global swarm fitness $F_{g,k}$ converges to a constant value, as shown in Fig. 6.2 a). For this theoretical identification with no noise or dynamical caused deviations, the best swarm fitness $F_{g,k}$ reaches a deviation value of almost 0 N. Fig. 6.2 b) shows the resulting value for K_{tc} if all 500 results are considered. The identified values of K_{tc} are normally distributed and the resulting mean value μ = 512.7 N/mm^2 almost corresponds to the exact reference value. This proves the effectiveness of the applied PSO algorithm. In the following section, the identification analysis is extended by tool runout.

6.1.2 Influence of Tool Runout on Process Force Coefficient Identification

The amplitudes of the process forces for each flute can noticeably vary in case of tool runout. The ACFM does not consider tool runout. An implementation into the analytical expression for the co-

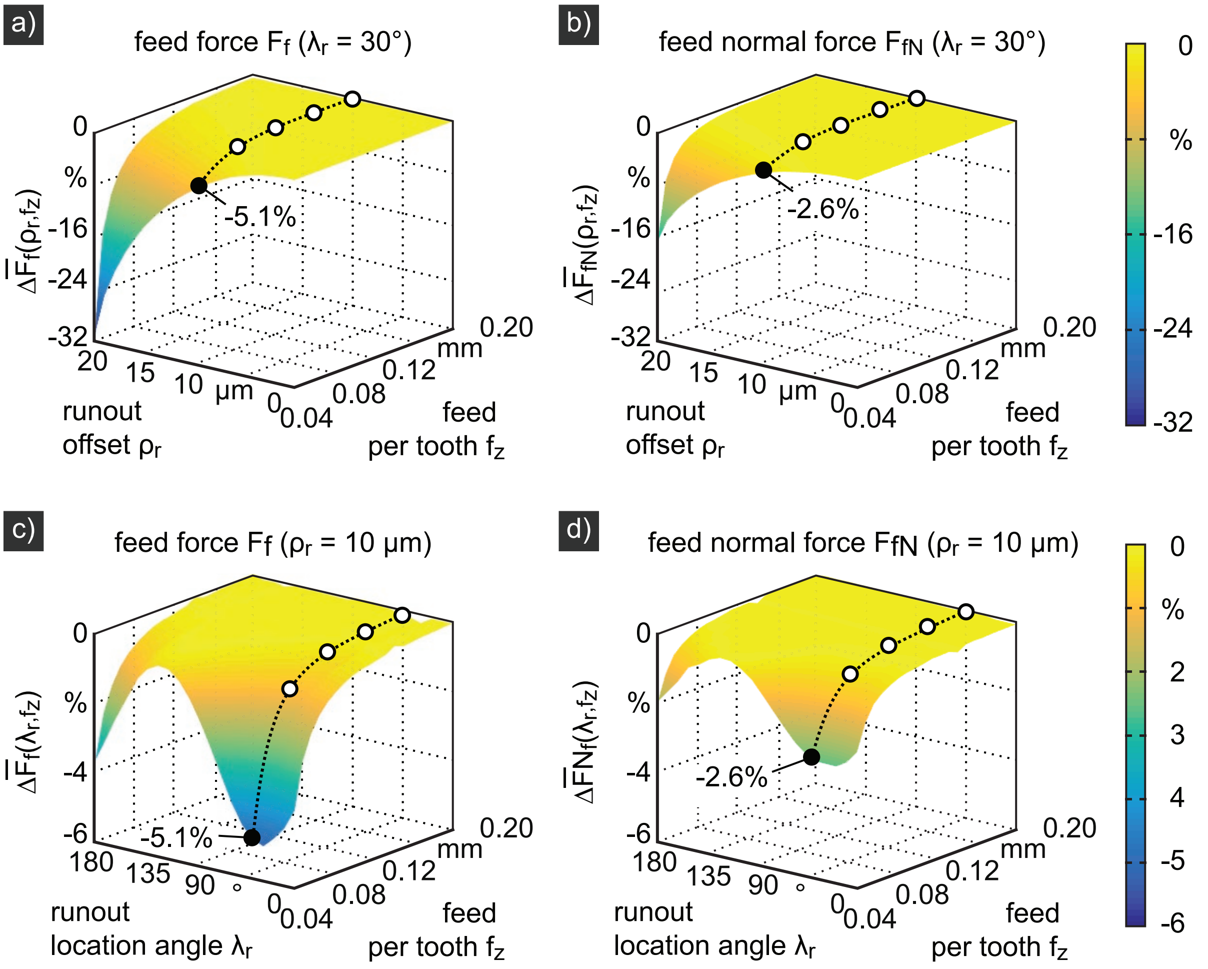

tool diameter:	D = 8 mm	radial depth of cut:	a_e = D
helix angle:	δ = 45°	axial depth of cut:	a_p = 4 mm
number of teeth:	N_t = 2	process:	full immersion

Gra/72793 ©IFW

Fig. 6.3: Influence of tool runout on the process forces. The dotted lines and round markers have the same runout error for all four diagrams.

efficient identification would increase the complexity significantly. For the ICFM, the consideration of tool runout errors is possible [Gro15]. For the following investigations, the same data as in the previous section is used (Fig. 6.1). Fig. 6.3 shows the resulting deviations for the mean values of the simulated process forces with and without tool runout. For the upper diagrams a) and b), λ_r is kept constant and ρ_r is varied. Similar to Eq. 6.1, the percentage difference is calculated as follows (Fig. 6.3 a) and b)):

$$\Delta\bar{F}_f\left(\rho_r, f_z\right) = \left(\frac{\bar{F}_f\left(\lambda_r = 30^\circ, \rho_r, f_z\right)}{\bar{F}_f\left(\lambda_r = 0^\circ, \rho_r = 0\mu\mathrm{m}, f_z\right)} - 1\right) \cdot 100\%. \tag{6.3}$$

With increasing λ_r and decreasing f_z the differences are very significant. In comparison to the variation of ρ_r, the variation of the runout location angle λ_r leads to a smaller influence on the

Table 6.3: Identification with the ACFM with trochoidal flute paths and runout (data from: [Gra04]).

immersion	K_{tc} [N/mm^2]	K_{rc} [N/mm^2]	K_{ac} [N/mm^2]	K_{te} [N/mm]	K_{re} [N/mm]	K_{ae} [N/mm]
full	1,891.6	538.0	1,139.9	31.4	57.7	–4.1
50%-down	2,044.7	536.3	1,149.1	21.8	54.8	–4.3
50%-up	1,829.1	677.2	1,131.0	34.3	48.1	–3.8
25%-down	2,183.4	668.2	1,171.5	19.6	48.4	–4.3
25%-up	1,919.5	824.7	1,145.0	29.7	43.4	–3.7
10%-down	2,481.6	1,047.3	1,202.4	16.3	37.7	–3.7
10%-up	2,200.1	1,212.3	1,172.8	22.0	35.3	–3.3

mean process forces. The resulting percentage error is calculated by (Fig. 6.3 c) and d)):

$$\Delta\bar{F}_f(\lambda_r, f_z) = \left(\frac{\bar{F}_f\left(\lambda_r, \rho_r = 10\ \mu\mathrm{m}, f_z\right)}{\bar{F}_f\left(\lambda_r = 0^\circ, \rho_r = 0\ \mu\mathrm{m}, f_z\right)} - 1\right) \cdot 100\% \qquad (6.4)$$

For $\lambda_r = 135^\circ$, the force deviation for the investigated process parameters almost disappears.

In such a case, and assuming that most runout errors are not caused by errors of the tool geometry shape, the influence of the tool runout on the process forces could be theoretically reduced by changing the orientation between the tool and the tool holder. However, the deviation would increase in case of an end mill with lower helix angle values δ_j. High helix angles lead to a more evenly distributed tool runout error (Fig. 2.10), which reduced the peak force differences between the teeth. For the coefficient identification, a runout offset of $\rho_r = 10\mu\mathrm{m}$ and runout location angle $\lambda_r = 30^\circ$ is chosen for the process force simulation. The identified coefficients based on the ACFM are listed in Table 6.3. As the results show, the consideration of runout is more than recommended. For example, without consideration of tool runout, K_{tc} for 10%-down-milling differs by 637.5 $\frac{\mathrm{N}}{\mathrm{mm}^2}$.

For the ICFM based on the PSO algorithm, the coefficients are initially determined without considering the runout error to demonstrate the influence of process force deviations. The boundary values from Eq. 6.2 are used. For 10%-down-milling, the best determined global swarm fitness value $F_{g,k}$ is 67.8N with the following identified coefficients: $K_{tc} = 1,435.0\,\frac{\mathrm{N}}{\mathrm{mm}^2}$, $K_{rc} = 597.2\,\frac{\mathrm{N}}{\mathrm{mm}^2}$, $K_{ac} = 1043.6\ \frac{\mathrm{N}}{\mathrm{mm}^2}$, $K_{te} = 54.8\ \frac{\mathrm{N}}{\mathrm{mm}}$, $K_{re} = 53.7\ \frac{\mathrm{N}}{\mathrm{mm}}$ and $K_{ac} = -1.4\ \frac{\mathrm{N}}{\mathrm{mm}}$. This indicates that the application of heuristic algorithms is susceptible for a wrong coefficient identification if the data of process forces contains errors. Very often experimental data can contain even more errors, caused by tool wear, runout, non-homogeneity of the workpiece, machine state variation, instrumental error, and human error [Ahn11]. The reason why the result of the best global swarm fitness value $F_{g,k}$ is misleading lies in the force curve shape of the various coefficients (see [Sel12b, p. 53]). This explains why the identified value for K_{tc} is too low and the value of K_{te} is too high, because both coefficients have similar force curve shapes and therefore have a similar influence on the overall process force curve shape. Same applies for K_{rc} and K_{re}. Thus, to overcome this problem, the mean values for the coefficients are calculated based on the normal distributed 500 results, which yield the following coefficient values: $K_{tc} = 1,834.6\ \frac{\mathrm{N}}{\mathrm{mm}^2}$, $K_{rc} = 512.9\ \frac{\mathrm{N}}{\mathrm{mm}^2}$,

Table 6.4: Identification with the ICFM and PSO algorithm with trochoidal flute paths and runout (data from: [Gra04]).

immersion	K_{tc} [N/mm^2]	K_{rc} [N/mm^2]	K_{ac} [N/mm^2]	K_{te} [N/mm]	K_{re} [N/mm]	K_{ae} [N/mm]	λ_r [°]	ρ_r [mm]
full	1,838.7	515.2	1,115.9	34.4	60.6	–4.0	21.6	10.2
50%-down	1,798.5	509.7	1,100.6	37.3	60.9	–3.0	30.5	10.8
50%-up	1,815.8	505.8	1,100.0	36.3	61.1	–2.7	14.9	10.7
25%-down	1,771.4	484.1	1,078.1	37.3	62.4	–2.2	28.3	10.3
25%-up	1,832.7	510.1	1,111.5	34.6	60.9	–3.8	30.2	10.2
10%-down	1,801.6	499.5	1,095.2	35.6	61.4	–3.2	32.3	10.3
10%-up	1,954.3	569.7	1,187.3	29.4	58.9	–6.7	13.2	9.8

$K_{ac} = 1,056.0\ \frac{N}{mm^2}$, $K_{te} = 30.0\ \frac{N}{mm}$, $K_{re} = 58.8\ \frac{N}{mm}$, and $K_{ac} = -1.3\ \frac{N}{mm}$. In case of tool runout, the undeformed chip thickness changes for varying values ρ_r and λ_r. This requires a recalculation of the undeformed chip thickness. Because of the amount of iterations, computational time would increase noticeably. Instead, the following procedure is performed: First, as already described and carried out, the coefficients are estimated without the consideration of tool runout.

Next, the identified coefficients are used for the identification of ρ_r and λ_r. This step still remains time consuming. However, if the coefficients are kept constant and only the runout values are varied, the likelihood that the PSO algorithm falls into a local optimum can be reduced. With the identified runout values, the calibration of the coefficients is repeated. The results listed in Table 6.4 show the validity of this procedure. In the next section, this method is applied for the calibration of coefficients and tool runout with experimentally obtained process force data.

6.1.3 Influence of Cutting Force Coefficients on Stability

If a dynamic system has a dominant compliance in one coordinate direction, and thus is asymmetric, the feed forward direction in combination with the feed and feed normal forces can have a crucial effect on the stability behavior. As it will be shown, whether an increase or decrease of the process forces or feed direction is an advantage or disadvantage for stability depends on the dynamics of the system and the engagement conditions (radial immersion).

Based on the system configuration from [Ins08], as already used in Chapter 6.1.1, the influence of the specific radial cutting force coefficient K_{rc} on process stability is investigated. First, the resulting feed and feed normal forces for different values of K_{rc}, as shown in Fig. 6.4 a), are considered. For an equally spaced tool with two flutes, the periodicity of the system is half a tool revolution. Therefore, the immersion angle φ in the diagrams ranges only from 0° to 180°. On the basis of the mean values of F_f and F_{fN} the influence on process stability can be assessed. For full immersion operations, it can be seen from the force profile along φ that the average value of the feed force F_f increases with increasing K_{rc}. For the feed normal force F_{fN}, it is obvious that the resulting mean value for F_{fN} is almost the same for small and high values of K_{rc}. This means that for full immersion operations the mean value of F_f increases if K_{rc} increases while the mean value of F_{fN} does not change. Thus a negative impact on stability can be assumed in case of full immersion milling.

However, an actual advantage can be achieved with smaller radial immersions a_e. In the dia-

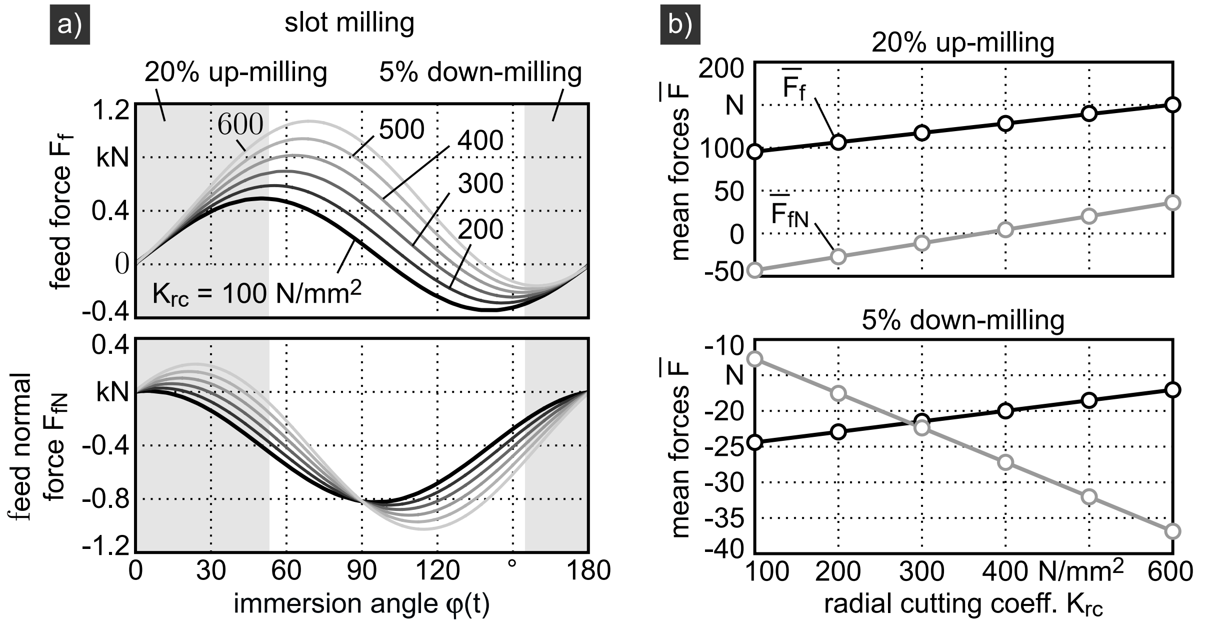

helix angle: δ = 0°

number of teeth: N_t = 2

axial depth of cut: a_p = 12 mm

tan. cutting coeff.: K_{tc} = 536 N/mm²

feed per tooth: f_z = 0.127 mm

Gra/72819 ©IFW

Fig. 6.4: Influence of the specific radial cutting force coefficient K_{rc} on feed and feed normal forces (data from [Ins08]).

grams in Fig. 6.4 a) the mean values for the process forces for 20% up- and 5% down-milling are highlighted. Outside these areas the forces equals 0. The resulting values for $\bar{F}_f$ and $\bar{F}_{fN}$ are shown in Fig. 6.4 b). In case of 20% up-milling, $\bar{F}_{fN}$ can be reduced for K_{rc} = 372 N/mm² to a value of 0. At the same time, the absolute value of $\bar{F}_f$ increases. For 5% down-milling, higher values for K_{rc} in the considered range leads to higher absolute values for $\bar{F}_{fN}$.

However, the absolute values for $\bar{F}_f$ decrease. Fig. 6.5 explains to which extent this affects process stability. The same 2 DOF system with identical modal parameters from [Ins08] for the x- and y-mode in feed and feed normal direction, respectively, is used as in Chapter 6.2.1. For the upper left stability chart (case 1), the modal damping $d_{t,y}$ and stiffness $k_{t,y}$ of the y-mode is reduced by the factor 0.5. Consequently, this mode is more prone to cause an unstable process behavior. The modal mass $m_{t,y}$ is also decreased by a factor of 0.5 to keep the eigenfrequency $f_{t,y}$ constant for all investigations. Otherwise, the position of the stability peaks would shift along the spindle speed axis. As shown, the stability is reduced with increasing K_{rc}. This can be explained by the higher load on the dominant y-mode, which corresponds to the feed normal direction. The frequency diagrams under the stability chart, which show the dominant chatter frequencies, show how the dominance of the x-mode for K_{rc} = 100 N/mm² is replaced by the y-mode in case of 200 N/mm² and 400 N/mm². For the stability chart in the middle (case 2), the x- and y-mode are identical. The stability boundaries seem to show a similar behavior as case 1. However, between n = 9,000 min^{-1} and 10,500 min^{-1} an increase of the stability boundary for K_{rc} = 200 N/mm² compared to 100 N/mm² can be observed. The filled areas outline the achieved stability increase. A look at the corresponding chatter frequencies reveals that compared to case 1 the shift from the x-mode to y-mode dominance appears first at K_{rc} = 400 N/mm². Furthermore, the influence

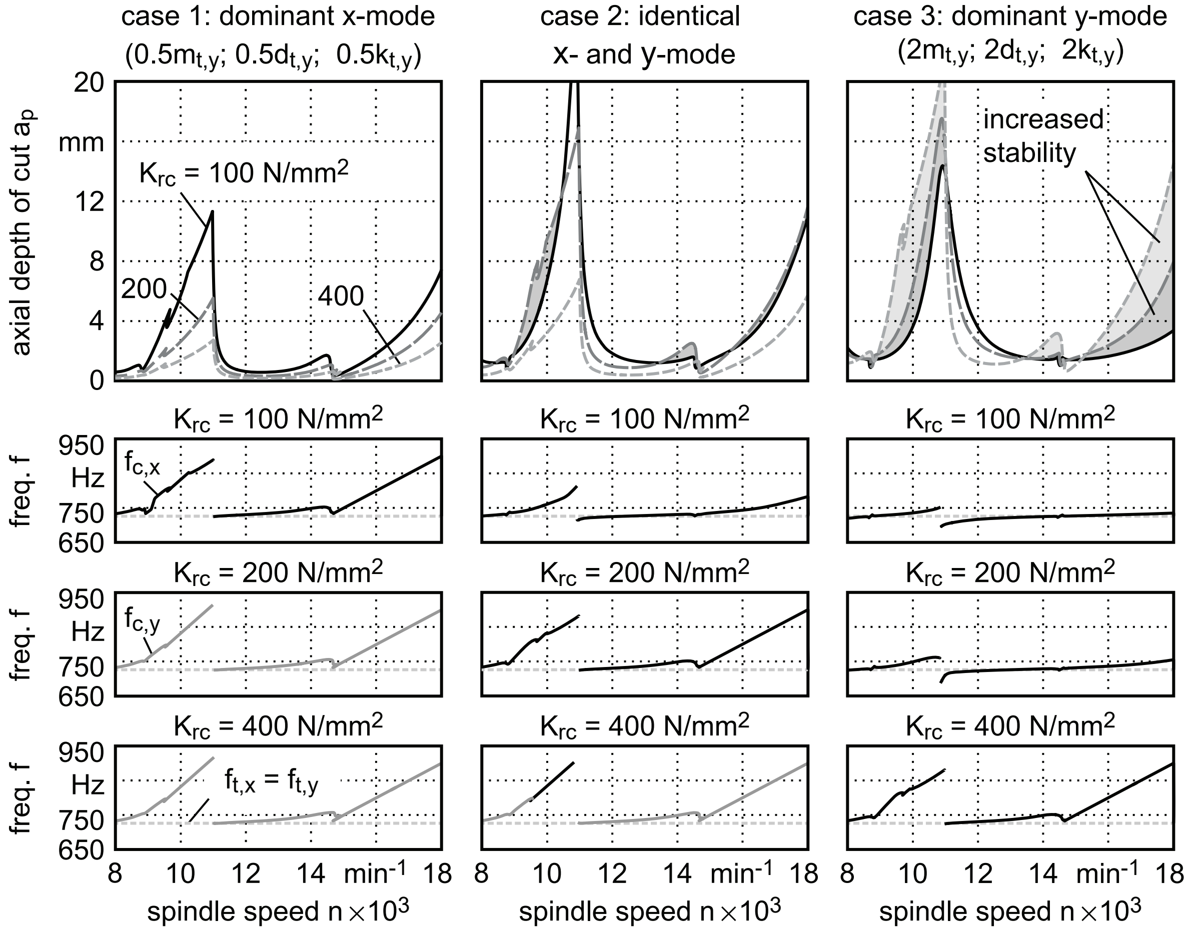

tool diameter:	D = 12.75 mm	process:	down-milling
helix angle:	δ = 0°	tan. cutting force coeff.:	K_{tc} = 536 N/mm^2
number of teeth:	N_t = 2	rad. cutting force coeff.:	K_{rc} = variable
radial depth of cut:	a_e = 0.05D	period resolution:	N_k = 720

Gra/72818 ©IFW

Fig. 6.5: Change of stability depending on the specific radial cutting force coefficient K_{rc} and modal parameters in feed normal direction (data from [Ins08]).

of K_{rc} on the eigenfrequencies is more obvious. For a wide range of spindle speeds n the bifurcation type changes from Hopf to flip (see [Sza04]) with increasing K_{rc} (i.e. from $n = 14,700\ \text{min}^{-1}$ to $18,000\ \text{min}^{-1}$). This explains why for increasing K_{rc} the stability boundaries not merely decrease as in case 1 but rather have sligthly different shapes. A wide range of increase for the chatter boundary is achieved for case 3, where the compliance in feed normal direction (y-mode) is dominant. Increasing K_{rc} lowers the mean value of F_f (see bottom diagram in Fig. 6.4 b)). This leads to an increase of the stability limit within a wide range of spindle speeds. Even for $K_{rc} = 400\ \text{N/mm}^2$ the dominant chatter frequencies result from the x-mode. Hopf bifurcation occurs for $K_{rc} = 400\ \text{N/mm}^2$ which, for the investigated dynamical system and based on the previously studied frequency diagrams, is a sign of lower stability limits if K_{rc} is further increased. The complexity of the shown effects increases with the variation of the milling geometry, i.e. with helix angle $\delta > 0°$, and for a higher number of eigenmodes. Nevertheless, it can be summarized that the knowledge of the shown effects can help to increase process stability.

6.1.4 Speed-Varying Process Force Coefficients

In Chapter 2.4.4 the dependence on the process forces on the cutting speed has been already discussed. Based on the results of the previous section, it can be deduced to what extent this affects the stability. Therefore, in the following, the influence of the speed-dependent variation of K_{tc} and K_{rc} as well as K_{pd} on the stability limit is investigated based on experimental data from [Sel12b], as shown in Fig. 6.6.

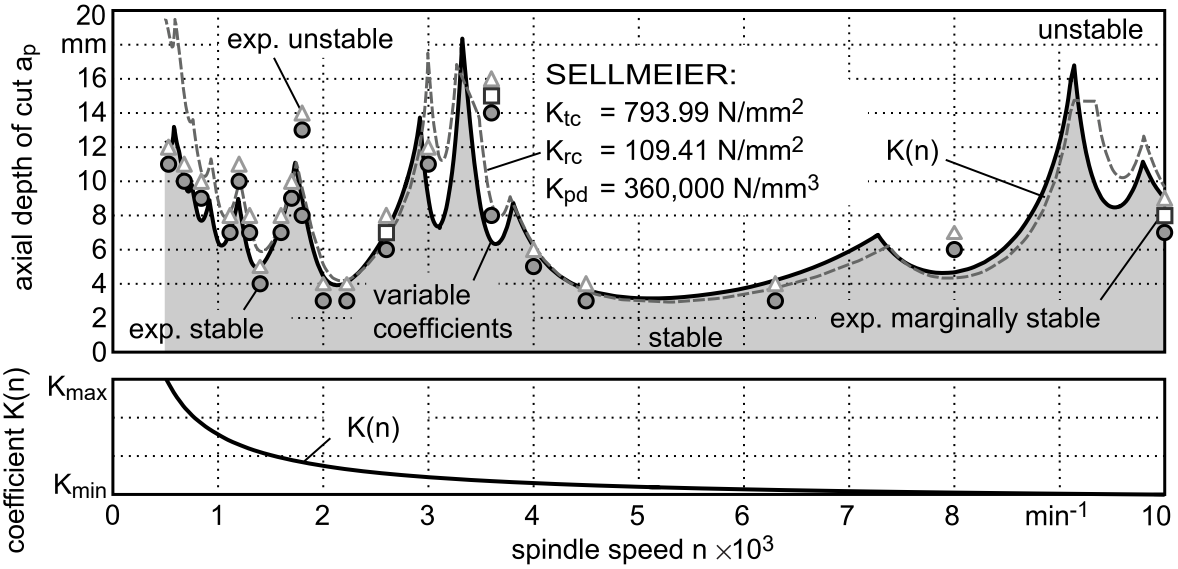

tool diameter:	D = 20 mm	process:	slot milling (no coolant)
helix angle:	δ = 30°	machine:	Heller MCi16
number of teeth:	N_t = 4	feed per tooth:	f_z = 0.12 mm
corner radius:	R = 1 mm	tangential force coeff.:	K_{tc} = variable
radial depth of cut:	a_e = D	radial force coeff.:	K_{rc} = variable
chamfer width	b_f = 0.05 mm	process damping coeff:	K_{pd} = variable
chamfer angle	α_f = 1°	coefficient of friction:	μ = 0.3
workpiece:	Al 7075 T651	period resolution:	N_k = 250

Gra/72820 ©IFW

Fig. 6.6: Influence of speed dependent coefficients on stability (data from [Sel12a, p. 101]).

The dashed line corresponds to the calculated stability limit with constant coefficients. It can be seen that compared to the experimental data the stability at low spindle speed is clearly overestimated. Adjusting the constant coefficients, however, would lead to a decrease of the agreement at higher spindle speeds. Alternatively, if significant higher coefficient values for lower spindle speeds are assumed, similar to [Gro14], the deviations between experimental and calculated stability can be reduced, as shown by the solid line in the stability chart. For the optimized calculation of the stability limit the coefficients follow the curve in the lower diagram in Fig. 6.6. The available coefficients, shown in the middle of the upper diagram, were probably determined at a spindle speed n between $1,000\,\text{min}^{-1}$ and $2,000\,\text{min}^{-1}$, which equals a cutting speed v_c between approximately 63 m/min and 126 m/min. Therefore, it is assumed that at lower cutting speeds the values of the coefficients might increase. In order to take this into account, the curve of the spindle speed dependent coefficients K (n) is described by the following equation:

$$K\,(n) \;=\; K_{min} + (K_{max} - K_{min}) \left(36n^{1.72} - \frac{48}{10^5} n + 0.07 \right) \qquad (6.5)$$

This equation is based on a curve fitting algorithm, with the aim to increase the agreement between experimental and calculated stability data from Fig. 6.6. K_{min} and K_{max} are the minimum and maximum values, respectively, for the spindle speed under consideration and were set as follows:

$$\begin{aligned} K_{tc} &= 1,200\ \text{N/mm}^2 && \cdots && 650\ \text{N/mm}^2 \\ K_{rc} &= 150\ \text{N/mm}^2 && \cdots && 95\ \text{N/mm}^2 \\ K_{pd} &= 480,000\ \text{N/mm}^3 && \cdots && 180,000\ \text{N/mm}^3 \end{aligned}$$

For reasons of clarity, the formula for the variation of the coefficients is presented here. However, for calculation reasons, it is advantageous to calculate the matrices $\mathbf{Q}_{j,u}$ and $\mathbf{Q}_{pd}$ from Eq. 5.1 for the highest and lowest coefficient values, and then apply analogous Eq. 6.5. In accordance to the literature, it can be summarized that the changes in the forces are particularly high at low spindle speeds and this must be taken into account for the coefficients for a more precise prediction of the stability limit. With the chosen equation, the decline of the coefficient values from approximately $n = 500\ \text{min}^{-1}$ to $2,000\ \text{min}^{-1}$ is considerably higher than the more linear decrease from $2,000\ \text{min}^{-1}$ to $10,000\ \text{min}^{-1}$. As shown in Fig. 6.6, the calculated stability limit with varying coefficients improves the agreement with the experimental data at low spindle speeds in comparison to the calculated stability limit from [Sel12b]. In order to determine the relevance and the actual spindle speed dependent course of the coefficients, for the following application cases the cutting forces for a wide spindle speed range will be determined experimentally.

6.1.5 Estimation of Process Damping Forces

As mentioned in Chapter 2.3.2, the interference between the workpiece and the chamfered face of the cutting edge is a complex process consisting of elastic and plastic deformation mechanisms. Thus, the idea of an indentation area A_{pd} is a simplification. Using experimental results from [Sel09], the consistency of modeling process damping forces based on A_{pd} will be investigated. SELLMEIER et al. used a machine which allows to generate an adjustable vibration during the machining process. To prevent vibration-induced fluctuations of the uncut chip thickness, the vibrational frequency in feed direction was chosen by the authors to match an integral multiple of the spindle speed. With the same parameters, including the intended vibration, a time-domain simulation was carried out to predict process damping forces. An example for the resulting forces for the one fluted tool with $b_f = 0.2\,\text{mm}$ is shown in Fig. 6.7. The illustrated workpiece shows the generated wavy material removal. The dashed line points to the ideal or vibration-free movement of the cutting edge. Based on BOOLean operations, the time-simulation model from Chapter 5.2 allows a highly precise numerical estimation of the indentation area, denoted as A^*_{pd}. The thick interrupted black lines mark the edge positions where this method identifies an overlap, which means that $A^*_{pd} > 0$. In comparison, the thick interrupted white lines show the identified overlap according to the simplified method for the estimation of the indentation area ($A_{pd} > 0$). Obviously, there are more indentation positions for A^*_{pd} than for A_{pd}. The detailed view for $\varphi = 161^\circ$

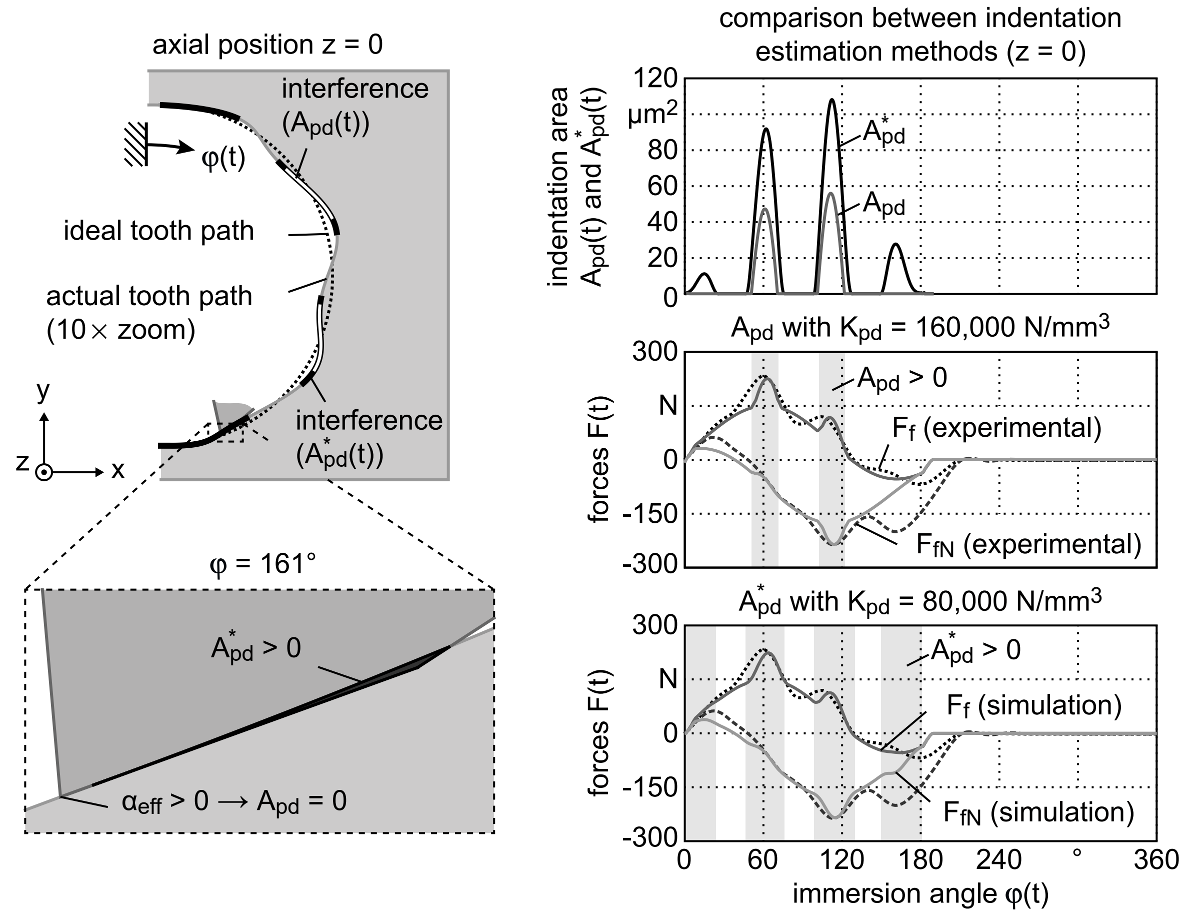

tool diameter:	D = 10 mm	workpiece:	Al 7075 T651
helix angle:	δ = 30°	machine:	Schnelle Maschine
corner radius:	R = 0 mm	process:	slot milling
chamfer width:	b_f = 0.2 mm	tan. cutting coeff.:	K_{tc} = 884 N/mm²
chamfer angle	α_f = 1°	rad. cutting coeff.:	K_{rc} = 479 N/mm²
clearance angle:	α = 14°	tan. edge coeff.:	K_{te} = 25 N/mm
feed per tooth:	f_z = 0.15 mm	rad. edge coeff.:	K_{re} = 24 N/mm
radial depth of cut:	a_e = D	process damping coeff:	K_{pd} = variable
axial depth of cut:	a_p = 1 mm	coefficient of friction:	μ = 0.3
spindle speed:	n = 1,631 min⁻¹		

Gra/72823 ©IFW

Fig. 6.7: Simulation of the experimentally determined forces for exact and simplified calculation method of A^*_{pd} and A_{pd}, respectively, with vibration frequency f_x = 190.26 Hz and amplitude A_x = 30µm (data from [Sel09]).

shows the reason for the differences. At this position, the effective clearance angle α_{eff} is greater than 0, which means for A_{pd} that no indentation occurs. However, the rear part of the chamfer overlaps with the workpiece, and thus, $A^*_{pd} > 0$. Due to these contact conditions, no indentation is identified for A_{pd} at the entrance and the exit sections. The values for the indentation areas for one tool revolution are shown in the top right diagram. This diagram also shows that with the simplified method the value of the indentation area is considerably lower. Consistency with experimental data from [Sel09] is shown in the further diagrams.

By applying the PSO algorithm from Chapter 4.4, the experimental process force data in case of no vibration was used for fitting (coefficients are given in the lower part of Fig. 6.7). Next, the process damping forces, resulting from the indentation area given in the upper diagram, were superimposed on the fitted non-vibrational forces. Experimental and simulated forces for A_{pd} are illustrated in the middle diagram. K_{pd} was iteratively estimated to reach the best fit. A good agreement for the appearing damping peaks at $\varphi = 60^\circ$ and 110° can be reached. Same applies for A^*_{pd} in the lower diagram. However, K_{pd} is considerably smaller due to the fact that $A^*_{pd} > A_{pd}$ for all immersion positions. The highest deviations arise in both cases at the entry and exit positions. Although in case of A^*_{pd} the indentation at these positions is identified, the values for the indentation area are obviously too small. It must be noted that in case of the entry deviation, the main source of error is a low fitness between the simulated and experimental process forces in case of no vibrations. Looking at the exit conditions, it is surprising that the immersion seems to end at $\varphi = 210^\circ$ instead of approximately at 180°. Presumably, for the real case, the indentation is so high that a smearing of the workpiece material occurs and the contact length between the tool and workpiece increases. This also leads to presumably additionally dominant elastic deformations at the entry and exit.

In the following, the differences between A_{pd} and A^*_{pd} are discussed by means of further simulations, as shown in Fig. 6.8. For the upper diagrams (Fig. 6.8 a)), the same excitation frequency and amplitude were used as previously. Additionally, an excitation in feed normal direction is considered. With constant excitation, the following mean values for the indentation areas for one revolution $\bar{A}_{pd}$ and $\bar{A}^*_{pd}$, respectively, are obtained for increasing spindle speeds n. In accordance with the findings from literature, as mentioned in Chapter 2.3.2, the low excitation frequency leads to a decrease of the indentation area with increasing n. Only in case of very low spindle speeds the effective clearance angle α_{eff} has such a high value that the following applies: $\bar{A}_{pd} > \bar{A}^*_{pd}$. This means that in this case the indentation area is overestimated by the simplified estimation method.

Fig. 6.8 b) shows the indentation areas for a constantly high spindle speed and increasing excitation frequencies. Both values of $\bar{A}_{pd}$ and $\bar{A}^*_{pd}$ increase with higher excitation frequencies. However, the increase of $\bar{A}^*_{pd}$ is greater than for $\bar{A}_{pd}$. The reason is that the indentation area exceeds the width of the chamfer b_f, similar to the detailed view for $\varphi = 161^\circ$ in Fig. 6.7, and exits the cutting edge under the clearance face and not the chamfer face. Theoretically, it is possible to extend the simplified method by basic trigonometric relations to take into account this area. However, with increasing excitation frequencies an overestimation occurs similar to the case in Fig 6.8 a). For the sake of completeness, it must be noted that further numerical issues may arise in case of low spindle speeds and high excitations frequencies. In such a case, multiple peaks of the workpiece are engaged with interruptions in the tool edge. Such an indentation condition is not considered by the simplified estimation method. Another noteworthy behavior for the excitation in feed normal direction is the sawtooth like increase of the indentation area. This effect is caused by the varying number of excitation peaks present on the tooth path, which can favor the overall indentation.

The studies shown here indicate possible errors in the calculation of process damping using the simple method for calculating the indentation area. The effects on the value of K_{pd} and at which immersion positions damping actually occurs are shown in Fig. 6.7. Especially with increasing excitation frequencies, the deviations may increase as well (Fig. 6.8). Since the system has to be

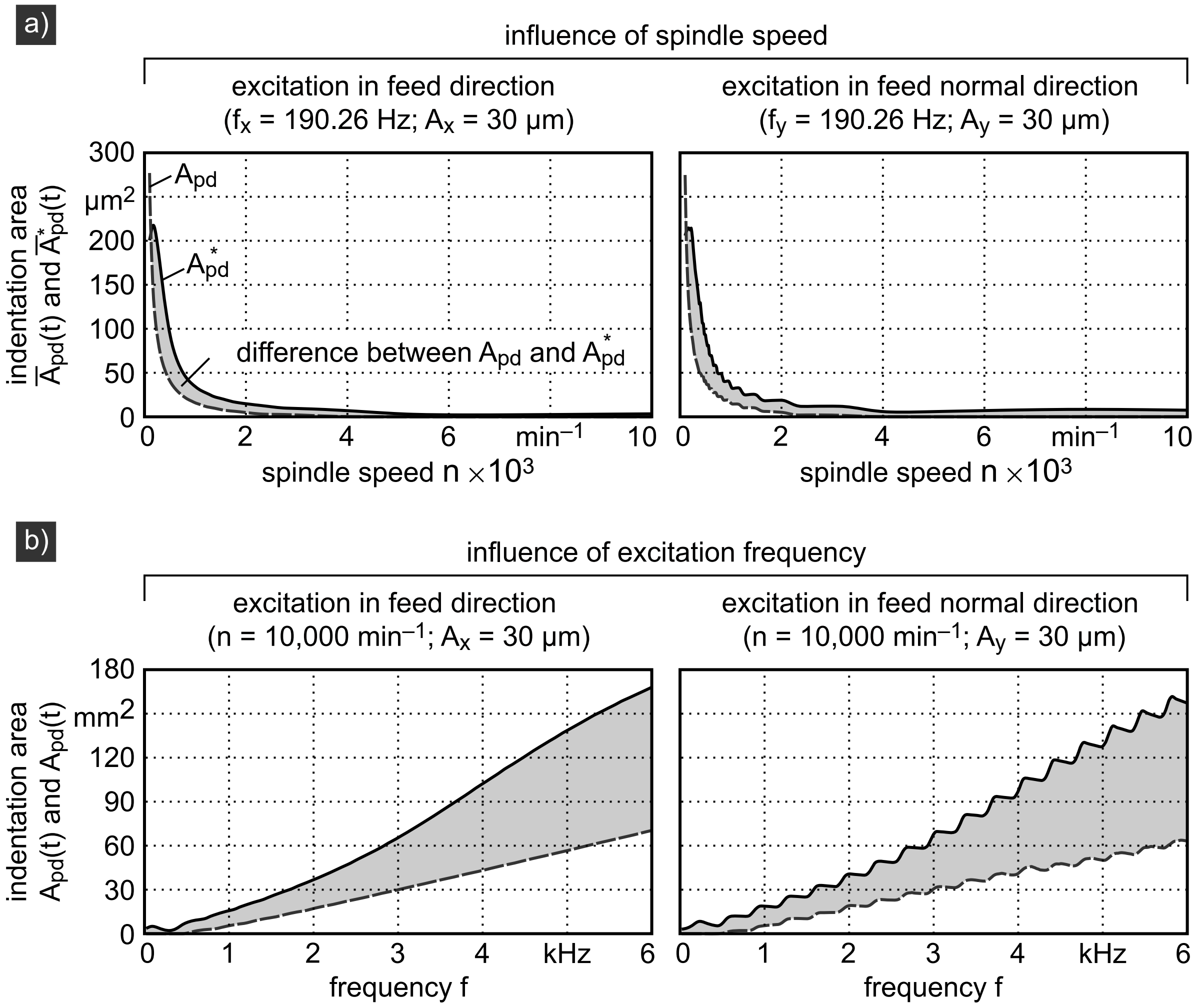

tool diameter:	D = 10 mm	clearance angle:	α = 14°
helix angle:	δ = 30°	process:	slot milling
corner radius:	R = 0 mm	feed per tooth:	f_z = 0.15 mm
chamfer width:	b_f = 0.2 mm	radial depth of cut:	a_z = D
chamfer angle:	α_f = 10°		

Gra/72824 ©IFW

Fig. 6.8: Comparison between the exact and simplified indentation areas A_{pd} and A^*_{pd}, respectively, for a) various spindle speeds and b) excitation frequencies.

linear to predict stability with the SD method, only this calculation method for taking the process damping into account is possible. Theoretically, an a priori calculation of the indentation area is possible to avoid non-linearity, as shown in [Bac10] using the shooting method. However, this method is limited to systems with a single time-delay and thus can not be applied in this work.

6.2 Tool Geometry

The geometric attributes of an end mill have a relevant influence on the dynamical process behavior as well as the machined surface quality. The following first section deals with time delay changes in case of recessed flutes and its impact on stability. In order to focus on the influence of the radial offset ΔR on stability, only sharp cutting edges are considered. Thus, process damping effects can be neglected. In the second section, runout is considered in the same way with the reasoning that although runout is a disturbance, it still is included in the tool geometry specifications (Chapter 4.3). Finally, it is shown how certain tool geometry attributes affect the shape and intensity of deformations of the machined surface. Again, the influence of radial offset and runout is the main focus.

6.2.1 Influence of Radial Offset on Time Delays and Stability

As mentioned in Chapter 2.3.1, the reduced uncut chip thickness h caused by a radial offset ΔR can be corrected by adjusting the tooth pitch p. For the sake of simplicity, a circular flute trajectory is assumed to calculate the necessary tooth pitch for an equally distributed load:

$$p = \frac{2\pi}{N_t}\left(1 - \frac{\Delta R}{f_z}\right) \tag{6.6}$$

From this equation it follows that a flute with a radial offset always has a smaller tooth pitch than the preceding flute with no offset ($\Delta R = 0\ \mu m$). Conversely, this equation can be solved for ΔR to determine the necessary radial offset to reach a balanced load for a given non-equal tooth pitch. This leads to an equal effective feed per tooth $f_{j,u}$ for all flutes (Eq. 4.7). In case of a four fluted end mill with a non-equal tooth pitch of $\mathbf{p} = [80^\circ, 100^\circ]$, a radial offset of $\Delta R = 13.3\ \mu m$ leads to a balanced load for all flutes. However, if the trochoidal trajectory of the flutes is considered, ΔR needs to be slightly reduced to reach a balanced load, as shown in Fig. 6.9. For the sake of clarity, a helix angle of $\delta = 0^\circ$ is chosen. The top left diagram shows the individual feed forces $F_{f,j}$ of all j-flutes in case of no radial offset. The unequal tooth pitch leads to alternating undeformed chip thickness values and maximum values of $F_{f,j}$. In comparison, the top right diagram represents the forces in case of a radial offset of $\Delta R = 10\ \mu m$. The gray lines correspond to the curves in the left diagram ($\Delta R = 0\ \mu m$). Undeformed chip thicknesses and maximum values of $F_{f,j}$ are almost equal for all flutes. However, entry and exit position of all flutes change due to ΔR, which is represented by the markers. The detailed view A shows how the point of entry of flute z_1 occurs earlier (square shaped marker). Simultaneously, the entry of flute z_4 ($\Delta R = 10\ \mu m$) is delayed (round shaped marker). The dotted trajectory shows the the position of flute z_4 in case of no radial offset (z_{4^*}). The exit situation is shown in the detailed view B. z_4 is earlier out of cut (triangle shaped marker) while the immersion range of z_1 increases (rhombus shaped marker). The position of the markers for all flutes are also included in the top right diagram. The shaded areas show the gaps which result from the shifted entry and exit position of the flutes. Accordingly, the course of the feed force changes (middle diagram). However, the most noteworthy difference is shown in the lower diagrams. In case of the tool with unequal tooth pitches and no radial offset, two different time delays occur during one revolution (left diagram). As it can be seen, the radial offset leads to additional time delays. Near $\varphi \approx 90^\circ$, the earlier exit of z_4 and delayed entry of z_2 cause a gap. At this position, only the time delay of z_1 is present. Same applies at $\varphi \approx 270^\circ$. At the entry and exit position of z_1 near $\varphi \approx 0^\circ$ and $\varphi \approx 180^\circ$, an additional time delay occurs (see detailed view C). Same applies for flute z_3. At these positions the recessed flutes are not in cut. Therefore, the additional time delay corresponds to the tooth pitch $p_{1,3} = p_{3,1} = 180^\circ$ of the diametrical arranged flutes z_1 and z_3.
The mentioned gaps combined with the additional time delays contribute to a disturbance of the regenerative effect. In analogy to end mills with unequal tooth pitches, this may induce additional

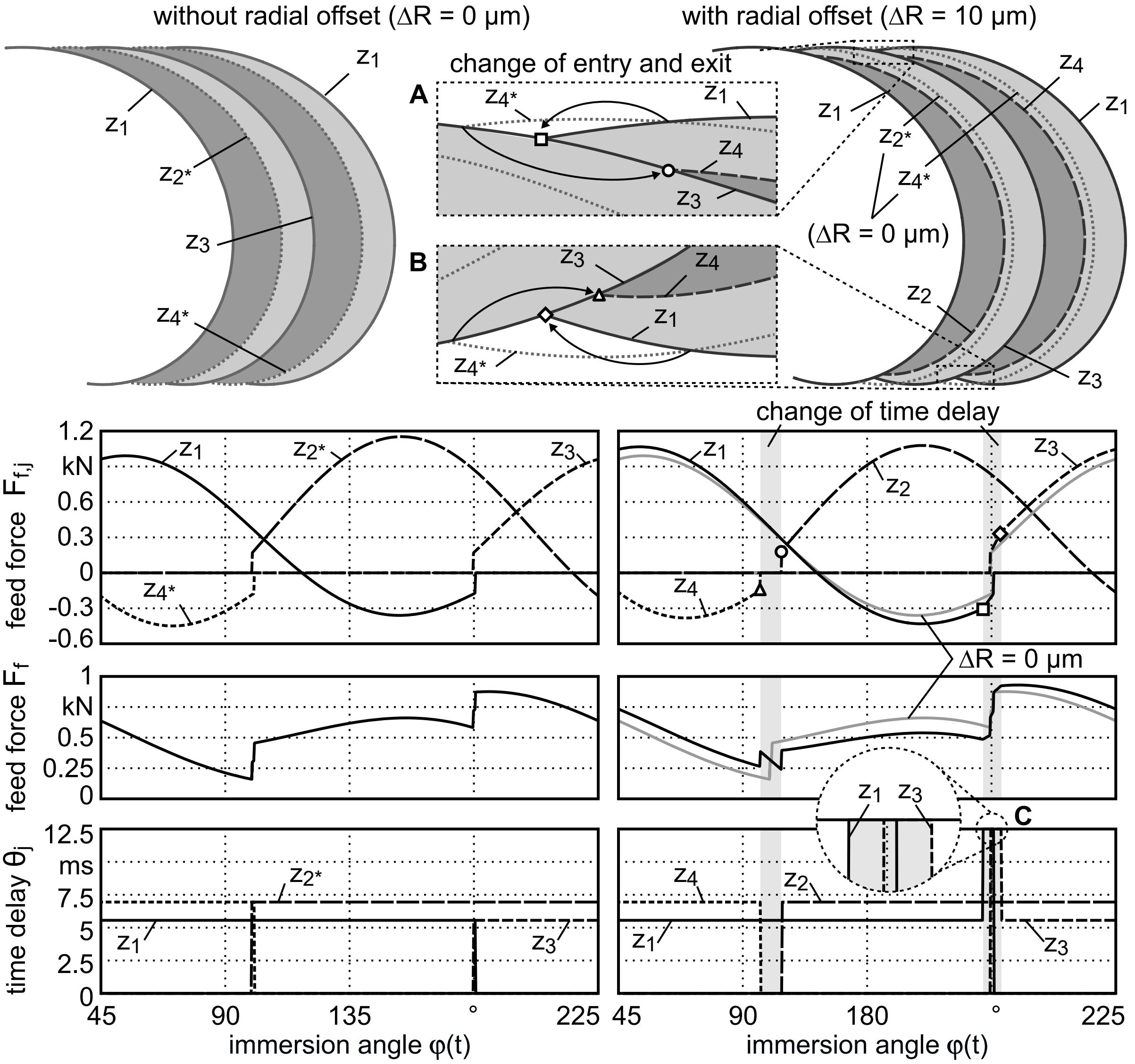

feed per tooth: f_z = 0.12 mm
radial depth of cut: a_e = 20 mm
axial depth of cut: a_p = 5 mm
spindle speed: n = 2,400 min^{-1}

process: slot milling
tool diameter: D = 20 mm
tooth pitch: **p** = [80°, 100°]
helix angle: δ = 0°

Gra/72840 ©IFW

Fig. 6.9: Force and time delay variation in case of flutes with $\Delta R > 0$ µm.

stable positions. By increasing the radial offset, the duration of these additional time delays can be expanded as shown in Fig. 6.10 a). The undeformed chip thickness area A_2 of the recessed flute z_2 decreases with increasing ΔR. As a consequence, the flute z_3 removes at its entry and exit position larger portions of material left behind by flute z_1.

For the given tool from Fig. 6.10, the possible immersion rate of a tooth pitch $p_{j,u}$ in de-

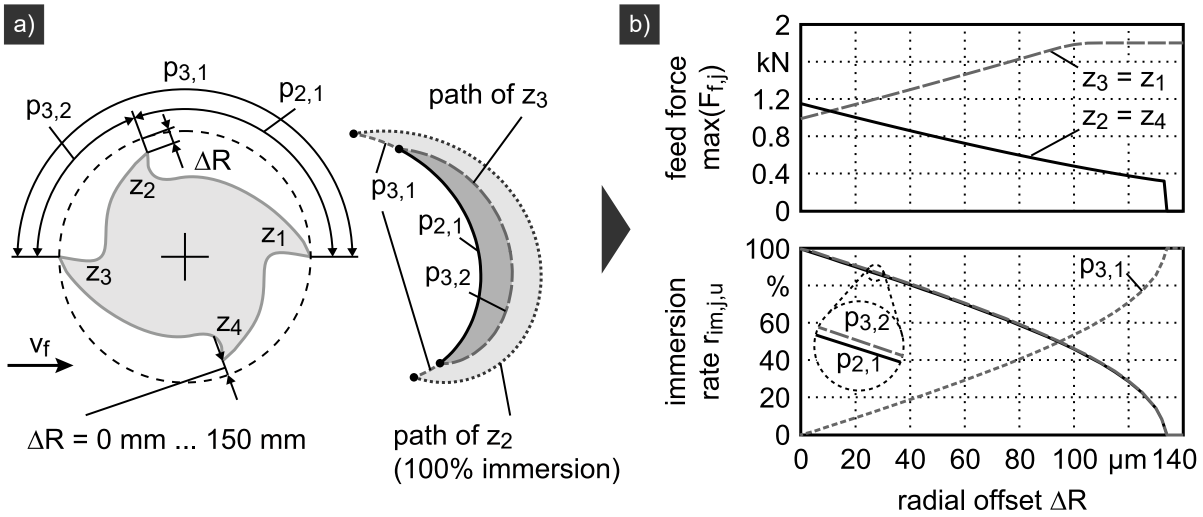

feed per tooth:	f_z = 0.12 mm		tool diameter:	D	= 20 mm
radial depth of cut:	a_e = 20 mm		tooth pitch:	**p**	= [80°, 100°]
axial depth of cut:	a_p = 5 mm		helix angle:	δ	= 0°
process:	slot milling				

Gra/72841 ©IFW

Fig. 6.10: Immersion conditions in dependance on the radial offset value ΔR.

pendance of ΔR can be determined by the following formula (Eq. 4.4):

$$r_{im,j,u} = \frac{\sum_{d=1}^{N_k} g_{j,u}\,(dT, \Delta R)}{\max\left\{\sum_{d=1}^{N_k} g_{j,u}\,(dT, \Delta R = 0)\,, \sum_{d=1}^{N_k} g_{j,u}\,(dT, \Delta R = D/2)\right\} 100\%} \tag{6.7}$$

As it can be seen, the immersion rate for the tooth pitch $p_{3,1}$ increases with higher values for ΔR. However, this also results in a higher load for the flutes z_3 and z_1, as shown in Fig 6.10 b). A balanced load based on the maximum value of the individual feed forces $F_{f,j}$ is reached near ΔR = 10.7 µm. It must be noted, however, that for the new tool concept it can be expected that the forces of the recessed flutes are higher due to induced damping forces of the chamfers. For ΔR = 110 µm, the flutes with no offset reach their maximum value. At higher values the recessed flutes are in cut outside the range of the highest undeformed chip thickness of the flutes with no offset. Finally, at ΔR = 133.5 µm the recessed flutes have no engagement into the material. The corresponding active tooth pitches are shown in the lower diagram. The immersion rate indicates how the radial offset affects the engagement length of a tooth pitch in comparison to the total engagement length in case of no radial offset. An increase of ΔR causes a decrease of the immersion rate of $p_{2,1}$. Same applies for $p_{3,2}$. However, the total immersion length for the regular flute z_3 does not decrease due to the increasing immersion range of $p_{3,1}$. As already mentioned, this shift of the time delay makes a disturbance of the regenerative effect more likely.

The influence of the radial offset ΔR on process stability is to be determined with the aid of realistic and general input parameters. Therefore, an experimental modal analysis was carried out on a

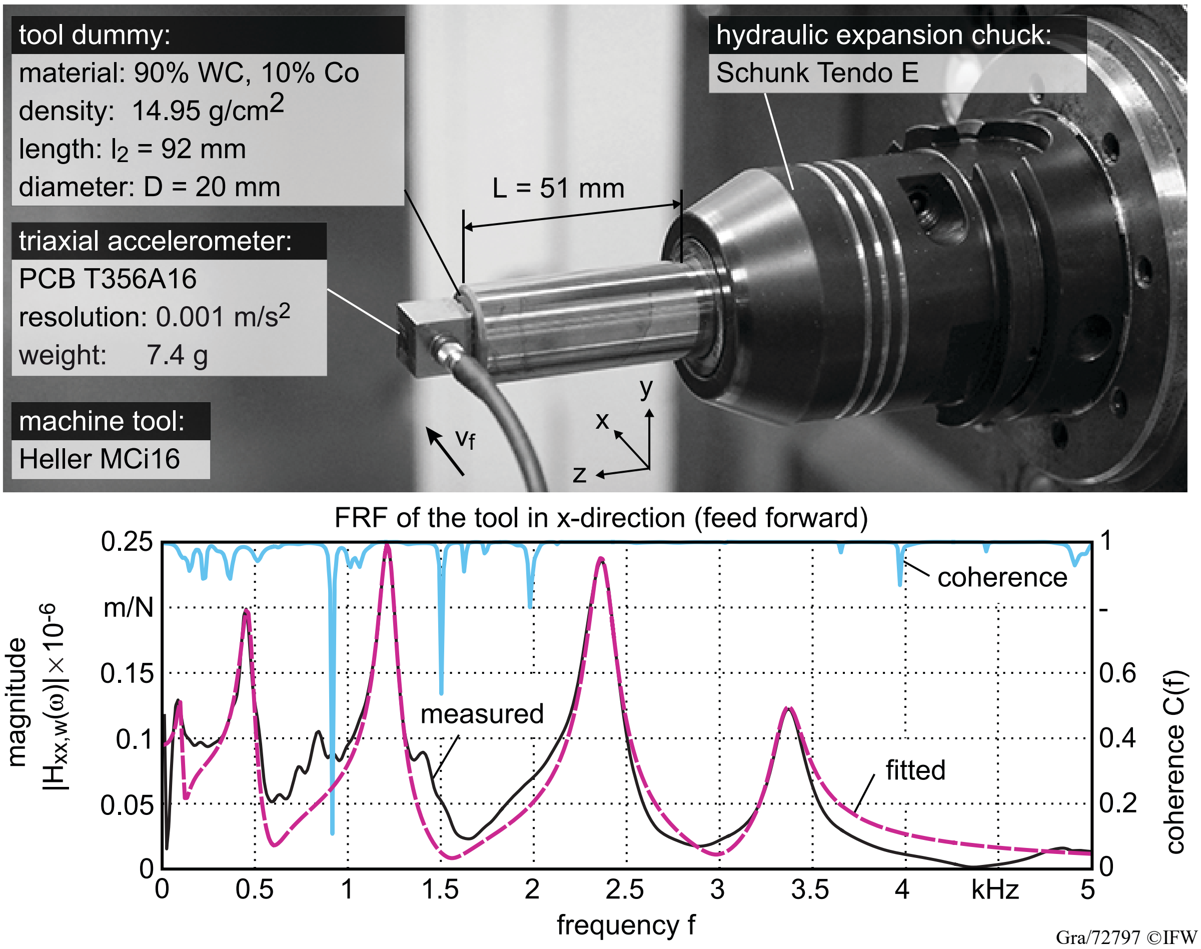

Gra/72797 ©IFW

Fig. 6.11: Experimental setup with dummy tool and obtained FRF.

Heller MCi16 machine tool. The experimental configuration is shown in Fig. 6.11. In order to obtain frequency responses which are independent of the tool geometry, e.g. the helix angle or the number of flutes, a dummy tool is used. The excitation of the dummy tool is performed at the uppermost exposed point with an impact hammer (PCB Piezotronics 086C03). The response is measured with a triaxial accelerometer. The experimental FRF in x-direction is shown in the lower part of Fig. 6.11. Furthermore, the spectral coherence is also given in the diagram to assure the causality between input (hammer impact) and output (tool deflection). The most dominant modes were selected for a fit of the experimental FRF, represented by the dashed line, using an adapted version of the presented PSO algorithm in Chapter 4.4. The resulting modal parameters are given in Table 6.5. It is assumed, for the sake of simplicity, that the compliance in x- and y-direction is similar. Thus, the modal parameters in y-direction have the same values. Furthermore, it is assumed that the workpiece has a high stiffness. Thus, in comparison to the dummy tool, its dynamical behavior is neglected. Stability charts for different values for the radial offset ΔR are shown in Fig. 6.12. For the calculation of the stability, the tool is modeled with equally distributed flutes and with a corner radius $R = 0$. Two diametrical arranged flutes have a radial offset with the same value. In order to underline the effect of ΔR on stability, a feed per tooth f_z of 0.3 mm is selected. Thus, a noticeable influence of ΔR on time delays can be achieved. This is particularly necessary because, as it can be seen in Fig. 6.12, there is no noticeable differences in the stability limit between a reference tool ($\Delta R = 0\ \mu m$, solid black line) and a tool with a low radial

Table 6.5: Modal parameters for the dummy tool in x-direction.

	mode i [–]	$f_{\cdot,\cdot i}$ [Hz]	$m_{\cdot,\cdot i}$ [kg]	$k_{\cdot,\cdot i}$ [N/µm]	$\zeta_{\cdot,\cdot i}$ [–]
f_{t,x_i}	1	105.4	111.55	48.93	0.1349
	2	468.86	3.74	32.48	0.0843
	3	1218.46	0.82	47.92	0.0429
	4	2364.13	0.28	62.41	0.0339
	5	3357.20	0.34	151.64	0.0275

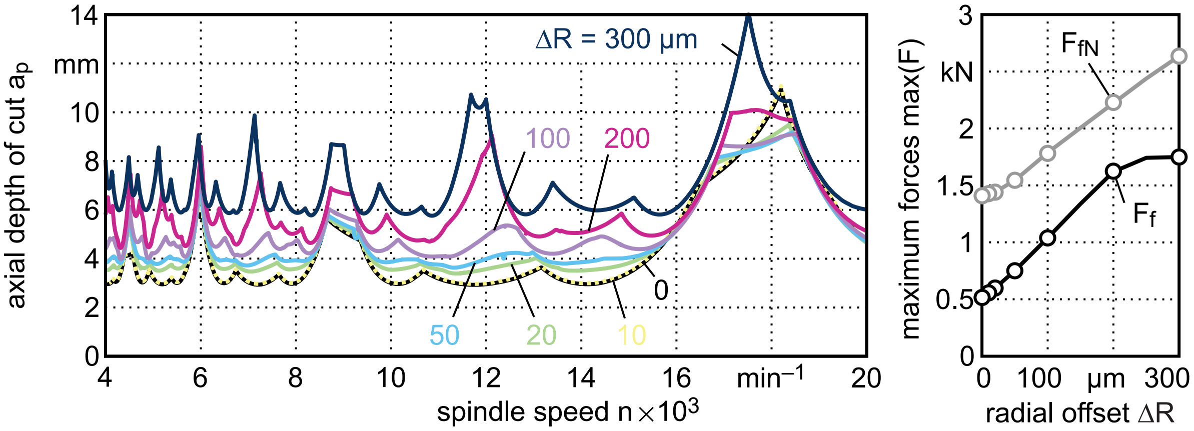

tool diameter: D = 20 mm
helix angle: δ = 30°
number of teeth: N_t = 4
radial depth of cut: a_e = D
feed per tooth: f_z = 0.30 mm

discretization: N_k = 720, N_z = 20
tan. cutting force coeff.: K_{tc} = 700 N/mm^2
rad. cutting force coeff.: K_{rc} = 200 N/mm^2
tan. edge coeff.: K_{te} = 10 N/mm
rad. edge coeff.: K_{re} = 10 N/mm

Gra/72844 ©IFW

Fig. 6.12: Stability increase due to radial offset ΔR. However, absolute maximum values of process forces in feed and feed normal direction increase as well.

offset (ΔR = 10 µm, dotted line). With increasing values for the radial offset, the gain in the stability limit also increases. For ΔR = f_z, the recessed flutes are almost out of cut. Thus, the increase is stability is not assigned to ΔR, but rather the reduced number of teeth contributing to the material removal. The resulting stability limit corresponds to the stability limit of a two fluted cutter. In this respect, these results are consistent with the knowledge that the asymptotic stability limit increases with decreasing tooth number N_t [Sil05, p. 1544 f.]. However, it should be noted that in this case, the actual tooth feed rate is doubled. This has an evident influence on the process forces, as shown in right diagram in Fig. 6.12. At the highest value for ΔR, the maximum value for the feed force F_f is more than tripled. This means that it can be assumed that severe forced vibrations would occur in experimental investigations. Forced vibrations can be investigated with time-domain simulations, as it will be shown in the next section for tools with runout.

6.2.2 Influence of Tool Runout on Time Delays and Stability

As mentioned in Chapter 4.3, a further change of the immersion conditions arises in case of runout. While the rounout offset ρ_r does not vary significantly within the same system configuration (machine tool, spindle, tool holder etc.), the runout location angle λ_r depends on how the tool is placed in the tool holder. Thus, this angle can vary considerably during each new clamping of a tool in the tool holder. The influence of λ_r on the immersion conditions for the hybrid tool is shown in Fig. 6.13. The radial offset ΔR is constant with a value of 10 µm. This corresponds roughly to the balanced force load shown in Fig. 6.10. The runout offset ρ_r has the same value as ΔR. Angular values for λ_r extend over the tooth pitch periodicity of 180°. There are several notable positions. From λ_r = 30° to 80°, three active tooth pitches, and thus time delays, occur for flute z_3 during its immersion. Furthermore, the immersion of tooth pitch $p_{3,1}$, caused by ΔR (Fig. 6.10), disappears from λ_r = 0° to 30°. In accordance to Eq. 4.40, the highest radius for flute z_4 occurs at λ_r = 100°. As a consequence, the highest immersion range for flute z_4 is reached at this angular position. These results show that runout can have a significant influence on the

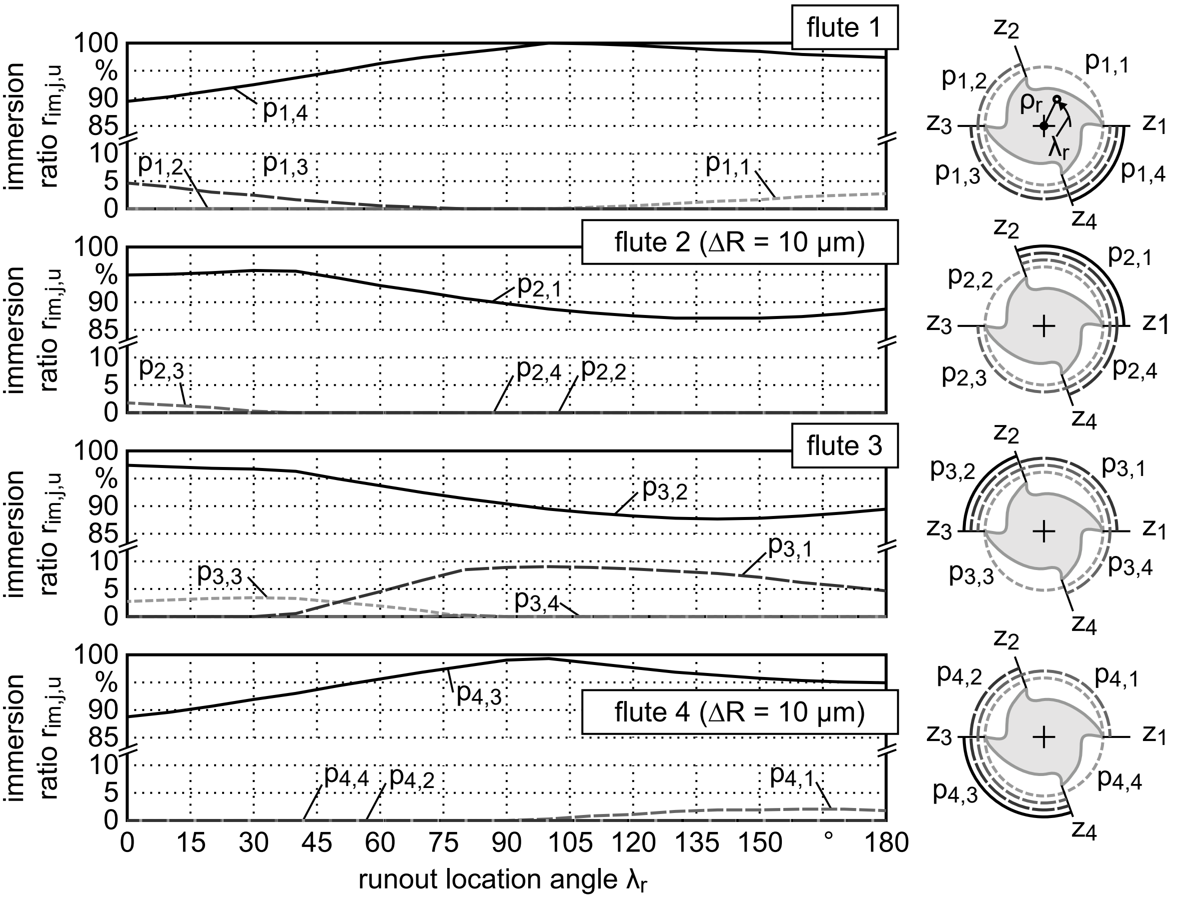

feed per tooth:	f_z = 0.12 mm	tool diameter:	D = 20 mm
radial depth of cut:	a_e = 20 mm	tooth pitch:	**p** = [80°, 100°]
axial depth of cut:	a_p = 5 mm	helix angle:	δ = 0°
process:	slot milling	runout offset:	ρ_r = 10 mm

Gra/72842 ©IFW

Fig. 6.13: Example of possible immersion conditions in case of a tool with an unequal tooth pitch **p**, radial offset ΔR and runout offset ρ_r with varying runout location angles λ_r.

engagement conditions, and thus, time delays of the hybrid tool. Consequently, runout should be taken into account for the stability prediction.

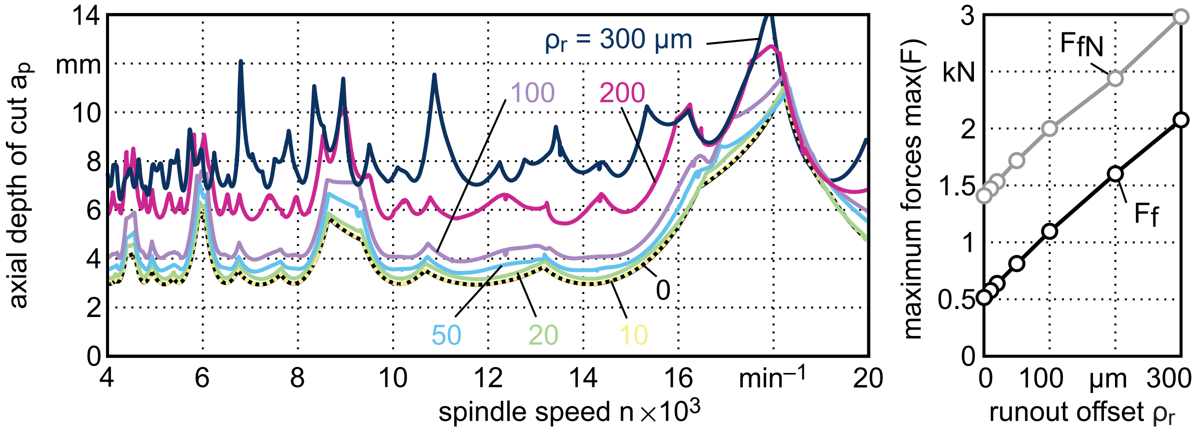

tool diameter: $D = 20$ mm
helix angle: $\delta = 30°$
number of teeth: $N_t = 4$
runout location angle: $\lambda_r = 30°$
radial depth of cut: $a_e = D$
feed per tooth: $f_z = 0.30$ mm

discretization: $N_k = 720$, $N_z = 20$
tan. cutting force coeff.: $K_{tc} = 700$ N/mm^2
rad. cutting force coeff.: $K_{rc} = 200$ N/mm^2
tan. edge coeff.: $K_{te} = 10$ N/mm
rad. edge coeff.: $K_{re} = 10$ N/mm

Gra/72845 ©IFW

Fig. 6.14: Stability increase due to runout offset ρ_r. Absolute maximum values of process forces in feed and feed normal direction increase as well.

On the basis of the experimental configuration from Chapter 6.2.1, stability charts for different runout errors are calculated, which is shown in Fig 6.14.

In analogy to the stability charts for tools with different radial offsets ΔR (Fig. 6.12), the stability is also significantly higher with increasing runout offsets ρ_r. The maximum value for the process forces is also increasing, shown at the right diagram in Fig. 6.14, which in turn may lead to forced vibrations. Comparatively low values for ρ_r have no effect on stability. This is in line with the findings from [Ins08]. However, it cannot be excluded that upon further modification of the tool geometry, e.g. unequal tooth pitch or radial offset ΔR, stability might be influenced even in case of low values of ρ_r. Furthermore, a different position of λ_r could also contribute to this (Fig. 6.13).

In contrast to the presented stability charts predicted by the SD method, the time-domain simulations carried out by Schmitz et al. showed that runout error can actually reduce the stability considerably and especially if the spindle frequency coincides with a natural frequency of the system [Sch07]. Thus, this is in contradiction to the fact that in general stability is particularly high at these frequencies (Fig. 2.4). This points to the already mentioned possible influence of forced vibrations. A detailed analysis for this case is given in Fig. 6.15. The left side shows the dynamical behavior during the machining operation in case of no runout. Severe chatter marks are visible at the flank faces of the machined surfaces (Fig. 6.15 a)). In case of a radial runout of $\rho_r = 200$ µm, chatter marks occur only at the exit position of the tool. Otherwise the process is stable. The visible surface marks correspond to the feed per tool revolution $N_t f_z = 1.2$ mm. Note that in case of $\rho_r > 0$, the radial immersion a_e increases, which is taken into account in the simu-

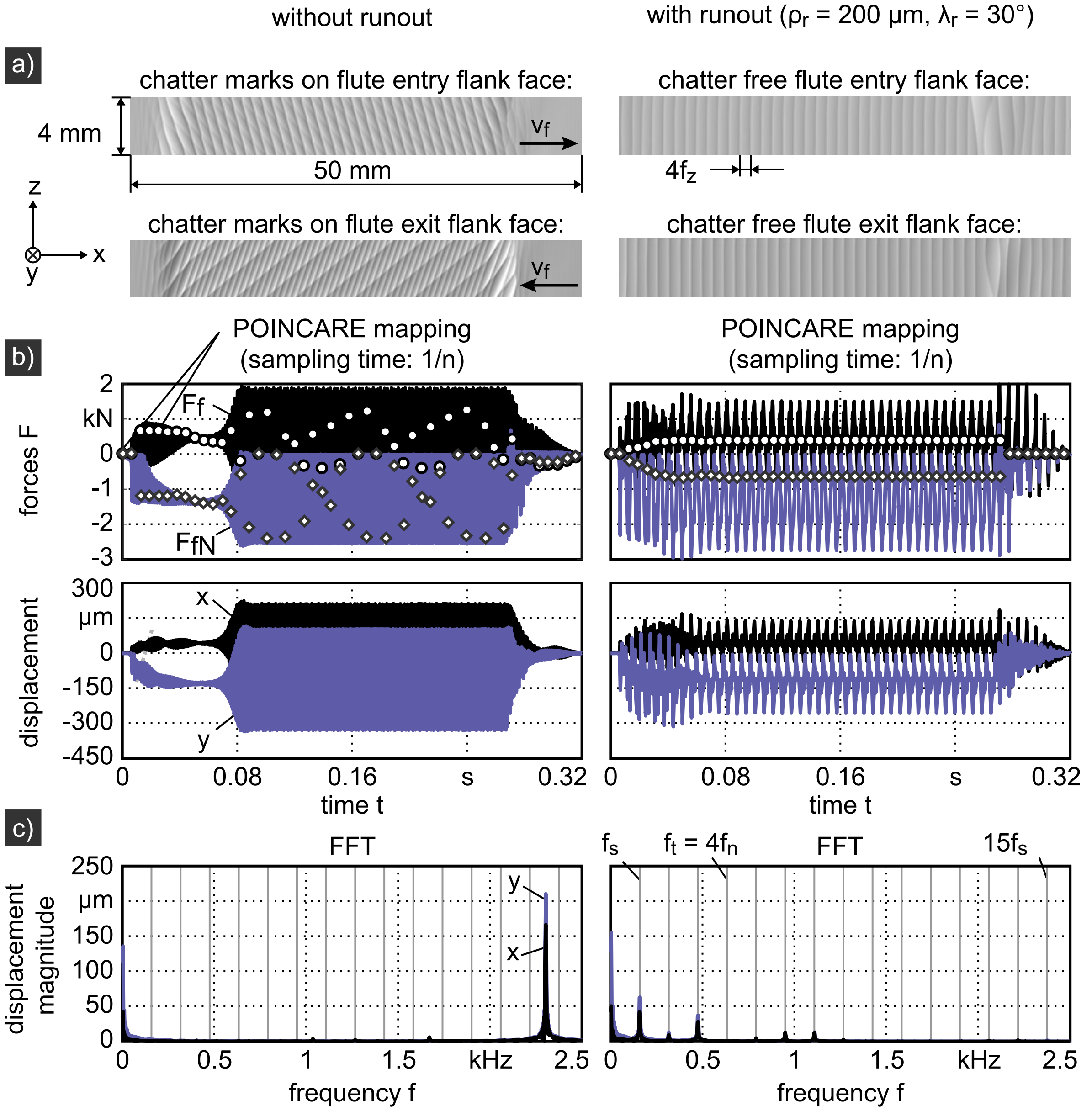

tool diameter:	D = 20 mm	discretization:	N_k = 720, N_z = 60
helix angle:	δ = 30°	spindle speed	n = 9,500 min^{-1}
corner radius:	R = 0 mm	tan. cutting force coeff.:	K_{tc} = 700 N/mm^2
number of teeth:	N_t = 4	rad. cutting force coeff.:	K_{rc} = 200 N/mm^2
radial depth of cut:	a_e = D	tan. edge coeff.:	K_{te} = 10 N/mm
axial depth of cut:	a_p = 4 mm	rad. edge coeff.:	K_{re} = 10 N/mm
feed per tooth:	f_z = 0.30 mm		

Gra/72846 ©IFW

Fig. 6.15: Comparison of the dynamical behavior of a tool in case of no runout and runout.

lation (Chapter 4.3). The increased a_e can be approximated as follows: $a_e \approx D + 2\rho_r = 20.4\,\text{mm}$. The upper diagrams in Fig. 6.15 b) show the feed and feed normal forces for the whole engagement time range. The maximum absolute force amplitudes for both processes are similar. However, it can be seen from the shape of the entire force curves that, in case of runout error, the maximum force amplitude is dominated by a single flute, as also visible in the machined flank surfaces. To emphasize that, despite the high amplitudes of the force signal in both cases, it can be detected that the process is stable in case of the runout error, the force signals are additionally represented as POINCARÉ maps, plotted as points in the force signal diagrams. The sampling time of the POINCARÉ maps corresponds to the time for one tool revolution 1/n. If the period of the force signals correspond to the tooth passing frequency f_t or the spindle frequency f_s, the POINCARÉ points have almost the same value, and thus, form a line. This is the case for the process with ρ_r = 200 µm. It means that f_t or f_s dominates the force signal, and not a chatter frequency. Thus, the process is stable. In accordance to this, it can be stated that if large vibration amplitudes occur but the machined surface has a regular pattern without chatter marks, the process can be classified as stable [Sté14]. For the process with no runout error, the POINCARÉ points have different values. This means that the signal is not dominated by f_t or a multiple of f_t, but rather a self-excited vibration. Thus, for the process with no runout, chatter vibrations cause an unstable process behavior.

In analogy to the simulated force signals, the simulated displacements, shown in the bottom diagrams in Fig. 6.15 b), leads again to similar maximum absolute amplitudes. In the case of no severe runout error, the distinction between a stable and unstable process can be made on the basis of the amplitude. However, this does not apply in case of high runout errors. Due to the dominance of a single cutting flute and the resulting high force amplitude, the displacement is correspondingly high. However, this results in forced vibrations and not as already mentioned chatter vibrations. This is also clear from the FFT of the displacement signals, as shown in Fig. 6.15 c). The chatter frequency in case of no runout corresponds to the 3rd eigenmode of the system (Table 6.5). Based on the comparison for this single operating point at $n = 9,500\ \text{min}^{-1}$, the results of the time-domain simulations are in line with the predicted stability with the SD method (Fig. 6.14).

Since the displacement for a tool with a severe runout error is almost always high due to forced vibrations, a direct comparison of the stability between a process with and without runout based on the maximum displacement amplitude is not expedient. Instead, the amplitude ratio metric r_{amp} is used (Chapter 5.2). On the basis of this procedure, two time-domain stability charts are predicted, as shown in Fig. 6.16. The spindle speed n and axial immersion a_p are discretized in $200\ \text{min}^{-1}$ and 1 mm steps, respectively. The upper diagram shows the predicted stability chart for ρ_r = 0 µm. The stability limit was set at an amplitude ratio of $r_{amp} = 2$. This delimitation is illustrated by the plotted contour line. For a direct comparison, the stability limit predicted with the SD method is also shown (represented by the dashed line, see Fig. 6.14). As can be seen, there is a good agreement between the stability limit derived from the SD method and time-domain simulation. The match can certainly be improved by reducing the increment for a_p and n in the time-domain simulation. Between $n = 16,000\ \text{min}^{-1}$ to $20,000\ \text{min}^{-1}$ high discrepancies arise. A possible cause is that for the time-domain simulation edge forces are taken into account, which can significantly increase or decrease stability [Cam03]. Due to the fact that the discrepancy for this spindle speed range occurs in both processes, it can be assumed that it is not caused by the runout error. Thus, the stability prediction with runout consideration yields the same result for both calculation methods.

For the process without runout, the highest values for r_{amp} are approximately 180. In comparison to that, the highest values for r_{amp} in case of runout range near 6. Thus, the transition between

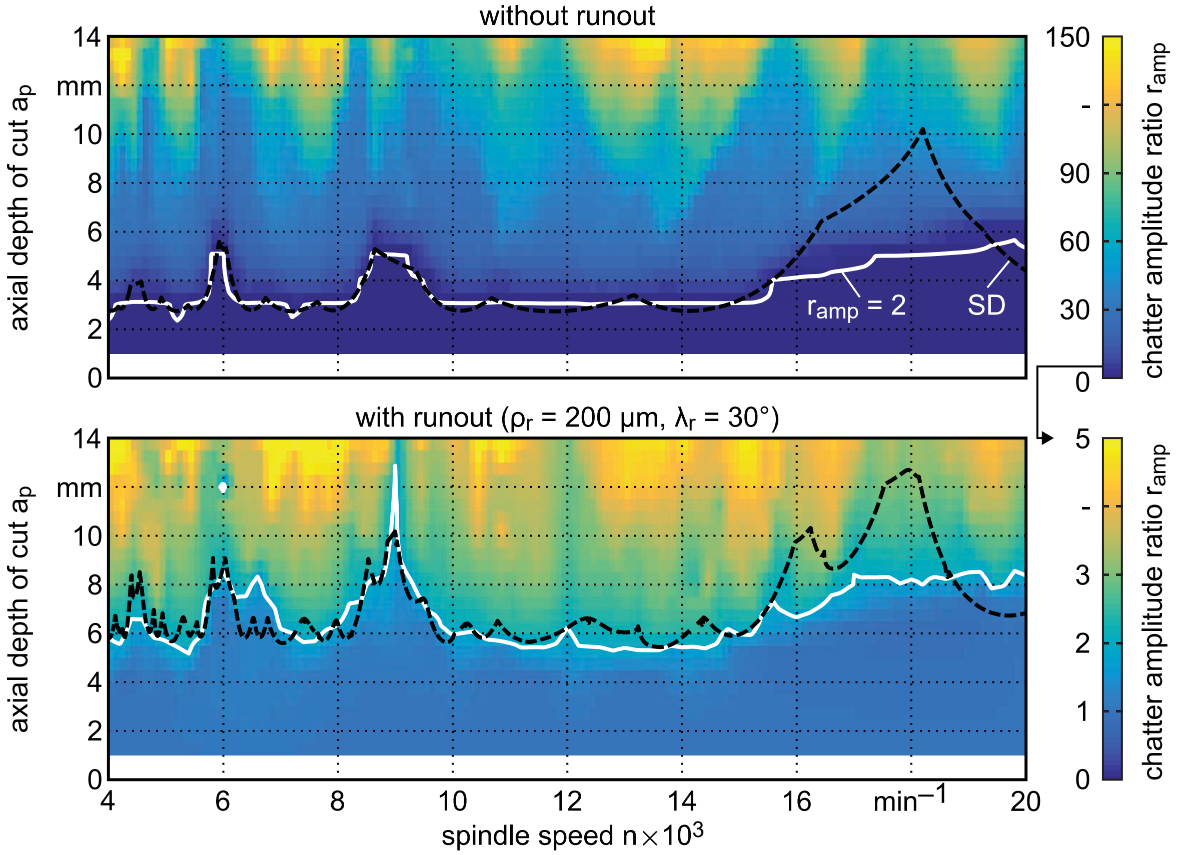

tool diameter:	D = 20 mm	discretization:	N_k = 720, N_z = 20
helix angle:	δ = 30°	tan. cutting force coeff.:	K_{tc} = 700 N/mm^2
corner radius:	R = 0 mm	rad. cutting force coeff.:	K_{rc} = 200 N/mm^2
number of teeth:	N_t = 4	tan. edge coeff.:	K_{te} = 10 N/mm
radial depth of cut:	a_e = D	rad. edge coeff.:	K_{re} = 10 N/mm
feed per tooth:	f_z = 0.30 mm		

Gra/72843 ©IFW

Fig. 6.16: Evaluation of the runout effect on stability based on time-domain simulations (dashed lines represent SD stability for comparison).

a stable and unstable process seems comparatively less distinctive. The reason for this lower values are the large periodic forces. Due to this fact the values for $A_{stat,f}$ increase, and thus, r_{amp} decreases, as it follows from Eq. 5.33. However, it can be seen that the predicted stability limit based on the time-domain simulation is higher for most spindle speeds compared to process without runout error. This illustrates that the regenerative effect in the case of high values for radial runout ρ_r may possibly be mitigated.

From the investigation of the previous and current section, it can be summarized that certain values for ΔR and ρ_r may lead to an increase of process stability. However, in the next section it will be explained to what extent even low values of these geometrical tool attributes can affect the surface quality.

6.2.3 Influence on Surface Deformation

With the time-domain simulation (Chapter 5.2), the shape of the surface deformation error of the flank face can be estimated based on the simulated process forces. The concept of this method will be explained using the example shown in Fig. 6.17.

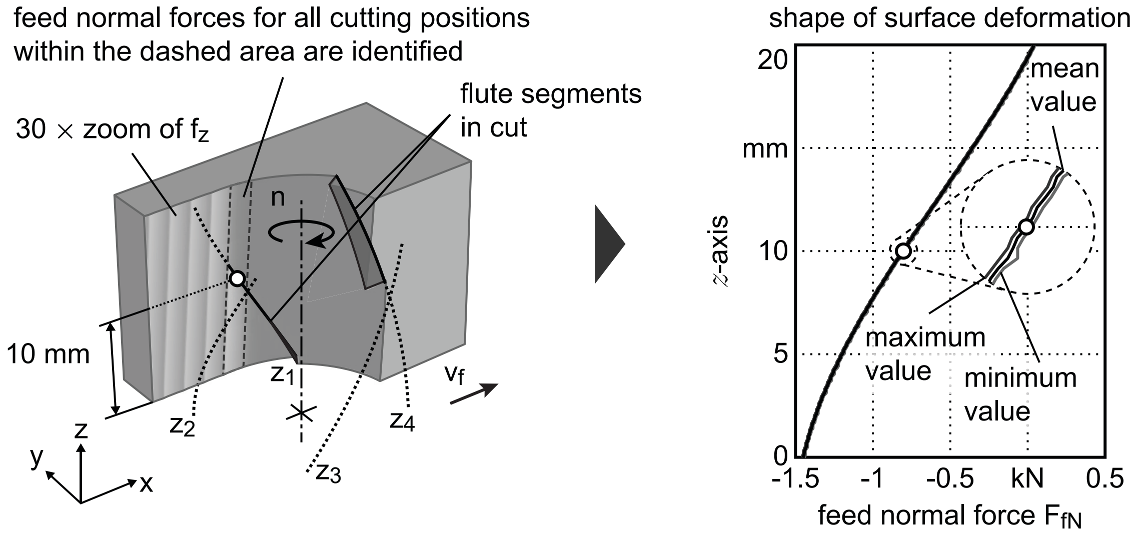
feed normal forces for all cutting positions
within the dashed area are identified
30 × zoom of f_z
flute segments
in cut
n
10 mm
z_1
z_2
z_3
z_4
v_f
z
y
x
shape of surface deformation
20
mm
10
5
0
z-axis
mean
value
maximum
value
minimum
value
-1.5
-1
-0.5
kN
0.5
feed normal force F_{fN}

radial depth of cut:	a_e = 10 mm	process:	up milling
axial depth of cut:	a_p = 20 mm	tool:	D = 20 mm, N_t = 4, δ = 30°
cutting speed:	v_c = 20.4 m/min	discretization:	N_k = 3,600, N_z = 200
feed per tooth:	f_z = 0.076 mm		

Gra/72812 ©IFW

Fig. 6.17: Example of the acting feed normal forces during the generation of the final surface (cutting and edge coefficients from Fig. 6.1, setup from [Fuj77]).

The data from Fujii is used due to the fact that the he made experimental investigations for different radial depth of cuts a_p as well as for up- and down-milling, while keeping all other parameters constant. The left picture shows the moment in which the final surface is cut at the position marked by a circle ($z = 10$ mm). It can be seen here that, for this moment, the teeth z_1 and z_4 are engaged. The resulting feed normal force is attributed to the current z-position. For each position in z-direction, the resulting feed normal forces withing the marked section (dashed lines) need to be identified. If all cutting edges have the same angular distance from each other, the length of this section corresponds approximately to f_z. In this example, it starts with the entrance of tooth z_1 and ends at the position of the entrance of the following tooth z_2. With the presented method for milling force calculation in Chapter 4, the corresponding discrete feed normal force F_{fN} along the z-axis can be associated with this section. The diagram on the right in Fig. 6.17 shows the resulting feed normal forces along the z-axis. Besides the mean value, the maximum and minimum values are also shown. The variation range between the maximum and minimum values for end mills with an ordinary geometric shape (equal tooth pitch, constant helix angle etc.) is rather small. The course of the curves illustrate the changing immersion conditions. With increasing axial position, the influence of the preceding flute decreases, leading to smaller values for the forces. This shape of the feed normal forces shows similarities to the shape of the deflection (see deflection in case of up-milling with low immersion in Fig. 2.11).

On the basis of the experimental data from [Fuj77], the similarities between the surface deformation error and the shape of the force curve, which result from the acting feed normal forces during the generation of the final surface, are investigated, as shown in Fig. 6.18.

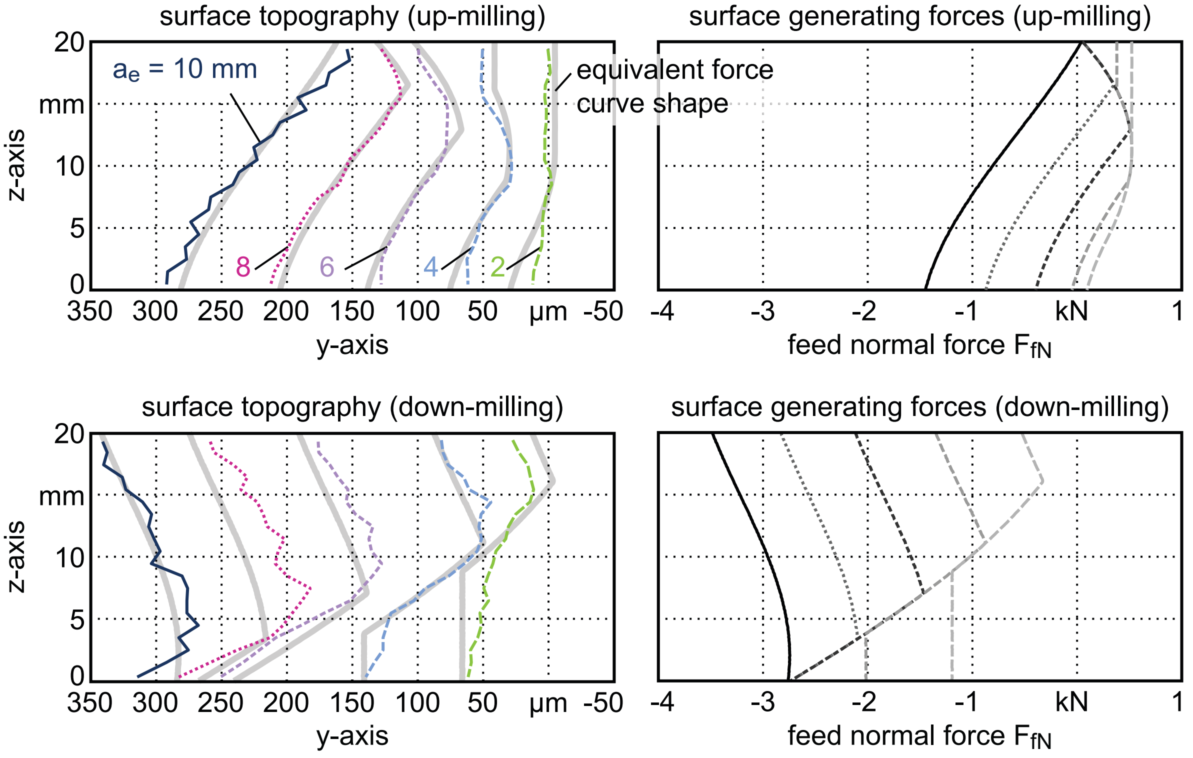

axial depth of cut: a_p = 20 mm
cutting speed: v_c = 20.4 m/min
feed per tooth: f_z = 0.076 mm
tool: D = 20 mm, N_t = 4, δ = 30°
workpiece: steel (SS41)
machine: Enshu VF

Gra/72810 ©IFW

Fig. 6.18: Comparison between the shape of the acting feed normal forces during the generation of the final surface and the surface deformation error for up- and down-milling (cutting and edge coefficients from Fig. 6.1, experimental data from [Fuj77]).

Fujii measured the surface topography of the workpiece with a dial gauge [Fuj77]. The diagrams at the top show the results for up-milling and different axial immersion conditions. Positive values for the y-axis correspond to a decrease in the material removal. As shown in the top left diagram, a significant increase of the surface deformation error occurs for a_e = 10 mm in comparison to a_e = 2 mm. The top right diagram shows the simulated acting feed normal forces during the generation of the final surface. Since the coefficients for the steel material SS41 cannot be derived from [Fuj77], cutting and edge coefficients as given in Fig. 6.1 were used for the simulation of the acting feed normal forces during the generation of the final surface. While a continuous curve is obtained for a_e = 10 mm, a discontinuity can be observed at lower radial immersions. In the case of low radial immersions, only one cutting edge is engaged. At high axial positions, the cutting flute is out of cut in the lower axial region and leads to the seen course [Des12]. The shapes of the acting feed normal forces during the generation of the final surface clearly correspond to the shapes of the measured surface deformations. For the sake of clarity, the force curves have been added to the surface topography diagram as thick gray lines. The same result is obtained in down-milling, as shown in the lower diagrams.

Consequently, this method enables the prediction of the shape deformation of the machined flank face. Thus, the influence of the end mill geometry on surface deformation error can be predicted, as shown in Fig. 6.19.

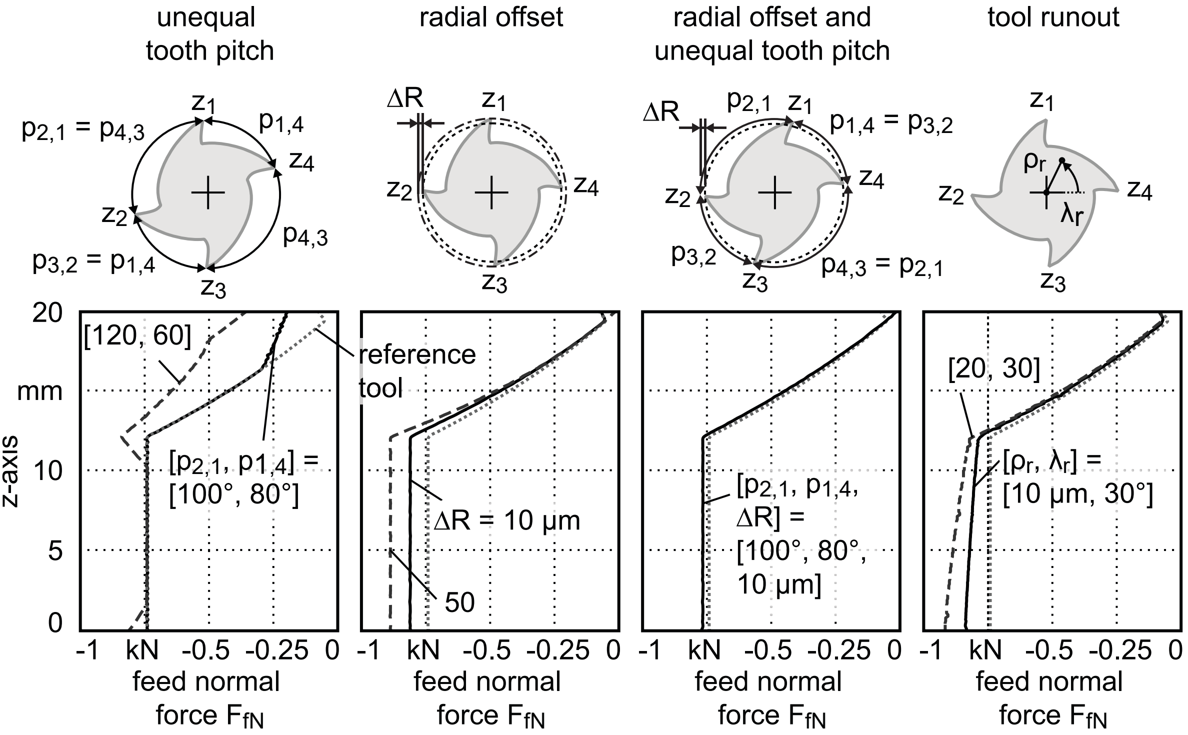

radial depth of cut: a_e = 1 mm
axial depth of cut: a_p = 20 mm
feed per tooth: f_z = 0.076 mm
process: down-milling
reference tool: D = 20 mm, N_t = 4, δ = 30°

Gra/72834 ©IFW

Fig. 6.19: Influence of the end mill geometry on the resulting feed normal forces during the generation of the final surface (cutting and edge coefficients from Fig. 6.1, setup from [Fuj77]).

The first diagram on the left shows the impact of an unequal tooth pitch. For a direct comparison, the dotted line in all diagrams represents the reference tool from [Fuj77]. As it can be seen, an unequal tooth pitch leads to an increased deflection at higher axial positions. The reason for this is that due to the reduced tooth pitch $p_{1,4} = 80^\circ$ (straight line), an earlier entry of the following cutting flute into the workpiece occurs. At the same time, the increased tooth pitch $p_{2,1} = 100^\circ$ leads to a later entry of the following cutting flute. The resulting curve shows the mean value, which is increased in comparison to the reference tool. The dashed lines have an even higher difference for the tooth pitches. As a result, the above-described effect is significantly increased and becomes even visible for small axial positions. An unequal tooth pitch leads not only to increased acting feed normal forces during the generation of the final surface. The kinematic roughness R_{th} also increased due to the varying feed per tooth values, as described in Eq. 2.9. Based on Eq. 2.9, for the reference tool and the given process parameters R_{th} equals 0.07 μm.

In analogy to this, R_{th} for end mills with an unequal tooth pitch can be calculated as follows:

$$R_{th} = \frac{D - \sqrt{D^2 - \left(\frac{\max(\mathbf{p})}{2\pi} N_t f_z\right)^2}}{2} \tag{6.8}$$

For the end mill with an unequal tooth pitch of [100°, 80°], $R_{th} = 0.09\,\mu m$. In case of [120°, 60°], R_{th} increases to 0.13 µm.

The next diagram shows the effect of the radial offset ΔR on the acting feed normal forces during the generation of the final surface. Due to the offset, teeth z_1 and z_3 need to remove more material which causes an increase of the feed normal forces. In case of $\Delta R = 50\,\mu m$, z_2 and z_4 are completely out of cut for the small radial immersion of $a_e = 1$ mm. Thus, only two flutes are in cut and consequently the feed per tooth is doubled. Therefore, the calculation of the kinematic roughness requires a case distinction:

$$R_{th} = \begin{cases} \dfrac{D - \sqrt{D^2 - 4f_z^2}}{2} & \text{, if} \quad \Delta R > \dfrac{D - \sqrt{D^2 - 4f_z^2}}{2} \\ \dfrac{D}{2}\left(1 - \sqrt{1 - \left(\dfrac{f_z^2 + D\Delta R - \Delta R^2}{Df_z}\right)^2}\right) & \text{, otherwise} \end{cases} \tag{6.9}$$

The first case is valid if the recessed flutes do not contribute to the machining of the final surface. Otherwise, the second case applies. For both radial offset values the first case applies. Thus, R_{th} does not depend on ΔR which leads to the same value for the kinematic roughness of 0.29 µm for $\Delta R = 10\,\mu m$ as well as for 50 µm. Moreover, the radial offset causes a kinematic roughness which is more than four times higher compared to the reference tool.

The third diagram shows how a radial offset and an unequal tooth pitch can be combined in order to decrease the absolute value of the acting feed normal forces during the generation of the final surface. A similar shape as for the reference tool can be obtained. For the calculation of R_{th}, it is sufficient to apply the first case of Eq. 6.9. Thus, the same R_{th} results as for the tool geometries with recessed flutes and uniform tooth pitch ($R_{th} = 0.29\,\mu m$). This end mill geometry corresponds to the hybrid tool geometry and will be further investigated in Chapter 7 on the basis of experimental data.

In the last diagram, the effect of tool runout on the acting F_{fN} during the generation of the final surface is shown. As described in Chapter 4.3, the immersion conditions change along z-axis. For the shown case, this leads to tilted increase of the acting feed normal forces during the generation of the final surface at lower axial positions. Furthermore, as mentioned in Chapter 4.3, this also changes R_{th} and may superimpose the influence of the end mill geometry.

7 Experimental Evaluation

In the following, experimental investigations are carried out with the new tool concept with different values for the radial offset ΔR. For comparison purposes, the investigations also include tools with chamfered flutes and without chamfered flutes (”sharp” cutting edges). Besides the chamfers and the radial offset, all other geometric attributes are the same for all used tools, as listed in Table 7.1

Table 7.1: Mutual geometric attributes of the end mills, which will be used. Tools are not coated.

cutting length:	l_2	= 26 mm
total length:	l_4	= 92 mm
tool diameter:	D	= 20 mm
number of teeth:	N_t	= 4
clearance angle:	α	= 14°
rake angle:	γ	= 14°
corner radius:	R	= 1 mm
helix angle:	δ	= 30°
tooth pitch:	$\mathbf{p}$	= [80°, 100°]
chamfer width (roughing and hybrid tool):	b_f	= 200 µm
chamfer angle (roughing and hybrid tool):	α_f	= 1°

To balance the load between the flutes of the hybrid tool in case of $\Delta R = 10$ µm, an unequal tooth pitch $\mathbf{p} \approx [80^\circ, 100^\circ]$ based on Eq. 6.6 was selected ($f_z = 0.12$ mm and $N_t = 4$). With increasing values for ΔR, the differences of the tooth pitches increase as well. However, it is not considered by Eq. 6.6 that the load on the roughing flutes may rise due to the chamfers. For this reason, the mentioned tooth pitch is used for all hybrid tools.

The first part of this Chapter focuses on the experimental identification of the input variables, cutting force coefficients and modal parameters, for the process stability calculation. Following, the machining process is analyzed based on experimental and predicted stability charts. Finally, the machined surface quality between the different tools is compared. In this context, the influence of the chamfer on the heat development in the workpiece is also investigated. As discussed in Chapter 2, depending on the aluminum alloy high temperatures can have a negative effect on the material properties.

7.1 Preliminary Experiments

First, an overall comparison between the three different tools (hybrid tool, chamfered cutting edges and sharp cutting edges) regarding the resulting process forces is performed. Afterwards, based on the results from Chapter 6.1, cutting force and edge force coefficients are identified with the instantaneous cutting force method and under consideration of the trochoidal flute path and the runout error influence. The effect of cutting speed on the coefficients is also considered. Furthermore, an experimental modal analysis is carried out to identify the dynamic properties of the system. In order to include the influence of the runout error in the stability prediction, process forces are measured for the tools that are actually used in the stability analysis. In order to keep the same conditions during the stability tests, the clamping between the tool and the toolholder must not be changed after these cutting tests.

7.1.1 Process Force Comparison with Sharp and Chamfered Tools

Sellmeier showed that if the chamfer width b_f and feed per tooth f_z are increased, the specific edge coefficients $K_{.e}$ increase significantly as well [Sel12a, p. 84]. A comparatively minor influence on the specific cutting coefficients $K_{.c}$ was also observed. Fig. 7.1 shows investigations for a larger feed per tooth range and including the new tool concept.

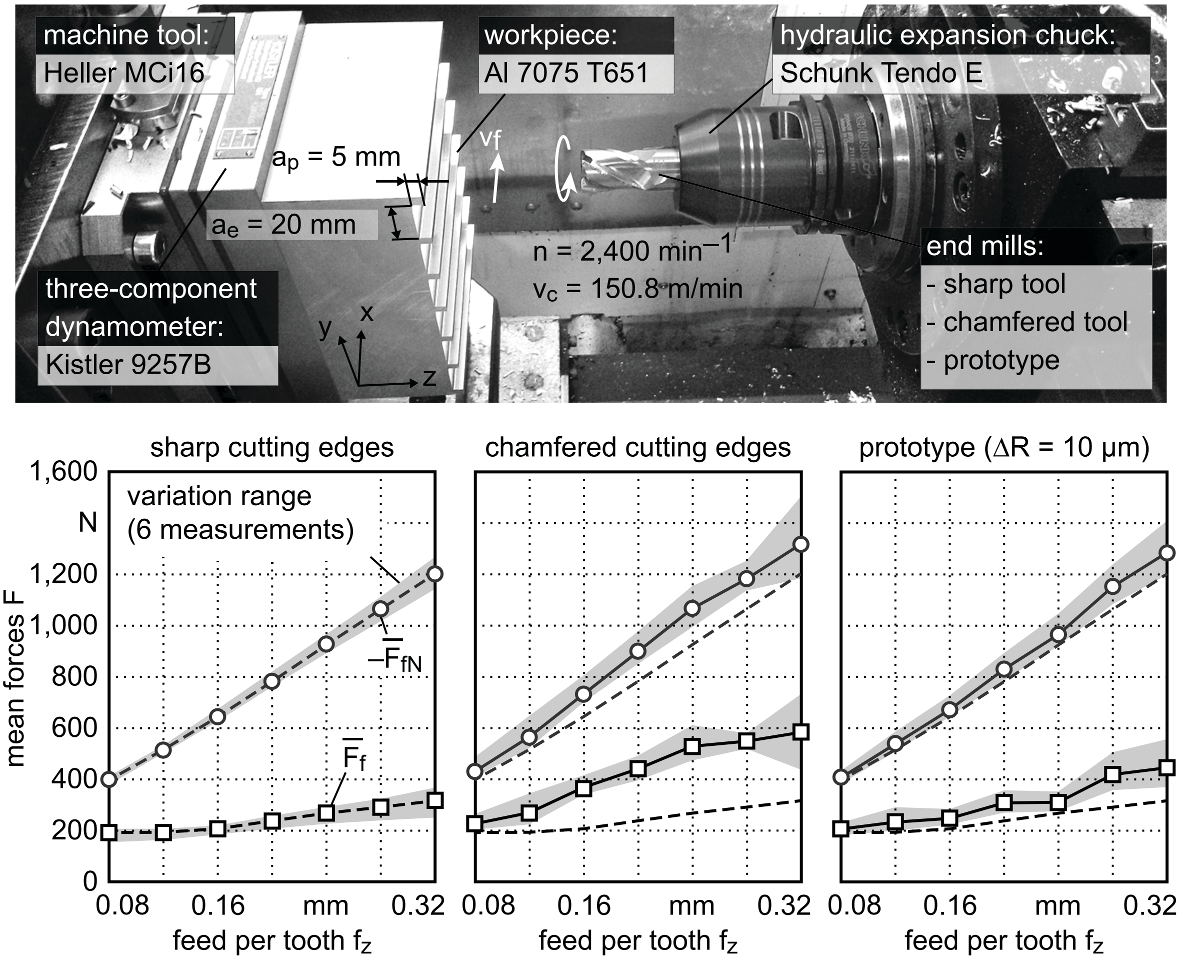

Gra/72815 ©IFW

Fig. 7.1: Influence of new tool concept on the mean values of the feed and feed normal force for full immersion milling tests in dependence of f_z.

The chamfer width b_f and the radial offset ΔR were determined using a contour measuring device (Perthometer Concept Contour PCV200) and an optical measuring machine (Walter Helicheck), respectively. Forces were measured with a three-component dynamometer. On the left diagram the arithmetic mean values of the feed and feed normal force $\bar{F}_f$ and $\bar{F}_{fN}$, respectively, for the tool with sharp cutting edges are shown. Six experiments were conducted at each feed per tooth. The feed distance was l_f = 100 mm for each experiment and corresponds to the length of the workpiece. The dashed lines with round markers correspond to the mean values of $\bar{F}_f$ and $\bar{F}_{fN}$ from the six experiments. The gray area corresponds to the deviation range. As expected, the forces increase linearly with f_z and with only small deviations.

A comparison of the process forces between the tool with sharp cutting edges (dashed lines) and chamfered cutting edges (solid lines) is given in the middle diagram. The distance from the ordinate and, in particular, the slope of $\bar{F}_f$ are significantly higher in case of chamfered cutting edges. For full immersion milling tests, the following convenient relationship between the mean process forces and the coefficients applies [Alt00, p. 46]:

$$\begin{aligned}\bar{F}_f &= -\frac{N_t a_p}{4} K_{rc} f_z - \frac{N_t a_p}{\pi} K_{re} \\ \bar{F}_{fN} &= +\frac{N_t a_p}{4} K_{tc} f_z - \frac{N_t a_p}{\pi} K_{te}\end{aligned} \tag{7.1}$$

For the sake of simplicity, influences such as non uniform tooth pitches are not considered at this point. In the case of high feed rates, the average value of the feed force is almost doubled. Furthermore, the chamfered cutting edges cause a higher variation range of the mean forces. In the event that the process is stable in the case of both cutting edge geometries, the use of tools with chamfered cutting edges results in an increased power consumption and thus in a reduced efficiency. The mean forces for a hybrid tool with a radial offset of $\Delta R = 10\ \mu m$ are shown in the right diagram of Fig. 7.1. The values of the mean forces range between the values of the tool with sharp and chamfered cutting edges. In particular, $\bar{F}_f$ is significantly lower than for the tool that has only chamfered edges. Consequently, the required power consumption is lower.

On the basis of these results, it is clear that the increased forces are due to a contact between the chamfer and the workpiece. No regenerative chatter or large vibrations occurred in all tests that were carried out. This makes clear that a contact between the chamfer and the workpiece also occurs when no large vibrations arise during the machining process. This can also be proven by similar simulations as already carried out in Chapter 6.1.5. Fig. 7.2 a) shows the indentation area A^*_{pd} in case of no vibrations.

A contact occurs between the rear part of the chamfer and the workpiece along the whole immersion range, similar to the detailed view in Fig. 6.7 at $\varphi = 161°$. If f_z increases, A^*_{pd} obviously increases significantly. Fig. 7.2 b) shows for this case how the damping forces contribute to the forces in feed and feed normal direction. For $f_z = 0.32$ mm, the mean value of the damping force in feed direction $F_{pd,f}$ is four times higher than the damping force in feed normal direction $F_{pd,fN}$. This higher increase in feed direction corresponds to the experimental results for the tool with chamfered cutting edges in Fig. 7.1. The increased damping at high feed rates also coincides with the experience that an unstable process often becomes stable if feed rate is increased. It must be noted that the simulation was carried out for a tool with a diameter of $D = 10$ mm. In case of $D = 20$ mm no immersion between the chamfered cutting edge and the workpiece occurs in the simulation. It can be assumed that the heat-induced expansion of the material as well as vibrations with small amplitudes are already sufficient for a contact. However, this is not taken into account during the simulation. The influence of the chamfer on heat development in the workpiece will be discussed in the experimental results.

In addition to the high forces, a further negative effect of the tool with chamfered cutting edges appeared at the highest feed rate, as shown in Fig. 7.3.

In two out of six experiments at $f_z = 0.32$ mm, severe smearing occurred. For such high feed

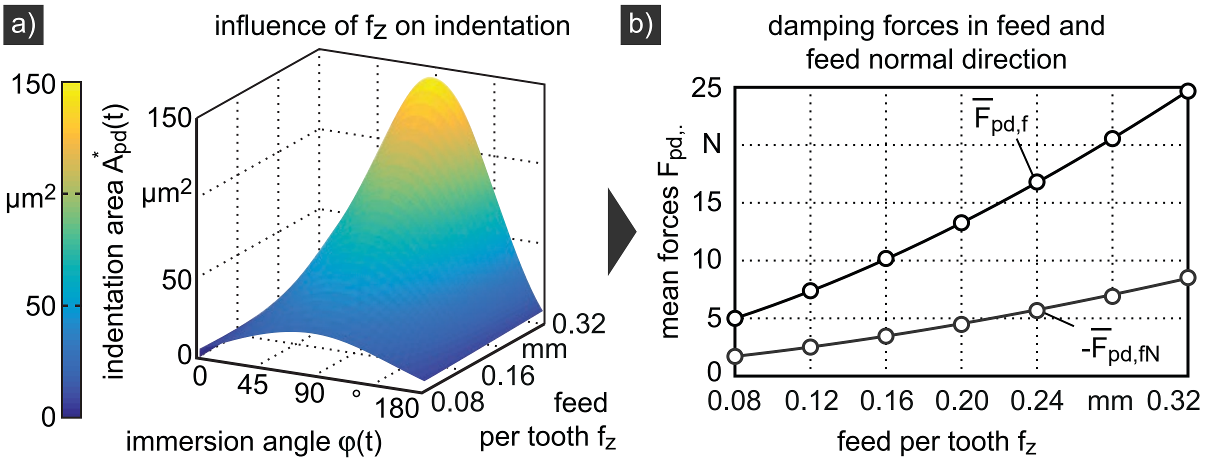

tool diameter:	D = 10 mm	process:	slot milling
helix angle:	δ = 0°	cutting speed:	v_c = 150.8 m/min
corner radius:	R = 0 mm	radial depth of cut:	a_e = D
chamfer width:	b_f = 0.2 mm	axial depth of cut:	a_p = 5 mm
chamfer angle:	α_f = 1°	process damping coeff:	K_{pd} = 80,000 N/mm³
clearance angle:	α = 14°	coefficient of friction:	μ = 0.3

Gra/72825 ©IFW

Fig. 7.2: Simulation of the influence of feed per tooth f_z on damping forces in case of no vibrations.

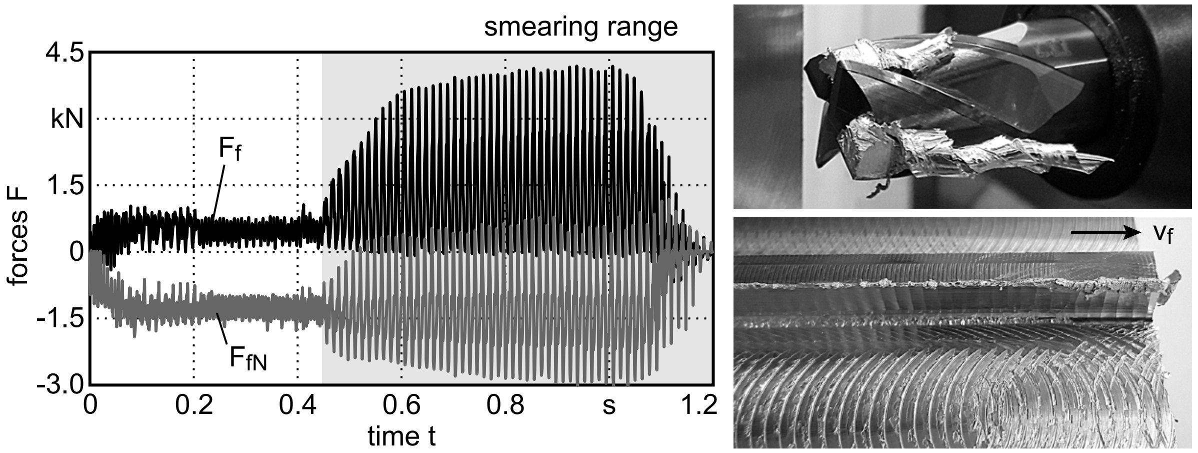

radial depth of cut:	a_e = 20 mm	process:	slot milling
axial depth of cut:	a_p = 5 mm	tool:	chamfered cutting edges
spindle speed:	n = 2,400 min^{-1}	workpiece:	Al 7075 T651
cutting speed:	v_c = 150.8 m/min	machine:	Heller MCi16
feed per tooth:	f_z = 0.32 mm		

Gra/72817 ©IFW

Fig. 7.3: Smearing caused by the end mill with chamfered cutting edges at high feed per tooth.

rates, the effective clearance angle α_{eff} can become negative in the area of the chamfer. Thus, the heat induced into the workpiece due to its contact with the chamfer increases noticeably. In such a case, the chamfer angle α_f must be increased. In addition to strong smearing traces at the machined surface, the workpiece material adhered on the tool. As shown in the diagram, forces increased abruptly, similar to chatter occurrence, at the beginning of the smearing after a feed distance of approximately 37 mm.

In summary, these investigations already show the first advantages of the new tool concept. The process forces are lower compared to the tool with chamfered cutting edges. As a result, the heat generation as well as the required power is also lower. This in turn can reduce the incidence of smearing and increase productivity, respectively.

7.1.2 Identification of Cutting Force Coefficients

Further process force experiments are carried out for the semi-empirical determination of the specific cutting and edge coefficients, which are necessary for the stability prediction. With the knowledge gained in the previous section, the following process force tests were designed to reduce as many occurring disturbances as possible. The goal is to find out, if under these conditions the same cutting coefficients (K_{tc}, K_{rc} and K_{ac}) can be used for stability prediction for all tools or if the chamfer also contributes to a change of the cutting forces. Fig. 7.4 shows the test setup. The image on the left shows the workpiece before the experiments are performed.

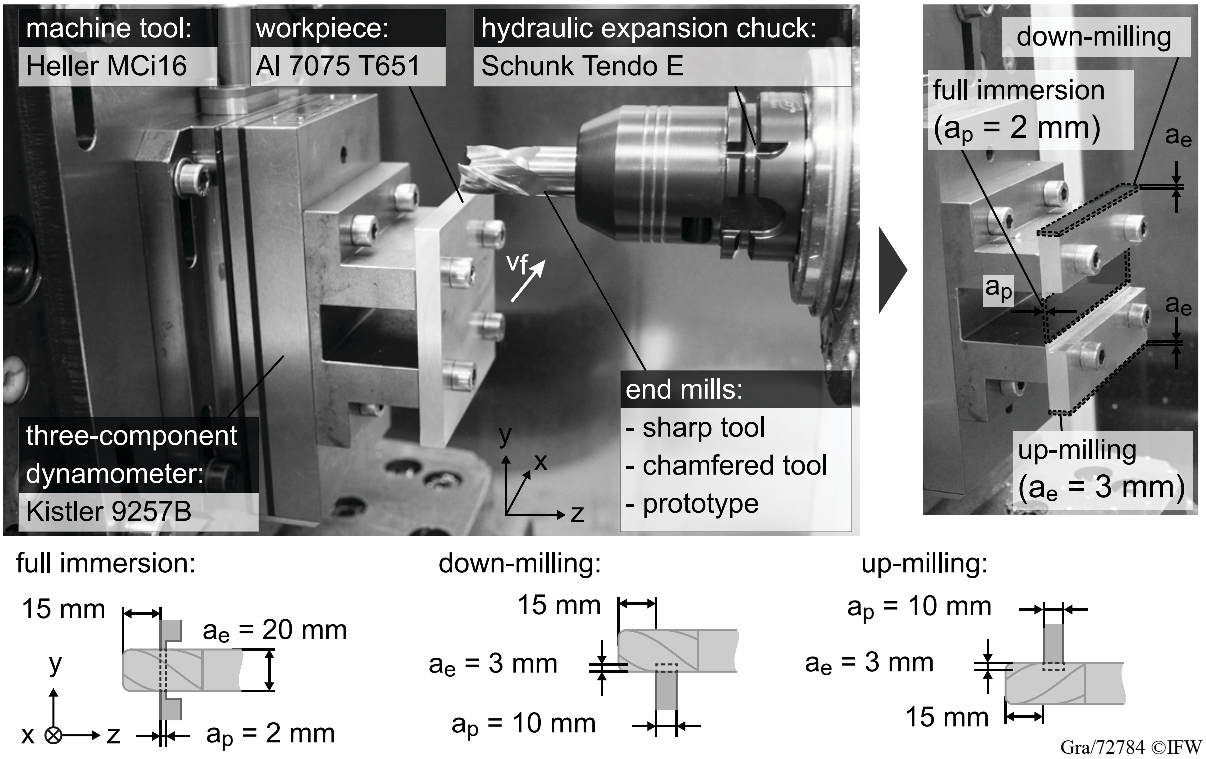
machine tool:
Heller MCi16
workpiece:
Al 7075 T651
hydraulic expansion chuck:
Schunk Tendo E
vf
three-component dynamometer:
Kistler 9257B
y
x
z
end mills:
- sharp tool
- chamfered tool
- prototype
down-milling
full immersion
(a_p = 2 mm)
a_e
a_p
a_e
up-milling
(a_e = 3 mm)
full immersion:
15 mm
a_e = 20 mm
y
x
z
a_p = 2 mm
down-milling:
15 mm
a_e = 3 mm
a_p = 10 mm
up-milling:
a_p = 10 mm
a_e = 3 mm
15 mm

Gra/72784 ©IFW

Fig. 7.4: Experimental setup for the identification of the specific cutting and edge coefficients.

The workpiece is mounted on a fixture to shift the height at which the end mill is in cut by 15 mm in z-direction. This reduces the effective cantilever length of the tool, thereby minimizing tool deflection deviations. Furthermore, material is removed in the center of the workpiece until a workpiece thickness of 2 mm is reached. In the next step, the actual milling test is performed with an axial immersion of $a_p = 2$ mm. Without the axial shift, the corner radius $R = 1$ mm would have a notable influence on the process forces in case of such a low axial immersion due to a decrease of the cutting speed ($v_c = \pi Dn$). This will be discussed in detail in the following section. However, due to the shift in in the tool axis direction, the corner edge radius is moved out from the cutting zone. Furthermore, the lower axial immersion in case of full immersion minimizes the risk of smearing, as it occurred in case of chamfered cutting edges (Fig. 7.3). The same workpiece is used for up- and down-milling. Tests and experiments are carried out with the same strategy of shifting the end mill by 15 mm in z-direction. In case of up- and down-milling, as shown in Chapter 6.1.2, both the ICFM and the ACFM predict values for the specific cutting and edge coefficients with considerable deviations. Therefore, it will be analyzed if the described method for process force measurement leads to an improved agreement.

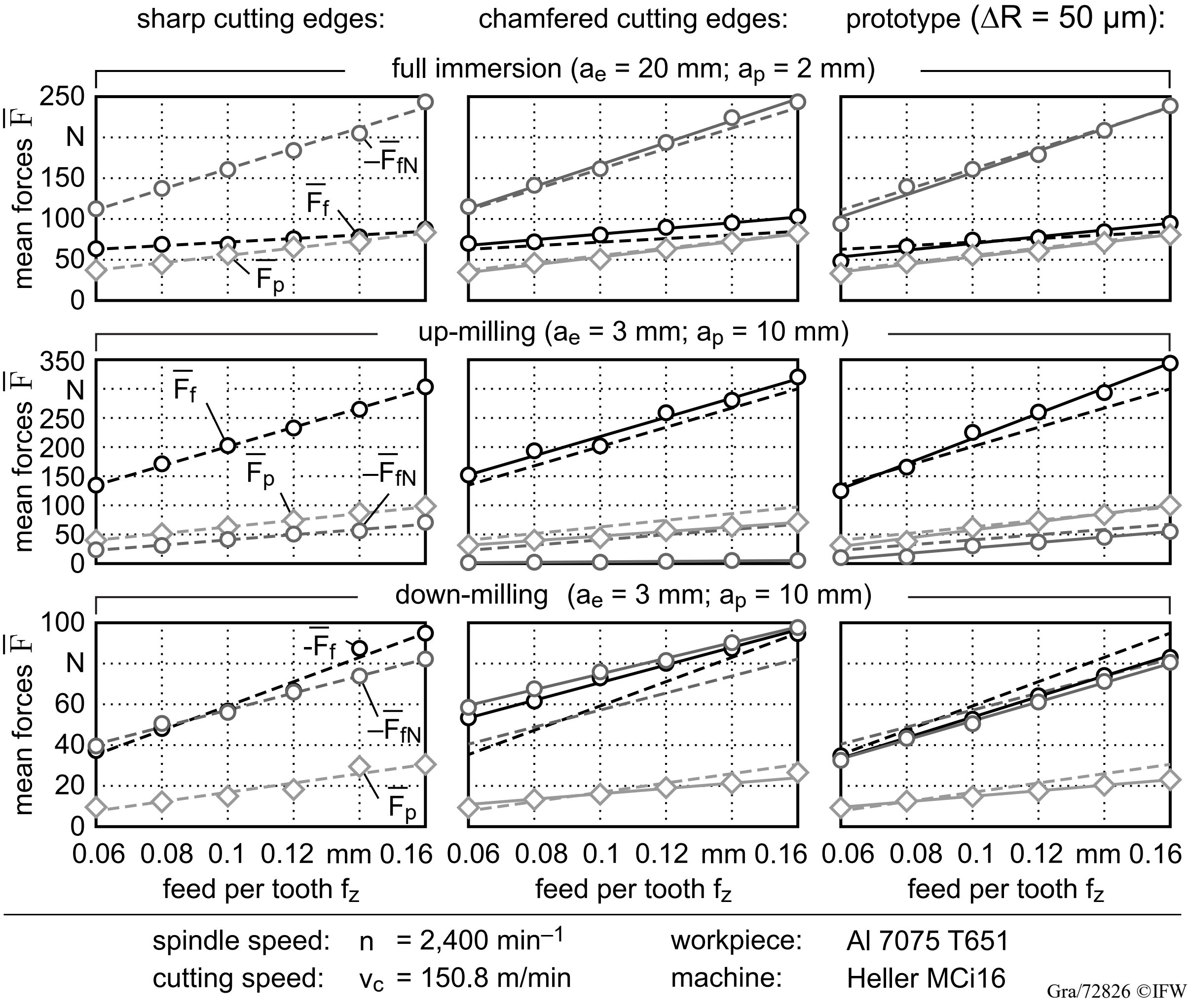

Fig. 7.5: Comparison of mean forces for full immersion, up- and down-milling for increasing values of f_z.

The mean values of the process forces for all experiments carried out are shown in Fig. 7.5. Compared to the previous tests, the feed range was shifted to smaller values. This also contributes to a reduction of thermally induced influences on the process forces. Furthermore, in order to obtain further findings regarding the influence of the radial offset ΔR on the process forces, a tool with a higher offset was used. A linear slope for all force components could be achieved for all tools and machining processes. Due to the chosen experimental setup, the differences between the three tools for full immersion tests are smaller compared to the results from Chapter 7.1.1. In particular, this can be seen by means of $\bar{F}_f$ for the end mill with chamfered cutting edges at f_z = 0.16 mm (compare Fig. 7.5 and Fig. 7.1). The slight deviations in the slopes are presumably due to different runout errors between the three end mills, as discussed in Chapter 6.1.2. In case of up- and down-milling with $a_e = 3$ mm, the differences between the tools increase. The influence of the runout error on the mean process forces increases with low immersions, as shown in Fig. 6.3. With a large helix angle δ and high values for a_p, the impact of the runout error can be reduced, which results from Eq. 4.37. As a result, the loading of the individual cutting edges is more uniform. Therefore, for up- and down-milling tests an axial depth of cut of $a_p = 10$ mm was chosen. However, this simultaneously causes an increase of tool deflection and may lead to a variation of the actual radial immersion (Chapter 6.2.3).

Supposing that thermal influences are negligible, it can be summarized that the deviating slopes between the tools and immersion conditions may be attributable to runout error and tool deflection. Thus, a closer look at the process forces for one revolution is considered, as shown in Fig. 7.6.

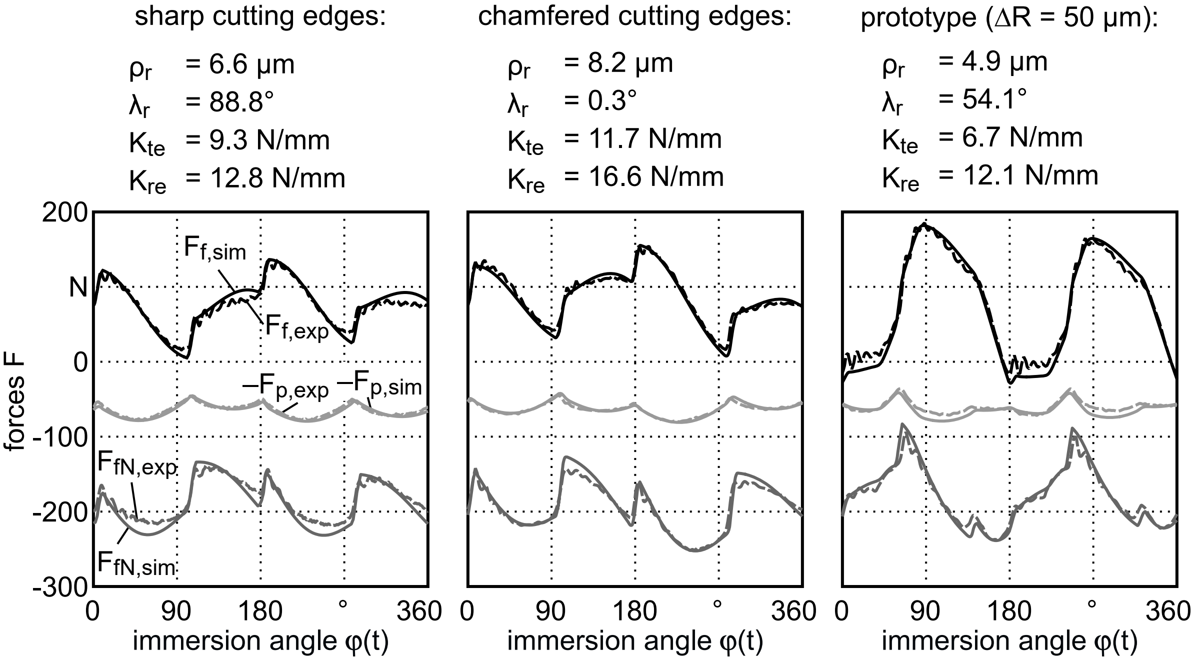

feed per tooth:	$f_z = 0.12$ mm	tan. cutting coeff.:	$K_{tc} = 673.3$ N/mm^2
radial depth of cut:	$a_e = 20$ mm	rad. cutting coeff.:	$K_{rc} = 169.1$ N/mm^2
axial depth of cut:	$a_p = 2$ mm	axial cutting coeff.:	$K_{ac} = 192.8$ N/mm^2
spindle speed:	$n = 2{,}400$ min^{-1}	axial edge coeff.:	$K_{ae} = 1.5$ N/mm
cutting speed:	$v_c = 150.8$ m/min	workpiece:	Al 7075 T651
process:	slot milling	machine:	Heller MCi16

Gra/72827 ©IFW

Fig. 7.6: Semi-empirical fit (solid lines) of the experimental determined process forces (dashed lines) by using the ICFM and the PSO algorithm.

The experimental process forces were averaged by means of several tool revolutions in order to reduce noise and other disturbances. The diagrams show the experimental and simulated data for full immersion and $f_z = 0.12$ mm. As mentioned in Chapter 6.1.2, the ACFM does not consider runout errors. Further difficulties arise for the consideration of the different immersion conditions of the flutes of the hybrid tool due to ΔR. Thus, the PSO algorithm is used to identify the specific cutting and edge coefficients based on the ICFM (Chapter 4.4). In the first step, the process forces for the tool with sharp cutting edges were fitted, as shown in the left diagram. The specific cutting

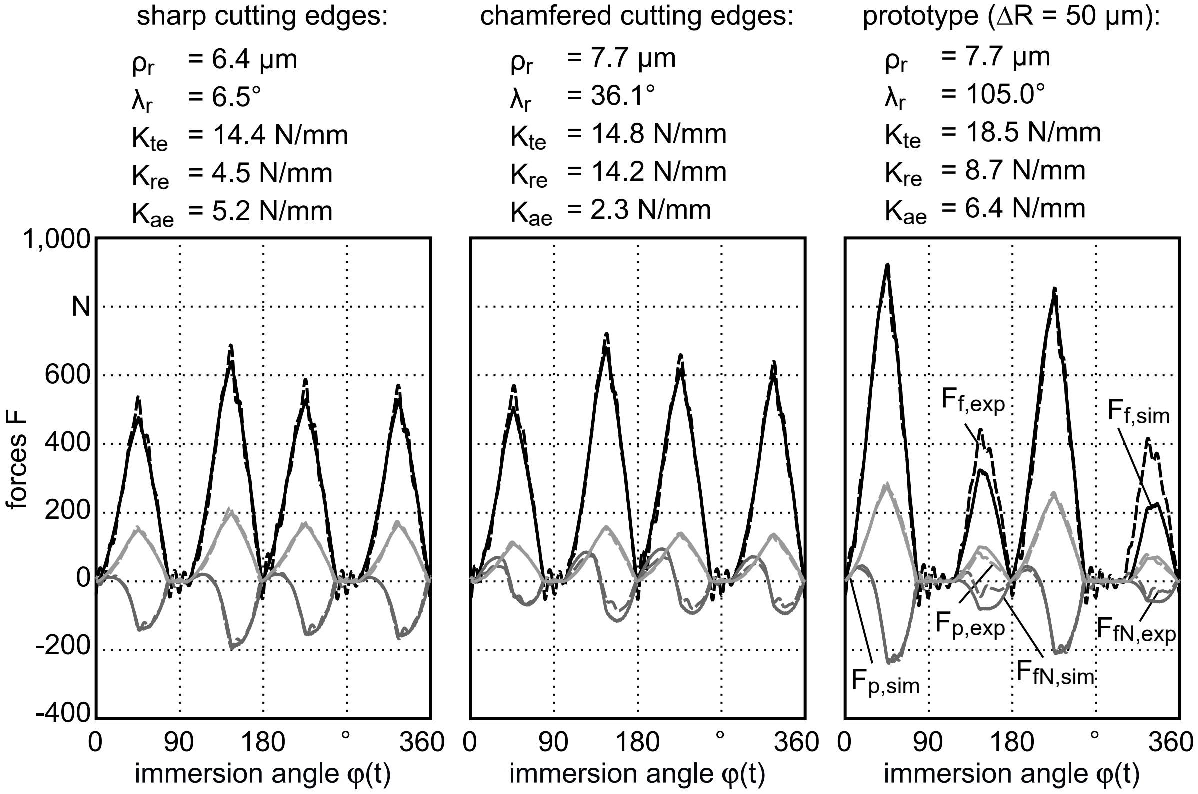

sharp cutting edges:
ρ_r = 6.4 µm
λ_r = 6.5°
K_{te} = 14.4 N/mm
K_{re} = 4.5 N/mm
K_{ae} = 5.2 N/mm

chamfered cutting edges:
ρ_r = 7.7 µm
λ_r = 36.1°
K_{te} = 14.8 N/mm
K_{re} = 14.2 N/mm
K_{ae} = 2.3 N/mm

prototype (ΔR = 50 µm):
ρ_r = 7.7 µm
λ_r = 105.0°
K_{te} = 18.5 N/mm
K_{re} = 8.7 N/mm
K_{ae} = 6.4 N/mm

feed per tooth:	f_z = 0.12 mm	tan. cutting coeff.:	K_{tc} = 673.3 N/mm^2
radial depth of cut:	a_e = 3 mm	rad. cutting coeff.:	K_{rc} = 169.1 N/mm^2
axial depth of cut:	a_p = 10 mm	axial cutting coeff.:	K_{ac} = 192.8 N/mm^2
spindle speed:	n = 2,400 min^{-1}	workpiece:	Al 7075 T651
cutting speed:	v_c = 150.8 m/min	machine:	Heller MCi16
process:	up-milling		

Gra/72828 ©IFW

Fig. 7.7: Semi-empirical fit (solid lines) of the experimental determined process forces (dashed lines) for up-milling tests.

coefficients and axial edge coefficient given in the process description result from this initial fit. The radial and tangential edge coefficients as well as the runout parameters are indicated above the diagram. A good agreement between the experimental and the simulated forces could be achieved for all force components. For the semi-empirical fit of the other tools, it was assumed that only the parameters specified above the diagrams vary. In order to minimize thermal influences on the forces caused by the contact of the chamfer with the workpiece, a low axial depth of cut was chosen. Thus, it is assumed that only the tangential and radial edge coefficients change due to the indentation between the chamfered cutting edge and the workpiece. With this approach, a well matched fit between experimental and simulated forces could be achieved for the tool with chamfered cutting edges and the hybrid tool. From these results it follows that the same cutting force coefficients can be used for the prediction of the stability for all tools.

The prediction of the surface topography is based on the surface generating forces, as described in Chapter 6.2.3. For this purpose, cutting force coefficients at low radial immersion a_e are analyzed. The cutting tests are carried out in analogy to the full immersion tests, as shown in Fig. 7.4. It is assumed that the friction conditions between the cutting edge and the workpiece material can

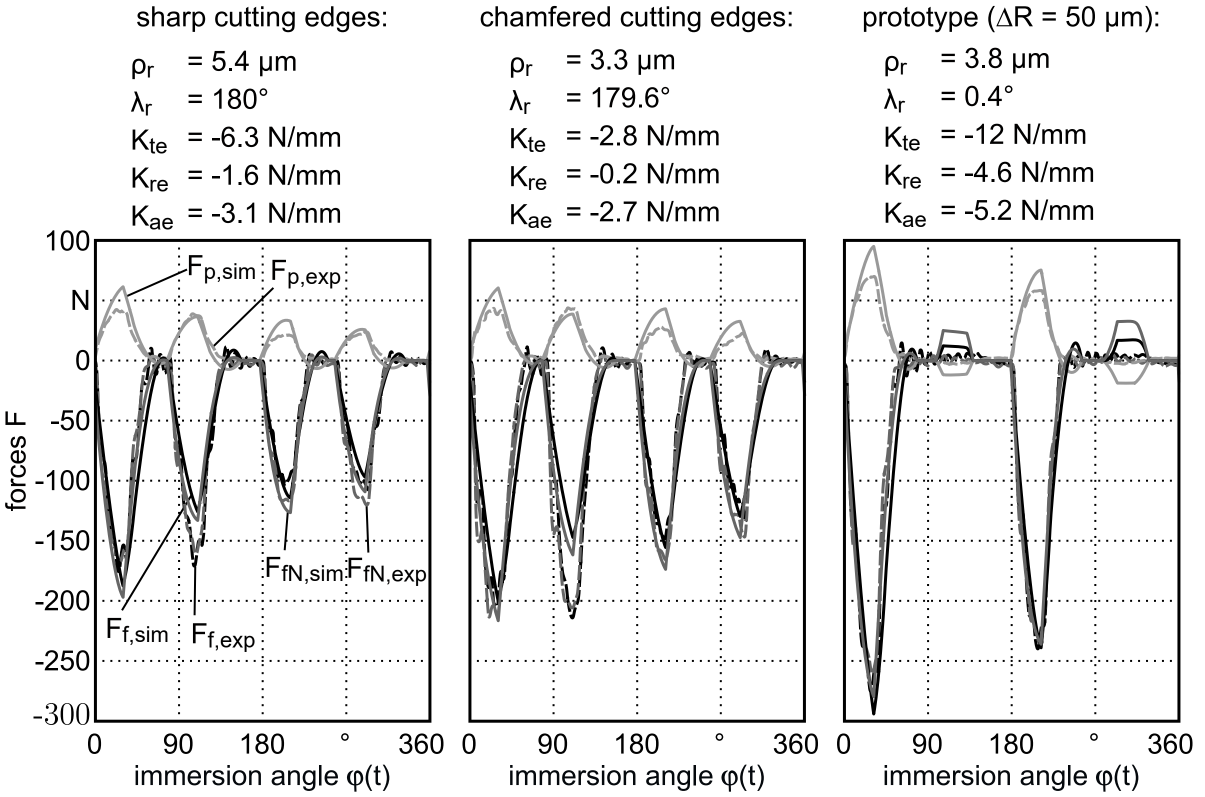

sharp cutting edges:
ρ_r = 5.4 µm
λ_r = 180°
K_{te} = -6.3 N/mm
K_{re} = -1.6 N/mm
K_{ae} = -3.1 N/mm

chamfered cutting edges:
ρ_r = 3.3 µm
λ_r = 179.6°
K_{te} = -2.8 N/mm
K_{re} = -0.2 N/mm
K_{ae} = -2.7 N/mm

prototype (ΔR = 50 µm):
ρ_r = 3.8 µm
λ_r = 0.4°
K_{te} = -12 N/mm
K_{re} = -4.6 N/mm
K_{ae} = -5.2 N/mm

feed per tooth: f_z = 0.12 mm
radial depth of cut: a_e = 3 mm
axial depth of cut: a_p = 10 mm
spindle speed: n = 2,400 min^{-1}
cutting speed: v_c = 150.8 m/min
process: up-milling

tan. cutting coeff.: K_{tc} = 673.3 N/mm^2
rad. cutting coeff.: K_{rc} = 169.1 N/mm^2
axial cutting coeff.: K_{ac} = 192.8 N/mm^2
workpiece: Al 7075 T651
machine: Heller MCi16

Gra/72848 ©IFW

Fig. 7.8: Semi-empirical fit (solid lines) of the experimental determined process forces (dashed lines) for down-milling tests.

change depending on the engagement position of the cutting edge. This assumption is based on the fact that for example the tangential edge coefficient shows for down- and up-milling operations in opposite directions to the feed velocity v_f. Thus, the edge coefficients are redetermined with the ICFM for up- and down-milling tests. For this identification step, the identified full immersion cutting coefficients are used. Within the individual test series, the tools were released from the holder and later re-clamped. In this respect, a new identification of the runout is necessary. While the runout location angle λ_r may differ from the identified values for the full immersion tests, the identified runout offset ρ_r should be expected to have similar values. A comparison between the experimental and fitted forces in case of up-milling is shown in Fig. 7.7. A good agreement between the experimentally determined and the fitted forces is achieved. With the selected low immersion conditions there is only a slight change in the direction of the force components to the feed direction. This has an obvious influence on the identified edge coefficients. Compared to the full immersion tests, the tangential cutting edge coefficient K_{te} increases significantly for all tested end mills. Furthermore, there is only a marginal difference in the identified values for ρ_r between full immersion and up-milling. This confirms the correctness of the identification of the runout error based on the ICFM and the PSO algorithm. Only one mentionable deviation between the experimental and fitted force curves results in the case of the hybrid tool (right diagram in Fig. 7.7). This difference is due to the increased contact of the chamfered cutting edge of the recessed flutes with the workpiece. Consequently, the absolute values of the experimental forces are greater. Thus, an individual value for the friction coefficient would have to be set for the different flutes.

The results for the down-milling tests are shown in Fig. 7.8. It can be seen that the identified edge coefficients are significantly lower and even negative compared to full immersion and up-milling. Especially in comparison to the up-milling tests, the tangential edge force shows in the opposite direction. This agrees with the assumption that the alignment between the edge force components and the feed velocity is decisive for the values of the edge coefficients. For the down-milling tests, a smaller feed per tooth f_z was chosen to match the conditions of finishing operations. When considering the force comparison, the deviations are slightly higher than in the previous investigations. Especially one flute in case of the tool with sharp cutting edges and chamfered cutting edges yields higher forces in the experimental data. A possible reason might be the influence of deflection (Chapter 2.4.2). Furthermore, in case of the hybrid tool, the roughing flutes do not contribute to the machining process at all. This shows that the value for the radial offset is too high for the selected feed per tooth. As a consequence, the load on the finishing flutes increases, which negatively impacts the surface finish. Thus, smaller values for ΔR are desirable for finishing. In case of the identified forces for the hybrid tool, the recessed flutes are in cut for a short immersion segment. This discrepancy between the experimental and fitted forces may results from the fact that the actual value ΔR of the tested hybrid tool is higher.

7.1.3 Cutting Speed Dependent Process Forces

In Chapter 2.4.4, the significant influence of the cutting speed on the process forces, and thus, process force coefficients was discussed. The influence of the process force coefficients on process stability was shown in the preliminary investigations in Chapter 6.1.4. In order to take this influence into account for stability prediction, further process force tests were carried out, in which only the spindle speed n was varied. The experimental configuration shown in Fig. 7.1 was used for this purpose. As discussed in Chapter 2.3.2, a non-linear relationship between process forces and low cutting speeds can be observed. In order to obtain a more linear correlation between mean values of the process forces and spindle speeds, only spindle speeds $\geq 2,000\,\mathrm{min}^{-1}$ were considered. The results are shown in Fig. 7.9. The experimental data of the tool with chamfered cutting edges shows a linear behavior with only slight deviations. Significantly higher fluctuations can be observed for the experimental data of the hybrid tool, especially in feed normal direction. However, for all tools, the mean values of the feed and feed normal forces decrease with a nearly identical slope. Apparently, the higher friction contribution in case of the end mill with chamfered cutting edges has no significant influence on the slope. Thus, it can be assumed that both the cutting forces as well as the edge forces and damping forces decrease equally with increasing spindle speeds. In this respect, the spindle speed dependent coefficients can be calculated as follows:

$$K_{tc}(n) = \frac{-7.08}{10^3}\frac{\mathrm{Ns}}{\mathrm{mm}^2}\left(n - 40\ \mathrm{s}^{-1}\right) + 673.3\ \frac{\mathrm{N}}{\mathrm{mm}^2} \tag{7.2}$$

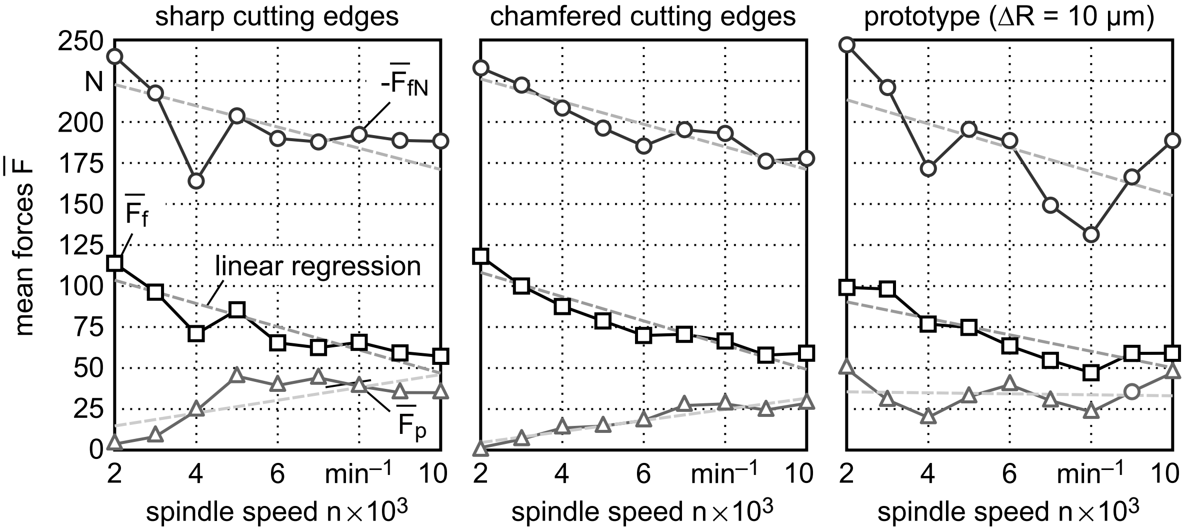

radial depth of cut: a_e = 20 mm
axial depth of cut: a_p = 2 mm
feed per tooth: f_z = 0.12 mm
process: slot milling
workpiece: Al 7075 T651
machine: Heller MCi16

Gra/72799 ©IFW

Fig. 7.9: Variation of the mean forces with increasing spindle speed. Dashed lines represent the linear regression.

$$K_{rc}(n) = \frac{-6.47}{10^3}\frac{\mathrm{Ns}}{\mathrm{mm}^2}\left(n - 40\ \mathrm{s}^{-1}\right) + 169.1\ \frac{\mathrm{N}}{\mathrm{mm}^2} \tag{7.3}$$

With the known relations from Eq. 7.1, the slopes for $K_{tc}(n)$ and $K_{rc}(n)$ can be derived from $\bar{F}_f$ and $\bar{F}_{fN}$, respectively. The values of the slopes are taken from the tool with sharp cutting edges. The initial values at $n = 2,400\ \mathrm{min}^{1} = 40\ \mathrm{s}^{-1}$ correspond to the determined coefficients in Chapter 7.1.2. $K_{tc}(n)$ and $K_{rc}(n)$ are used in Eq. 4.15 for the calculation of $\mathbf{Q}_{j,u}(t, z_i)$. In order to lower the computational time during the stability calculation using the SD method, it is not required to recalculate $\mathbf{Q}_{j,u}(t, z_i)$ explicitly for each considered spindle speed. Instead, $\mathbf{Q}_{j,u}(t, z_i)$ is calculated only for the lowest and highest spindle speed and is interpolated in between.

7.1.4 Modal Analysis of Experimental Setup for Stability Tests

The test setup shown in Fig. 7.10 was used for stability studies. An unidirectional flexure with an in-build displacement sensor similar to [Man03] was designed for the experiments. The advantage of such a structure lies in the reduction of the load on expensive components, in particular the spindle. Most components are made of aluminum. Only the side walls, which have a thickness of 2 mm, are made of steel C45. The dimensions of the side walls decisively determine the compliance behavior of the system. For the shown setup, the compliant direction of the flexure corresponds to the feed direction. To compare forces between the different tools for stable and unstable conditions, the flexure is mounted on a dynamometer. Furthermore, an accelerometer is installed beneath the workpiece. Part of the signal bandwidth of the mentioned signal transducers may be altered due to either the sensor's frequency response, signal filtering or sensitivity [Del92], which might affect chatter frequency determination. Therefore, the in-build microphone of a common smartphone (LG P936) was used additionally to record an audio signal of the ma-

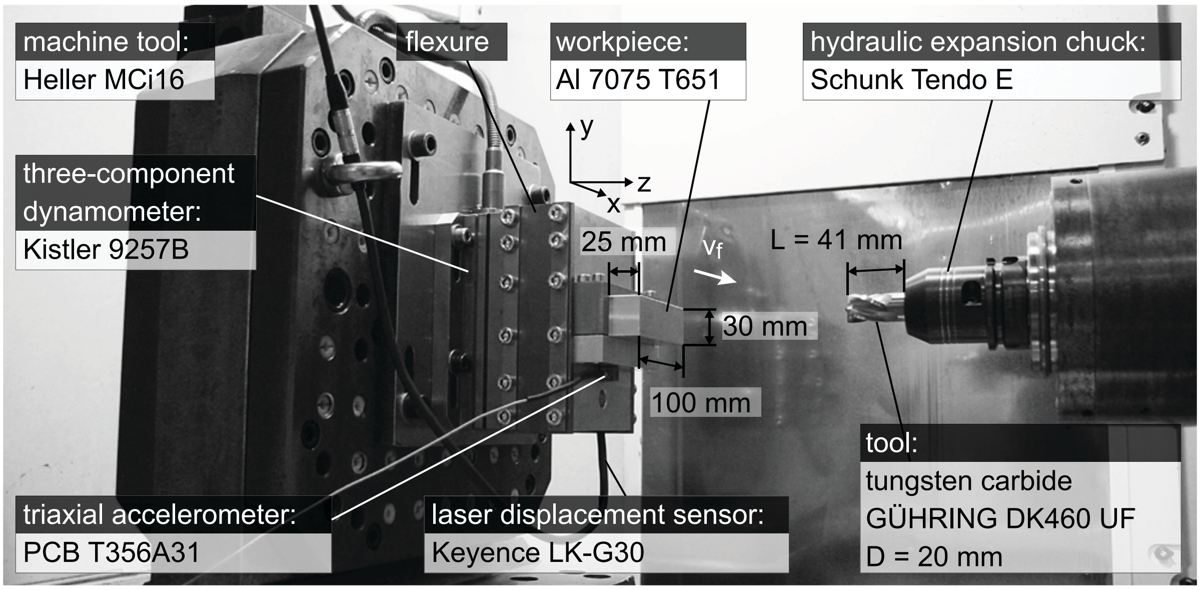
machine tool:
Heller MCi16
flexure
workpiece:
Al 7075 T651
hydraulic expansion chuck:
Schunk Tendo E
y
z
x
three-component
dynamometer:
Kistler 9257B
25 mm
v_f
L = 41 mm
30 mm
100 mm
tool:
tungsten carbide
GÜHRING DK460 UF
D = 20 mm
triaxial accelerometer:
PCB T356A31
laser displacement sensor:
Keyence LK-G30

Gra/72821 ©IFW

Fig. 7.10: Experimental setup for machining stability analysis.

chining process. As mentioned in [Mon13, p. 21], there already exist software solutions to use smartphones for chatter identification. Thus, it will be investigated if such a low cost device can be used for an acoustic control. Fig. 7.10 shows the protruding part of the clamped workpiece. The actual height of the workpiece is 50 mm. After every cutting test a new workpiece is used. This approach is intended to keep influences due to mass reduction low. For thin walled workpieces [Bra05] but also in case of multiple full immersion tests with large workpieces [Gro14], the mass reduction can have a significant influence on the natural frequencies and compliance. Thus, this can lead to a deviation between the experimental and calculated stability limit.

For the identification of the FRF of the workpiece system, consisting of the actual workpiece, the flexure and the dynamometer, the accelerometer is used for the output signal. The input signal is acquired with an impact hammer (PCB Piezotronics 086C03) equipped with a medium impact cap (plastic insert). For the FRF of the tool system, consisting of the actual tool, tool holder and spindle, a hard impact cap (steel insert) is used. The output signal for the tool system is acquired with a laser Doppler vibrometer (Polytec OFV 303). Fig. 7.11 shows the resulting FRFs. For all measurements, the spectral coherence is also given in the diagrams to assure the causality between input (hammer impact) and output (tool or workpiece deflection). The low coherence for the FRFs of the tool is due to the fact that a manual impact is always carried out with a certain deviations from the intended spatial direction. However, by establishing FRFs by means of several impact tests, a necessary high coherence could be reached, in most decisive frequency ranges. As desired, the FRF of the workpiece/flexure in y-direction has the highest compliance at 531 Hz with a magnitude of approximately 1.4 µm/N. To illustrate the discussed impact of a mass decrease, the measurement for the FRF of the workpiece system was also carried out without the actual workpiece being clamped on the flexure. The mass reduction of 420 g caused a frequency shift of the aforementioned compliance to 714 Hz and an magnitude decrease to 0.4 µm/N. For the identification of the modal parameters, the PSO algorithm described in Chapter 4.4 has been adapted. The determined modal parameters are given in Table 7.2.

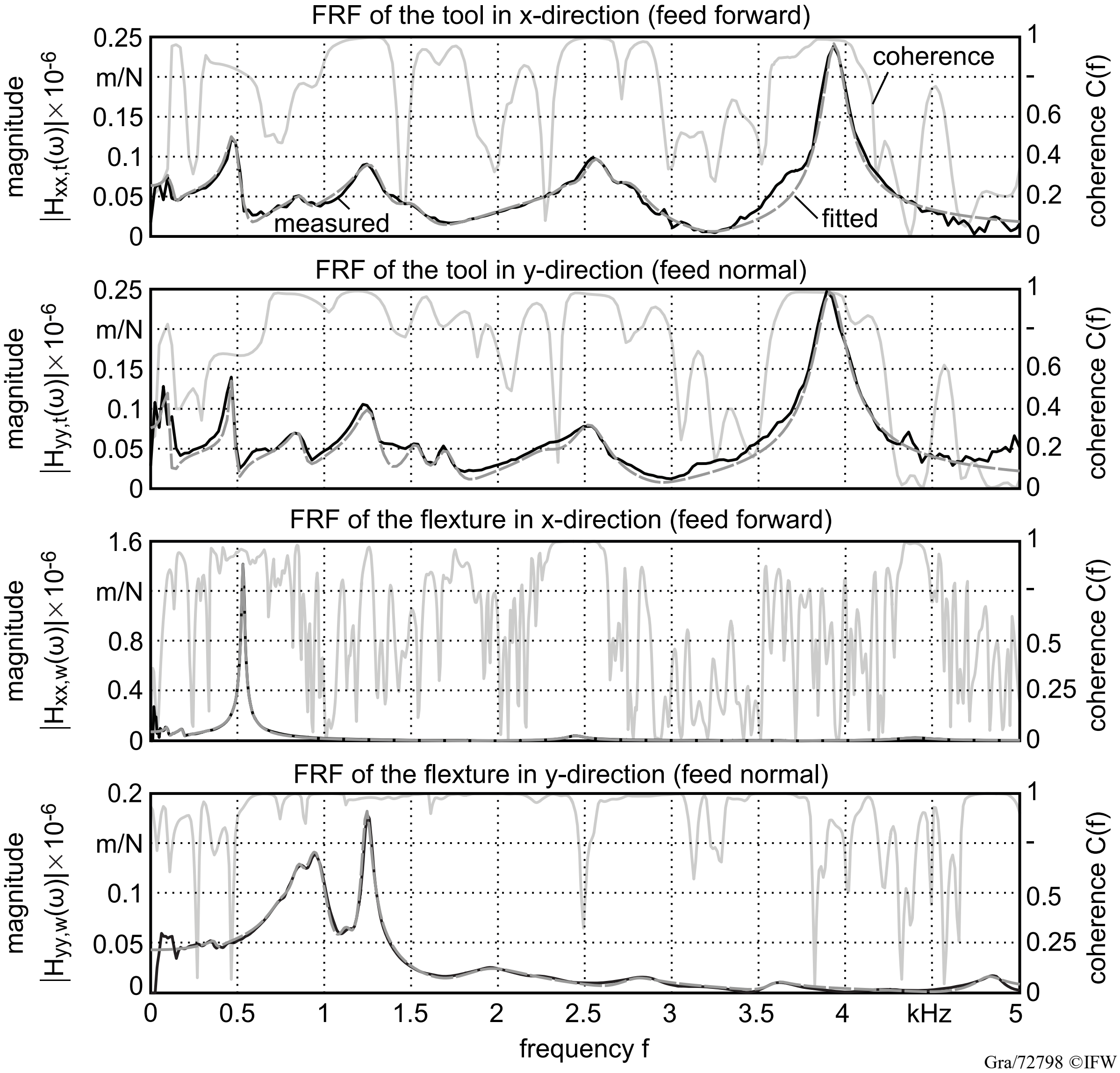

Fig. 7.11: Measured and curve fitted FRFs for the tool and workpiece system in x- and y-direction. Note the different scales of the x-axis.

7.1.5 Identification of Runout Error

For the process stability prediction, the influence of the runout error is also to be taken into account. The measured process forces during stability tests are used to determine the runout location angle λ_r and the runout offset ρ_r using the PSO algorithm (Chapter 7.1.2). Edge coefficients were also adapted by the PSO algorithm to increase agreement between experimental and fitted forces. In order to prevent a change of the runout values, the tools must not be removed from the tool holder during the stability tests. Thus separate tool holders are used for every tool and clamping is not changed during the tests. Furthermore, the runout identifcation was carried out during the stability test to prevent any deviations caused by a change of the experimental environment. Thus, the experimental setup from Fig. 7.10 was used for the runout identifcation.

The identified runout parameters based on the experimental process force fitting are shown in Fig. 7.12. With the determined runout parameters ρ_r and λ_r, it is possible to check if the rough-

Table 7.2: Modal parameters of the flexure with workpiece mounted on a dynamometer (f_{w,x_i} and f_{w,y_i}) and of the tool, tool holder and spindle (f_{t,x_i} and f_{t,y_i}).

	mode i [–]	$f_{\bullet,\bullet i}$ [Hz]	$m_{\bullet,\bullet i}$ [kg]	$k_{\bullet,\bullet i}$ [N/μm]	$\zeta_{\bullet,\bullet i}$ [–]
f_{t,x_i}	1	120.3	177.3	101.3	0.1320
	2	487.17	6.29	58.97	0.0763
	3	881.05	16.48	505	0.0538
	4	1285.59	1.42	92.89	0.0740
	5	1508.55	3.21	288.02	0.0640
	6	2270.51	1.34	272.68	0.1157
	7	2406.28	4.59	1048.49	0.0320
	8	2572.97	0.75	195.98	0.0344
	9	2746.44	1.04	310.95	0.0384
	10	3931.65	0.20	121.62	0.0171
f_{t,y_i}	1	97.65	85.27	32.1	0.1410
	2	471.93	17.10	150.33	0.0264
	3	862.28	7.58	222.59	0.0493
	4	1269.31	1.76	111.93	0.0529
	5	1534.23	4.00	371.30	0.0328
	6	1703.38	3.60	412.15	0.0308
	7	2294.63	2.31	480.49	0.0531
	8	2535.21	0.64	162.20	0.0418
	9	3911.80	0.15	87.87	0.0231
f_{w,x_i}	1	97.66	197.57	74.38	0.1004
	2	183.11	126.98	168.08	0.0545
	3	531.01	1.77	19.69	0.0178
	4	2447.51	2.91	687.22	0.0159
	5	4388.9	1.00	758.34	0.0300
f_{w,y_i}	1	373.01	260.34	1430	0.0500
	2	771.25	15.33	360	0.0845
	3	861.07	8.30	243	0.0490
	4	957.75	1.52	55	0.0740
	5	1126.88	6.24	312.74	0.0480
	6	1239.04	2.00	121	0.0254
	7	1928.71	1.59	233.81	0.1106
	8	2774.08	3.78	1148.43	0.0418
	9	3594.45	5.88	3001	0.0200
	10	4811.52	2.19	2000	0.0160

ing flutes of the hybrid tool contribute to the machining of the finished surface, as described in Chapter 4.3. With a fitted runout offset ρ_r of 9.6μm the sufficient condition $\Delta R > 2\rho_r$ from Eq. 4.43 is actually not met. Therefore, as recommended in Chapter 4.3, the flute radii with runout $r_{r,j}(z_i)$ are calculated at the axial positions z_i = 1 mm and z_i = max(a_p) = 20 mm, additionally. The resulting values are given in Table 7.3. The difference in the flute radii for the regular tools with

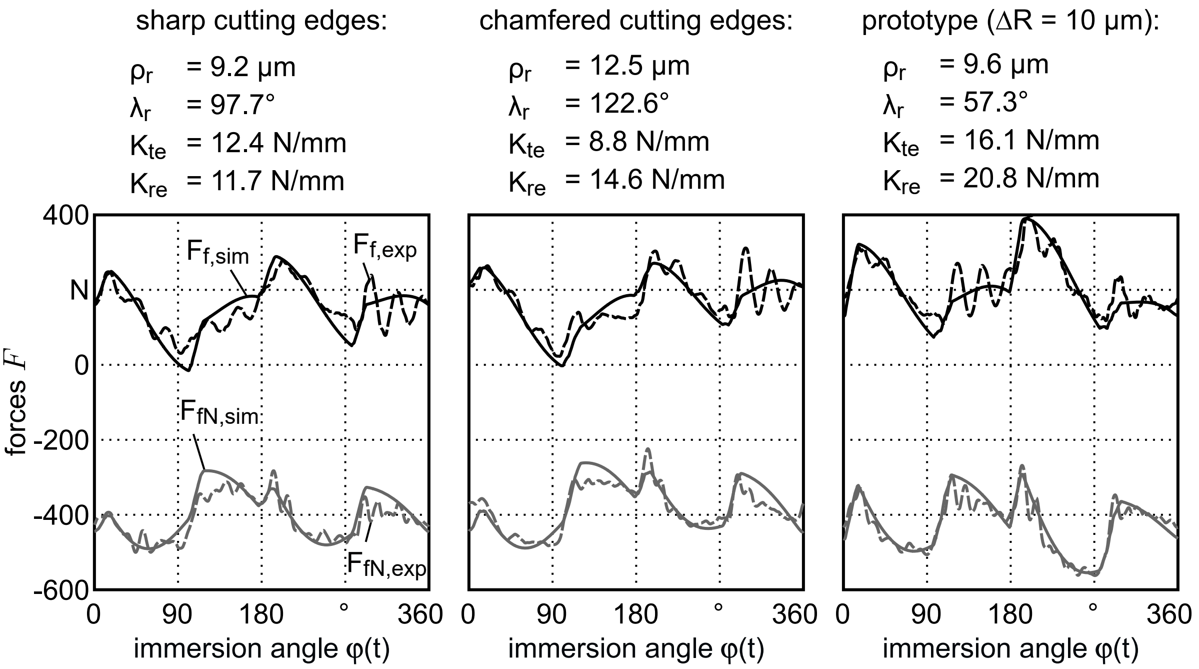

feed per tooth: f_z = 0.12 mm
radial depth of cut: a_e = 20 mm
axial depth of cut: a_p = 4 mm
spindle speed: n = 2,500 min^{-1}
cutting speed: v_c = 157.1 m/min
tan. cutting coeff.: K_{tc} = 672.6 N/mm^2
rad. cutting coeff.: K_{rc} = 168.5 N/mm^2
workpiece: Al 7075 T651
machine: Heller MCi16
process: slot milling

Gra/72839 ©IFW

Fig. 7.12: Runout determination with PSO algorithm for consideration in process stability prediction.

Table 7.3: Flute radii $r_{r,j}(z_i)$ and angular position $\varphi_{r,j}(z_i)$ with runout values from Fig. 7.12. The radii of the flutes with a radial offset are marked with bold letters.

		sharp cutting edges		chamfered cutting edges		hybrid tool ΔR = 10 µm	
	flute j [–]	$r_{r,j}(z_i)$ [mm]	$\varphi_{r,j}(z_i)$ [°]	$r_{r,j}(z_i)$ [mm]	$\varphi_{r,j}(z_i)$ [°]	$r_{r,j}(z_i)$ [mm]	$\varphi_{r,j}(z_i)$ [°]
z_i = 1 mm	1	10.001	3.26	10.096	3.25	9.994	3.26
	2	9.991	103.31	9.988	103.28	**9.983**	103.35
	3	9.999	183.36	9.994	183.37	10.006	183.35
	4	10.009	283.30	10.012	283.33	**9.997**	283.27
z_i = 20 mm	1	9.992	66.13	9.993	66.10	9.991	66.17
	2	9.997	166.21	9.994	166.21	**9.993**	166.28
	3	10.008	246.19	10.007	246.22	10.009	246.15
	4	10.003	346.11	10.009	346.11	**9.987**	346.17

sharp and chamfered cutting edges is rather marginal. In case of the hybrid tool, runout levers the radial offset ΔR. At z_i = 1 mm, the radius of the recessed flute 4 is higher than of flute 1. For z_i = 20 mm the radius of flute 1 is higher again, due to the influence of the helix angle δ. Instead, however, the flute 2 has a higher radius than flute 1. Thus, the determined runout theoretical leads to a contribution of the recessed flutes to the machining of the final surface. However, it might be assumed that the contribution is rather marginal and might be neglected, which will be investigated in Chapter 7.3.1.

7.2 Process Stability Analysis

Experimental stability test are carried out for the tools with sharp as well as chamfered cutting edges and for the hybrid tool with different values for the radial offset ΔR. A detailed description of the procedure to classify the dynamic behavior of each cutting test as stable, unstable or marginally stable is given. The experimental stability results are compared with calculated stability charts based on the SD method and time-domain simulation.

7.2.1 Comparison with Sharp and Chamfered Tools

Full immersion cutting tests at a series of spindle speeds n and axial immersions a_p with the setup shown in Fig. 7.10 were conducted. Chatter detection is carried out on the basis of the mentioned sensors in Chapter 7.1.4 as well as the evalution of the machined surface. Two experimental results for the end mill with sharp cutting edges are shown in Fig. 7.13.
The left side shows an unstable cutting process at $n = 8,000$ min^{-1} and $a_p = 6$ mm. Chatter marks are clearly visible on the machined surface. First, the audio signal is used for the chatter frequency detection. Furthermore, a short-time FOURIER transform (STFT) is performed in order to distinguish between frequency amplitudes which occurred during the machining process and ambient noise. The spectrogram shows which dominant frequencies occurred during the cutting test. The line within the dashed area represents the chatter frequency f_c at approximately 4,000 Hz. The same frequency can be seen in the FFT of the acceleration sensor in x- and y-direction. On the basis of the amplitudes, it can be stated that the flexibility of the system in the y-direction is responsible for the instability. This corresponds to the dominant mode of the tool system (Fig. 7.11).
The right side of Fig. 7.13 shows an unstable machining process at $n = 8,500$ min^{-1} and $a_p = 10$ mm. In this case, the chatter frequency was approximately 500 Hz. The spectrogram shows further dominant lines during the immersion, which are an exact multiple of f_c. Analogously to the previous evaluation, the direction of chatter can be determined by means of the signal of the acceleration sensor. In this case, unstable behavior has been caused in the x-direction. Furthermore, this frequency corresponds to the dominant mode of the flexure (Fig. 7.11). These two examples underline that a microphone of a smartphone enables chatter frequency detection. However, for the identification of the chatter direction, additional sensors are necessary.

The chatter analysis for all cutting test is shown in the stability charts in Fig. 7.14. The top diagram shows the stability chart for the end mill with sharp cutting edges. Velocity-dependent cutting coefficients from Eq. 7.2 and Eq. 7.3 and modal parameters from Table 7.2 were used for the calculation of the stability chart. As mentioned in Chapter 7.1.3, only spindle speeds $\geq 2,000$ min^{-1} were considered to avoid the nonlinear behavior of the cutting force coefficients at low cutting speeds (Chapter 2.3.2). The dotted line represents the stability limit if runout error is neglected. At the lowest considered spindle speed $n = 2,000$ min^{-1}, K_{tc} and K_{rc} have a value of $686.76 \frac{N}{mm^2}$ and $181.39 \frac{N}{mm^2}$, respectively. For $n = 10,000$ min^{-1}, the values of K_{tc} and K_{rc} are $619.46 \frac{N}{mm^2}$ and $119.92 \frac{N}{mm^2}$, respectively. A good agreement between the experimental

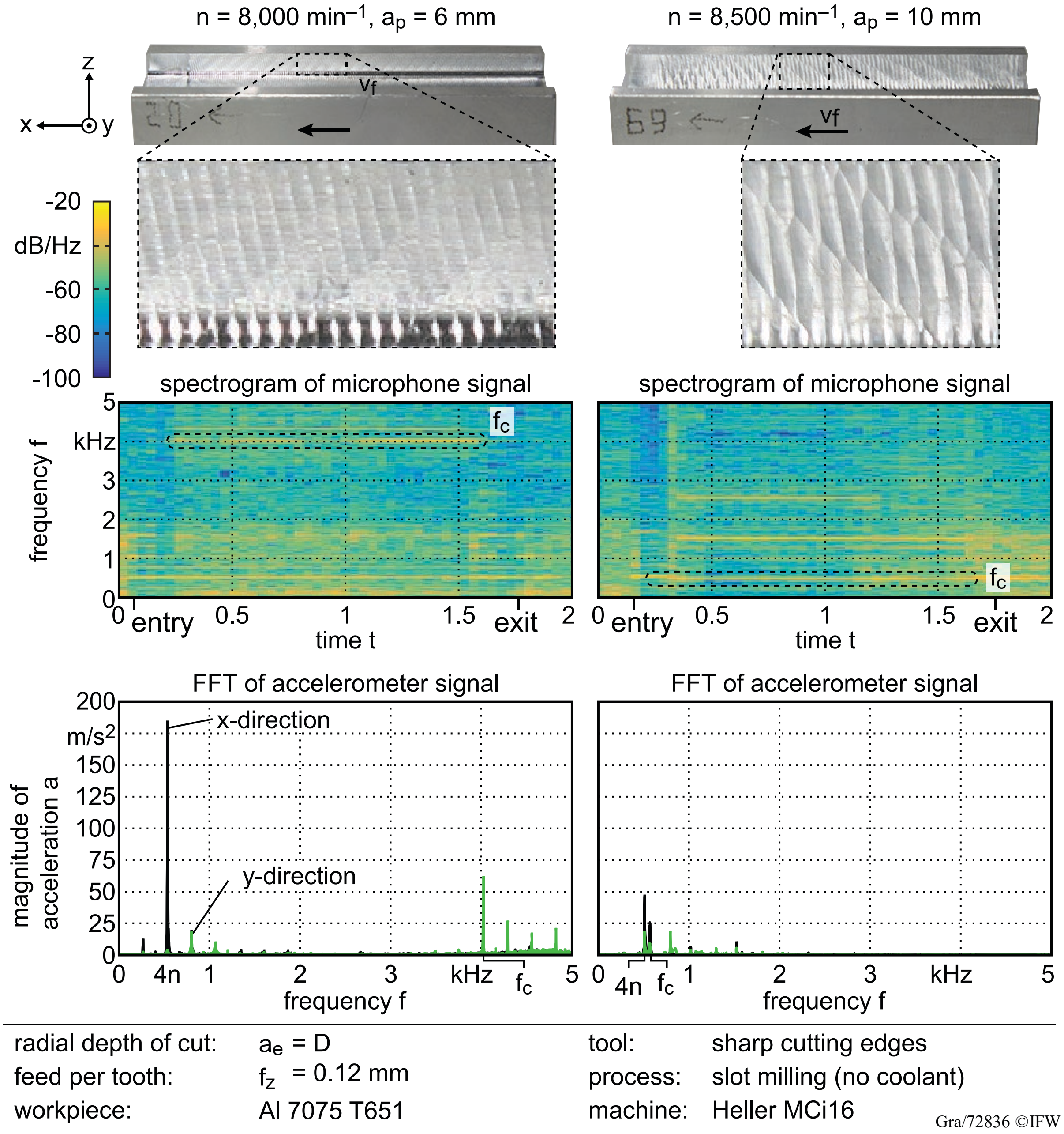

Fig. 7.13: Example of two unstable cutting processes with different chatter frequencies.

data and the computed stability limit can be found for the investigated spindle speed range. The spindle speeds n with the highest stability at 6,500 min^{-1} and 7,500 min^{-1} are correctly predicted. Furthermore, as already shown in Chapter 6.2.1, there is no significant difference between the stability prediction with and without runout consideration. The evaluation of the stability based on the experimental data at n = 6,500 min^{-1} illustrates that, depending on the evaluation method, a clear distinction between a stable and an unstable process is not always given. Based on Fig. 7.15, the selected procedure for stability classification is explained. For a_p = 14 mm clear chatter marks are recognizable, as can be seen in Fig. 7.15 a). The unstable process behavior at this operating point is also confirmed by the signal evaluation in Fig. 7.15 b). The left and right diagrams show the FFT of the accelerometer in y-direction and of the microphone, respectively. Both signals show a recognizable chatter frequency f_c for a_p = 14 mm at 602 Hz. All other

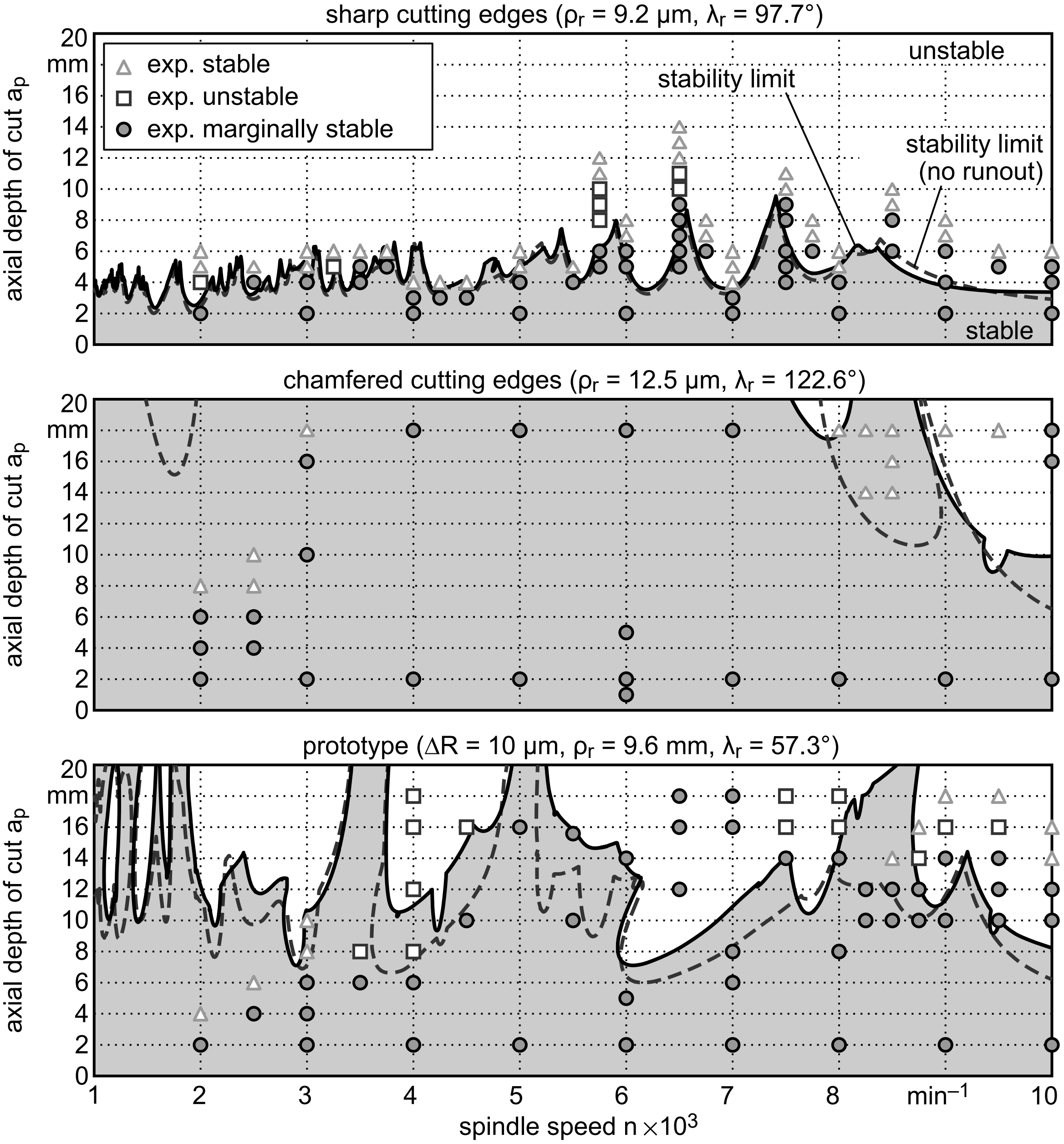

radial depth of cut:	a_e = D	machine:	Heller MCi16
feed per tooth:	f_z = 0.12 mm	tan. cutting force coeff.:	K_{tc} = variable
workpiece:	Al 7075 T651	rad. cutting force coeff.:	K_{rc} = variable
process:	slot milling (no coolant)	process damping coeff:	K_{pd} = variable
discretization:	N_k = 720, N_z = 40	coefficient of friction:	µ = 0.3

Gra/72822 ©IFW

Fig. 7.14: Experimental and calculated stability charts for the three different end mills.

peaks correspond to a multiple or exactly the spindle speed frequency f_S. There are also chatter marks visible at a_p = 13 mm and 12 mm. However, these chatter marks are not as severe as at 14 mm. Furthermore, there is no peak corresponding to a chatter frequency visible in the FFT of the accelerometer. The existing peaks are multiples of f_S. However, the FFT of the microphone signal shows for the radial depth of cuts chatter peaks at approximately 4, 100 Hz. The FRF of the tool systems has its highest magnitude near this frequency (Fig. 7.11). Due to the fact

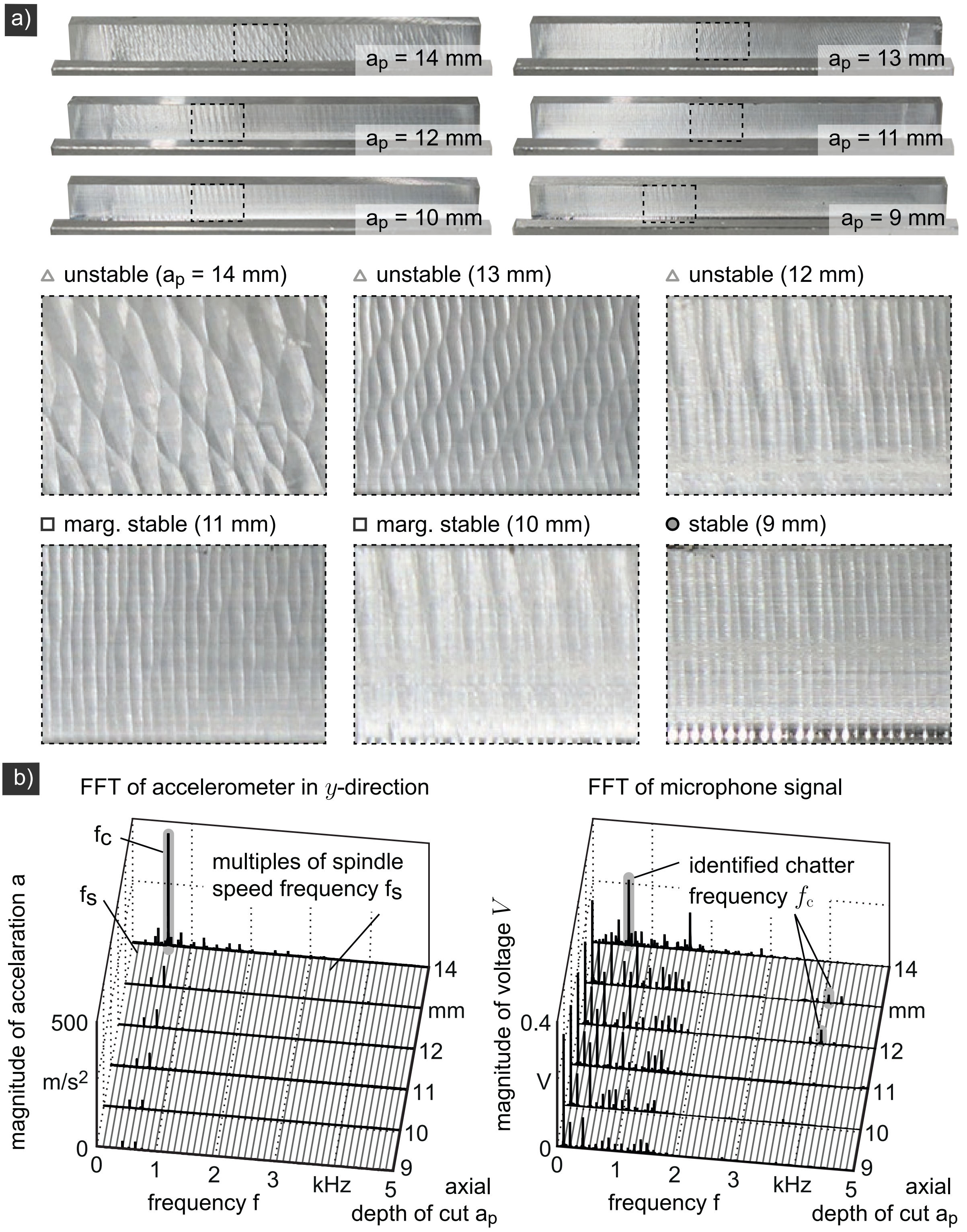

radial depth of cut: a_e = D
feed per tooth: f_z = 0.12 mm
spindle speed: n = 6,500 min^{-1}
cutting speed: v_C = 408.4 m/min

workpiece: Al 7075 T651
tool: sharp cutting edges
process: slot milling (no coolant)
machine: Heller MCi16

Gra/72850 ©IFW

Fig. 7.15: Exemplary procedure for stability classification based on a) surface analysis and b) signal processing.

that besides the chatter marks on the surface a chatter frequency can be identified in one of the measured signals, these two cutting tests are also classified as unstable. The machined surfaces at a_p = 12 mm and a_p = 11 mm have similar chatter marks as at 14 mm and 13 mm. However, no chatter magnitude arises at any of the measured signals. In this case, no additional load on the machine tool can be assumed. Thus, both machining operations are classified as marginally stable. For a_p = 9 mm, no chatter marks occured on the machined surface. Therefore, this process is classified as stable.

The diagram in the middle of Fig. 7.14 shows the stability of the tool with chamfered cutting edges. As expected, there is a signifiant increase in stability compared to the tool with sharp cutting edges. For the calculated stability limit the value of the process damping coefficient K_{pd} was selected in such a way as to achieve the closest possible match between the experimental and calculated data. In analogy to the cutting force coefficients, a linear dependence of K_{pd} on the spindle speed was chosen. Since the process damping force acts mainly in radial direction, the same relative slope was selected as for K_{rc} from Eq. 7.3. This leads to the following equation:

$$K_{pd}(n) = -2.043 \frac{\mathrm{Ns}}{\mathrm{mm}^3} n + 54,086 \ \frac{\mathrm{N}}{\mathrm{mm}^3} \qquad (7.4)$$

For n = 2,000 min^{-1} and 10,000 min^{-1}, the process damping coefficient K_{pd} has a value of 50,000$\frac{\mathrm{N}}{\mathrm{mm}^3}$ and 33,656$\frac{\mathrm{N}}{\mathrm{mm}^3}$, respectively. A comparison between the experimental data with the calculated stability limit reveals obvious differences. In particular, the unstable behavior at the low spindle speed is not correctly predicted. Furthermore, the difference between the stability limit with and without runout consideration is more distinct in case of process damping. As shown in [Sel12b] for tools with different chamfer lengths b_f, small geometrical variations have a significant influence on the stability limit in case of process damping. Without consideration of the runout error, the correspondence between the calculated stability limit and the experimental data even increases at high spindle speeds. However, since significant deviations are evident in both calculated stability charts, it can be assumed that the incorrect identification is mainly caused by the simplified model of the process damping, as discussed in Chapter 6.1.5. Furthermore, as shown in Chapter 7.1.1, process forces of end mills with chamfered cutting edges may change during the machining process due to the thermal load, which will be investigated in Chapter 7.3.3.

The bottom diagram shows the stability chart of the hybrid tool with a radial offset of $\Delta R = 10\,\mu\mathrm{m}$. When looking at the experimental data, a decrease in stability occurs compared with the tool with chamfered cutting edges. This applies in particular to spindle speeds up to 5,500 min^{-1}. From 6,000 min^{-1}, the results are very similar. This shows that, with the right choice of n, the hybrid tool can provide the same stability as the tool with chamfered cutting edges. In analogy to the result for the tool with chamfered cutting edges, the consideration of runout yields higher stability limits for almost all spindle speeds. However, it can also be seen that the computed stability limit has obvious discrepancies to the experimental data. Thus, no reliable prediction of the dynamical behavior is possible. It should be mentioned that a change in the damping coefficient K_{pd} does not lead to an increase in the consistency. There are probably multiple reasons which cause the inaccuracies in the prediction. One is the calculation of the simplified indentation area A_{pd}, as described in Chapter 6.1.5. Furthermore, the implemented process damping model for the SD method does not consider the fact that damping is not active along the whole immersion range

(Fig. 6.7). These are model based sources of errors. However, the frictional forces between the chamfer and the workpiece material lead to an increase of the workpiece material temperature, which might lower cutting forces. This will be investigated in Chapter 7.3.3. Furthermore, due to the process damping related deviations, an improvement of stability prediction in case of runout consideration cannot be stated. Carrying out stability tests with tools with sharp cutting edges under variation of the runout location angle λ_r would help to reveal the possible improvement of the stability prediction in case of runout consideration.

On the basis of the experimental and predicted chatter frequencies, shown in Fig. 7.16, possible reasons for the deviations between the experimental data and the calculated stability limits can be determined. The chatter frequencies belong to the stability prediction with runout consideration. For the tool with sharp cutting edges, the consideration of chatter frequencies confirms the correct prediction of the stability limit. There is a good agreement between the experimentally determined and calculated chatter frequencies. This also applies to the direction of the chatter frequency. Obviously, the chatter frequencies examined in Fig. 7.13 are dominant in the entire speed range. From the data it can be seen that up to $n = 3,000 \text{ min}^{-1}$ and above $8,000 \text{ min}^{-1}$ the dominant mode of the flexure in x-direction caused the instability (Fig. 7.11). In between, the dominant mode can be assigned to the tool system in y-direction. It can be seen from the FRF of the tool system that a dominant mode with the same amplitude is present at approximately 4000 Hz in both directions. The reason why the y-direction is dominant at the chatter frequencies lies in the higher forces in the feed-normal direction (Fig. 7.1).

The diagram with the chatter frequencies for the tool with the chamfered cutting edges shows that stability is particularly low in the areas where the natural frequency of the flexure is dominant. Due to the low frequency, the overlapping area between the chamfered cutting edge and the workpiece decrease, as explained in Chapter 2.3.2. Thus, based on the determined chatter frequencies of the tool with sharp cutting edges, it is possible to estimate at which spindle speeds the highest stability can be achieved with the tool with chamfered cutting edges.

The bottom diagram shows the chatter frequencies of the hybrid tool. The chatter frequencies of the experimental tests and calculation actually match in most cases. Again, it can be assumed that the insufficient process damping model leads to the wrong stability limit.

For further analysis of the deviations caused by process damping forces, stability charts are predicted based on time-domain simulations (compare with Fig. 6.16). As described in Chapter 5.2, the time-domain simulation allows for a more precise modeling of the contact between the workpiece and the chamfer possible. This allows to consider process damping forces that arise if only the rear part of the chamfer is in contact with the workpiece (Chapter 6.1.5). The resulting stability charts for all three investigated end mills are shown in Fig. 7.17. The identified cutting edge coefficients shown in Fig. 7.12 are applied to the simulation. For a direct comparison the stability charts resulting from the SD method are also included (dashed lines). In the case of tool with sharp cutting edges, there is a good match between the stability limit from the time-domain simulation (solid line with $r_{amp} = 2$) and the experimental results. For high spindle speeds above $8,000 \text{ min}^{-1}$ the agreement with the experimental data is more precise in comparison with the stability limit from the semi-discrete method. The time-domain simulation takes into account the edge forces. This explains the differences with the stability limit based on the SD method, as

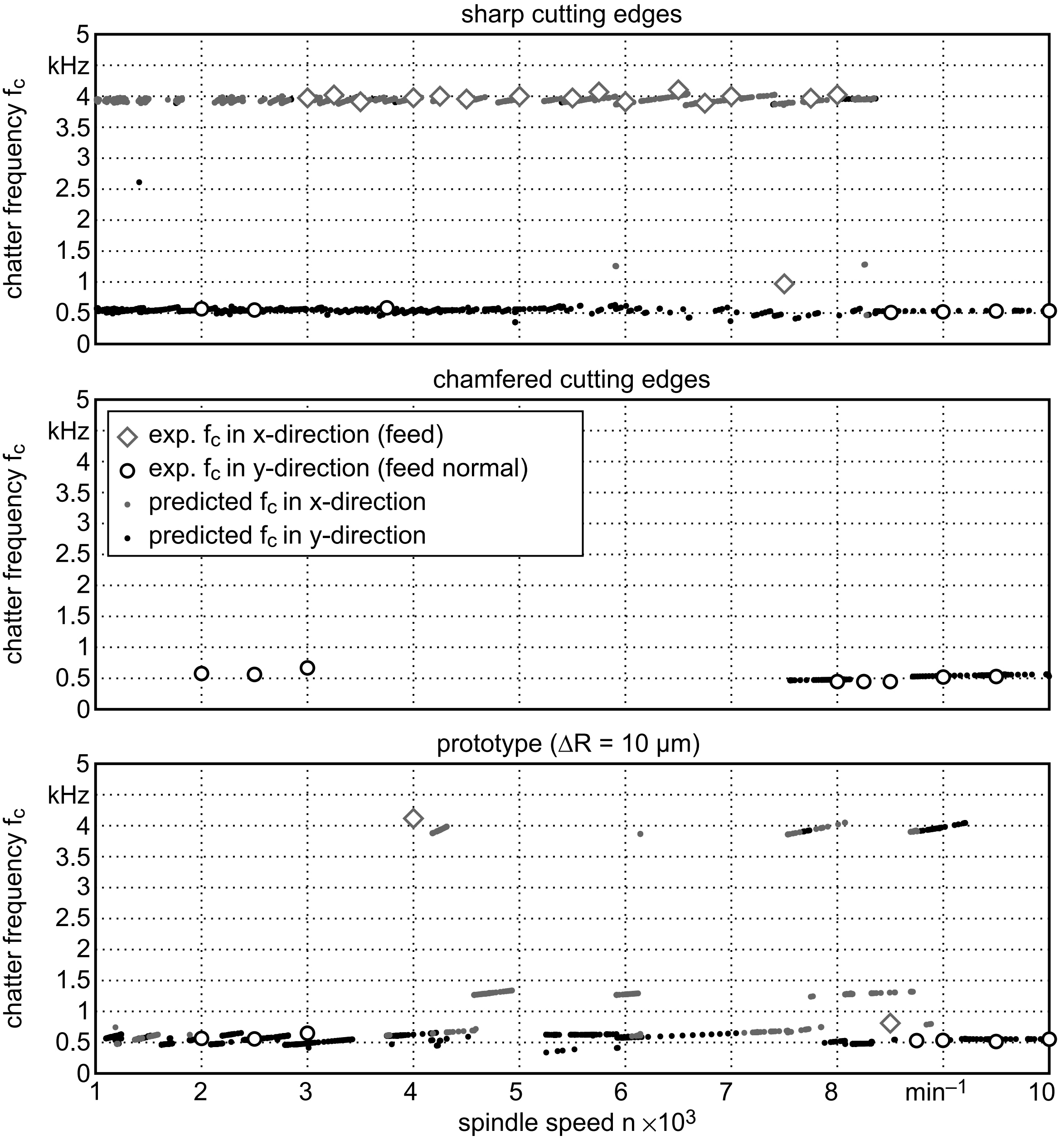

radial depth of cut:	a_e = D	machine:	Heller MCi16
feed per tooth:	f_z = 0.12 mm	tan. cutting force coeff.:	K_{tc} = variable
workpiece:	Al 7075 T651	rad. cutting force coeff.:	K_{rc} = variable
process:	slot milling (no coolant)	process damping coeff:	$K_{pd^\wedge}$ = variable
discretization:	N_k = 720, N_z = 40	coefficient of friction:	µ = 0.3

Gra/72835 ©IFW

Fig. 7.16: Experimental and calculated dominant chatter frequencies f_c. The calculated frequencies f_c are linked to the stability charts with runout consideration.

described in Chapter 6.2.2. For a visible comparison between the different tools, the color scale is set to a maximum value of r_{amp} = 15. The crosshairs in each diagram mark the position with the highest value for r_{amp}. In case of the tool with sharp cutting edge, the peak value r_{amp} = 40 occurs at n = 3, 000 min^{-1} and a_p = 20 mm. The maximum value of r_{amp} is significantly reduced in case of the end mill with chamfered cutting edges. Furthermore, the stability limit resulting from

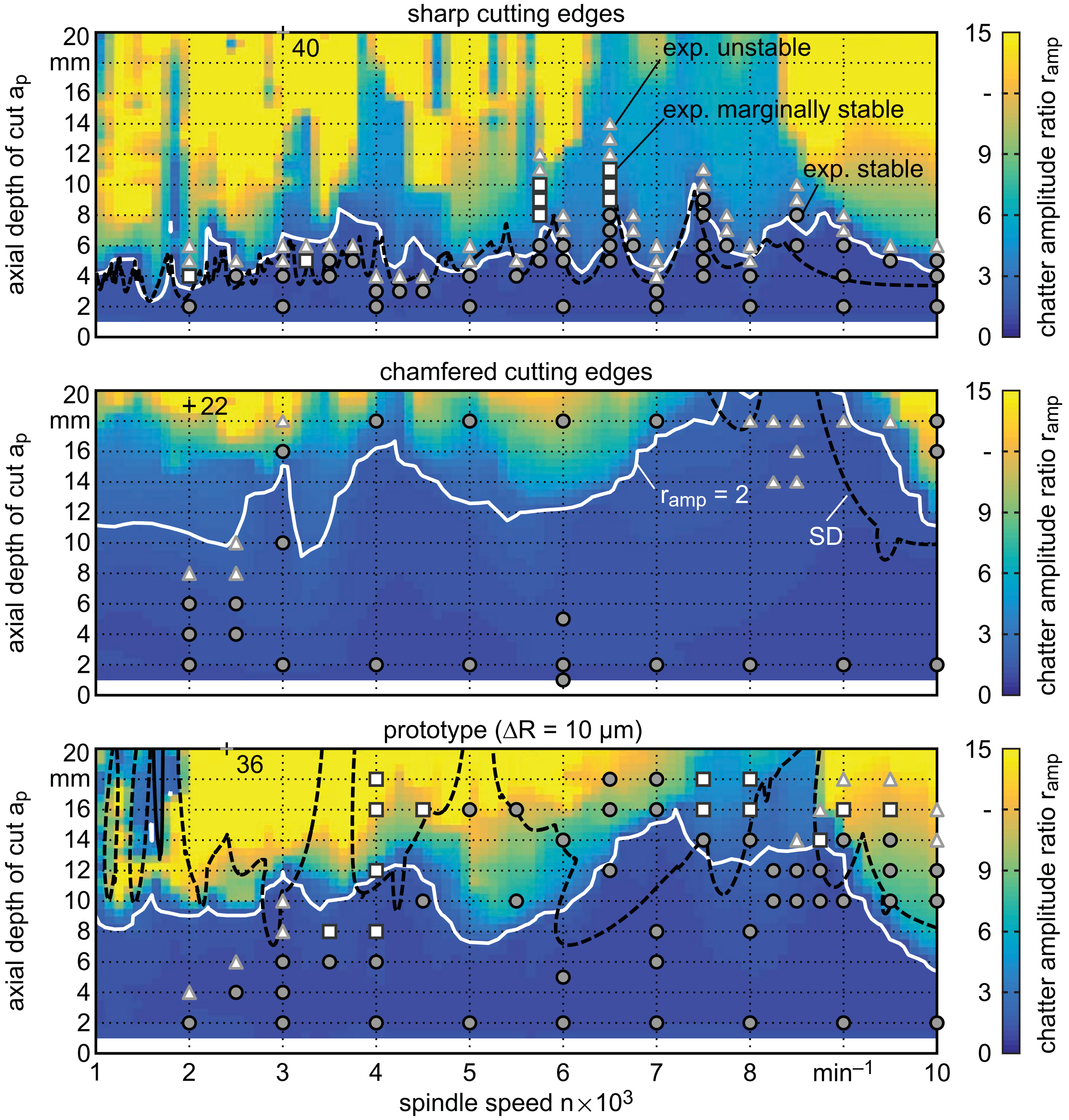

radial depth of cut:	a_e = D	machine:	Heller MCi16
feed per tooth:	f_z = 0.12 mm	tan. cutting force coeff.:	K_{tc} = variable
workpiece:	Al 7075 T651	rad. cutting force coeff.:	K_{rc} = variable
process:	slot milling (no coolant)	process damping coeff:	K_{pd} = variable
discretization:	N_k = 720, N_z = 40	coefficient of friction:	µ = 0.3

Gra/72849 ©IFW

Fig. 7.17: Stability prediction based on time-domain simulations. The cutting edge coefficients for the three tools are given in Fig. 7.12.

the time-domain simulation is also increased. With the proposed method for process damping consideration, the stability at low cutting speeds is decreased and a better agreement with the experimental data is reached. With higher spindle speeds, the stability increases. However, the predicted stability limit lies below the experimental stable data points. Similar to the stability limit based on the SD method, there is an obvious discrepancy above n = 8,000 min^{-1}. Discrepancies also occur for the hybrid tool. At low spindle speeds, although, the stability limit resulting from the time-domain simulation is decreased in comparison to the SD method, which leads to a better agreement with the experimental data. However, especially between $n = 4,000\,\mathrm{min}^{-1}$ and $6,000\,\mathrm{min}^{-1}$, the predicted stability is significant lower compared to the experimental results. As shown in [Sel12a, p. 100 ff.], the discrepancies between experimental and calculated process stability increases with higher values for the width of chamfer (from $b_f = 50\ \mu m$ to $b_f = 200\ \mu m$). The results for the tool with chamfered edges only and the hybrid tool illustrate that the modeling of the damping effect needs further extension, e.g. the consideration of the thermal load. The influence of chamfered cutting edges on stability will be investigated in Chapter 7.3.3.

7.2.2 Influence of the Radial Offset Value on Stability

As it was shown in Chapter 6.2.1, an increased radial offset ΔR can increase the process stability. This is due to the change in the immersion range of the resulting time-delays, as shown in Fig. 6.10 b). However, if the recessed flutes have chamfered cutting edges, an increase of ΔR decreases the effect of process damping. Consequently, there are two competing effects. Therefore, experimental tests were performed for two further hybrid tools with increased radial offsets. The resulting stability charts are shown in Fig. 7.18 a). For both hybrid tools the runout error was taken into account for the calculation of the stability limit. Analogous to the previous section, deviations between the experimental data and the calculated stability limit arises due to the influence of process damping forces. Fig. 7.18 b) summarizes the achieved experimental stability with the hybrid tools. Based on these results, it can be stated that with a small radial offset, there exist more spindle speed ranges with a high stability limit. However, the tool with a radial offset of $\Delta R = 45\ \mu m$ achieved a similar or even slightly higher stability for multiple spindle speed values. It follows, if the focus of a given machining task lies on finishing, a higher radial offset can be used. In addition, from this finding the possibility can be deduced to use a milling cutter with only one chamfered cutting edge and to adjust the radial offset accordingly. The influence of chamfered cutting edges on the surface quality is included in the investigations in the following section.

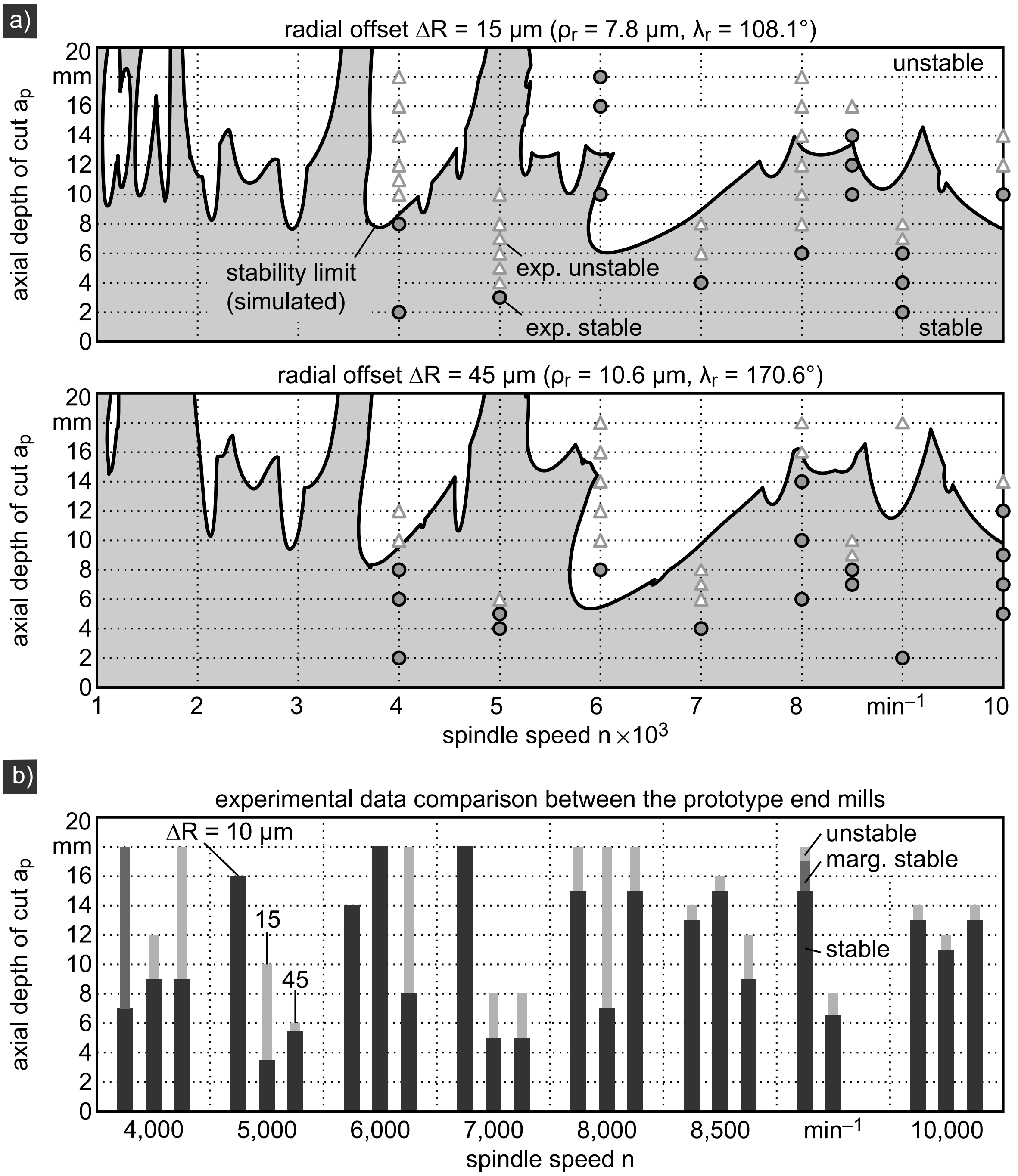

radial depth of cut:	a_e = D	machine:	Heller MCi16
feed per tooth:	f_z = 0.12 mm	tan. cutting force coeff.:	K_{tc} = variable
workpiece:	Al 7075 T651	rad. cutting force coeff.:	K_{rc} = variable
process:	slot milling (no coolant)	process damping coeff:	K_{pd} = variable
discretization:	N_k = 720, N_z = 40	coefficient of friction:	μ = 0.3
tool:	prototype		

Gra/72837 ©IFW

Fig. 7.18: a) Experimental data and predicted stability charts based on the SD method for hybrid tools with higher radial offset values ΔR. b) Comparison of the achieved experimental stability for all investigated hybrid tools.

7.3 Assessment of Surface Quality

The investigations of the process forces have shown that the runout offset ρ_r is less than 10 µm for the used experimental configuration (Fig. 7.6). Thus, due to the fact that the achievable process stability is highest at a low offset value (Chapter 7.2.2), the hybrid tool with the smallest radial offset $\Delta R = 10$ µm is used for the following surface quality investigations. In this respect, it is assumed that no unintended contact can occur between the chamfers of the hybrid tool and the machined surface finish. Otherwise, this could lead to an increased burr formation.
In this chapter, the surface quality is evaluated based on the surface topography and burr formation. Cutting tests are carried out to measure the surface topography. Additionally, the shape of the surface deformation error is predicted based on the analysis of the acting forces during the machining of the final flank surface. Further cutting tests are also carried out for the evaluation of burr formation. Additionally, heat inducement into the workpiece during milling with chamfered cutting edges will be investigated. This is of importance due to the reason that high temperatures can lead a negative effect on the material properties.

7.3.1 Surface Topography

First, the surface quality is judged on the basis of the deformed surface resulting from the tool deflection, as shown in Fig. 7.19. Based on the feed normal force analysis, as described in Chapter 6.2.3, the shape of the surface topography is predicted and compared with experimental data. The procedure for measuring the resulting surface influenced by the tool deflection is shown in Fig. 7.19. In order to compare the results for the different tools, constant immersion conditions had to be ensured. Therefore, two steps were taken prior to the actual experiment. As step 1, material was removed to ensure the correct radial immersion a_e. Next, step 2 was carried out to prevent deviations of a_p. Step 3 was the actual experiment. For the measurement of the surface topography a profilometer with a confocal point sensor (NanoFocus µscan) is used. The measurement of the surface topography was not carried out in situ. Thus, in order to avoid the measurement of an incorrect deformation due to an alignment error of the workpiece on the measuring table of the profilometer, a reference plane is necessary. The resulting surface after step 2 at both sides of the workpiece is used for this purpose. Therefore, the same process parameters and tool were used to machine the reference surfaces to ensure identical topographies. Based on the symmetry of the reference surfaces, the surface of the actual experiments is aligned accordingly. Fig. 7.19 shows the result for the end mill with chamfered cutting edges and $a_e = 2$ mm. The surface topography for the entire engagement path is projected on the workpiece on the left side. As it can be seen, the displacement is uniform in feed direction. Only at the point where the tool exits the workpiece the surface topography changes noticeably. The data in the range of the marked area **A** is used to calculate the mean value of the deformation in z-direction, as shown in the first diagram on the right in Fig. 7.19. The second diagram shows the calculated forces (Chapter 6.2.3). The shape of the solid lines in both diagrams shows similarities and correlate with the results for down-milling with $a_e = 2$ mm from Fig. 6.18. In case of the feed normal forces acting during the machining of the final surface, a wide variation for the maximum and minimum value of the force between $z = 14$ mm and 20 mm can be seen. This is caused by the unequal tooth pitch of the end mill. This also applies to the measured surface topography, based on the deformation range. A similar behavior with less impact occurs between $z = 0$ mm

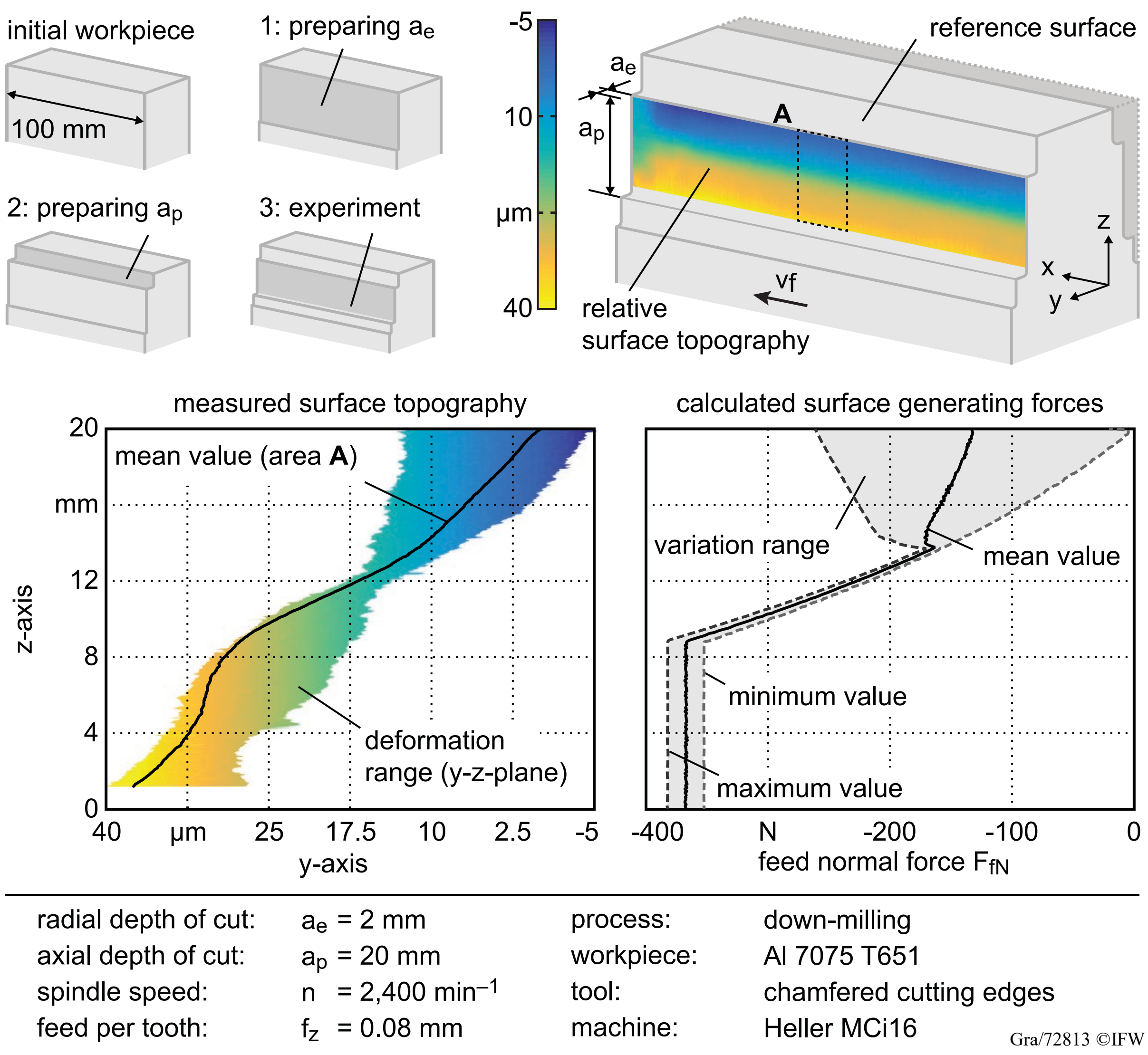

radial depth of cut:	a_e = 2 mm	process:	down-milling
axial depth of cut:	a_p = 20 mm	workpiece:	Al 7075 T651
spindle speed:	n = 2,400 min^{-1}	tool:	chamfered cutting edges
feed per tooth:	f_z = 0.08 mm	machine:	Heller MCi16

Fig. 7.19: Experimental procedure to verify the prediction of the shape of the surface topography. Cutting and edge coefficients for the chamfered tool were chosen as given in Fig. 7.6

and 8 mm. In this range, the deviations from the measured values are also greater. This results from the fact that in this section the deflection of the tool increases in accordance with the beam theory, leading to increased deformation errors, which is not considered by the method based on the feed normal force analysis.

The resulting surface topographies for all used end mills are shown in Fig. 7.20. The upper diagrams show the results for $a_e = 2$ mm and $f_z = 0.08$ mm. All tools lead to a similar deformation error. However, the highest surface error is caused by the end mill with chamfered cutting edges. This result is also provided by the calculated feed normal forces during the machining of the final flank face. Furthermore, the hybrid tool has no discontinuity at $z = 14$ mm compared to the other two tools. This is attributable to the reduced radial immersion of the radial recessed chamfered cutting edges. As a result, the forces are dominated by the equally pitched sharp cutting edges. The influence of the unequal tooth pitch on the forces can also be reduced by runout errors. In this case, a single cutting edge dominates the forces, which reduces discontinuities [Gey02, p. 56].

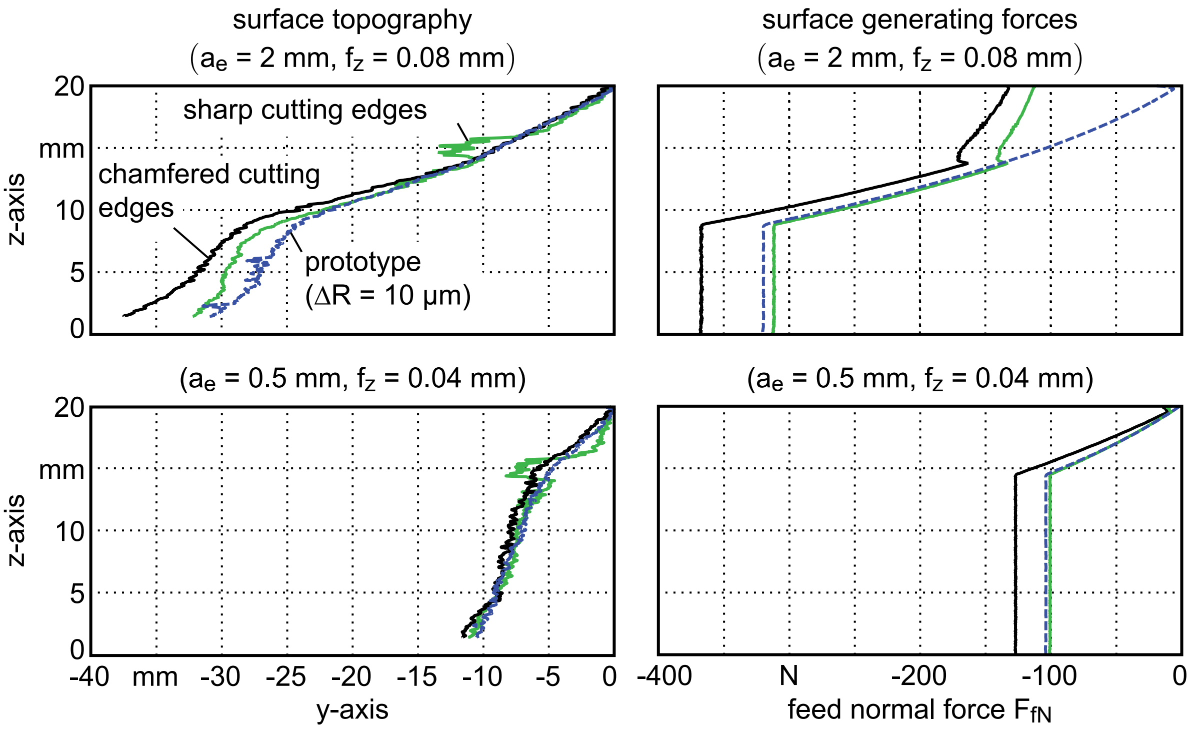

axial depth of cut:	a_p = 20 mm	tan. cutting coeff.:	K_{tc} = 673.3 N/mm^2
spindle speed:	n = 2,400 min^{-1}	rad. cutting coeff.:	K_{rc} = 169.1 N/mm^2
cutting speed:	v_c = 150.8 m/min	axial cutting coeff.:	K_{ac} = 192.8 N/mm^2
workpiece:	Al 7075 T651	axial edge coeff.:	K_{ae} = 1.5 N/mm
machine:	Heller MCi16	process:	down-milling

Gra/72830 ©IFW

Fig. 7.20: Experimental determined surface topography and adequate predicted topography. Cutting and edge coefficients for the tools were chosen as given in Fig. 7.6

This is also shown by the measured surface topography. All workpiece surfaces have no discontinuity at z = 14 mm. Thus, it can be assumed that a runout error based dominance of a single flute occurred for all tools.

The lower diagrams show the results for a_e = 0.5 mm and f_z = 0.04 mm. Surface topography errors are considerable smaller in comparison to the previous discussed results. The shape of the topography for all end mills correlates with the calculated feed normal forces. Due to the small radial immersion a_e, only a small discontinuity at z = 19.5 mm occurs for the end mills with chamfered and sharp cutting edges. A noticeable detail in the resulting surface topography for the end mill with sharp cutting edges can be seen for a_e = 2 mm and 0.5 mm. An artifact around z = 15 mm occurs for both tests. This artifact is attributable to wear of the dominant flute, due to runout, at this position, which is directly projected on the finishing surface.

As it can be seen, an increasing radial immersion leads to a higher tool deflection. Consequently, the surface topography shape error rises. This increase is lower with the new hybrid tool. The calculation of the forces allows to predict the shape of the surface topography without experiments, and thus, can support the design of tools for finishing.

7.3.2 Burr Formation

Additional investigations with the same experimental setup were carried out for burr investigations. A detailed assessment of burr formation is made by digital microscope images (Keyence VHX-600 DSO, Fig. 7.21).

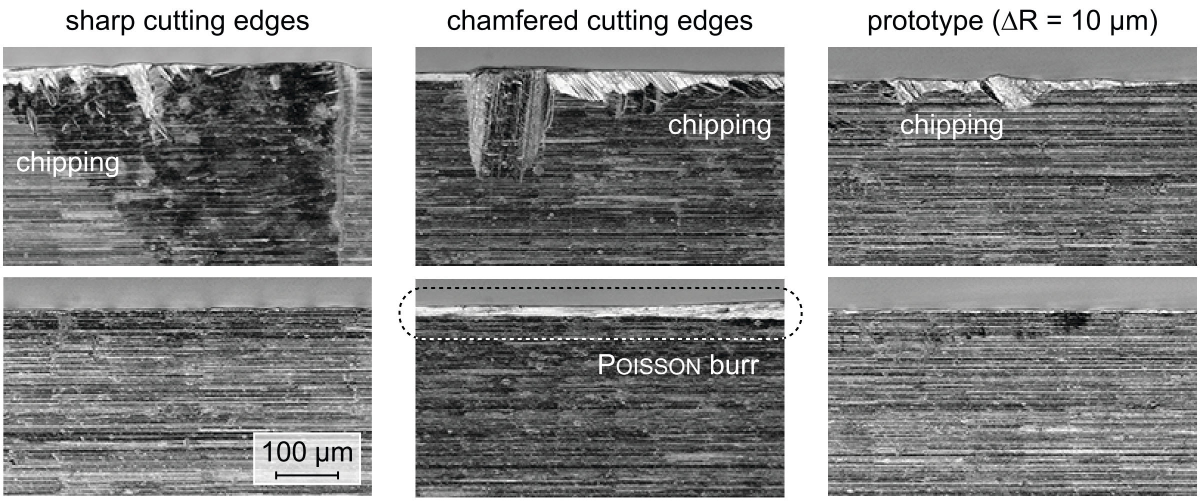

radial depth of cut:	a_e = 0.5 mm	feed per tooth:	f_z = 0.04 mm
axial depth of cut:	a_p = 10 mm	process:	down-milling
spindle speed:	n = 2,400 min^{-1}	workpiece:	Al 7075 T651
cutting speed:	v_c = 150.8 m/min	machine:	Heller MCi16

Gra/72833 ©IFW

Fig. 7.21: Digital microscope images (Keyence VHX-600 DSO) of chipping and burr formation along the workpiece edge.

These images show only a partial section of the 100 mm long path in feed direction. The upper pictures for each tool show a section with a distinctive appearance from the rest of the workpiece edge. Chipping occurred at the workpiece edge for all end mills. Milling processes are prone to this kind of chipping due to the interrupted cut. The lower images show a section of the workpiece edge which is representative for the whole workpiece edge. It can be seen that the end mill with chamfered cutting edges lead to a greater burr formation. Furthermore, these insights of the workpiece edge conditions form the basis to asses the results of the following investigations.

Due to the interrupted cut, burr formation in milling can be uneven along the machined workpiece edge [Gro06, p. 26]. Thus, a detailed analysis of Poisson burr along the whole feed path range is carried out by a three dimensional scanning of the workpiece edge with the previously used confocal point sensor (NanoFocus µscan). The burr height h_0 is determined according to the method shown in Fig. 7.22 a). The workpiece lies on a 30-degree inclined support. The inclination enables the sensor to capture the entire workpiece edge. As shown in the detailed view, the measurement is carried out only near the edge with a resolution of 1 µm in both directions along the path. As shown in the middle picture in Fig. 7.22, a discrepancy occurs between the actual and measured profile. Despite this deviation, the burr height h_0 can be identified by further data processing, as shown in the right picture. Using multiple measuring points at the beginning and at the end of the measuring path, respectively, linear regression lines are determined (dashed lines). Ideally, the two lines are perpendicular to each other. The intersection of the two straight

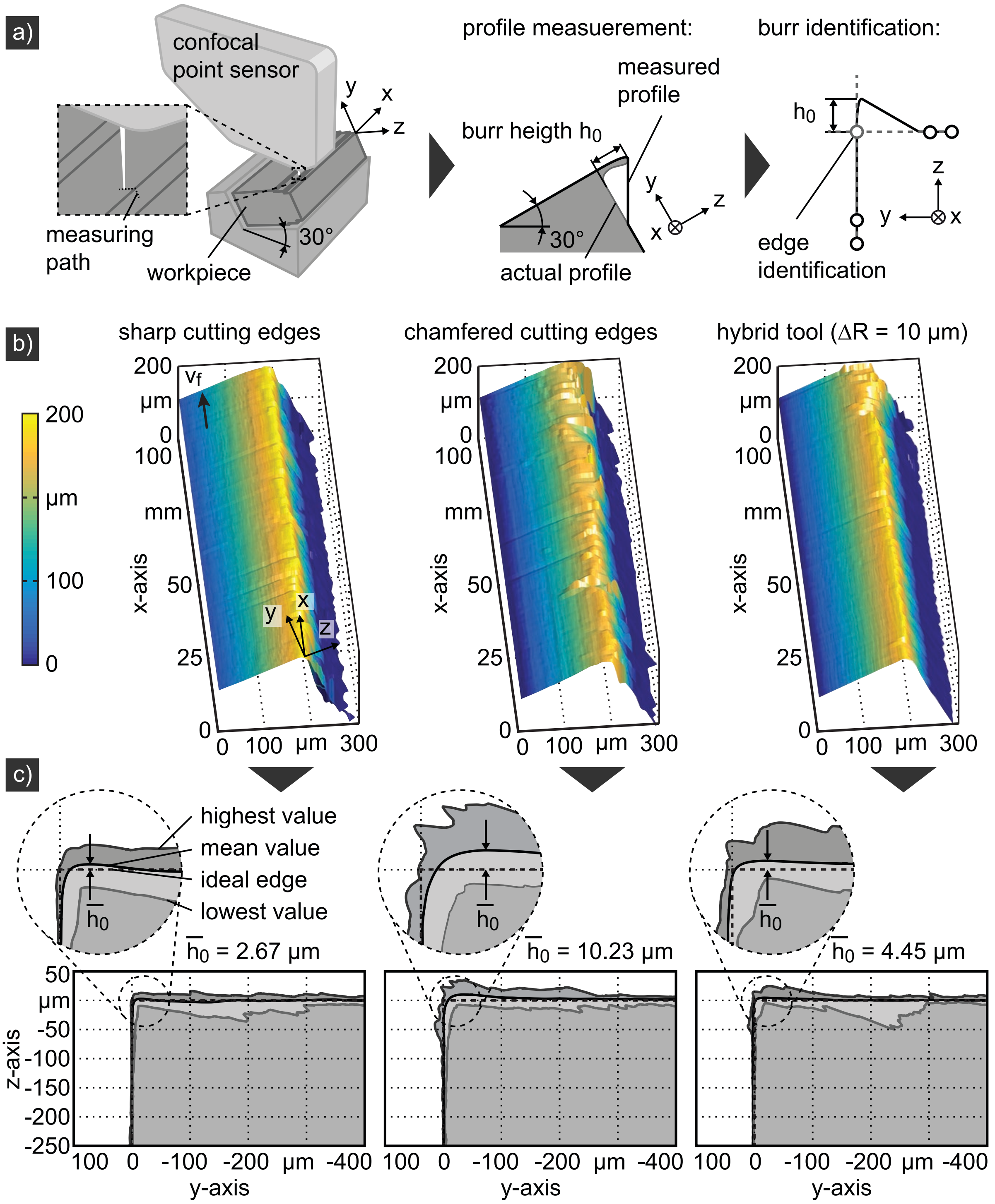

radial depth of cut:	a_e = 0.5 mm	feed per tooth:	f_z = 0.04 mm
axial depth of cut:	a_p = 10 mm	process:	down-milling
spindle speed:	n = 2,400 min^{-1}	workpiece:	Al 7075 T651
cutting speed:	v_c = 150.8 m/min	machine:	Heller MCi16

Gra/72831 ©IFW

Fig. 7.22: a) Method for burr height identification, b) three dimensional overview of the machined workpiece edge and c) resulting mean burr height $\bar{h}_0$.

lines corresponds to the ideal position of the cutting edge. Further, a rotational transformation is performed to provide the data in the machine coordinate system. Finally, h_0 can be determined

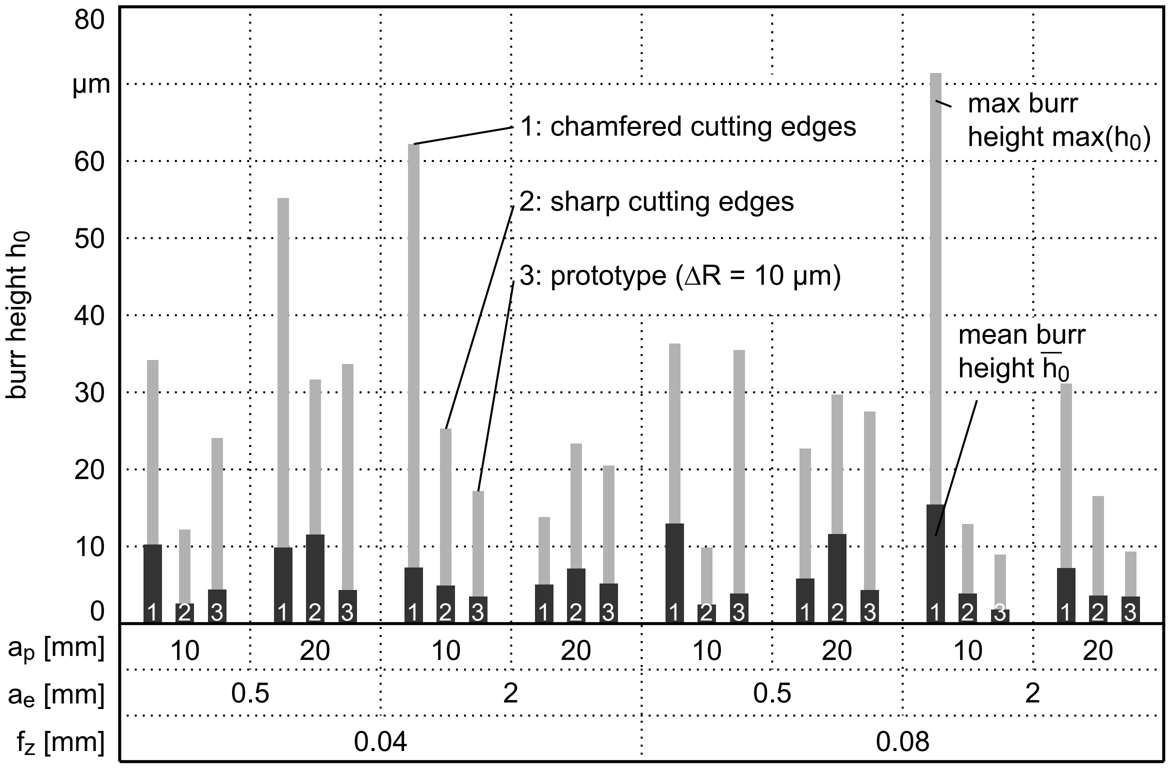

spindle speed: n = 2,400 min^{-1}
cutting speed: v_c = 150.8 m/min
process: down-milling
workpiece: Al 7075 T651
machine: Heller MCi16

Gra/72832 ©IFW

Fig. 7.23: Burr height formation depending on process parameters. The data for the hybrid tool is highlighted by the filled area

on the basis of the difference in z-direction between the ascertained ideal edge position and the highest value of the measured profile. This procedure is applied for all measured profiles along the x-axis. The next measurement in x-direction is carried out at intervals of 0.1 mm. To reduce the influence of individual outliers, a mean value is formed from ten adjacent measurements. Thus, for a workpiece length of 100 mm , this results in 100 averaged measuring paths.

A representation of the workpiece edge shape for all three tools along the entire workpiece length can be seen in Fig. 7.22 b). GOURAD shading [Gou71] was added to outline surface irregularities. These irregularities are particularly pronounced in the workpiece edge area machined with the tool with chamfered cutting edges. Obviously, the contact between the chamfers and the just cut surface are the main reason for this result. This contact heats the workpiece and promotes the formation of burr. With the hybrid tool, this negative effect of the chamfer almost disappears. Irregularities only appear at the exit. However, this could be less due to heat development than to the changed dynamic behavior at the exit. This will be investigated by further experiments with varying process parameters.

The resulting deviations from the measured and ideal workpiece edge shape are summarized in the diagrams in Fig. 7.22 c). The dashed lines represent the ideal workpiece edge location. Furthermore, the highest and lowest measured values of all measured paths are given. These data illustrate the maximum range of deviation from the ideal edge. The low values represent chipping (Fig. 7.21) and the high value the maximum burr height max(h_0). For the calculation of the mean value of burr height $\bar{h}_0$, based on the proposed method (Fig. 7.22 a)), the paths with outbreaks were filtered out. For the chosen process parameters in Fig. 7.22, the tools with chamfered and sharp cutting edges have the highest and lowest value for $\bar{h}_0$, respectively. The hybrid end mill has a slightly higher value than the tool with sharp cutting edges.

A burr comparison between the tools for all carried out experiments is given in Fig 7.23. The process parameters a_e, a_p and f_z were varied. The diagram shows the mean value $\bar{h}_0$ and the maximum value max(h_0). Process parameters related tendencies can not be ascertained from the results. A more extensive experimental plan would be necessary. However, the tool with chamfered cutting edges leads in most cases to the highest values for $\bar{h}_0$ and max(h_0). The hybrid tool has a similar range as the tool with sharp cutting edges. This shows that even chamfered cutting edges with a small radial offset of $\Delta R = 10\ \mu m$ are sufficient to decrease the negative effect of the chamfer on the finished surface.

7.3.3 Thermal Load

As shown in Chapter 7.1.1, the contact between the chamfer and the workpiece material can lead to smearing due to the intense heat input. In case of thin-walled workpieces the heat input can also lead to soft spots or component distortions (Chapter 2.4.4). As stated by Davis the feed and cutting speed must be chosen adequately to reduce the risk of soft spots [Dav94, p. 336]. At the same time, such components have a low rigidity and tend to an unstable machining behavior. This in turn justifies the use of chamfered cutting edges. In the following investigations, the main focus lies in determining the influence of chamfered cutting edges on the heat input into the workpiece material. Thus, only the tools with sharp and chamfered cutting edges are compared and the hybrid tool is neglected.

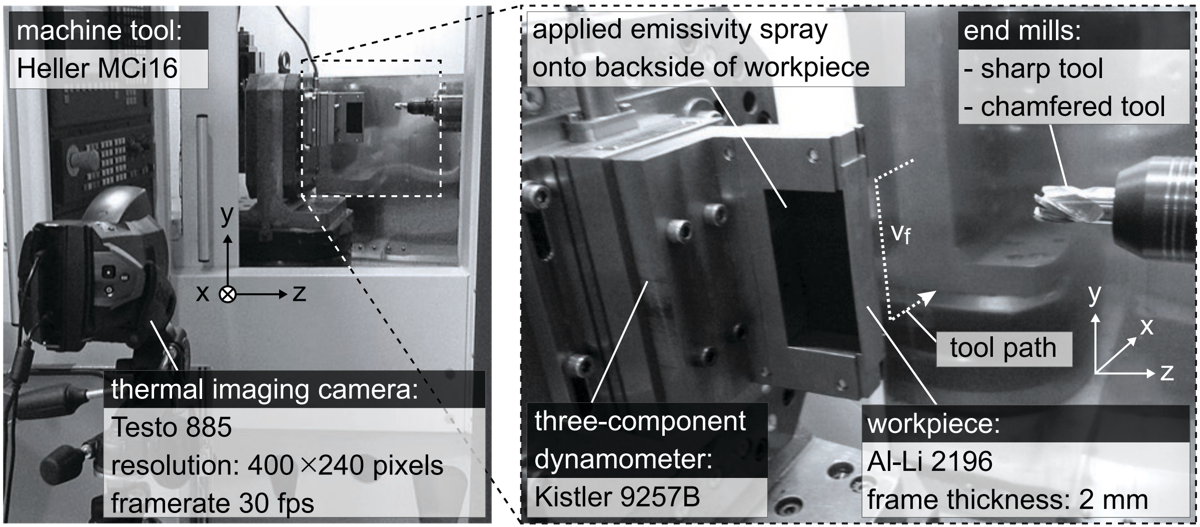
machine tool:
Heller MCi16
y
x
z
thermal imaging camera:
Testo 885
resolution: 400×240 pixels
framerate 30 fps
applied emissivity spray
onto backside of workpiece
end mills:
- sharp tool
- chamfered tool
v_f
tool path
y
x
z
three-component
dynamometer:
Kistler 9257B
workpiece:
Al-Li 2196
frame thickness: 2 mm

Gra/72802 ©IFW

Fig. 7.24: Experimental setup for the determination of thermomechanical effects of chamfered cutting edges (based on [Lau13]).

The experimental setup shown in Fig. 7.24 was applied to study the heat impact during the machining process. Small probes of a fuselage frame of an airplane, consisting of Al-Li 2196, are

used as workpieces. Al-Li 2196 can be considered a replacement for 7075 [Sri14]. This 3rd-Generation Al-Li alloy has a reduced density of ρ = 2.63g/cm^3 due to Li content and allows for weight reduction in aerospace applications [Rio12]. The 2 mm-thin workpiece is mounted on an adapter to increase rigidity. A thermal camera is used to measure the temperature within the black area of the workpiece. This area is covered with an emissivity layer to reduce heat reflections. The tool path is shown in the right picture. Along this path the process parameters are not changed. To isolate the effect of the chamfered area on heat generation, sharp tools are used additionally. In order to be able to investigate the temperature development in a large area, the axial immersion is set to a_p = 25 mm. The radial immersion is a_e = 1 mm. Note that the immersion area is on the opposite side of the temperature measurement area. Due to the thin frame thickness it can be assumed that during the experiment the temperature on the back and front are almost the same, as shown with a heat flux model in [Den16].
A comparison of the temperature distribution between the two tool variants can be seen in Fig. 7.25.

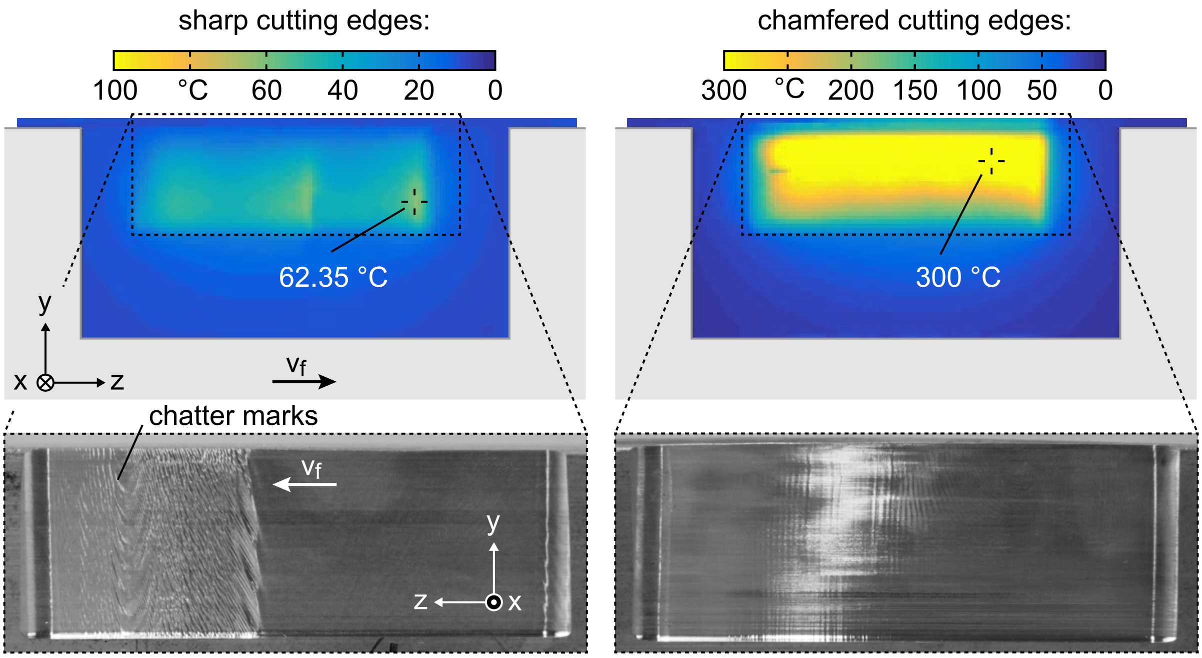

radial depth of cut: a_e = 1 mm
axial depth of cut: a_p = 25 mm
spindle speed: n = 6,000 min^{-1}
cutting speed: v_c = 377 m/min

feed per tooth: f_z = 0.04 mm
process: down-milling (no coolant)
workpiece: Al-Li 2196
machine: Heller MCi16

Gra/72800 ©IFW

Fig. 7.25: Comparison of the heat generation in the workpiece for sharp and chamfered cutting edges.

The illustrated thermograms show the highest temperatures occurring during the machining process by superimposing all recorded images. For the tool with sharp cutting edges, the highest temperature spot reached a temperature of 62.35 °C. This value is clearly exceeded by the tool with chamfered cutting edges and reaches a value of 300 °C for most of the immersion area. The images beneath the thermograms show the machined surfaces, with opposite feed forward direction due to the different record orientation. Clear chatter marks are visible on the surface machined with the tool with sharp cutting edges. A closer look at the thermography map shows

an interruption in the otherwise uniform heat distribution. At the position were chatter begins, the temperature rises. In contrast to that, the contact of the chamfered cutting edges may lead to a significant increased heat generation, but the machining process remains stable.
The coherence between the heat generation and the process forces is given in Fig. 7.26 for another set of process parameters.

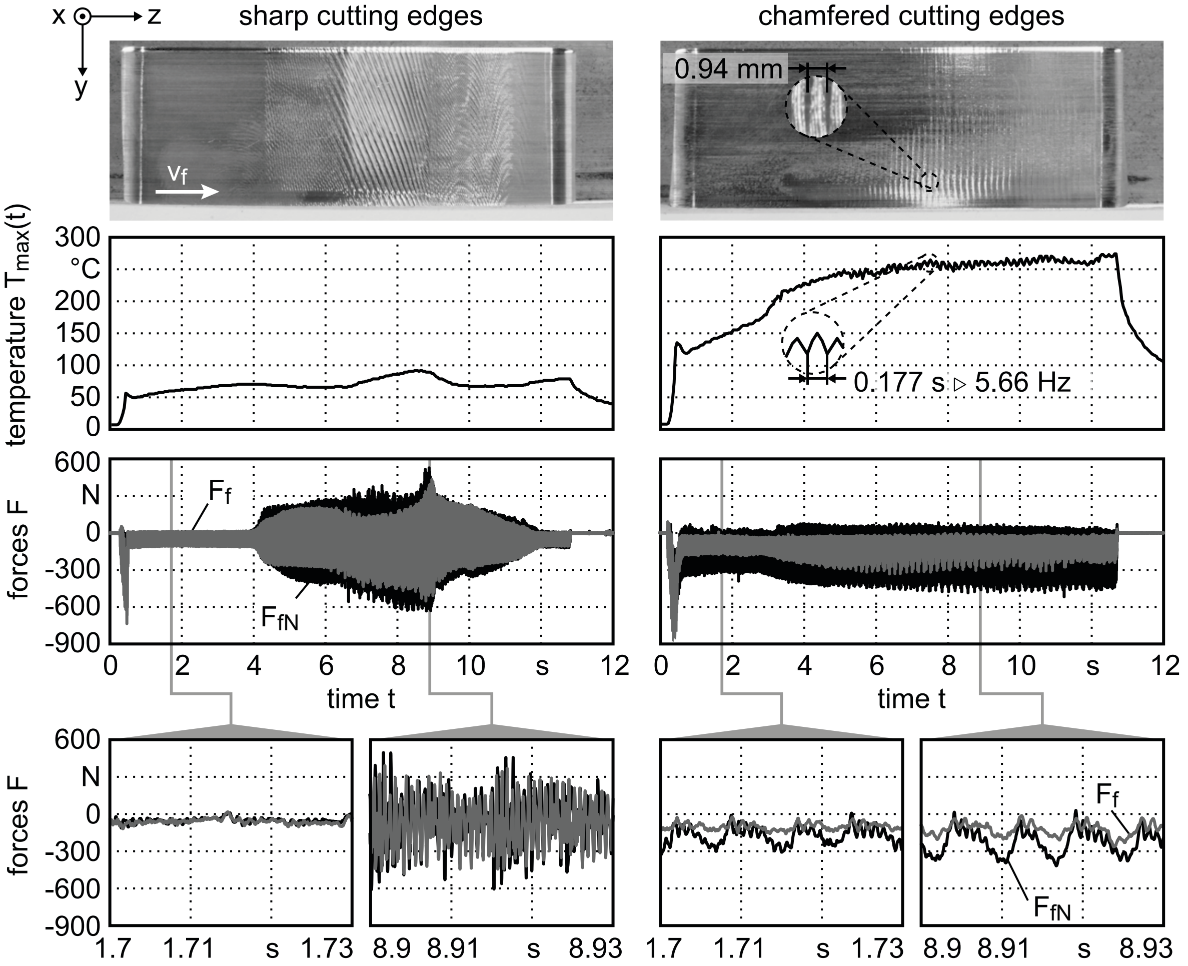

radial depth of cut:	a_e = 1 mm	feed per tooth: f_z	= 0.04 mm
axial depth of cut:	a_p = 25 mm	process:	down-milling (no coolant)
spindle speed:	n = 2,000 min^{-1}	workpiece:	Al-Li 2196
cutting speed:	v_c = 125.7 m/min	machine:	Heller MCi16

Gra/72807 ©IFW

Fig. 7.26: Change of process forces due to contact of chamfered area with flexible workpiece.

On the workpiece, which was processed with the end mill with sharp cutting edges, again chatter marks are clearly visible. As described in [Dav00] the workpiece modes changed with tool movement leading to different dominant chatter frequencies, as it is also visible on the machined workpiece. For the first 9 s of machining, the chatter frequency is 995 Hz in feed direction. Afterward, the chatter frequency shifts to 1, 455 Hz and acts in feed normal direction. The temperature diagram shows the highest measured temperature spot of a single frame. As it can be seen, the maximum temperature T_{max} rises at the spot with the most severe chatter marks. This is caused by the increased process forces, as it can be seen in the force diagram. In comparison, the machining process with the end mill with chamfered cutting edges can be classified as marginally stable, as it will be explained in the following. Already at the beginning of the process, the temperature is significantly higher than in case of the tool with sharp cutting edges and even rises up to 250 °C.In general, the process forces are much higher than with the tool with sharp cutting edges. Especially the forces in feed normal direction experience a significant increase. This results from the low radial immersion, which leads to a contact of the chamfer with the workpiece, causing process damping forces mainly in feed normal direction. In case of full immersion, the increase of the feed force is higher, as shown in Fig. 7.1, due to the fact that in that case the process damping forces act mainly in feed direction. The detailed force views for one tool revolution ($\frac{1}{n}$ = 0.03 s) in the lower diagrams shows that in case of the tool with chamfered cutting edges the forces are not dominated by a chatter frequency. In contrast, this is clearly the case for the tool with sharp cutting edges. The process forces for the tool with chamfered cutting edges are additionally superimposed by a force amplitude with a frequency of approximately 1, 000 Hz. This corresponds to the identified chatter frequency in case of the tool with sharp cutting edges. It can be assumed that a wavy surface is generated, which corresponds to this frequency, and induces a contact between the chamfer and the workpiece and thereby leads to process damping forces, as explained in Chapter 6.1.5, and thus, to an increased heat generation. However, after a machining time of 6 s passed, noticeable marks appear on the machined surface (dashed enlarged segments). In this area, even a fluctuation in the temperature signal can be seen, corresponding to a frequency of 5.66 Hz. There is no significant force increase visible, which is why this process can be assumed to be marginally stable. The reason for this visible marks is that at such low frequencies, the high wavelength of the wavy surface decrease the contact of the chamfer with the workpiece, and thus, no process damping forces can be induced in such a case (Chapter 2.2). Based on the curvature of the process forces it can be stated that the resulting chatter amplitude is not severe.

Further experiments were carried out to investigate the influence of the spindle speed and feed rate on the heat input into the workpiece, as shown in Fig. 7.27. The upper diagrams show the evaluation of the temperature records. The resulting points present the arithmetic mean of the 1, 000 highest temperature values of all recorded frames during one experiment. The left diagrams shows the influence of the feed rate on heat generation. As it can be seen, higher feed rates lower the maximum temperature in case of both tools. The influence of the increasing feed rate, and thus, shorter machining time, exceeds the influence of the increasing process forces. The machining time decreases from 8.3 s (f_z = 0.03 mm) to 1.7 s (f_z = 0.15 mm). The shorter a tool remains at his current position, the less heat is generated in the workpiece at that position. Obviously, large temperature differences arise between the two tools, which results from the process forces. In particular, the feed normal forces for the tool with chamfered cutting edges are significantly higher in comparison to the tool with sharp cutting edges. This is due to the process damping forces, as discussed on the basis of Fig. 7.26, and is also confirmed by the evaluation of stability, as shown in the lower diagram. It must be noted that at f_z = 0.04 mm and 0.08 mm, the heat generation exceeded the adjusted measurement range of the thermal imaging camera (300 °C).

The right diagrams show the results of the spindle speed n dependence. With increasing n, the machining time decreases from 25 s (n = 1, 000 min^{-1}) to 2.5 s (n = 10, 000 min^{-1}). As already discussed in Chapter 6.1.4, the process forces decrease with increasing spindle speeds.

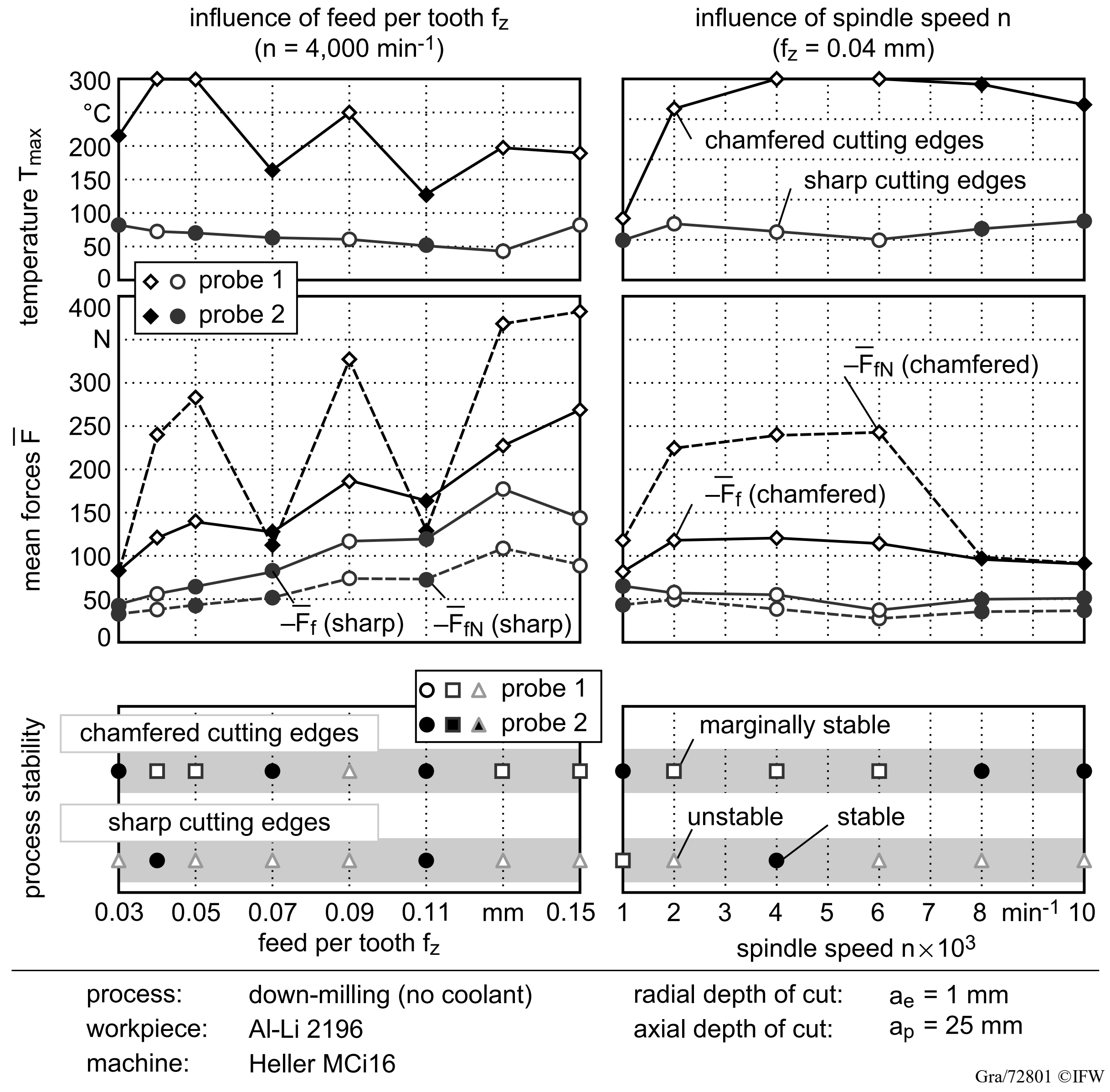

process: down-milling (no coolant)
workpiece: Al-Li 2196
machine: Heller MCi16
radial depth of cut: a_e = 1 mm
axial depth of cut: a_p = 25 mm

Fig. 7.27: Influence of spindle speed and feed per tooth on heat generation and process forces. Material properties were different between white (probe 1) and dark (probe 2) filled markers.

In case of the end mill with sharp cutting edges the resulting maximum temperature is even low for the longest machining time. Thus, no considerable influence of the spindle on the heat generation can be observed, which is in line with the results from [Lau13]. In case of chamfered cutting edges an evident influence arises. Especially from $n = 1,000\,\text{min}^{-1}$ to $2,000\,\text{min}^{-1}$, the maximum temperature rises by almost 150°C. In analogy to a low eigenfrequency (Fig. 7.26), the machined wavy surface has a high wavelength at low spindle speeds, as described in Chapter 2.3.2. This leads to a decreased contact between the chamfer and the workpiece, and thus, only small process damping forces at $n = 1,000\ \text{min}^{-1}$. This correlates with the measured forces. As it can be seen in the force diagram, an evident increase of the feed normal force between the discussed spindle speeds occurs. This also corresponds to the stability investigations from Chapter 7.2.1, where instability occurred at low axial immersion a_p in case of low spindle speeds (Fig. 7.14). A noticeable point is the fact that for the tool with chamfered cutting edges, which are labeled by a black instead of a white filled marker, the measured temperatures are noticeable lower. Same applies for the measured process forces, especially for the feed normal force F_{fN}. The reason for this can be attributed to different micro-structural properties of the workpieces, as shown in Figure 7.28.

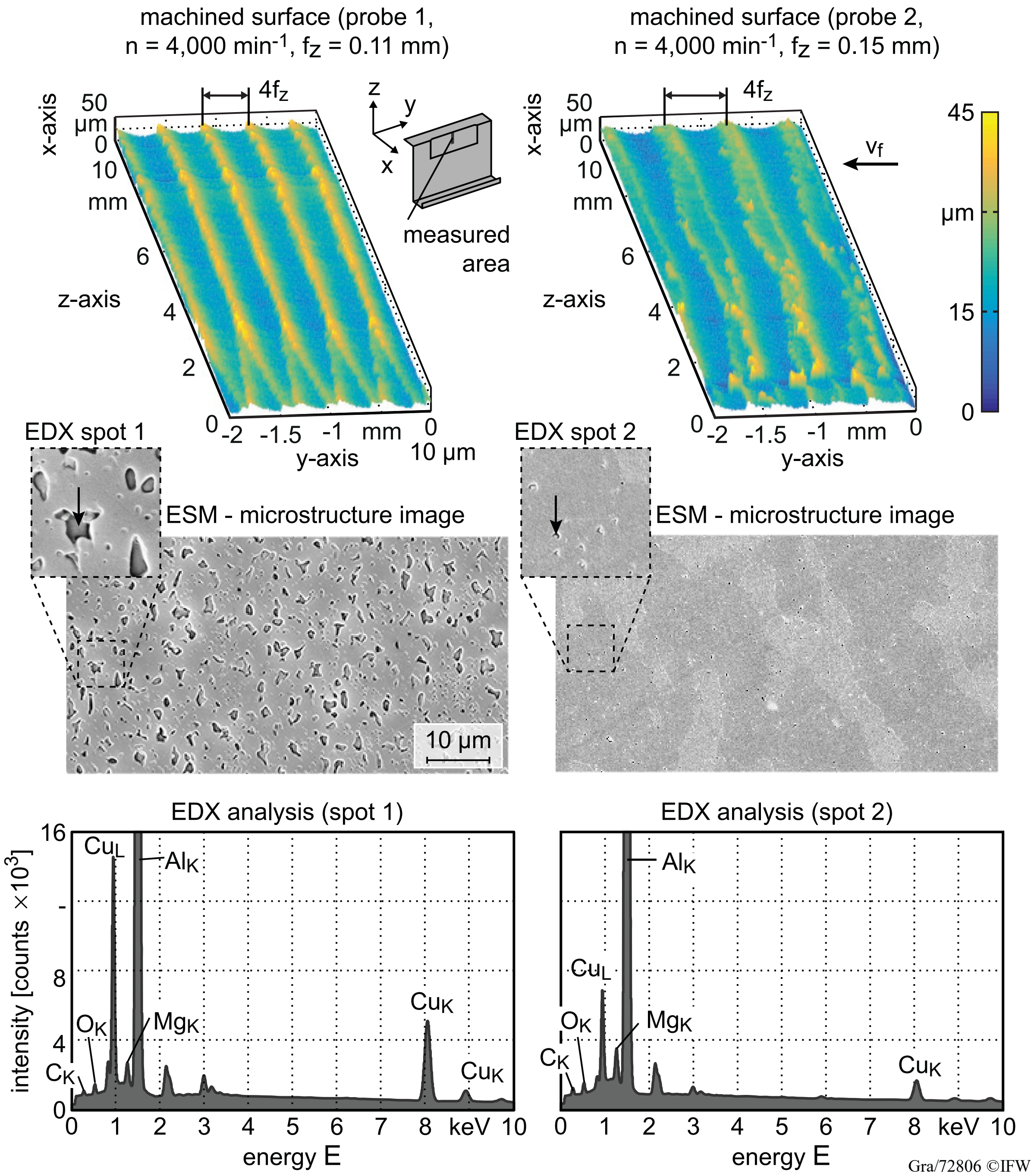

Gra/72806 ©IFW

Fig. 7.28: Analysis of the micro-structural properties of the workpieces (machined by the tool with chamfered cutting edges).

The upper diagrams show a detailed view of the machined surfaces. The left side shows the results for the dark filled markers with low feed normal forces (probe 1). Evident smearing of the feed marks occurred for probe 2 (white filled markers). It can be assumed that the smearing is caused by the contact between the chamfer and the machined surface. This correlates with the high feed normal forces and temperatures. In order to explain the reason for the different behavior during cutting, an image was taken of both probes with a scanning electron microscope (SEM). The view of the microstructure reveals that different thermal treatments where performed on the workpieces. The differences in chemical composition are also confirmed by the elemental analysis carried out by energy-dispersive x-ray spectroscopy (EDX). Based on the measured process forces for the end mill with sharp cutting edges, it can be assumed that the different heat treatments have no significant effect on the tensile strength. Otherwise, larger differences in the process forces would occur between the tests. Based on the smearing and the high forces in feed normal direction in case of the end mill with chamfered cutting edges, a reduction of the elasticity can be assumed. Furthermore, due to the high temperatures, soft spots may occur (Chapter 2.4.4). This risk can be reduced by using the hybrid tool. The resulting heat generation should lie between the tools with chamfered cutting edges and sharp cutting edges. Stability prediction for chamfered cutting edges may be improved if the smearing effect is correctly modeled.

8 Design Recommendation

In this work, enhanced simulation methods and preliminary investigations for the use of a new hybrid tool for roughing and finishing operations were presented. Usually, tools with complex cutting flute geometries, e.g. with unequal helix angles or serrated flutes, are used for such applications. Such end mills enable a process stability increase. The improvement of the stability is based on the geometrically caused disturbance of the regenerative effect. However, those flute geometries have no effect on chatter caused by mode coupling. A much greater increase in process stability can be achieved by using milling cutters with chamfers on the flank face. One of the disadvantages of chamfers is a reduced surface quality.
Based on this knowledge, a tool concept was developed that uses the stability enhancing properties of chamfered cutting edges and at the same time promises the necessary surface qualities for finishing operations. This concept tool has two pairs of the same flutes: two roughing and two finishing flutes. The roughing cutters have chamfered cutting edges and provide the necessary stability. These flutes are radially recessed in comparison to the finishing flutes. This ensures that final surface is cut only by the finishing flutes.

In the following, the most important findings from experiment and simulation are summarized for a practical application. In order to asses the experimental behavior of the hybrid end mill, tools with sharp cutting edges and chamfered cutting edges were included in the experimental investigations. Table 8.1 summarizes the achieved machining results.

Table 8.1: Mutual comparison between the used end mills (●●●: best, ❍●●: average, ❍❍●: worst).

		sharp	chamfered	hybrid tool
machining behavior	process forces:	●●●	❍●●	❍●●
	process stability:	❍❍●	●●●	❍●●
surface finish	smearing:	●●●	❍❍●	●●●
	surface deformation error:	●●●	❍●●	●●●
	burr formation:	●●●	❍❍●	●●●
	thermal load on workpiece:	●●●	❍❍●	

With the hybrid tool the mean values of the **process forces** can be reduced compared to a tool with only chamfered cutting edges. However, the radial offset ΔR leads to different force amplitudes between the sharp and chamfered cutting flutes of the hybrid tool. To balance the load between the different flutes, the necessary tooth pitch p needs to be adjusted. As given in Eq. 6.6, The optimum for p can be calculated as a function of ΔR and the feed per tooth f_z. It follows from Eq. 6.6 that with higher values for f_z the radial offset DeltaR can be increased as well to keep a balanced force load between the flutes. Additionally, the chamfer increases the process forces of the roughing flutes. Therefore, empirical data for the cutting force coefficients are necessary.

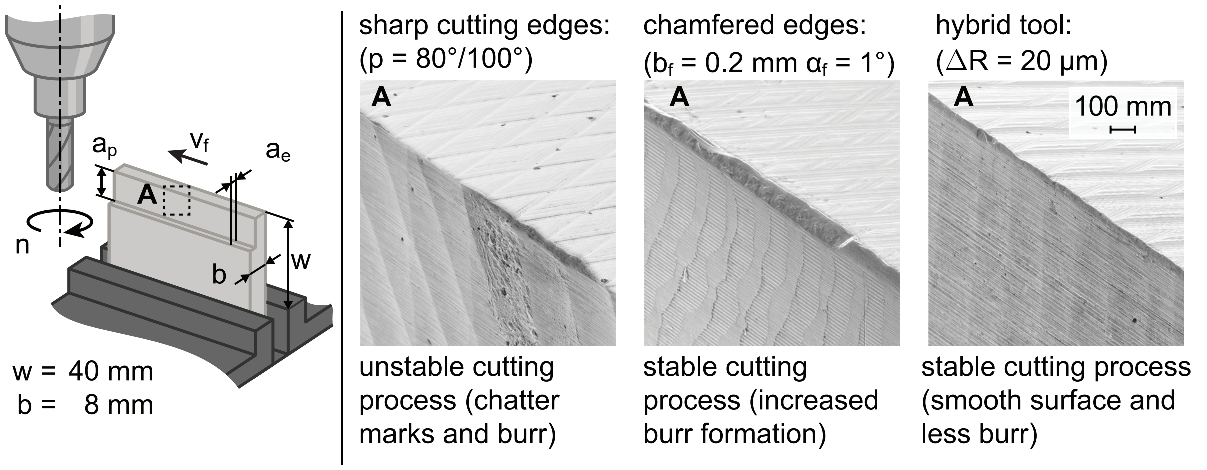

sharp cutting edges: (p = 80°/100°) — unstable cutting process (chatter marks and burr)

chamfered edges: (b_f = 0.2 mm α_f = 1°) — stable cutting process (increased burr formation)

hybrid tool: (ΔR = 20 µm) — stable cutting process (smooth surface and less burr)

feed per tooth: f_z = 0.12 mm
spindle speed: n = 4,000 min^{-1}
axial immersion: a_p = 10 mm
radial immersion: a_e = 2 mm
process: flank milling (no coolant)
workpiece: Al 7075 T651
machine: Heller MCi 16
tool data: D = 20 mm, z = 4

Gra/72781 ©IFW

Fig. 8.1: Final experiments with the hybrid tool.

As it was shown experimentally, tools with chamfered cutting edges offer an obvious **process stability** increase compared to end mills with sharp cutting edges. The hybrid tool allows a stable machining process with the same axial depth of cuts as a tool with only chamfered cutting edges (Fig. 7.14). However, this is only the case for certain ranges of spindle speeds. Thus, the knowledge of these spindle speed ranges is crucial. As it was shown, stable spindle speed areas depend on the geometrical shape of the hybrid tool, e.g. radial offset. Predicted stability charts assist to identify these ranges.

When using chamfered cutting edges, intense **smearing** on the workpiece can occur at high values for f_Z. This risk is minimized by the hybrid tool. If smearing should appear, ΔR needs to be increased. Consequently, the tooth pitch p must be adjusted to keep a balanced force load between the different cutting flutes. For a feed per tooth f_Z of 0.32 mm an increase of ΔR by 10 μm changes p or the distance to the previous sharp cutting flute by –2.8°. In this case the relationship between ΔR and p is linear.

It is important to note the irregularities between individual cutting edges, e.g. unequal tooth pitches, can lead to irregularities in the **surface deformation error**. With the presented method for the prediction of the shape of the surface deformation on the flank face, the influence by the geometrical properties of an end mill can be taken into account.

In order to reduce **burr formation** it must be ensured that the chamfered flutes of the hybrid tool do not contribute to the final surface of the flank face. This might be the case, if the value of the tool runout offset ρ_r is too high. If ρ_r can be estimated or predicted, the necessary minimum value for ΔR results from Eq. 4.43.

If aluminum alloys are machined which are prone to form soft spots, the **thermal load** induced by the contact between the chamfer and the workpiece needs to be considered. In this case, high values for f_Z can be favorable. Although the hybrid tool was not included in these investigations, it can be assumed that the overall temperature development might be reduced. In addition, it must be considered whether the temperature input can be reduced by reducing the chamfer width b_f

or increasing the chamfer angle α_f. The prerequisite is that the process remains stable.

To clarify the possible advantages of the hybrid tool, the following final machining operation was carried out (Fig. 8.1). With a tool with only sharp cutting edges, the process was unstable. Chatter marks are visible on the detailed view A. A tool with only chamfered cutting edges led to a stable machining process but increased burr formation. Using the hybrid tool with ΔR = 20 µm, the process was stable and burr formation, compared to chamfered cutting edges, was reduced. This clarifies that depending on the machining process requirements, the use of the hybrid tool delivers the best result.

9 Summary and Outlook

In order to enable a process-optimized design of the geometry of the new hybrid tool, the necessary mathematical models were derived in this work. For the modeling of the process forces, it was taken into account that the engagement conditions along the cutting flutes can change in the z-direction. This is the case when the tooth pitch changes due to uneven helix angles or in case of a runout error. Furthermore, a runout error or a radial offset of a cutting flute can lead to a sudden change of the engagement conditions. These changes occur near the entry and exit positions of a flute into the workpiece. If a circular flute path is modeled, which is a simplification of the actual flute path, high deviations occur for the modeled engagement conditions at the entry and exit positions. Therefore, a new model was presented, which calculates the resulting chip thicknesses as well as time-delays based on trochoidal flute paths. Furthermore, the derived model for the calculation of the process forces was combined with the heuristic PSO algorithm to determine cutting force coefficients as well as runout errors based on experimental process force data fitting and the ICFM.
The described time-delay changes also had to be integrated into the modeling of the process stability based on the semi-discretization method. Therefore, the existing mathematical models have been extended accordingly. In addition to the SD method, a model for a time-domain simulation of the milling process was derived. This allows the consideration of nonlinearities in comparison to the SD method. Furthermore, the consideration of the process damping forces was extended for the time-domain simulation.

On the basis of preliminary investigations the derived mathematical models were analyzed. It was shown that by combining the trochoidal flute path model with the PSO algorithm and the known ICFM, the identification of the process force coefficients can be performed more accurately than with the known ACFM. Especially when assuming a runout error, the coefficients identified with the ACFM showed significant deviations. With the proposed method, process force coefficients could be determined more exactly due to the implemented runout error identification. Process damping forces are a further influential factor on process stability, and thus, were investigated: The indentation between the cutting edge and the workpiece is described by the process damping area A_{pd} based on the slope of the inner modulation at the cutting edge tip. On the basis of experimental process forces, it could be shown that this assumption can lead to significant deviations. Such a deviation can occur if only the rear part of the chamfer and the workpiece overlap. In this case, it applies that $\alpha_{eff} > 0$, and thus, $A_{pd} = 0$. With increasing vibration frequency, the deviation increases as well. Thus, in case of the stability prediction with the time-domain simulation, the overlapping area between the chamfer and the workpiece is identified based on a Boolean operation.
The second part of the preliminary investigations focuses on theoretical studies to estimate the influence of the geometrical attributes of the hybrid tool on stability and machined surface quality. First, the influence of the radial offset ΔR on process stability was investigated. Increasing values for ΔR lead to a longer immersion length of the additional time-delays caused by the offset. Calculated stability charts with the SD method show a significant increase of stability with larger values for ΔR. This illustrates the disturbance of the regenerative effect by the radial offset. In

addition, the influence of the radial offset, runout error and unequal tooth pitches on the shape of the surface deformation error of the flank face was investigated. It could be shown that the shape of the surface deformation error can be predicted on the basis of the feed normal forces. Thus, during the phase of the tool design optimization the deformation error can be taken into account.

The loads occurring during the machining process were assessed on the basis of a comparison of the process forces. First, mean values for the process forces in dependence of the process parameters were compared. In case of full immersion and varying feed per tooth f_z the feed forces F_f for the tool with chamfered cutting edges are doubled compared to the tool with sharp cutting edges. As it was shown, the increase of F_f results from the fact that the additional load, due to the indentation between the chamfer and the workpiece, acts mainly if a flute segments is near $\varphi(t) = 90^\circ$. With the used hybrid tool, the increase of F_f was almost avoided and similar mean values for the process forces as for the tool with sharp cutting edges were achieved. One of the reason for this result is that the radial recession $\Delta R = 10\ \mu m$ of the chamfered flutes is comparable to a reduction of f_z. Furthermore, the high load during machining with the tool with chamfered cutting edges led to smearing of the workpiece material. This occured due to the high temperature input into the workpiece. With the alternating engagement of sharp and chamfered cutting edges in case of the new hybrid tool, smearing could be avoided. For the identification of the cutting force coefficients based on the ICFM, full immersion, up- and down-milling operations were carried out. In order to avoid vibrations, a low spindle speed n was chosen. In addition, small values were chosen for the radial and axial depth of cut. As a result of this procedure, even slight overlaps occurred accordingly. In combination with the used hybrid tool, which had a high radial offset of $\Delta R = 50\ \mu m$, high force amplitudes occurred during the immersion of the sharp cutting edges. However, these differences decrease with high values for the feed forward velocity v_f (if $f_z >> \Delta R$) and high spindle speeds n (additional load due to indentation between chamfered flutes and workpiece).

The process stability was investigated based on the identified input and distortion data (process force coefficients, modal parameters and runout error) within the scope of the preliminary experiments. As expected, the stability of the tool with sharp cutting edges was the lowest of all investigated tools over the entire spindle speed range. The tool with chamfered cutting edges yielded a high stability for almost all performed cutting tests. In a wide speed range, stability tests were limited to $a_p = 19$ mm due to high forces and the risk of smearing. The lowest stability was achieved at low spindle speeds. In general, lower eigenfrequencies are excited at low speeds. This results in a wavy workpiece surface with a long wavelength, and thus, the indentation between the chamfered cutting edge and the workpiece decreases. Furthermore, chatter occurred due to the excitement of low eigenfrequencies within a range of high spindle speeds. First, a hybrid tool with a radial offset of $\Delta R = 10\ \mu m$ was considered. The achieved stability limit was significant higher than for the tool with sharp cutting edges. For a wide spindle speed range, the same stability was achieved as with the tool with chamfered cutting edges. Thus, with the knowledge of the process parameters that assure a stable machining behavior, the hybrid tool can provide the best possible stability. In addition to the experimental stability data, process stability was also calculated using the SD method. In case of the tool with sharp cutting edges, a good agreement between the experimental and calculated process stability was achieved. This proofs that the coefficients and the modal parameters have been identified correctly and with the required accuracy. Furthermore, the calculated stability charts with and without the consideration of runout error show only marginal differences. In case of the tool with chamfered edges as well as the hybrid tool, runout consideration leads to apparent changes in the stability. However, significant differences between the experimental and calculated process stability occurred. One of the reasons for this error is the applied process damping model for the stability prediction based on the SD method. This model assumes an indentation between the chamfered flank face and the workpiece without an interruption during the immersion. Thus, a process damping model which considers at which immersion positions an indentation occurs was applied for time-domain simulations. However, the predicted stability charts showed again noticeable differences from the experimental results. In this respect, other factors must be considered, e.g. the influence of temperature development in the workpiece due to the contact with the chamfer. It is likely that higher temperatures affect the material properties and thus also the resulting process forces. This was evident in the preliminary experiments, were smearing occurred for the tool with chamfered cutting edges. Further experimental investigations were carried out to determine the influence of the radial offset on the stability. For this purpose, additional hybrid tools with different radial offsets ΔR were used. With a higher radial offset, the variation of time-delays increases. To a certain extent, this corresponds with a higher stability. At the same time, however, the immersion range of the chamfered cutting edges is shortened, and thus, the effect of process damping is weakened. This influence is much more dominant, so that a decrease in stability could be observed with increasing ΔR at most of the investigated spindle speeds.

The quality of the surface finish was first evaluated based on the surface deformation error. For the hybrid tool a similar result was achieved as for the tool with sharp cutting edges. The largest surface deformation errors occurred for the end mill with chamfered cutting edges. The surface deformation error was determined experimentally. Furthermore, the shape of the deformation was also predicted based on the feed normal forces. A good match between this method and the experimental results could be achieved. Thus, the shape of the surface deformation error of the flank face can be predicted on the basis of the calculation of the feed normal forces as a function of the process parameters and the tool geometry.

For the investigation of urr formation, the radial and axial immersion as well as the feed per tooth were varied. In analogy to the preliminary investigations, it was found that the tool with chamfered cutting flutes had the largest burr formation. The hybrid tool returned similar results as the tool with sharp cutting edges. In this respect, it can be stated that the hybrid tool is suitable for finishing operations.

Another negative effect of the chamfer on the surface quality is caused by the high thermal load on the workpiece. As shown, the contact between the chamfer and the workpiece leads to a significant increase in temperature. This can cause a negative influence on the material properties of aluminum alloys. These investigations focused on the comparison between sharp and chamfered cutting edges. THus, the hybrid tool was not included. However, as shown in the previous experimental investigations, the risk of smearing can be reduced with the hybrid tool. In this respect, it can be assumed that the temperature increase is lower than with the tool with chamfered cutting edges.

The achieved results and gained knowledge provide a solid foundation concerning the roughing and finishing capability of the proposed hybrid end mill. However, in the course of this thesis, further research topics arose which are worth to investigate:

- The deviations between the the experimental and predicted stability show clearly that the applied model for the velocity dependent force component (process damping forces) is insufficient. The indentation between the chamfered cutting edge and the workpiece materials is a complex process. Due to the machining process and the additional load caues by the indentation between the chamfer and the workpiece, the temperature in the workpiece increase. This may cause a corresponding influence on the material properties. This, in turn, may abbreviate the process forces. In addition, plastic deformations of the material occur (smearing) which also influence the contact between the chamfer and the workpiece. In this respect, basic research, e.g. plane cutting tests, for an extended understanding of the contact is recommended.
- The deviations in the stability calculation due to insufficient process damping modeling superimposed the study of the radial offset. Same applies for the influence of the runout error. Thus, stability investigations for end mills with sharp cutting edges and with a defined runout error and recessed flutes are recommended.
- The investigations carried out focused on a tool with four cutting flutes. However, the principle of the hybrid tool can also be applied to milling cutters with a different number of flutes. Furthermore, in case of a four fluted end mill, the number of chamfered (sharp) cutting edges can be increased to improve stability (surface finish).
- The advantages of the proposed hybrid tool in terms of productivity need to be verified with industrial application. The design of the hybrid tool can be carried out based on the analysis of the machining requirements and in accordance to the achieved knowledge in this thesis. Subsequently, an experimental comparison can be made between the hybrid tool and standard tools used for the practice example.

In conclusion, it can be stated that the obtained results and the developed simulation methods for the hybrid tool have laid a solid foundation for application-oriented research topics.

Bibliography

[Abd73] Abdelmoneim, M. E.; Scrutton, R. F.: The tribology of cutting tools during finish machining. Wear 25(1973), no. 1, pp. 45–53. ISSN 0043-1648. DOI: 10.1016/0043-1648(73)90119-1.

[Ack83] Ackermann, J.: Analyse und Synthese, vol. 1. Springer, Berlin, 2 edn. ISBN 3540119159. URL `http://www.worldcat.org/oclc/888828072`. 1983.

[Ahm10] Ahmadi, K.; Ismail, F.: Machining chatter in flank milling. International Journal of Machine Tools and Manufacture 50(2010), no. 1, pp. 75–85. ISSN 0890-6955. DOI: 10.1016/j.ijmachtools.2009.09.005.

[Ahm11a] Ahmadi, K.: Machining Chatter in Flank Milling and Investigation of Process Damping in Surface Generation. Ph.D., Department of Mechanical and Mechatronics Engineering , University of Waterloo, Waterloo, Ontario, Canada. 2011.

[Ahm11b] Ahmadi, K.; Ismail, F.: Analytical stability lobes including nonlinear process damping effect on machining chatter. International Journal of Machine Tools and Manufacture 51(2011), no. 4, pp. 296–308. ISSN 08906955. DOI: 10.1016/j.ijmachtools.2010.12.008.

[Ahm12] Ahmadi, K.; Ismail, F.: Stability lobes in milling including process damping and utilizing Multi-Frequency and Semi-Discretization Methods. International Journal of Machine Tools and Manufacture 54-55(2012), no. 0, pp. 46–54. ISSN 0890-6955. DOI: 10.1016/j.ijmachtools.2011.11.007.

[Ahn11] Ahn, I. H.; Hwang, J. H.; Choi, W. C.: Error analysis of the cutting coefficients and optimization of calibration procedure for cutting force prediction. Proceedings of the Institution of Mechanical Engineers, Part B: Journal of Engineering Manufacture 1(2011), no. -1, pp. 1–14. ISSN 0954-4054. DOI: 10.1243/09544054JEM2006.

[Air22] Airey, J.; Oxford, C. J.: On the Art of Milling. In: American Society of Mechanical Engineers (Ed.), Transactions of the American Society of Mechanical Engineers, vol. 43, pp. 549–614. ASME, New York. 1922.

[Alt00] Altintas, Y.: Manufacturing automation: Metal cutting mechanics, machine tool vibrations, and CNC design / Yusuf Altintas. Cambridge University Press, Cambridge, 1 edn. ISBN 0521659736. URL `http://www.worldcat.org/oclc/41211659`. 2000.

[Alt04] Altintas, Y.; Weck, M.: Chatter Stability of Metal Cutting and Grinding. CIRP Annals - Manufacturing Technology 53(2004), no. 2, pp. 619–642. ISSN 0007-8506. DOI: 10.1016/S0007-8506(07)60032-8.

[Alt08] Altintas, Y.; Eynian, M.; Onozuka, H.: Identification of dynamic cutting force coefficients and chatter stability with process damping. CIRP Annals - Manufacturing Technology 57(2008), no. 1, pp. 371–374. ISSN 0007-8506. DOI: 10.1016/j.cirp.2008.03.048.

[And61] Andrew, C.; Tobias, S. A.: A critical comparison of two current theories of machine tool chatter. International Journal of Machine Tool Design and Research 1(1961), no. 4, pp. 325–335. ISSN 0020-7357. DOI: 10.1016/0020-7357(61)90010-5.

[Ari09] Arizmendi, M.; Fernández, J.; Gil, A.; Veiga, F.: Effect of tool setting error on the topography of surfaces machined by peripheral milling. International Journal of Machine Tools and Manufacture 49(2009), no. 1, pp. 36–52. ISSN 0890-6955. DOI: 10.1016/j.ijmachtools.2008.08.004.

[Arm89] Armarego, E.; Deshpande, N. P.: Computerized Predictive Cutting Models for Forces in End-Milling Including Eccentricity Effects. CIRP Annals - Manufacturing Technology 38(1989), no. 1, pp. 45–49. ISSN 0007-8506. DOI: 10.1016/S0007-8506(07)62649-3.

[Arr13] Arrazola, P.; Özel, T.; Umbrello, D.; Davies, M.; Jawahir, I.: Recent advances in modelling of metal machining processes. CIRP Annals - Manufacturing Technology (2013).

[Ast05] Astakhov, V. P.: On the inadequacy of the single-shear plane model of chip formation. International Journal of Mechanical Sciences 47(2005), no. 11, pp. 1649–1672. ISSN 0020-7403. DOI: 10.1016/j.ijmecsci.2005.07.002.

[Ast06] Astakhov, V. P.: An opening historical note. International Journal of Machining and Machinability of Materials 1(2006), no. 1, p. 3. ISSN 1748-5711. DOI: 10.1504/IJMMM.2006.010656.

[Aur09] Aurich, J.; Dornfeld, D.; Arrazola, P.; Franke, V.; Leitz, L.; Min, S.: Burrs - Analysis, control and removal. CIRP Annals - Manufacturing Technology 58(2009), no. 2, pp. 519–542. ISSN 0007-8506. DOI: 10.1016/j.cirp.2009.09.004.

[Bac10] Bachrathy, D.; Stepan, G.: Time-periodic velocity-dependent process damping in milling processes: Conference proceedings. In: Y. Altintas (Ed.), 2nd International CIRP Process Machine Interactions Conference, vol. 2, pp. 1–12. University of British Columbia, Vancouver. ISBN 9780986633102. 2010.

[Bha14] Bhattacharya, A.; Bera, T. K.; Thakur, A.: On Cutter Deflection Profile Errors in End Milling: Modeling and Experimental Validation. Materials and Manufacturing Processes 30(2014), no. 8, pp. 1042–1059. ISSN 1042-6914. DOI: 10.1080/10426914.2014.973598.

[Bra05] Bravo, U.; Altuzarra, O.; López de Lacalle, L. N.; Sánchez, J. A.; Campa, F. J.: Stability limits of milling considering the flexibility of the workpiece and the machine. International Journal of Machine Tools and Manufacture 45(2005), no. 15, pp. 1669–1680. ISSN 0890-6955. DOI: 10.1016/j.ijmachtools.2005.03.004.

[Bud94] Budak, E.; Altintas, Y.: Peripheral milling conditions for improved dimensional accuracy. International Journal of Machine Tools and Manufacture 34(1994), no. 7, pp. 907–918. ISSN 0890-6955. DOI: 10.1016/0890-6955(94)90024-8.

[Bud96] Budak, E.; Altintass, Y.; Armarego, E. J. A.: Prediction of Milling Force Coefficients From Orthogonal Cutting Data. Journal of Manufacturing Science and Engineering 118(1996), no. 2, pp. 216–224. DOI: 10.1115/1.2831014.

[Bud10] Budak, E.; Tunc, L.: Identification and modeling of process damping in turning and milling using a new approach. CIRP Annals - Manufacturing Technology 59(2010), no. 1, pp. 403–408. ISSN 0007-8506. DOI: 10.1016/j.cirp.2010.03.078.

[Cah05] Cahlon, B.; Schmidt, D.: Asymptotic stability of a mechanical robotics model with damping and delay. Journal of Mathematical Analysis and Applications 303(2005), no. 1, pp. 36–53. DOI: 10.1016/j.jmaa.2004.06.036.

[Cam02] Campomanes, M. L.: Kinematic and Dynamics of Milling with Roughing Endmills. In: D. Dudzinski; A. Molinari; H. Schulz (Eds.), Metal cutting and high speed machining, pp. 129–140. Kluwer Academic/Plenum, New York and London. ISBN 0306467259. 2002.

[Cam03] Campomanes, M. L.; Altintas, Y.: An Improved Time Domain Simulation for Dynamic Milling at Small Radial Immersions. Journal of Manufacturing Science and Engineering 125(2003), no. 3, p. 416. ISSN 10871357. DOI: 10.1115/1.1580852.

[Che88] Chen, N.; Pun, W. K.: Stresses at the cutting tool wear land. International Journal of Machine Tools and Manufacture 28(1988), no. 2, pp. 79–92. ISSN 0890-6955. DOI: 10.1016/0890-6955(88)90021-1.

[Chi98] Chiou, R. Y.; Liang, S. Y.: Chatter stability of a slender cutting tool in turning with tool wear effect. International Journal of Machine Tools and Manufacture 38(1998), no. 4, pp. 315–327. ISSN 0890-6955. DOI: 10.1016/S0890-6955(97)00079-5.

[Coo55] Cook, N. H.: Self-excited vibrations in metal cutting. Ph.D. thesis, Cambridge, MIT. 1955.

[Coo59] Cook, N. H.: Self-excited vibrations in metal cutting. Journal of Engineering for Industry 81(1959), pp. 183–186.

[Dav90] Davies, J.: Machining of Aluminum and Aluminum Alloys. In: J. Davies (Ed.), ASM Handbook, pp. 761–804. ASM International, Materials Park, Ohio. ISBN 978-0-87170-022-3. 1990.

[Dav94] Davies, J.: Aluminium and aluminium alloys. ASM International, Materials Park, 2 edn. ISBN 978-0871704962. 1994.

[Dav00] Davies, M. A.; Balachandran, B.: Impact Dynamics in Milling of Thin-Walled Structures. Nonlinear Dynamics 22(2000), no. 4, pp. 375–392. ISSN 0924090X. DOI: 10.1023/A:1008364405411.

[Dav17] Davoudinejad, A.; Parenti, P.; Annoni, M.: 3D finite element prediction of chip flow, burr formation, and cutting forces in micro end-milling of aluminum 6061-T6. Frontiers of Mechanical Engineering 12(2017), no. 2, pp. 203–214. ISSN 2095-0233. DOI: 10.1007/s11465-017-0421-6.

[Del92] Delio, T.; Tlusty, J.; Smith, S.: Use of Audio Signals for Chatter Detection and Control. Journal of Manufacturing Science and Engineering 114(1992), no. 2, p. 146. ISSN 10871357. DOI: 10.1115/1.2899767.

[Dem09] Demir, H.; Gündüz, S.: The effects of aging on machinability of 6061 aluminium alloy. Materials & Design 30(2009), no. 5, pp. 1480–1483. ISSN 02613069. DOI: 10.1016/j.matdes.2008.08.007.

[Den10] Denkena, B.; Leon, L. d.; Grove, T.: Prozessstabilität eines kordelierten Schaftfräsers. ZWF - Zeitschrift für wirtschaftlichen Fabrikbetrieb 105(2010), no. 1-2, pp. 37–41. URL `http://www.zwf-online.de/ZW110246`.

[Den12] Denkena, B.; Koehler, J.; Rehe, M.: Influence of the Honed Cutting Edge on Tool Wear and Surface Integrity in Slot Milling of 42CrMo4 Steel. Procedia CIRP 1(2012), pp. 190–195. ISSN 22128271. DOI: 10.1016/j.procir.2012.04.033.

[Den16] Denkena, B.; Brüning, J.; Niederwestberg, D.; Grabowski, R.: Influence of Machining Parameters on Heat Generation During Milling of Aluminum Alloys. Procedia CIRP 46(2016), pp. 39–42. ISSN 22128271. DOI: 10.1016/j.procir.2016.03.192.

[Den17] Denkena, B.; Köhler, J.; Grabowski, R.: Patent: FRÄSWERKZEUG UND UMFANGSFRÄSVERFAHREN. Weltorganisation für geistiges Eigentum - Internationales Büro (WO 2015/082029 Al1). 2017.

[Des12] Desai, K. A.; Rao, P.: On cutter deflection surface errors in peripheral milling. Journal of Materials Processing Technology 212(2012), no. 11, pp. 2443–2454. ISSN 0924-0136. DOI: 10.1016/j.jmatprotec.2012.07.003.

[Dom10] Dombovari, Z.; Altintas, Y.; Stépán, G.: The effect of serration on mechanics and stability of milling cutters. International Journal of Machine Tools and Manufacture 50(2010), no. 6, pp. 511–520. ISSN 0890-6955. DOI: 10.1016/j.ijmachtools.2010.03.006.

[Ebe07] Eberhart, R. C.; Shi, Y.: Computational intelligence: Concepts to implementations. Elsevier/Morgan Kaufmann Publishers, Amsterdam and Boston. ISBN 978-1-55860-759-0. 2007.

[Eis70] Eisele, J. A.; Mason, R. M.: Applied matrix and tensor analysis. Wiley-Interscience, New York. ISBN 978-0471234654. 1970.

[Elb94] Elbestawi, M. A.; Ismail, F.; Du, R.; Ullagaddi, B. C.: Modelling Machining Dynamics Including Damping in the Tool-Workpiece Interface. Journal of Engineering for Industry 116(1994), no. 4, p. 435. DOI: 10.1115/1.2902125.

[Ema89] Ema, S.; Davies, R.: Cutting performance of end mills with different helix angles. International Journal of Machine Tools and Manufacture 29(1989), no. 2, pp. 217–227. ISSN 0890-6955. DOI: 10.1016/0890-6955(89)90033-3.

[Eng99] Engin, S.; Altintas, Y.: Generalized modeling of milling mechanics and dynamics: part 1 - helical end mills. American Society of Mechanical Engineers, Manufacturing Engineering Division, MED 10(1999), pp. 345–352.

[Eno02] Enomoto, S.; Ioi, T.; Kato, K.; Zhou, L.; Liu, X.: Burr reduction with a fine-scrape cutter. Journal of Materials Processing Technology 124(2002), no. 1-2, pp. 255–258. ISSN 0924-0136. DOI: 10.1016/S0924-0136(02)00112-7.

[Faa07] Faassen, R. P. H.; van de Wouw, N.; Nijmeijer, H.; Oosterling, J. A. J.: An Improved Tool Path Model Including Periodic Delay for Chatter Prediction in Milling. Journal of Computational and Nonlinear Dynamics 2(2007), no. 2, p. 167. ISSN 15551423. DOI: 10.1115/1.2447465.

[Fan05] Fang, N.; Wu, Q.: The effects of chamfered and honed tool edge geometry in machining of three aluminum alloys. International Journal of Machine Tools and Manufacture 45(2005), no. 10, pp. 1178–1187. ISSN 0890-6955. DOI: 10.1016/j.ijmachtools.2004.12.003.

[Far94] Farkas, M.: Periodic Motions, *Applied Mathematical Sciences*, vol. 104. Springer, New York, NY. ISBN 978-1-4419-2838-2. DOI: 10.1007/978-1-4757-4211-4. 1994.

[Fis97] Fischer, H.: Die Größe der Widerstände gegen das Abheben von Metallspänen. Zeitschrift des Vereins deutscher Ingenieure 18(1897), pp. 504–508.

[Flo83] Floquet, G.: Sur les équations différentielles linéaires à coefficients périodiques. Annales scientifiques de l'École Normale Supérieure 12(1883), no. 2, pp. 47–88.

[Fuj77] Fujii, Y.; IWABE, H.; SUZUKI, M.: Effect of Dynamic Behaviour of End Mill in Machining on Work Accuracy (1st Report). Journal of the Japan Society of Precision Engineering 43(1977), no. 511, pp. 807–813. ISSN 0374-3543. DOI: 10.2493/jjspe1933.43.807.

[Gas98] Gasparetto, A.: A System Theory Approach to Mode Coupling Chatter in Machining. Journal of Dynamic Systems, Measurement, and Control 120(1998), no. 4, p. 545. ISSN 00220434. DOI: 10.1115/1.2801501.

[Gey02] Gey, C.: Prozessauslegung für das Flankenfräsen von Titan. Dr.-Ing.-Dissertation, Leibniz-Universität Hannover, Institut für Fertigungstechnik und Werkzeugmaschinen. 2002.

[Gil76] Gillespie, L. K.; Blotter, P. T.: The Formation and Properties of Machining Burrs. Journal of Engineering for Industry 98(1976), no. 1, p. 66. ISSN 00220817. DOI: 10.1115/1.3438875.

[Gou71] Gouraud, H.: Continuous Shading of Curved Surfaces. IEEE Transactions on Computers C-20(1971), no. 6, pp. 623–629. ISSN 0018-9340. DOI: 10.1109/T-C.1971.223313.

[Gov05] Govekar, E.; Gradisek, J.; Kalveram, M.; Insperger, T.; Weinert, K.; Stépàn, G.; Grabec, I.: On Stability and Dynamics of Milling at Small Radial Immersion. CIRP Annals - Manufacturing Technology 54(2005), no. 1, pp. 357–362. ISSN 0007-8506. DOI: 10.1016/S0007-8506(07)60122-X.

[Gra04] Gradišek, J.; Kalveram, M.; Weinert, K.: Mechanistic identification of specific force coefficients for a general end mill. International Journal of Machine Tools and Manufacture 44(2004), no. 4, pp. 401–414. ISSN 0890-6955. DOI: 10.1016/j.ijmachtools.2003.10.001.

[Gro06] Groppe, M.: Prozessauslegung für die Hochleistungsfräsbearbeitung von Aluminium-Strukturbauteilen. Dr.-Ing.-Dissertation, Leibniz-Universität Hannover, Institut für Fertigungstechnik und Werkzeugmaschinen. 2006.

[Gro14] Grossi, N.; Sallese, L.; Scippa, A.; Campatelli, G.: Chatter Stability Prediction in Milling Using Speed-varying Cutting Force Coefficients. Procedia CIRP 14(2014), pp. 170–175. ISSN 22128271. DOI: 10.1016/j.procir.2014.03.019.

[Gro15] Grossi, N.; Sallese, L.; Scippa, A.; Campatelli, G.: Speed-varying cutting force coefficient identification in milling. Precision Engineering 42(2015), pp. 321–334. ISSN 0141-6359. DOI: 10.1016/j.precisioneng.2015.04.006.

[Gur16] Gurdal, O.; Ozturk, E.; Sims, N. D.: Analysis of Process Damping in Milling. Procedia CIRP 55(2016), pp. 152–157. ISSN 22128271. DOI: 10.1016/j.procir.2016.09.012.

[Han83] Hann, V.: Kinetik des Schaftfräsens - Auswirkung auf die Fertigungsgenauigkeit, vol. 66. VDI-Verl., Düsseldorf. ISBN 9783181466025. 1983.

[Has99] Hashimura, M.; Hassamontr, J.; Dornfeld, D. A.: Effect of In-Plane Exit Angle and Rake Angles on Burr Height and Thickness in Face Milling Operation. Journal of Manufacturing Science and Engineering 121(1999), no. 1, p. 13. ISSN 10871357. DOI: 10.1115/1.2830566.

[Has05] Hassan, R.; Cohanim, B.; de Weck, O.; Venter, G.: A Comparison of Particle Swarm Optimization and the Genetic Algorithm. In: 46th AIAA/ASME/ASCE/AHS/ASC Structures, Structural Dynamics and Materials Conference. American Institute of Aeronautics and Astronautics, Reston, VA. ISBN 978-1-62410-065-9. DOI: 10.2514/6.2005-1897. 2005.

[Hem00] Hemami, H.; Özbay, H.: Modeling and control of biological systems with multiple afferent and efferent transmission delays. Journal of Robotic Systems 17(2000), no. 11, pp. 609–622. ISSN 0741-2223. DOI: 10.1002/1097-4563(200011)17:11<609::AID-ROB3>3.0.CO;2-V.

[Hen08] Henninger, C.; Eberhard, P.: Improving the computational efficiency and accuracy of the semi-discretization method for periodic delay-differential equations. European Journal of Mechanics - A/Solids 27(2008), no. 6, pp. 975–985. ISSN 09977538. DOI: 10.1016/j.euromechsol.2008.01.006.

[Hon95] Hong, M. S.; Ehmann, K. F.: Generation of engineered surfaces by the surface-shaping system. International Journal of Machine Tools and Manufacture 35(1995), no. 9, pp. 1269–1290. ISSN 0890-6955. DOI: 10.1016/0890-6955(94)00114-Y.

[Ins02] Insperger, T.; Stépán, G.: Semi-discretization method for delayed systems. International Journal for Numerical Methods in Engineering 55(2002), no. 5, pp. 503–518. ISSN 0029-5981. DOI: 10.1002/nme.505.

[Ins03a] Insperger, T.; Mann, B. P.; Stépán, G.; Bayly, P. V.: Stability of up-milling and down-milling, part 1: Alternative analytical methods. International Journal of Machine Tools and Manufacture 43(2003), no. 1, pp. 25–34. ISSN 0890-6955. DOI: 10.1016/S0890-6955(02)00159-1.

[Ins03b] Insperger, T.; Stépán, G.; Bayly, P. V.; Mann, B. P.: Multiple chatter frequencies in milling processes. Journal of Sound and Vibration 262(2003), no. 2, pp. 333–345. ISSN 0022-460X. DOI: 10.1016/S0022-460X(02)01131-8.

[Ins04] Insperger, T.; Stepan, G.: Stability transition between 1 and 2 degree-of-freedom models of milling. Periodica Polytechnica, Mechanical Engineering 48(2004), no. 1, pp. 27–39. URL `http://www.mm.bme.hu/\protect\unhbox\voidb@x\penalty\@M\inspi/`.

[Ins08] Insperger, T.; Mann, B. P.; Surmann, T.; Stépán, G.: On the chatter frequencies of milling processes with runout. International Journal of Machine Tools and Manufacture 48(2008), no. 10, pp. 1081–1089. ISSN 0890-6955. DOI: 10.1016/j.ijmachtools.2008.02.002.

[Ins11] Insperger, T.; Stépán, G.: Semi-Discretization for Time-Delay Systems - Stability and Engineering Applications: Stability and engineering applications, vol. 178. Springer New York and Springer, New York, 1 edn. ISBN 978-1-4614-0335-7. 2011.

[Jin08] Jing, L. L.; An, Q. L.; Chen, M.: Study on Burr Formation in Face Milling of Stainless Steel with Chamfered Cutting Tool. Advanced Materials Research 53-54(2008), pp. 83–88. ISSN 1662-8985. DOI: 10.4028/www.scientific.net/AMR.53-54.83.

[Kat02] Kataria, A.; Özbay, H.; Hemami, H.: Controller design for natural and robotic systems with transmission delays. Journal of Robotic Systems 19(2002), no. 5, pp. 231–244. ISSN 0741-2223. DOI: 10.1002/rob.10037.

[Kau87] Kaufeld, M.: Milling Tool for Roughing and Smoothing Workpieces. Deutsches Patent- und Markenamt (DE3742942C1). 1987.

[Keg69] Kegg; R. L.: Chatter Behaviour at Low Cutting Speed. Annals of the CIRP 17(1969), pp. 97–106.

[Ken95] Kennedy, J.; Eberhart, R.: Particle swarm optimization. In: Proceedings / 1995 IEEE International Conference on Neural Networks, the University of Western Australia, Perth, Western Australia, 27 November - 1 December 1995, vol. 4, pp.

1942–1948. IEEE Service Center, Piscataway, NJ. ISBN 0-7803-2768-3. DOI: 10.1109/ICNN.1995.488968. 1995.

[Kle08] Kleckner, J.: Abweichungen in der theoretischen Stabilitätsgrenze als Folge einer nur hinreichend genauen linearen Approximation der Prozess- und Strukturdynamik. In: K. Weinert (Ed.), Spanende Fertigung. Vulkan Verlag, 5 edn. 2008.

[Kli82] Kline, W. A.; DeVor, R. E.; Lindberg, J. R.: The prediction of cutting forces in end milling with application to cornering cuts. International Journal of Machine Tool Design and Research 22(1982), no. 1, pp. 7–22. ISSN 0020-7357. DOI: 10.1016/0020-7357(82)90016-6.

[Kli83] Kline, W.; DeVor, R.: The effect of runout on cutting geometry and forces in end milling. International Journal of Machine Tool Design and Research 23(1983), no. 2-3, pp. 123–140. ISSN 0020-7357. DOI: 10.1016/0020-7357(83)90012-4.

[Koc13] Koca, R.; Budak, E.: Optimization of Serrated End Mills for Reduced Cutting Energy and Higher Stability. Procedia CIRP 8(2013), pp. 570–575. ISSN 22128271. DOI: 10.1016/j.procir.2013.06.152.

[Krü13] Krüger, M.; Denkena, B.: Model-based identification of tool runout in end milling and estimation of surface roughness from measured cutting forces. The International Journal of Advanced Manufacturing Technology 65(2013), no. 5-8, pp. 1067–1080. ISSN 0268-3768. DOI: 10.1007/s00170-012-4240-y.

[Krü14] Krüger, M.: Modellbasierte Online-Bewertung von Fräsprozessen. Dr.-Ing.-Dissertation, Leibniz-Universität Hannover, Institut für Fertigungstechnik und Werkzeugmaschinen. 2014.

[Kum07] Kumanchik, L. M.; Schmitz, T. L.: Improved analytical chip thickness model for milling. Precision Engineering 31(2007), no. 3, pp. 317–324. ISSN 0141-6359. DOI: 10.1016/j.precisioneng.2006.12.001.

[Lac09] López de Lacalle, L.; Lamikiz, A.: Machine Tools for High Performance Machining. Springer London, London. ISBN 978-1-84800-379-8. DOI: 10.1007/978-1-84800-380-4. 2009.

[Lan04] Landon, Y.; Segonds, S.; Lascoumes, P.; Lagarrigue, P.: Tool positioning error (TPE) characterisation in milling. International Journal of Machine Tools and Manufacture 44(2004), no. 5, pp. 457–464. ISSN 0890-6955. DOI: 10.1016/j.ijmachtools.2003.12.001.

[Lan05] Lange, M.: Hochleistungsfräsen von Aluminium-Bauteilen für den Flugzeugbau. In: K. Weinert (Ed.), Spanende Fertigung, pp. 59–67. Vulkan Verl., Essen. ISBN 978-3802729355. 2005.

[Lau13] Lauro, C. H.; Brandão, L. C.; Ribeiro Filho, L. M.: Monitoring the temperature of the milling process using infrared camera. Scientific Research and Essays 8(2013), no. 23, pp. 1112–1120. DOI: 10.5897/SRE12.579.

[Lee95] Lee, B. Y.; Tarng, Y. S.; Ma, S. C.: Modeling of the process damping force in chatter vibration. International Journal of Machine Tools and Manufacture 35(1995), no. 7, pp. 951–962. ISSN 0890-6955. DOI: 10.1016/0890-6955(94)00046-M.

[Lee96] Lee, P.; Altintas, Y.: Prediction of ball-end milling forces from orthogonal cutting data. International Journal of Machine Tools and Manufacture 36(1996), no. 9, pp. 1059–1072. ISSN 0890-6955. DOI: 10.1016/0890-6955(95)00081-X. URL `http://www.sciencedirect.com/science/article/B6V4B-3VTW8G1-7/2/7709ba6051f08d51cc3837e20d346761`.

[Lee07] Lee, K.; Kim, H.; Park, S.: A run-out measuring method using modeling and simulation in four-fluted end milling. Journal of Materials Processing Technology 187-188(2007), pp. 207–211. ISSN 0924-0136. DOI: 10.1016/j.jmatprotec.2006.11.203.

[Lös15] Löser, M.: Ein Beitrag zur effizienten Analyse der Prozessstabilität beim HSC-Fräsen. Ph.D. thesis, Technische Universität Dresden, Fak. Maschinenwesen, Inst. für Werkzeugmaschinen und Steuerungstechnik, Dresden. URL `http://www.worldcat.org/oclc/908597872`. 2015.

[Lun08] Lunze, J.: Regelungstechnik 2: Mehrgrößensysteme, Digitale Regelung, vol. 2. Springer, Berlin, 5 edn. ISBN 9783540784623. 2008.

[Ma16] Ma, Y.; Wan, M.; Zhang, W.: Effect of Cutter Runout on Chatter Stability of Milling Process. In: Y. Li; J. Gao; P. Maropoulos (Eds.), The 9th International Conference on Digital Enterprise Technology, *Procedia CIRP*, vol. 56, pp. 115–118. ISBN 9781510832855. DOI: 10.1016/j.procir.2016.10.034. 2016.

[Man03] Mann, B. P.; Insperger, T.; Bayly, P. V.; Stépán, G.: Stability of up-milling and down-milling, part 2: Experimental verification. International Journal of Machine Tools and Manufacture 43(2003), no. 1, pp. 35–40. ISSN 0890-6955. DOI: 10.1016/S0890-6955(02)00160-8.

[Mar41] Martellotti, M. E.: An Analysis of the Milling Process. Transactions of the ASME 63(1941), pp. 667–695.

[Mer65] Merritt, H. E.: Theory of Self-Excited Machine-Tool Chatter: Contribution to Machine-Tool Chatter Research—1. Journal of Engineering for Industry 87(1965), no. 4, p. 447. ISSN 00220817. DOI: 10.1115/1.3670861.

[Mic14] Michalik, P.; Zajac, J.; Hatala, M.; Mital, D.; Fecova, V.: Monitoring surface roughness of thin-walled components from steel C45 machining down and up milling. Measurement 58(2014), pp. 416–428. ISSN 0263-2241. DOI: 10.1016/j.measurement.2014.09.008.

[Mon91] Montgomery, D.; Altintas, Y.: Mechanism of cutting force and surface generation in dynamic milling. Journal of Engineering for Industry 113(1991), no. 2, pp. 160–168. DOI: 10.1115/1.2899673. URL `http://link.aip.org/link/?MSE/113/160/1`.

[Mon13] Monnin, J.: Active structural methods for chatter mitigation in milling process. Ph.D. thesis, ETH Zurich, Institute for Machine Tools and Manufacturing (IWF). DOI: 10.3929/ethz-a-009920936. 2013.

[Muk05] Mukhopadhyay, B.; Bhattacharyya, R.: Dynamics of a delayed epidemiological model with nonlinear incidence: The role of infected incidence fraction. Journal of Biological Systems 13(2005), no. 04, pp. 341–361. DOI: 10.1142/S0218339005001562.

[Olg97] Olgac, N.; Hosek, M.: Active Vibration Absorption Using Delayed Resonator With Relative Position Measurement. Journal of Vibration and Acoustics 119(1997), no. 1, p. 131. DOI: 10.1115/1.2889680.

[Opi66] Opitz, H.; Dregger, E. U.; Roese, H.: Improvement of the dynamic stability of the milling process by irregular tooth pitch. In: Proceedings of the 7th M.T.D.R, pp. 213–227. 1966.

[Per07] Perez, J. R.; Basterrechea, J.: Comparison of Different Heuristic Optimization Methods for Near-Field Antenna Measurements. IEEE Transactions on Antennas and Propagation 55(2007), no. 3, pp. 549–555. ISSN 0018-926X. DOI: 10.1109/TAP.2007.891508.

[Pol06] Polevoi, I.: Fräse. Deutsches Patent- und Markenamt (DE102004040580A1). 2006.

[Por80] Porter, C. T.: Strength in Machine Tools. In: American Society of Mechanical Engineers (Ed.), Transactions of the American Society of Mechanical Engineers, vol. 1. ASME, New York. 1880.

[Rah09] Rahnama, R.; Sajjadi, M.; Park, S. S.: Chatter suppression in micro end milling with process damping. Journal of Materials Processing Technology 209(2009), no. 17, pp. 5766–5776. ISSN 0924-0136. DOI: 10.1016/j.jmatprotec.2009.06.009.

[Ran99] Ranganath, S.; Narayanan, K.; Sutherland, J. W.: The Role of Flank Face Interference in Improving the Accuracy of Dynamic Force Predictions in Peripheral Milling. Journal of Manufacturing Science and Engineering 121(1999), no. 4, pp. 593–599. DOI: 10.1115/1.2833071.

[Rio12] Rioja, R. J.; Liu, J.: The Evolution of Al-Li Base Products for Aerospace and Space Applications. Metallurgical and Materials Transactions A 43(2012), no. 9, pp. 3325–3337. ISSN 1073-5623. DOI: 10.1007/s11661-012-1155-z.

[Rub17] Rubeo, M. A.; Schmitz, T. L.: Amplitude Ratio: A New Metric for Milling Stability Identification. Procedia Manufacturing 10(2017), pp. 351–362. ISSN 23519789. DOI: 10.1016/j.promfg.2017.07.004.

[Sch07] Schmitz, T. L.; Couey, J.; Marsh, E.; Mauntler, N.; Hughes, D.: Runout effects in milling: Surface finish, surface location error, and stability. International Journal of Machine Tools and Manufacture 47(2007), no. 5, pp. 841–851. ISSN 08906955. DOI: 10.1016/j.ijmachtools.2006.06.014.

[Sch09] Schmitz, T. L.; Smith, K. S.: Machining Dynamics: Technique and indications. Springer US, Boston, MA. ISBN 978-0-387-09645-2. DOI: 10.1007/978-0-387-09645-2. 2009.

[Sel09] Sellmeier, V.; Hackelöer, F.; Denkena, B.: Process Damping in Milling - Measurement of Process Damping Forces for Chamfered Tools by Means of an Electromagnetically Guided Spindle. Proceedings of the 12th CIRP Conference on Modelling of Machining Operations (2009), no. 2, pp. 911–918.

[Sel11] Sellmeier, V.; Denkena, B.: Stable Islands in the Stability Chart of Milling Processes Due to Unequal Tooth Pitch. International Journal of Machine Tools and Manufacture 51(2011), no. 2, pp. 152–164. ISSN 0890-6955. DOI: 10.1016/j.ijmachtools.2010.09.007.

[Sel12a] Sellmeier, V.: Über den Einfluss der Werkzeuggestalt auf die dynamische Stabilität des Fräsprozesses. Dr.-Ing.-Dissertation, Leibniz-Universität Hannover, Institut für Fertigungstechnik und Werkzeugmaschinen. 2012.

[Sel12b] Sellmeier, V.; Denkena, B.: High speed process damping in milling. CIRP Journal of Manufacturing Science and Technology 5(2012), no. 1, pp. 8–19. ISSN 1755-5817. DOI: 10.1016/j.cirpj.2011.12.001.

[Ser01] Serwa, R.: Roughing and finishing rotary tool apparatus and method. U.S. Patent (US20020090273A1). 2001.

[Shi96] Shirase, K.; Altintaş, Y.: Cutting force and dimensional surface error generation in peripheral milling with variable pitch helical end mills. International Journal of Machine Tools and Manufacture 36(1996), no. 5, pp. 567–584. ISSN 0890-6955. DOI: 10.1016/0890-6955(95)00063-1.

[Sil05] Silva, C. W. d.: Vibration and Shock Handbook. Mechanical engineering series. Taylor & Francis, Boca Raton. ISBN 978-0-8493-1580-0. 2005.

[Sla65] Slavíček, J.: The effect of irregular tooth pitch on stability of milling. In: Proceedings of the 6th M.T.D.R Conference, pp. 15–22. 1965.

[Smi90] Smith, S.; Tlusty, J.: Update on High-Speed Milling Dynamics. Journal of Engineering for Industry 112(1990), no. 2, pp. 142–149. DOI: 10.1115/1.2899557.

[Smi00] Smithey, D. W.; Kapoor, S. G.; DeVor, R. E.: A worn tool force model for three-dimensional cutting operations. International Journal of Machine Tools and Manufacture 40(2000), no. 13, pp. 1929–1950. ISSN 0890-6955. DOI: 10.1016/S0890-6955(00)00017-1.

[Son13] Song, G.; Li, J.; Sun, J.: Approach for modeling accurate undeformed chip thickness in milling operation. The International Journal of Advanced Manufacturing Technology 68(2013), no. 5-8, pp. 1429–1439. ISSN 0268-3768. DOI: 10.1007/s00170-013-4932-y.

[Sri14] Srivatsan, T. S.; Lavernia, E. J.; Eswara Prasad, N.; Kutumbarao, V. V.: Quasi-Static Strength, Deformation, and Fracture Behavior of Aluminum–Lithium Alloys. In: N. E. Prasad; A. A. Gokhale; R. J. H. Wanhill (Eds.), Aluminum-lithium alloys, pp. 305–339. Elsevier Butterworth-Heinemann, Oxford. ISBN 978-0-12-401698-9. DOI: 10.1016/B978-0-12-401698-9.00010-0. 2014.

[Sté14] Stépán, G.; Munoa, J.; Insperger, T.; Surico, M.; Bachrathy, D.; Dombovari, Z.: Cylindrical milling tools: Comparative real case study for process stability. CIRP Annals - Manufacturing Technology 63(2014), no. 1, pp. 385–388. ISSN 0007-8506. DOI: 10.1016/j.cirp.2014.03.137.

[Sto70] Stone, B.: The Effect on the Chatter Behavior of Machine Tools of Cutters with Different Helix Angles on Adjacent Teeth. In: Advances in Machine Tool Design and Research, Proceedings of the 11th International MTDR Conference, University of Birmingham, Vol. A, pp. 169–180. 1970.

[Sub13] Subramanian, M.; Sakthivel, M.; Sooryaprakash, K.; Sudhakaran, R.: Optimization of Cutting Parameters for Cutting Force in Shoulder Milling of Al7075-T6 Using Response Surface Methodology and Genetic Algorithm. Procedia Engineering 64(2013), pp. 690–700. ISSN 18777058. DOI: 10.1016/j.proeng.2013.09.144.

[Sza04] Szalai, R.; Stepan, G.; Hogan, S. J.: Global dynamics of low immersion high-speed milling. Chaos (Woodbury, N.Y.) 14(2004), no. 4, pp. 1069–1077. ISSN 1054-1500. DOI: 10.1063/1.1807395.

[Tak13] Takuya, K.; Suzuki, N.; Hino, R.; Shamoto, E.: A Novel Design Method of Variable Helix Cutters to Attain robust Regeneration Suppression. Procedia CIRP 8(2013), pp. 363–367. ISSN 22128271. DOI: 10.1016/j.procir.2013.06.117.

[Tan07] Tang, Z.; White, J.; Chiasson, J.; Birdwell, J. D.: Modeling and Closed Loop Control for Resource-Constrained Load Balancing with Time Delays in Parallel Computations. In: J. Chiasson; J. J. Loiseau (Eds.), Applications of Time Delay Systems, vol. 352, pp. 57–76. Springer Berlin Heidelberg. ISBN 978-3-540-49556-7. 2007.

[Tan09] Tang, Z. T.; Liu, Z. Q.; Pan, Y. Z.; Wan, Y.; Ai, X.: The influence of tool flank wear on residual stresses induced by milling aluminum alloy. Journal of Materials Processing Technology 209(2009), no. 9, pp. 4502–4508. ISSN 0924-0136. DOI: 10.1016/j.jmatprotec.2008.10.034.

[Tay07] Taylor, F. W.: On the Art of Cutting Metals. The American Society of Mechanical Engineers, New York. URL `http://catalog.hathitrust.org/Record/006563337`. 1907.

[Tlu78] Tlusty, J.: Analysis of the state of research in cutting dynamics. Annals of the CIRP 27(1978), no. 2, pp. 583–589.

[Tlu81] Tlusty, J.; Ismail, F.: Basic Non-Linearity in Machining Chatter. CIRP Annals - Manufacturing Technology 30(1981), no. 1, pp. 299–304. ISSN 0007-8506. DOI: 10.1016/S0007-8506(07)60946-9.

[Tlu83] Tlusty, J.; Zaton, W.; Ismail, F.: Stability Lobes in Milling. CIRP Annals - Manufacturing Technology 32(1983), no. 1, pp. 309–313. ISSN 0007-8506. DOI: 10.1016/S0007-8506(07)63411-8.

[Tlu86] Tlusty, J.: Dynamics of High-Speed Milling. Journal of Engineering for Industry 108(1986), no. 2, pp. 59–67. DOI: 10.1115/1.3187052.

[Tob61] Tobias, S.: Machine tool vibration research. International Journal of Machine Tool Design and Research 1(1961), no. 1-2, pp. 1–14. ISSN 0020-7357. DOI: 10.1016/0020-7357(61)90040-3.

[Tön13] Tönshoff, H. K.; Denkena, B.: Basics of Cutting and Abrasive Processes. Springer Berlin Heidelberg. DOI: 10.1007/978-3-642-33257-9. 2013.

[Tre03] Trelea, I. C.: The particle swarm optimization algorithm: Convergence analysis and parameter selection. Information Processing Letters 85(2003), no. 6, pp. 317–325. ISSN 00200190. DOI: 10.1016/S0020-0190(02)00447-7.

[Tun12] Tunç, L.; Budak, E.: Effect of cutting conditions and tool geometry on process damping in machining. International Journal of Machine Tools and Manufacture 57(2012), no. 0, pp. 10–19. ISSN 0890-6955. DOI: 10.1016/j.ijmachtools.2012.01.009.

[Tur07] Turner, S.; Merdol, D.; Altintas, Y.; Ridgway, K.: Modelling of the stability of variable helix end mills. International Journal of Machine Tools and Manufacture 47(2007), no. 9, pp. 1410–1416. ISSN 0890-6955. DOI: 10.1016/j.ijmachtools.2006.08.028.

[Tyl13] Tyler, C. T.; Schmitz, T. L.: Analytical process damping stability prediction. Journal of Manufacturing Processes 15(2013), no. 1, pp. 69–76. ISSN 15266125. DOI: 10.1016/j.jmapro.2012.11.006.

[Uhl11] Uhlmann, E.; Rasper, P.: Influences on specific cutting forces and their impact on the stability behaviour of milling processes. Production Engineering 5(2011), no. 2, pp. 175–181. ISSN 0944-6524. DOI: 10.1007/s11740-010-0296-4.

[Van65] Vanherck, P.: Increasing Milling Machine Productivity by Use of Cutters with Non-Constant Cutting-Edge Pitch. In: Proceedings of the 6th M.T.D.R Conference, pp. 947–960. DOI: 10.1016/B978-0-08-012629-6.50017-1. 1965.

[Var07] Vareille, J.; Parc, P. L.; Marcé, L.: Web Remote Control of Mechanical Systems: Delay Problems and Experimental Measurements of Round Trip Time. In: J. Chiasson; J. J. Loiseau (Eds.), Applications of Time Delay Systems, vol. 352, pp. 117–132. Springer Berlin Heidelberg. ISBN 978-3-540-49555-0. 2007.

[Wal99] Waldorf, D.; Kapoor, S. G.; DeVor, R. E.: Worn Tool Forces Based on Ploughing Stresses. In: Transactions of the North American Manufacturing Research Institution of SME, vol. 27, pp. 165–170. 1999.

[Wan96] Wang, J.-J. J.; Liang, S. Y.: Chip Load Kinematics in Milling With Radial Cutter Runout. Journal of Engineering for Industry 118(1996), no. 1, p. 111. ISSN 00220817. DOI: 10.1115/1.2803631.

[Wan03] Wang, J.-J.; Zheng, C. M.: Identification of cutter offset in end milling without a prior knowledge of cutting coefficients. International Journal of Machine Tools and Manufacture 43(2003), no. 7, pp. 687–697. ISSN 0890-6955. DOI: 10.1016/S0890-6955(03)00028-2.

[Wan09] Wan, M.; Zhang, W.-H.; Dang, J.-W.; Yang, Y.: New procedures for calibration of instantaneous cutting force coefficients and cutter runout parameters in peripheral milling. International Journal of Machine Tools and Manufacture 49(2009), no. 14, pp. 1144–1151. ISSN 0890-6955. DOI: 10.1016/j.ijmachtools.2009.08.005.

[Wei99] Weinert, K.: Trockenbearbeitung und Minimalmengenkühlschmierung. Springer Berlin Heidelberg, Berlin and Heidelberg. ISBN 978-3-642-63671-4. DOI: 10.1007/978-3-642-58624-8. 1999.

[Wu88] Wu, D. W.: Application of a comprehensive dynamic cutting force model to orthogonal wave-generating processes. International Journal of Mechanical Sciences 30(1988), no. 8, pp. 581–600. ISSN 0020-7403. DOI: 10.1016/0020-7403(88)90101-4.

[Wu89] Wu, D. W.: A New Approach of Formulating the Transfer Function for Dynamic Cutting Processes. Journal of Engineering for Industry 111(1989), no. 1, p. 37. ISSN 00220817. DOI: 10.1115/1.3188730.

[Zat14] Zatarain, M.; Dombovari, Z.: Stability analysis of milling with irregular pitch tools by the implicit subspace iteration method. International Journal of Dynamics and Control 2(2014), no. 1, pp. 26–34. ISSN 2195-268X. DOI: 10.1007/s40435-013-0052-7.

[Zur97] Zurmühl, R.; Falk, S.: Matrizen und ihre Anwendungen 1. Springer Berlin Heidelberg, Berlin, Heidelberg. DOI: 10.1007/978-3-642-17543-5. 1997.

Curriculum Vitae

Persönliches

Name	Roman Grabowski
Geboren	9. Mai 1985 in Bydgoszcz, Polen
Familienstand	verheiratet

Schule

2005	Abitur, Gymnasium Burgdorf

Zivildienst

2005 – 2006	DRK Rettungswache, Burgdorf

Studium

2006 – 2012	Studium des Maschinenbaus an der Leibniz Universität Hannover
2010	Auslandsstudium an der Keio University in Tokio, Japan
2012	Abschluss: Diplom-Ingenieur

Auszeichnungen

2010	Auslandsstipendium, Dr. Jürgen und Irmgard Ulderup Stiftung
2010	Scholarship for Study in Japan, Japan Student Services Organization
2013	Ernst-Blickle-Diplomandenpreis, SEW-Eurodrive-Stiftung

Beruf

2012 – 2017	Wissenschaftlicher Mitarbeiter am Institut für Fertigungstechnik und Werkzeugmaschinen der Leibniz Universität Hannover
seit 2017	IAV, Entwicklungsingenieur